September 2001 • NREL/SR-500-29708

Subcontractor Report

Control and Health Monitoring of Variable-Speed Wind Power Generation Systems

Period of Performance: July 10, 1997 to July 10, 2000

Y.D. Song, M. Bikdash, and M.J. Schulz
North Carolina A&T State University
Greensboro, North Carolina

wable Energy Laboratory

1617 Cole Boulevard
Golden, Colorado 80401-3393

NREL is a U.S. Department of Energy Laboratory
Operated by Midwest Research Institute • Battelle • Bechtel

Contract No. DE-AC36-99-GO10337

September 2001 • NREL/SR-500-29708

Control and Health Monitoring of Variable-Speed Wind Power Generation Systems

Period of Performance: July 10, 1997 to July 10, 2000

Y.D. Song, M. Bikdash, and M.J. Schulz
North Carolina A&T State University
Greensboro, North Carolina

NREL Technical Monitor: Alan Laxson
Prepared under Subcontract No. RCX-7-16469

wable Energy Laboratory

1617 Cole Boulevard
Golden, Colorado 80401-3393

NREL is a U.S. Department of Energy Laboratory
Operated by Midwest Research Institute • Battelle • Bechtel

Contract No. DE-AC36-99-GO10337

NOTICE

Available electronically at http://www.doe.gov/bridge

Available for a processing fee to U.S. Department of Energy
and its contractors, in paper, from:

U.S. Department of Energy
Office of Scientific and Technical Information
P.O. Box 62
Oak Ridge, TN 37831-0062
phone: 865.576.8401
fax: 865.576.5728
email: reports@adonis.osti.gov

Available for sale to the public, in paper, from:

U.S. Department of Commerce
National Technical Information Service
5285 Port Royal Road
Springfield, VA 22161
phone: 800.553.6847
fax: 703.605.6900
email: orders@ntis.fedworld.gov
online ordering: http://www.ntis.gov/ordering.htm

Printed on paper containing at least 50% wastepaper, including 20% postconsumer waste

Preface

Supported by the National Renewable Energy Laboratory (NREL) under subcontract REP No. RCX-7-16469, North Carolina A&T State University initiated a 3-year research project in the field of renewable energy on July 10, 1997. Under the umbrella of this project are three subprojects that were coordinated by Song, Bikdash and Schulz, respectively. This report presents the accomplishments achieved by the PIs during the period from July 10, 1997 to approximately July 10, 2000. The report consists of three parts:

Part 1 Variable Speed Control of Wind Turbines (Song)
Part 2 Furling Analysis of Wind Turbines (Bikdash)
Part 3 Health Monitoring of Wind Turbines (Schulz)

We would like to take this opportunity to express our sincere thanks to our technical monitors at the NREL, Mike Robinson and Alan Laxson, for their technical support and guidance throughout this project.

Table of Contents

Executive Summary

This document reports our accomplishments on variable speed control, furling analysis and health monitoring of wind turbines. It consists of three parts prepared by Song, Bikdash and Schulz, respectively. Publications related to these topics are listed at the end of each part of the report.

In the first part of the report, variable speed control of wind turbines is discussed in detail. The main contributions in this area can be summarized as follows. First we explored a memory-based method for wind speed prediction and wind turbine control. This method is based on observing and generalizing past system responses and control experience. It does not demand detailed information about the system dynamics. Second, we developed a nonlinear excitation control method based on the rotor dynamics and the excitation dynamics. This method achieved smooth and asymptotic rotor speed tracking, and was verified by both analysis and computer simulation. Our third major contribution lies in the derivation of nonlinear pitch control algorithms for variable speed operation of wind turbines. In this method the rotor speed is regulated via a pitch servo-mechanism. Because the pitch angle cannot be adjusted directly and instantly, actuator dynamics were explicitly considered. Three types of pitch actuator dynamics were examined and integrated into the pitch control scheme. We found that with the derived control algorithms, smooth and asymptotic rotor speed tracking is ensured. Most of the results in this report have been published in international journals or presented at international conferences or both. We have also successfully organized a special session on wind turbine control at an international conference[1] and edited a special issue on wind turbine modeling, control, and health monitoring in an international journal[2]. Furthermore, this project has encouraged several students to study renewable energy and related technologies at the master level.

The second part addresses the yaw dynamics of wind turbines. This work falls into three general areas: Modeling, Analysis, and Control. The first major contribution of the modeling effort was in learning neuro-fuzzy models of the aerodynamics from extensive aerodynamic simulation data provided by the computational fluid dynamics code YawDyn. The experimental data can be used for learning, and we modeled the aerodynamics of the rotors and nacelle using simple expressions for the coefficients of power and thrust. These fuzzy implementations are used to alleviate the complexity of real-time simulations. Our second major contribution in modeling was to derive an analytical model for the furling mechanism. We have also developed a methodology for a more systematic multidisciplinary modeling based on Lagrangian differential algebraic equations that will enable us to build a complete model of the turbine from the aerodynamics to the electrical load. We use differential algebraic equations for modeling the dynamics of wind turbines because they allow accurate modeling of the complex dynamics without the need to eliminate the constraint equations which can lead to approximations and is error prone. We have also developed a procedure to design bounded control laws that are applicable because of the limited actuation authority of the proposed actuators.

In the third part of the report, new analytical techniques were developed and tested to detect initial damage to prevent failures of wind turbine rotor blades. The techniques consider the particular requirements for developing a practical wind turbine monitoring system, in terms of cost, materials, size, and life expectancy. Different sensor types were also modeled and tested, including accelerometers, piezoceramic patches, and a scanning laser doppler vibrometer. We performed modeling and simulation of wave propagation in fiberglass plates and evaluated different

[1] American Control Conference, June 1998, Organized by Dr. Y. D. Song (NC A&T) and Dr. M. Robinson (NREL)

[2] Journal of Wind Engineering and Industrial Aerodynamics, Vol. 85, No. 3, April 2000, Organized by Dr. Y. D. Song (NC A&T) and Dr. M. Robinson (NREL).

configurations of passive piezoceramic sensor systems capable of measuring propagating strain waves and identifying damage. We also carried out a preliminary experiment to determine the damage detection capability of piezoceramic sensors and actuators during a static test of a full size wind turbine blade at the National Wind Technology Center, a laboratory of the National Renewable Energy Laboratory in Golden, Colorado. In the experiment, we monitored the stress wave propagation characteristics of the blade while increasing the load level on the monitored blade until blade failure occurred. This experiment indicated that the technique can detect evolving damage in composite wind turbine blades. The effects of the blade stress and curvature on wave propagation were found to be important parameters that need further study to allow us to more accurately predict buckling failure of the blade. The work in this project has also led to a patent application for a new sensor array system for structural health monitoring, and we have developed the initial design of an analogic synthetic bionic system and neural composite material that will give wind turbine blades a human-like sensitivity to pain represented as damage to the material.

Part 1

Variable Speed Control of Wind Turbines

Dr. Yong D. Song

Contents

List of Figures

List of Tables

Summary of Technical Results

Automatic control is essential for efficient and reliable operation of wind power conversion systems. The major objective of this work is to design, analyze, and test new control algorithms for wind turbines. The main contributions in this area can be summarized as follows. First we explored a memory-based method for wind speed prediction and wind turbine control. This method is based on observing and generalizing past system responses and control experience. It does not demand detailed information about the system dynamics. Second, we developed a nonlinear excitation control method using both rotor dynamics and excitation dynamics. This method was shown to achieve smooth and asymptotic rotor speed tracking, as justified by both analysis and computer simulation.

The third major technical result is the derivation of nonlinear pitch control algorithms for variable speed operation of wind turbines. In this method the rotor speed is regulated via a pitch servo-mechanism. Because pitch angle cannot be adjusted directly and instantly, actuator dynamics need to be explicitly considered. We examined three types of pitch actuator dynamics and integrated them into the pitch control scheme. We showed that the derived control algorithms ensured smooth and asymptotic rotor speed tracking.

Technical Description and Discussion

Memory-Based Pitch Control of Wind Turbines

Introduction

Control design for wind power generation systems represents an interesting yet challenging research topic. In contrast to conventional power generation where input energy can be scheduled and regulated, wind energy is not a controllable resource, because of its intermittent and stochastic nature. Most wind turbines operate at fixed rotational speeds. However, fixed-speed operation means that the maximum coefficient of performance is available only at a particular wind speed. A low coefficient of performance is observed for all other wind speeds, which reduces the energy output below what might be expected from variable speed operation. Apparently, if the turbine speed could be adjusted in relation to the wind speed, a higher power output could be realized. Therefore, variable speed control of wind turbines is of practical interest.

The main objective of this work is to develop a memory-based method for variable speed control of wind turbines. Memory-based approaches to solving engineering problems have a long history and having been applied to pattern classification, weather prediction, speech recognition, medical diagnosis, and protein structure prediction among others [1–11]. In this work we focus on the development of short-term (low-order) memory-based control algorithms that allow variable speed operation of wind turbine systems. The proposed control consisted of two parts: one for preliminary compensation and one for memory-based compensation. Analysis and simulation showed that the proposed control method is effective in dealing with system nonlinearities and uncertainties. Several operating conditions with varying wind speeds were tested with satisfactory results. It is worth mentioning that the controller does not require wind speed to be measured or estimated.

System Description

The ability of a wind turbine to extract power from varying wind is a function of three main factors: the wind power available, the power curve of the machine, and the ability of the

machine to respond to wind fluctuations. It is well known that the power produced by a wind turbine is proportional to the cube of the wind speed; that is,

$$P = \frac{1}{2} C_{\mathrm{p}}(\lambda, \beta) \rho \pi R^2 u^3, \qquad \text{(Eq. 1-1)}$$

where ρ is the air density, R is the radius of rotor, β is the pitch angle, u represents wind speed, C_{p} is the power coefficient of the wind turbine calculated from aerodynamic data, and λ denotes the tip-wind speed ratio defined by

$$\lambda = \frac{R\omega}{u}, \qquad \text{(Eq.1-2)}$$

where ω is the rotor speed. Note that C_{p} is a nonlinear function of factors such as blade radius, and pitch angle as well as tip-speed ratio. Typically the power coefficient C_{p} bears the shape as shown in Figure 1-1 [12,13]. Two important observations can be made from this figure:

- If the wind speed is constant, any deviation of rotor speed (due to, for instance, load change) leads to the variation of power efficiency. For instance, consider a wind turbine operating at some "optimal point." If the rotor speed ω increases, λ increases and C_{p} deviates from the "optimal value".
- If the rotor speed is kept constant, any change in wind speed leads to a change in tip-speed ratio (λ), causing the change in power generation efficiency.

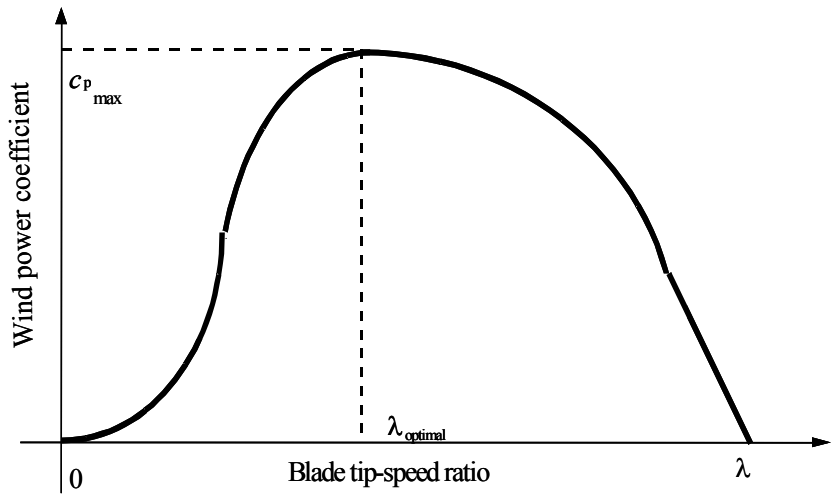

Figure 1-1. Power coefficient versus tip-speed ratio

The important indication of these observations is that variable rotor speed control is essential to achieving maximum power extraction from the potential wind power. Although automatic controls have long been known to increase power quality and reliability, most existing controls are restricted to classical/linear model-based methods which exhibit only limited capability in dealing with varying operational points and external disturbances inherent in such systems.

In this section we explore the application of memory-based concepts to variable speed control of wind turbine systems (WTS). We begin with the discussion of dynamic modeling of WTS.

Wind Turbine Dynamics. Driven by an effective torque τ_r, the wind turbine speed is governed by [12–14]

$$J\dot{\omega} = \tau_r - \tau_s, \tag{Eq.1-3a}$$

where J denotes the moment of inertia of the turbine-transmission-generator (all referred to the turbine shaft), and τ_s represents the generalized shaft torque necessary to turn the generator and to balance the driving torque [14]

$$\tau_r = \frac{0.5C_p\rho\pi R^2u^3}{\omega}. \tag{Eq.1-3b}$$

Expressed at a particular operational point (OP), the above nonlinear model can be approximated by

$$J\dot{\omega} = \alpha_0\omega + \gamma_0 u + d_0\beta, \tag{Eq.1-4}$$

where α_0, γ_0, and d_0 are system parameters depending on the OP. Such a linear approximation model has been widely used in practice [12–15].

However, note that if the wind turbine operates at varying speed, the system parameters are no longer constants. Furthermore, the linear approximation error may become significant as the operational point changes. Therefore, in this work we consider the following modified model

$$J\dot{\omega} = (\alpha_0 + \Delta\alpha)\omega + (d_0 + \Delta d)\beta + \gamma(u) + \aleph(\omega, u, \beta) \tag{Eq.1-5a}$$

$$\beta = cV, \tag{Eq.1-5b}$$

where $\aleph(\omega, u, \beta)$ accounts for the effect of linear approximation, V denotes the control voltage and c is a constant.

For simplicity, the pitch angle is assumed to be proportional to the applied voltage (the more general relationship between the pitch angle and the applied voltage will be addressed in a forthcoming paper). Note that both c and J do not vary with operational point. The modified model as shown in Equation 1-5 seems to be more effective in describing the dynamic behavior of the system. For the purpose of control design, we express Equation 1-5 as:

$$J\dot{\omega} = \alpha_0\omega + d_0cV + L(\gamma, \omega, u, \beta), \tag{Eq.1-6a}$$

with

$$L(.) = \Delta\alpha\omega + \Delta dcV + \gamma(u) + \aleph(\omega, u, \beta), \tag{Eq.1-6b}$$

where $L(.)$ represents the lumped uncertainty of the system that results from varying OP. The precise expression for $L(.)$ is generally unavailable. However, for a practical wind turbine system, such lumped uncertainty does not change abruptly. Hence we assume that

$$\max_{t\geq 0}\left|\frac{dL(.)}{dt}\right| \leq c_0 < \infty, \tag{Eq.1-7}$$

implying that the variation rate of $L(.)$ is finite, as is usually the case in most practical wind power systems.

Operational Modes. To effectively extract wind power while maintaining safe operation, the wind turbine should be driven according to the following three fundamental modes depending on the wind speed, maximum allowable rotor speed and the rated power:

Mode 1 - variable speed/optimum tip-speed ratio

$$u_C \le u \le u_B$$

Mode 2 - constant speed/variable tip-speed ratio

$$u_B \le u \le u_R$$

Mode 3 - variable speed/constant power

$$u_R \le u \le u_F .$$

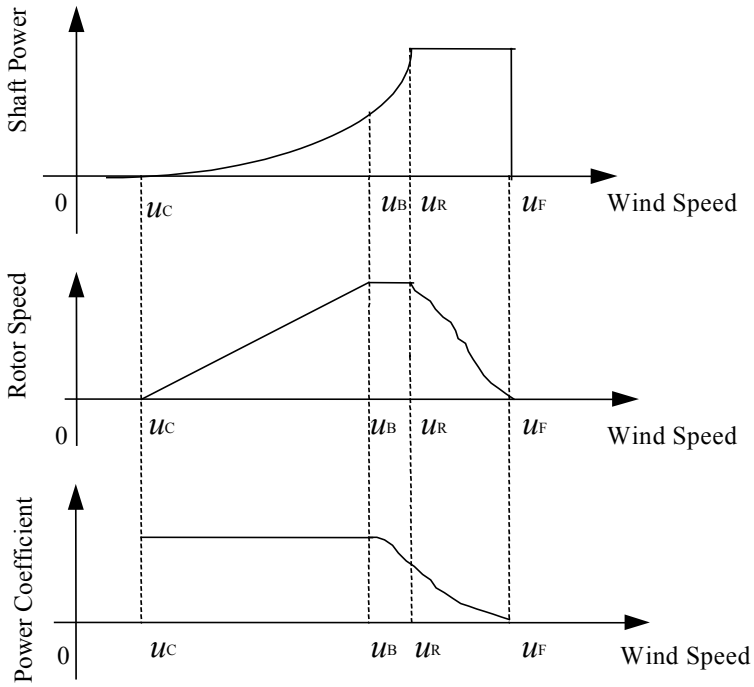

Figure 1-2. The three operation modes of WTS

These three modes are illustrated in Figure 1-2, where u_C is the cut-in wind speed, u_B denotes the wind speed at which the maximum allowable rotor speed is reached, u_R is the wind speed that leads to rated power and u_F is the *furling wind speed* at which the turbine needs to be shut down for protection.

In this work, pitch control is used to adjust the rotor speed so as to match the three operational modes in Figure 1-2. More specifically, the control problem considered here is:

Design a control voltage (V) so that the rotor speed (ω) of the wind turbine closely tracks the desired speed (ω^*), which is specified according to the above three operational modes.

Memory-Based Pitch Control. The control signal consists of two parts:

$$V = V^c + V^m, \tag{Eq.1-8a}$$

where V^c denotes preliminary compensation and V^m represents memory-based compensation. We construct the first part by using the existing information about the system:

$$V^c = \frac{J}{cd_0}(-\frac{\alpha_0}{J}\omega - k_0 e + \dot{\omega}^*), \tag{Eq.1-8b}$$

where $k_0 > 0$ is the design parameter and $e = \omega - \omega^*$ is the rotor speed tracking error.
The second part - memory-based control - is of the following form,

$$V_k^m = w_0 V_{k-1}^m + w_1 e_k + w_2 e_{k-1}, \tag{Eq.1-8c}$$

where V_{k-1}^m stands for the previous control experience recorded at the time instant $t = kT$, $e_{k-1} = \omega_{k-1} - \omega_{k-1}^*$ is the previous tracking error and w_0, w_1 and w_2 are the memory coefficients to be determined. Equation 1-8c is referred to as memory-based compensation because it is built on memorized information. To completely specify V^m, let us examine the closed-loop system. Upon substituting Equations 1-8a and 1-8b into Equation 1-6, we have:

$$J\dot{e} = -k_0 J e + L(.) + d_0 c V^m; \tag{Eq.1-9}$$

that is

$$\dot{e} = -k_0 e + \widetilde{L}(.) + \frac{d_0 c}{J} V^m, \tag{Eq.1-10}$$

where $\widetilde{L} = \frac{1}{J} L(.)$. To incorporate the memorized information, we consider the digital version of Equation 1-10,

$$e_{k+1} = (1 - k_0 T) e_k + T(\widetilde{L}_k + \frac{cd_0}{J} V_k^m), \tag{Eq.1-11}$$

which is obtained by the Euler method as described in [16]. To make use of previous control experience, we shift backward in time one step in Equation 1-11 to obtain:

$$e_k = (1 - k_0 T) e_{k-1} + T(\widetilde{L}_{k-1} + \frac{cd_0}{J} V_{k-1}^m). \tag{Eq.1-12}$$

Subtracting Equation 1-12 from Equation 1-11 gives

$$e_{k+1} = (2 - k_0 T) e_k + (k_0 T - 1) e_{k-1} + T(\widetilde{L}_k - \widetilde{L}_{k-1}) + T\frac{cd_0}{J}[V_k^m - V_{k-1}^m]. \tag{Eq.1-13}$$

Inspecting Equations 1-8c and 1-13 reveals that if the memory coefficients w_0, w_1, and w_2 are specified as

$$w_0 = 1$$
$$w_1 = (k_0 - 2/T)\frac{J}{cd_0}$$
$$w_2 = (1/T - k_0)\frac{J}{cd_0},$$

then the memory-based control Equation 1-8c reduces Equation 1-13 to

$$e_{k+1} = T(\widetilde{L}_k - \widetilde{L}_{k-1}). \tag{Eq.1-14}$$

In view of Equation 1-7, it follows that [16]

$$\begin{aligned} |\, e_{k+1} \,| &= T\left|(\widetilde{L}_k - \widetilde{L}_{k-1})\right| \\ &\le T^2 \max_{t\ge 0}\left|\frac{d\widetilde{L}}{dt}\right| \le T^2 c_0; \end{aligned} \tag{Eq.1-15}$$

that is, bonded stable tracking is ensured with the memory-based control method. Note that with T denoting the sampling period, fairly good tracking precision can be achieved by choosing T properly. It should be mentioned that there is no need to estimate c_0 as defined in Equation 1-7. We only need to use the fact that such a constant exists. Also note that the measurement of wind is not needed, for its effect has been treated as part of external disturbance.

In the implementation, the magnitude of applied voltage needs to be constrained. This can be done by using the following function:

$$\phi(\sigma, z) = \kappa \frac{2}{\sigma}\left(\frac{1 - e^{-\sigma z}}{1 + e^{-\sigma z}}\right),\ \sigma > 0, \tag{Eq.1-16}$$

where κ and σ are constants to be chosen by the designer. Regarding Equation 1-16, we note that

$$i) \qquad \lim_{\sigma \to 0} \phi(z, \sigma) \to \kappa z$$

and

$$ii) \qquad \left|\phi(\sigma, z)\right| \le \kappa \frac{2}{\sigma},$$

meaning that $\phi(.)$ approaches to a linear function as σ tends to a small number and that the magnitude of the control signal can be adjusted by choosing a proper value for σ and κ. The overall control scheme is depicted in Figure 1-3.

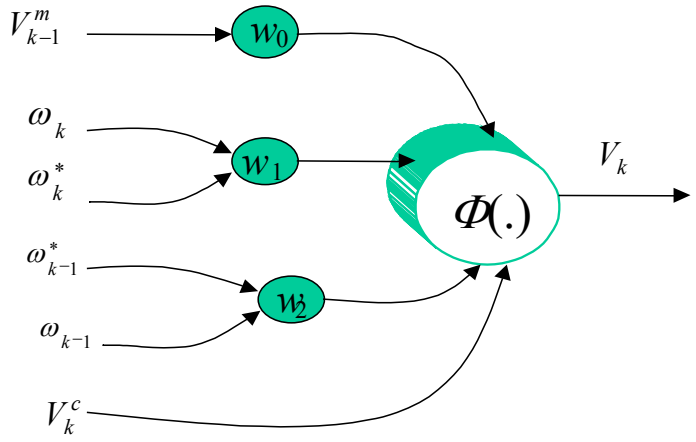

Figure 1-3. Memory-based pitch control

The proposed memory-based control exhibits attractive features that can be summarized as follows:

- The controller is purely built on the past control experience, along with current and most recent system responses. No ad hoc design process is involved.
- The control scheme assumes little prior information about the system - it does not involve estimating specific parameters, repetitive actions, infinite switching frequencies, or discontinuous control.
- The novelty of the proposed method also lies in its flexibility in that the structure of the controller remains unchanged for varying operational conditions. Furthermore, the memory size does not grow with time, which facilitates real-time implementation.

Simulation. To verify the effectiveness of the proposed control method, we performed a series of test with different OPs. The nominal parameters of the wind turbine operating at the OP (u_{OP} = 7.5 *m/s*, ω_{OP}=11 rad/s, β_{OP}= 9 deg) are

$$J = 1270 kg/m^2$$

$$\alpha_0 = 303.9 N.s$$

$$d_0 = -151.9 N.m/\deg$$

and

$$c = 6.8 \deg/V \ .$$

In the simulation, the term that results from wind speed variation is treated as part of the disturbance. The parameters α and d are given by

$$\alpha = \alpha_0 + \Delta\alpha, \quad d = d_0 + \Delta d$$

in which the perturbation of α and d caused by the OP variation is shown in Table 1-1.

Table 1-1. Parameter Variation Resulting from Varying OPs

Operational Point	Variation of α	Variation of d
OP(I)	$\Delta\alpha_1 = 10\%\alpha_0$	$\Delta d_1 = 10\% d_0$
OP(II)	$\Delta\alpha_2 = 20\%\alpha_0$	$\Delta d_2 = 20\% d_0$
OP(III)	$\Delta\alpha_3 = 30\%\alpha_0$	$\Delta d_3 = 30\% d_0$

The variations of the parameters α and d that result from the change in operating conditions are illustrated in Figures 1-4 and 1-5. Observe that variations in both magnitude and rate are involved in these parameters. The design parameters used for simulation are:

$$\kappa = 1, \quad \sigma = 0.1, \quad T = 0.1(\text{sec}), \quad k_0 = 5.$$

The tracking performance in terms of tracking error for the three OPs is depicted in Figure 1-6. Figure 1-6(a) is a two-dimension profile and Figure 1-6(b) is a three-dimension profile. Although significant uncertainty is involved because of the varying OPs, we observed that the proposed control method achieved satisfactory tracking performance over all the operating conditions.

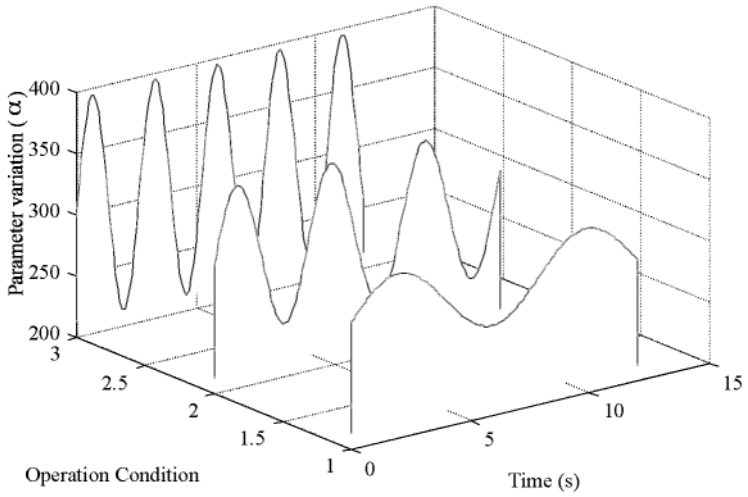

Figure 1-4. Variation of α resulting from varying OPs

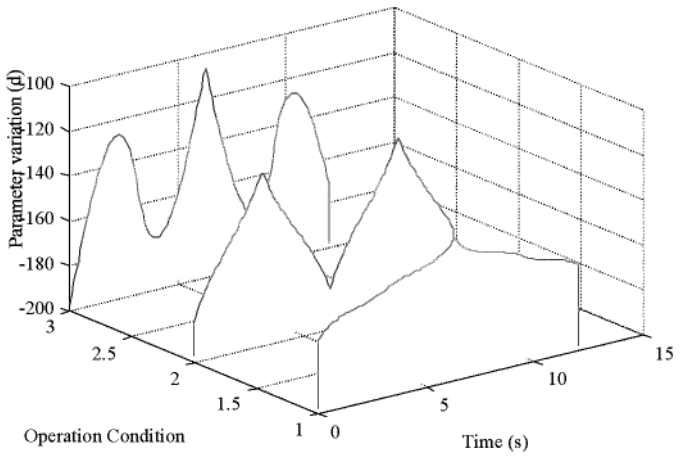

Figure 1-5. Variation of *d* resulting from varying OPs

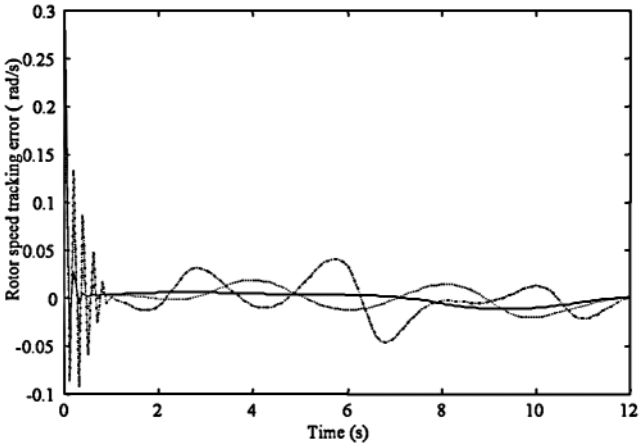

Figure 1-6(a). Rotor speed tracking error (two-dimension profile)

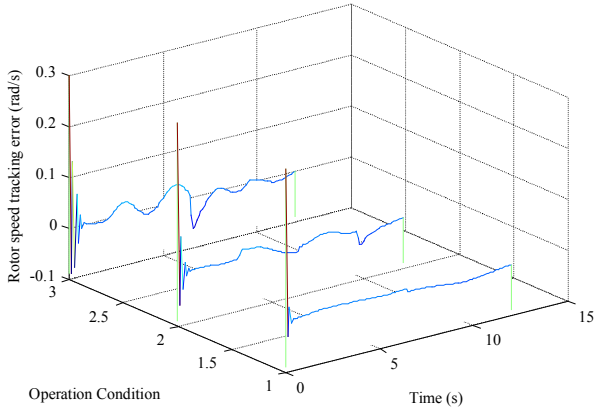

Figure 1-6(b). Rotor speed tracking error (three-dimension profile)

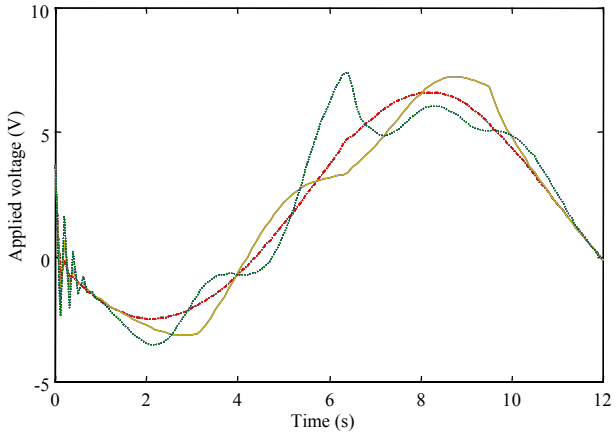

Figure 1-7(a). Applied control voltage (two-dimension profile)

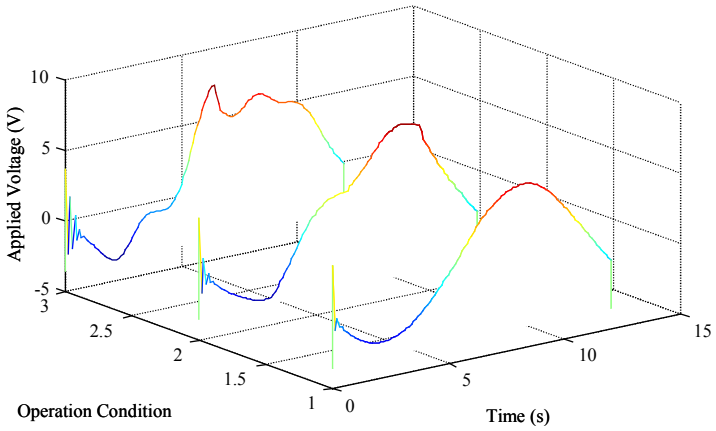

Figure 1-7(b). Applied control voltage (three-dimension profile)

Nonlinear Excitation Control of Wind Turbines

Overview

There has been considerable interest in using wind power to produce electricity [20–29]. Figure 1-8 below represents a schematic wind power generation system (WPGS), where the electric power P_e is produced from the wind power P_{wind} (P_m) via the wind turbine.

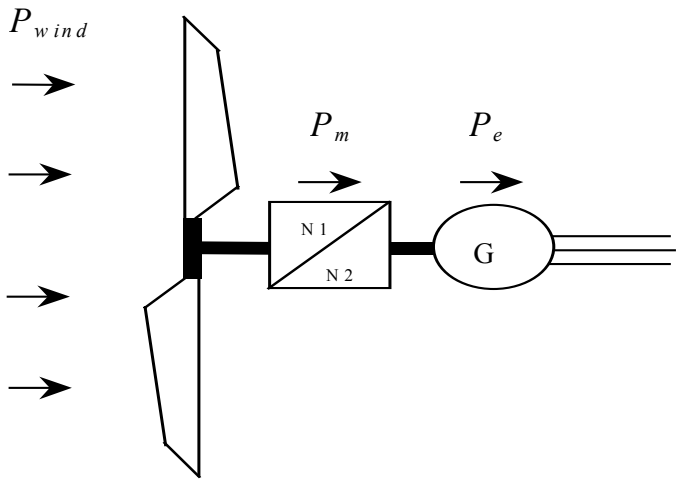

Figure 1-8. A schematic wind power system

In this work we explored a nonlinear method for variable speed control of wind turbines. The objective was to make the rotor speed track the desired speed that is specified according to the three fundamental operating modes described earlier. This is achieved by the corresponding control of regulation in the excitation winding voltage. Such a control scheme leads to more energy output without adding mechanical complexity to the system. It is worth mentioning that the controller does not require the measurement or estimation of wind speed. We simulated the proposed method based on a two-bladed horizontal axis wind turbine similar to DOE MOD-0 [12].

For the purpose of control design, we combine Equations 1-1 and 1-2 to obtain

$$P_m(\omega) = k_1 \omega^3 \qquad \text{(Eq.1-17)}$$

where

$$k_1 = \frac{1}{2} C_p \rho \pi \frac{R^5}{\lambda^3}.$$

In the next section, we derive the dynamic model that governs the behavior of the wind turbine.

Modeling of the System

For a typical wind power generation system, the simplified block diagram shown in Figure 1-9 can be used to illustrate the fundamental work principle. Note that the rotor speed and generator speed are not the same in general, because of the use of the gearbox. The following equations are established to characterize the behavior of the system:

$$T_m - T = J_m \dot{\omega} + B_m \omega + K_m \theta \qquad \text{(Eq.1-18)}$$

and

$$T_p - T_e = J_e\dot{\omega}_e + B_e\omega_e + K_e\theta_e, \quad \text{(Eq.1-19)}$$

where T_m and T_e denote the shaft torque at the turbine end and generator end, respectively, T is the shaft torque before the gearbox; T_p is the shaft torque delivered by the gearbox; J_m and J_e denote the moment of inertia of the turbine and the generator; ω and ω_e represent rotor speed of the turbine and the generator; and B_m, B_e, K_m, and K_e are friction-related constants. By defining the gear ratio γ as

$$\gamma = \frac{\omega_e}{\omega}, \quad \text{(Eq.1-20)}$$

and using the relation

$$T_p\omega_e = T\omega \ , \quad \text{(Eq.1-21)}$$

we obtain from Equations 1-18 and 1-19

$$J\dot{\omega} + B\omega + K\theta = T_m - \gamma T_e, \quad \text{(Eq.1-22)}$$

where

$$J = J_m + \gamma^2 J_e, B = B_m + \gamma^2 B_e, K = K_m + \gamma^2 K_e.$$

In terms of power, Equation 1-22 can be rewritten as

$$J\dot{\omega} + B\omega + K\theta = \frac{P_m}{\omega} - \gamma\frac{P_e}{\omega_e}, \quad \text{(Eq.1-23)}$$

where P_m represents the wind power as defined in Equation 1-17 and P_e is the electrical power given by

$$P_e = \frac{k_g V_l \omega}{x_g}\sin\delta\ c(I_f), \quad \text{(Eq.1-24)}$$

where k_g is a machine related constant, V_l is the phase voltage, x_g is equivalent reactance, δ denotes the rotor angle of the generator, and $c(I_f)$ denotes the field flux.

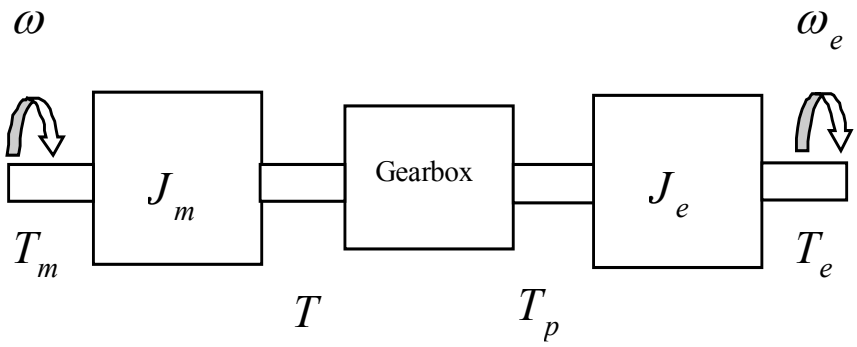

Figure 1-9. A simplified diagram of WPGS

In this work, the nonlinear relation $\phi = c(I_f)$ between the flux (ϕ) and the field current (I_f) is assumed to account for the magnetic saturation property. Substituting for P_m and P_e in Equation 1-23 yields

$$J\dot{\omega} + B\omega + K\theta = k_1\omega_1^{\,2} - \gamma\frac{V_l}{x_g}k_g \sin(\delta)\, c(I_f), \qquad \text{(Eq.1-25)}$$

which can be further expressed as

$$\dot{\omega} = \varphi(\omega) - A(\delta)\, c(I_f), \qquad \text{(Eq.1-26a)}$$

where

$$\varphi(\omega) = \frac{k_1\omega^2 - B\omega - K\theta}{J}, \qquad \text{(Eq.1-26b)}$$

and

$$A(\delta) = \gamma\frac{k_g V_l}{Jx_g}\sin(\delta). \qquad \text{(Eq.1-26c)}$$

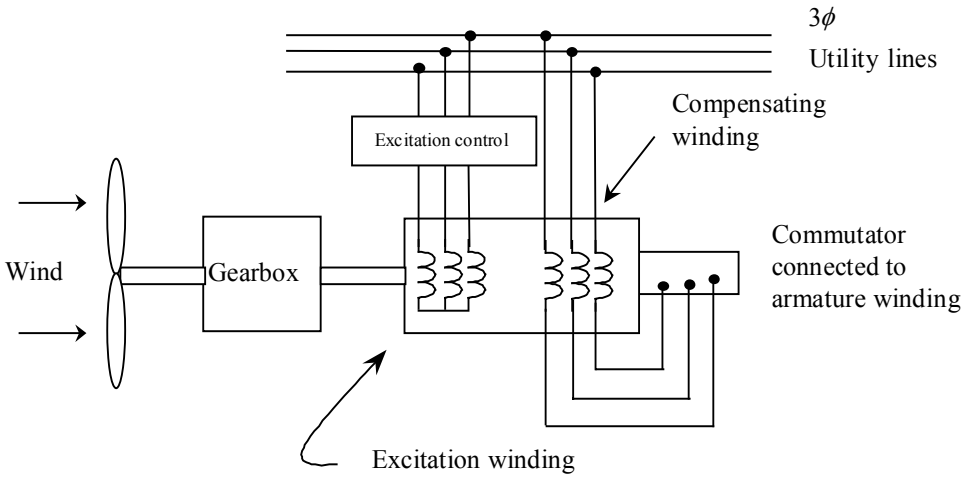

Figure 1-10. Wind Power System with Field Excitation

For a wind power generation system with field excitation as shown in Figure 1-10, the current to the field winding of the synchronous generator is supplied by an exciter with the following dynamics:

$$L\dot{I}_f + I_f R_f = V_f, \tag{Eq.1-27}$$

where L is the inductance of the exciter circuit, I_f is the field current, R_f is the resistance of the rotor field, and V_f denotes the field voltage. To achieve rotor speed tracking, the control design will be based on the mechanic dynamics Equation 1-26 and the excitation dynamics Equation 1-27, as detailed in the next section.

Nonlinear Control Scheme

The rotor speed of the wind turbine is controlled by adjusting the excitation winding voltage. The main idea behind this method is to control the reaction torque (power) of the generator by changing the winding voltage so that the rotor speed is correspondingly adjusted. As such, the control problem can be stated as follows.

Design a control voltage (V_f) such that the rotor speed (ω) of the wind turbine closely tracks the desired speed (ω^*), which is pre-specified according to the three operation modes.

As the first step of controller design, let us define the rotor tracking error as

$$\varepsilon = \omega - \omega^* \tag{Eq.1-28}$$

and rewrite Equation 1-26 in terms of the tracking error (ε) to obtain

$$\begin{aligned} \dot{\varepsilon} &= \varphi(\omega) - A(\delta)c(I_f) - \dot{\omega}^* \\ &= -k_\omega \varepsilon + V, \end{aligned} \tag{Eq.1-29}$$

where

$$V = k_\omega \varepsilon + \varphi(\omega) - A(\delta)c(I_f) - \dot{\omega}^* \tag{Eq.1-30}$$

and $k_\omega > 0$ is a design constant. Before presenting our control algorithms, we need the following result.

Theorem 1

Consider the dynamic system described by

$$\dot{\varepsilon} = -k_\varepsilon \varepsilon + V$$

If $k_\varepsilon > 0$ and $V \to 0$ as $t \to \infty$, then $\varepsilon \to 0$ as $t \to \infty$.

Proof

Upon integrating, we have

$$\varepsilon(t) = e^{-k_\varepsilon t}\varepsilon(0) + \frac{\mu(t)}{e^{k_\varepsilon t}},$$

where

$$\mu(t) = \int_0^t e^{k_\varepsilon \tau} V d\tau \,.$$

Now let us consider two cases: (1) $\mu \to \text{constant}\, t$ as $t \to \infty$ and (2) $\mu \to \infty$ as $t \to \infty$. For case 1, we readily have $\varepsilon \to 0$ as $t \to \infty$. For case 2, on using L'Hopital's rule, we have

$$\lim_{t\to\infty} \frac{\mu(t)}{e^{k_\varepsilon t}} = \lim_{t\to\infty} \frac{\frac{d}{dt}\mu(t)}{k_\varepsilon e^{k_\varepsilon t}}$$

$$= \lim_{t\to\infty} \frac{V}{k_\varepsilon} \to 0 \text{ as } V \to 0.$$

Thus for either case, $\varepsilon \to 0$ as $t \to \infty$ if $k_\varepsilon > 0$ and $V \to 0$ as $t \to \infty$, which completes the proof.

It is interesting to note that because k_ω is a positive constant that the user chooses, we can ensure that the tracking error tends to zero asymptotically if $V \to 0$ as $t \to \infty$. Therefore, the following development is focused on making V tend to zero as $t \to \infty$. To this end, we differentiate Equation 1-30 to obtain

$$\dot{V} = k_\omega \varepsilon + \frac{\partial \varphi}{\partial \omega}\dot{\omega} - \frac{\partial A}{\partial \delta}\dot{\delta}\, c(I_f) - A(\delta)\frac{\partial c}{\partial I_f}\dot{I}_f - \ddot{\omega}^* .$$

Upon substituting for $\dot{\omega}$ from Equation 1-28, $\dot{I}_f$ from Equation 1-27 and $\dot{\varepsilon}$ from Equation 1-29 in the above equation we arrive at

$$\dot{V} = F + bV_f \,, \qquad \text{(Eq.1-31)}$$

where

$$F = k_\omega(\varphi(\omega) - A(\delta)c(I_f) - \dot{\omega}^*) - \frac{\partial A}{\partial \delta}\dot{\delta}\, c(I_f)$$

$$+ \frac{\partial \varphi}{\partial \omega}(\varphi(\omega) - A(\delta)c(I_f)) - \ddot{\omega}^* + A(\delta)\frac{\partial c}{\partial I_f}\frac{R_f}{L}I_f \qquad \text{(Eq.1-32a)}$$

and

$$b = -A(\delta)\frac{\partial c}{\partial I_f}\frac{1}{L} \qquad \text{(Eq.1-32b)}$$

Because we need to have $V \to 0$ as $t \to \infty$, we choose V_f such that

$$V_f = \frac{1}{b}(-F - k_v V) \,, \qquad \text{(Eq.1-33)}$$

where *F* and *b* are defined as in Equation 1-32 and $k_v > 0$ is a design constant chosen by the designer. Consequently, such a control leads to

$$\dot{V} = -k_v V \,, \qquad \text{(Eq.1-34)}$$

implying that $V \to 0$ as $t \to \infty$. To summarize, we have the following theorem.

Theorem 2

Consider the wind power generation system represented by equations Equation 1-26 and Equation 1-27. If the field voltage V_f is adjusted according to Equation 1-33, then rotor speed of the wind turbine (ω) follows the desired speed (ω^*) exponentially.

Proof

The result can be justified by considering the Lyapunov function candidate

$$L = 0.5e^2 + 0.5V^2 \,,$$

which leads to

$$\begin{aligned} \dot{L} &= -\begin{bmatrix} \varepsilon \\ V \end{bmatrix}^T \begin{bmatrix} k_\varepsilon & -1 \\ 0 & k_v \end{bmatrix} \begin{bmatrix} \varepsilon \\ V \end{bmatrix} \le -\lambda_{\min}(k_\varepsilon, k_v) \left\| \begin{matrix} \varepsilon \\ V \end{matrix} \right\|^2 \\ &= -\lambda_{\min}(k_\varepsilon, k_v) L. \end{aligned}$$

Regarding the control scheme, the following convergence result can be established.

Theorem 3

The convergent rate of the tracking error with the proposed control can be found as $e^{-k_0 t}$, where $k_0 = \min(k_\omega, k_v)$.

Proof

In fact, from Equations 1-29 and 1-34, we have

$$\varepsilon(t) = \varepsilon(0)e^{-k\omega t} + e^{-k\omega t} \int_0^t e^{k\omega t} V(\tau) d\tau$$

and

$$V(t) = V(0)e^{-k_v t} \,.$$

Therefore, it can be verified that

$$\varepsilon(t) = \begin{cases} \varepsilon(0)e^{-k\omega t} + V(0)te^{-k\omega t} & \text{if } k_\omega = k_v \\ \varepsilon(0)e^{-k\omega t} + \dfrac{V(0)}{k_v - k_\omega}(e^{-k\omega t} - e^{-k_v t}) & \text{otherwise} \end{cases}$$

implying the convergent rate of the tracking error is at least k_0.

Remarks

- The design and implementation of the proposed control turns out to be fairly simple because it involves only two straightforward steps: choosing k_ω, k_v and generating V_f as in Equation 1-33.

- The idea is to control V_f, so that I_f is controlled. This, in turn, leads to the change of the flux ϕ. Thus, the rotor speed is correspondingly adjusted.

Table 1-2. Wind Turbine Specifications

Allowable rotor speed	40 r/m
Generator output power	100 kW
Optimal coefficient of performance $C_{p\max}$	0.375
Cut-in wind speed u_c	4.3 m/s
Rated wind speed u_r	7.7 m/s
Furling wind speed u_f	17.9 m/s
Rotor diameter	37.5 m
Hub height	30 m
Coning angle	7°
Effective swept area	1072 m^2
Weight of blades	2090 kg
Generator voltage	480 V

Simulation Study

We performed the simulation study to verify the proposed control strategy. A two-bladed horizontal-axis wind turbine similar to DOE MOD-0 [12] as shown in Figure 1-11 was considered. Figure 1-12 illustrates the detail structure inside the wind turbine. System parameters used for simulation are:

$$R_f = 0.02\Omega, L = 0.001H, x_g = 0.4\Omega$$

and

$$V_l = 440V, J = 16Kgm^2, P = 8, f = 60Hz, k_2 = 5\times10^{-5}.$$

The specifications of the wind turbine are given in Table 1-2.

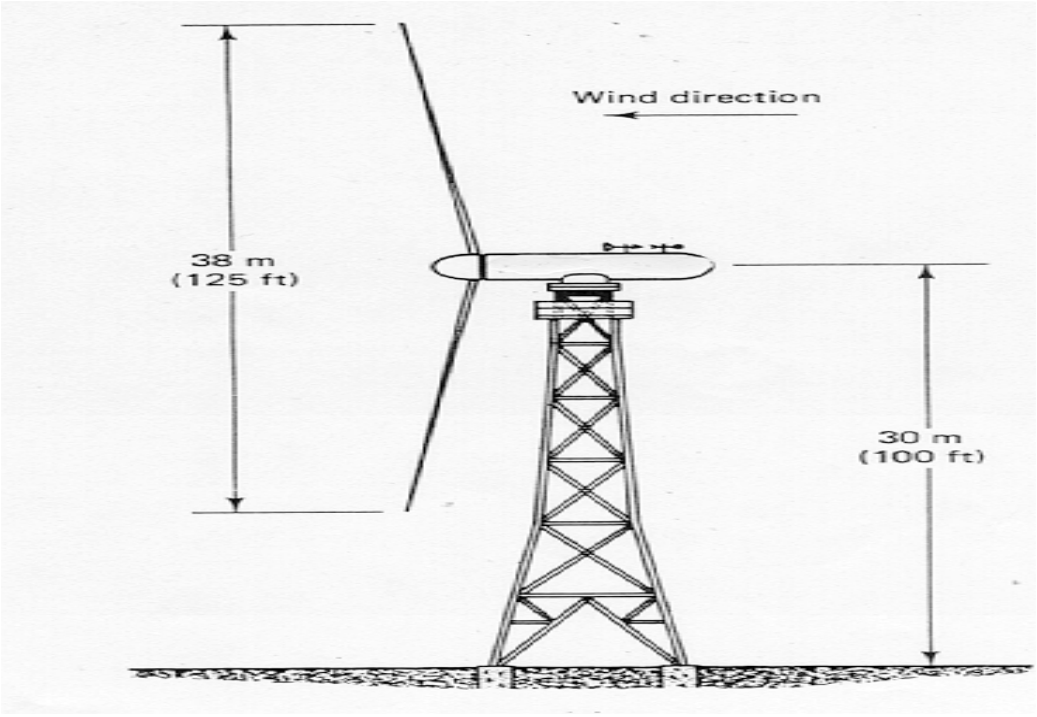

Figure 1-11. General view of MOD-0 wind turbine

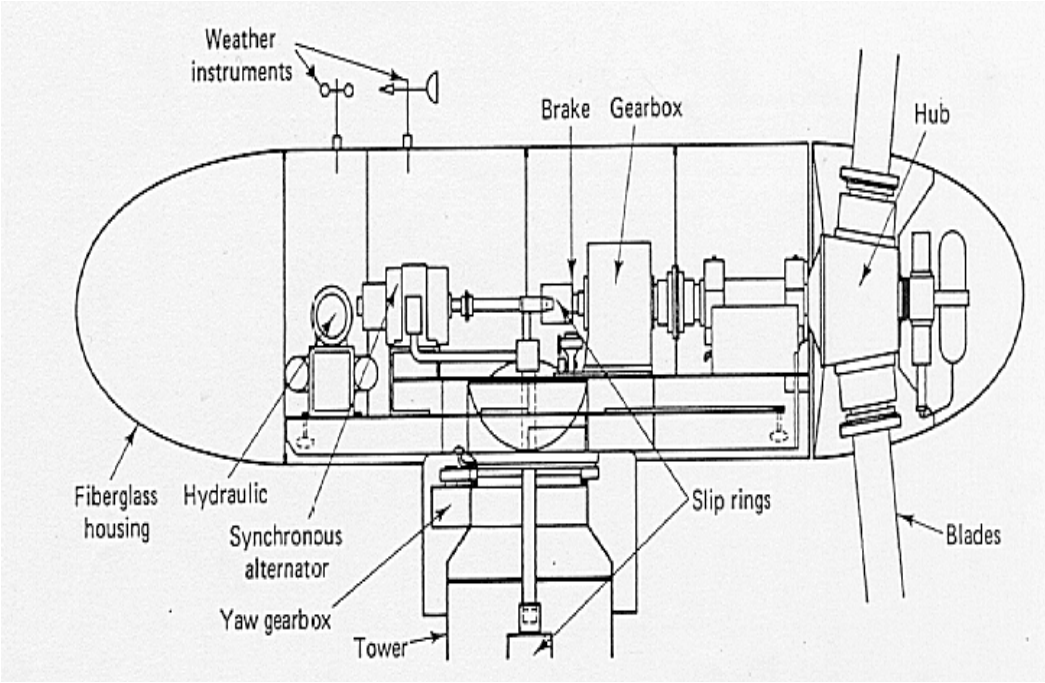

Figure 1-12. Superstructure and equipment of MOD-0

The control parameters were chosen as

$$k_\omega = 150, \quad k_v = 60.$$

The first case considered is the tracking of rotor speed to a sine wave. With the proposed control scheme, we saw the tracking performance illustrated by Figure 1-13. The control voltage is shown in Figure 1-14.

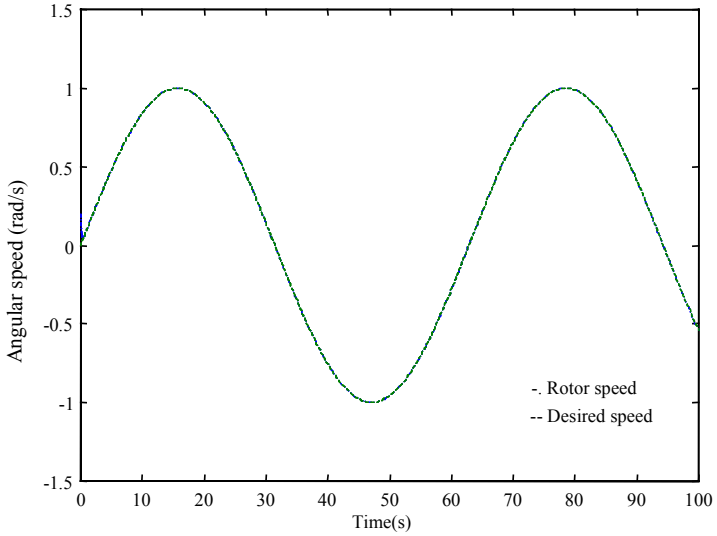

Figure 1-13a. Tracking process

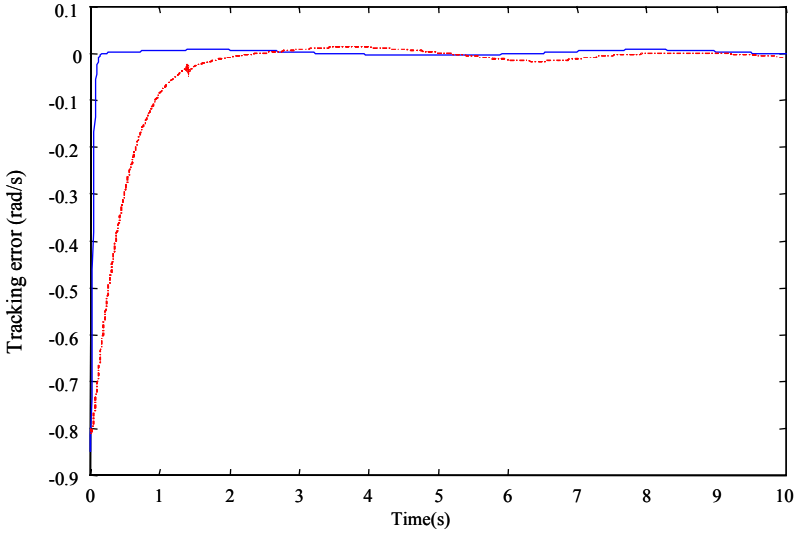

Figure 1-13b. Tracking error

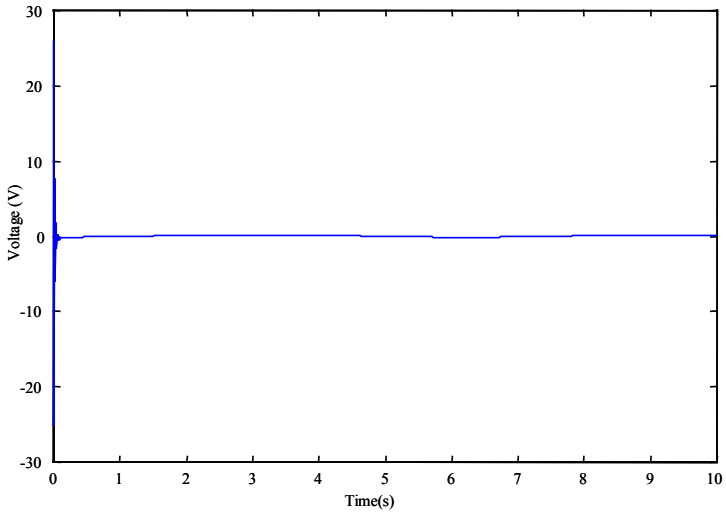

Figure 1-14. Applied control voltage

The next simulation considers a more practical desired rotor speed trajectory motivated by the three operational modes described earlier. Namely, the rotor speed (ω) is to be adjusted to follow the desired trajectory given below

$$\omega^* = \begin{cases} 0 & u(k) < u_c \\ X_m(1+\sin(\frac{\pi}{2}\frac{(u(k)-s_1)}{d_1}) & u(k) < u_r \\ X_m & u(k) < u_f, \\ X_m(1-\sin(\frac{\pi}{2}\frac{(u(k)-s_2)}{d_2}) & u(k) < u_s \\ 0 & u(k) > u_s \end{cases} \quad \text{(Eq.1-35)}$$

where

$$s_1 = \frac{u_c + u_r}{2}$$

$$d_1 = \frac{u_r - u_c}{2}$$

$$s_2 = \frac{u_f + u_s}{2}$$

$$d_2 = \frac{u_s - u_f}{2}$$

$$u_s = 21.3 \text{ m/s}$$

and

$$X_m = 4.1 \text{ rad/s}.$$

Note that X_m (rad/s) is specified according to the allowable rotor speed (r/m) of the wind turbine. The values for $u_c, u_r,$ and u_f are given in Table 1-1 and u_s was chosen so as to give a smooth shut-down profile. The same system control parameters and control parameters were used in the simulation. The tracking process is shown in Figure 1-15 and the rotor speed tracking error is presented in Figure 1-16. As seen the simulation results show the proposed control gives a fairly good control performance over all the operation modes. Also note that the control signal, shown in Figure 1-17, is bounded and smooth everywhere. The controller was tested for different system and control parameters and similar results were obtained (not shown here because of space constraints).

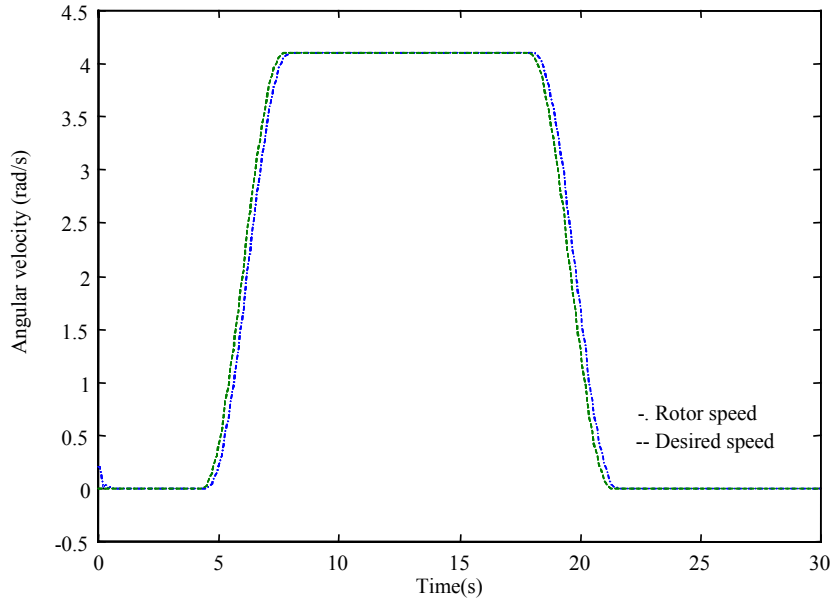

Figure 1-15. Rotor speed tracking

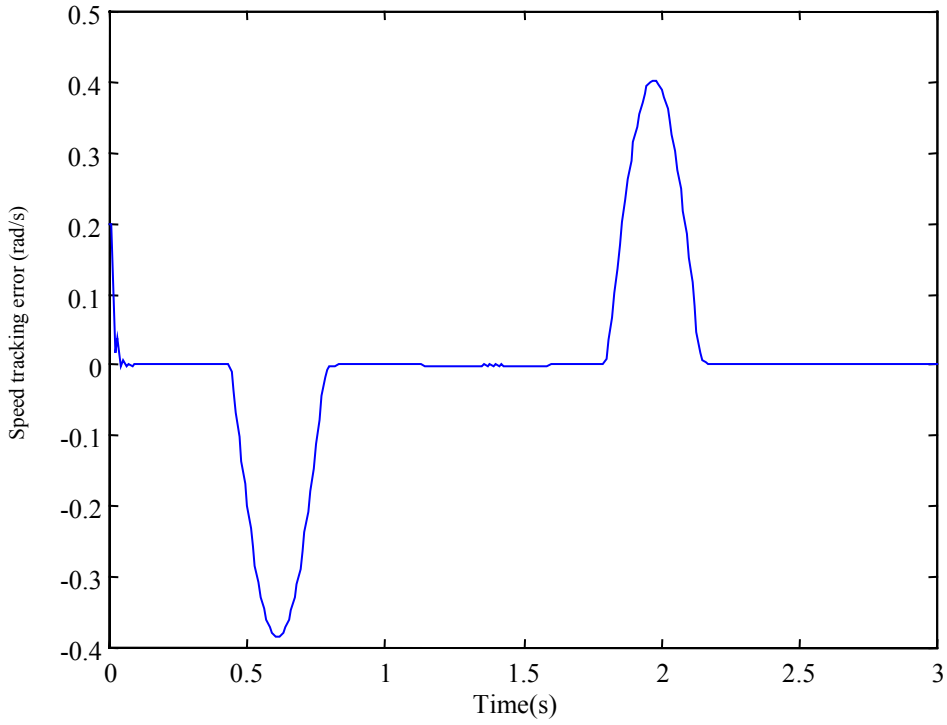

Figure 1-16. Rotor speed tracking error

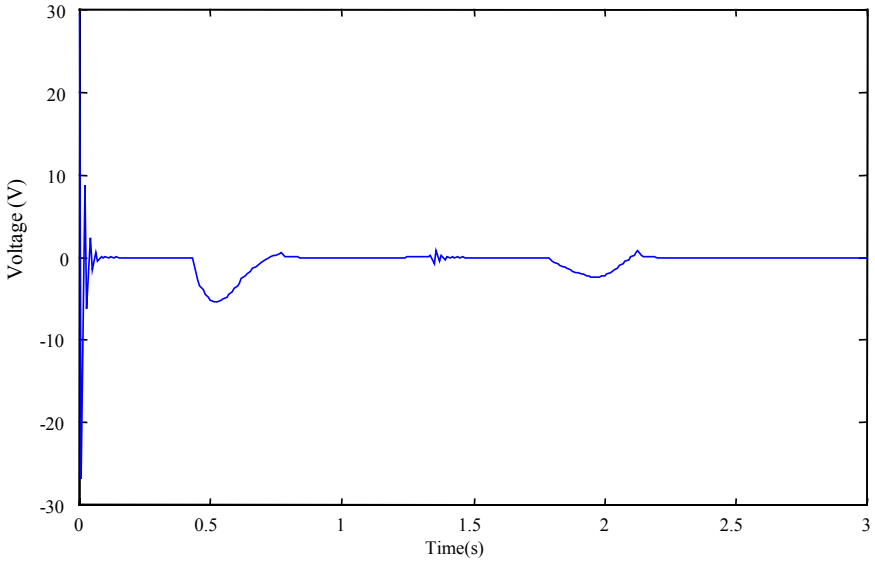

Figure 1-17. Applied control voltage

Nonlinear Pitch Control of Wind Turbines

Introduction

The main objective here is to develop a nonlinear pitch control method for variable speed operation of wind turbines. In this method, the rotor speed was adjusted by controlling the turbine's pitch angle. Note that, however, pitch angle cannot be adjusted directly and instantly. To address this issue, we explicitly considered the pitch servo dynamics in the wind turbine model. The actuator dynamics are important in controller designing. We studied three types of pitch actuator dynamics. Control algorithms were derived using the back-stepping method. The advantages of the proposed pitch control as compared to traditional pitch control can be summarized as follows: The proposed pitch control algorithms are based on the nonlinear model instead of the commonly used linear or linear plus perturbation model. Also, we considered the actuator dynamics in our design. This consideration is motivated by the fact that the pitch angle cannot be controlled directly. Consequently new pitch control algorithms were derived that were shown to be insensitive to operating points. The detail design, analysis, and test are presented in what follows.

Modeling and Problem Statement

Figure 1-18 shows a typical wind energy conversion system. The turbine dynamics can be described by

$$J\dot{\omega} = \tau_r - \tau_e, \qquad \text{(Eq.1-36a)}$$

where J denotes the moment of inertia of the turbine transmission-generator (all referred to the turbine shaft), τ_r represents the aerodynamic torque at the turbine end necessary to the turbine, and τ_e is the electrical shaft torque at the generator end to balance the system. Note that the torque resulting from the wind is modeled by

$$\tau_r = K_\omega C(\beta,\gamma)\phi(\omega) \qquad \text{(Eq.1-36b)}$$

with

$$\gamma = \frac{\omega R}{V_w}, \qquad \text{(Eq. 1-36c)}$$

where K_ω is a constant determined by the rotor radius R, the rotor disk area A, the air density ρ, and others; $C(\beta,\gamma)$ is a nonlinear function (named torque coefficient in the literature) depending on pitch angle β and tip-speed ratio γ; and $\phi(\omega) = \omega^2$ is a nonlinear function.

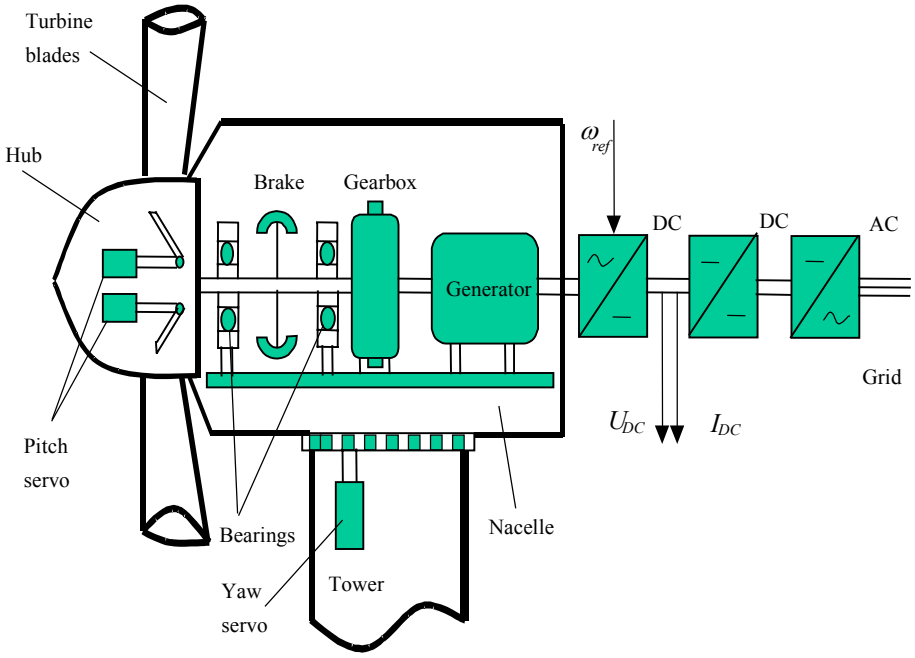

Figure 1-18. Wind turbine model

Note that $C(\beta,\gamma)$ is a turbine specific nonlinear function that describes how efficiently the turbine converts wind energy into mechanical energy at some pitch angle β and some tip-speed ratio γ. An example of how $C(\beta,\gamma)$ varies with β and γ for the wind turbine is shown by the surface plot in Figure 1-19. The figure shows only the region where the value of $C(\beta,\gamma)$ is positive, reassigning all negative values to zero.

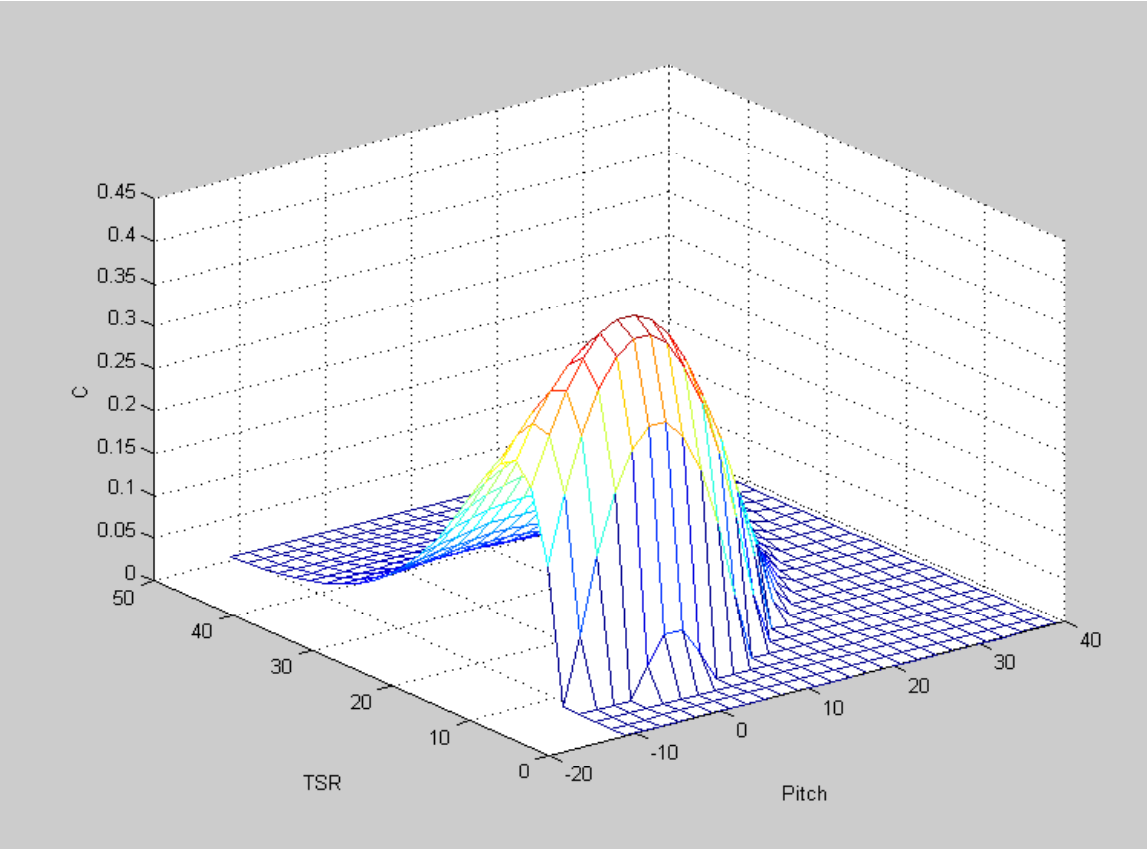

Figure 1-19. $C(\beta,\gamma)$ **versus tip-speed ratio** γ **and pitch angle** β

For later development, we combine Equations 1-3ba and 1-36b to obtain

$$J\dot{\omega} = K_{\omega}C(\beta,\gamma)\phi(\omega) - \tau_e \,. \qquad \text{(Eq.1-37)}$$

As mentioned earlier, pitch angle cannot be adjusted directly and instantly because of the actuator dynamics. To address this issue, we considered the following three cases associated with pitch actuator dynamics.

Case I

$$\beta = dV_f \qquad \text{(Eq.1-38)}$$

Case II

$$\dot{\beta} + a\beta = dV_f \qquad \text{(Eq.1-39)}$$

Case III

$$\ddot{\beta} + a\dot{\beta} + b\beta = dV_f \qquad \text{(Eq.1-40)}$$

where a, b, and d are system parameters depending on the operating point; β is the pitch angle; and V_f denotes the control voltage.

Case I represents the most commonly assumed actuation in the literature, where the pitch angle is assumed to be adjustable directly by a control variable (V_f). Cases II and III, however, are more effective in accounting for the actuator dynamics in the pitch servo-mechanism. Control algorithms based on the above three cases are derived in the next.

Development of Pitch Control Algorithms

The rotor speed of the wind turbine is controlled by adjusting pitch angle of the blade. The control problem can be stated as follows.

Design an actuator voltage V_f such that the rotor speed ω of the wind turbine closely tracks the desired speed ω^* given according to the operational modes of wind turbines. It is assumed that ω^*, $\dot{\omega}^*$, $\ddot{\omega}^*$ are bounded.

As the first step of the design procedure, we express Equation 1-37 as follows:

$$\dot{\omega} = g(.)C(\beta,\gamma) + f(.), \tag{Eq.1-41}$$

where

$$f(.) = -\frac{\tau_e}{J} \tag{Eq.1-42}$$

and

$$g(.) = \frac{K_\omega \phi(\omega)}{J}. \tag{Eq.1-43}$$

The rotor tracking control design is based on Theorem 1, which is repeated here for convenience.

Observation

Consider the error dynamic system

$$\dot{e} = -k_0 e + r, \tag{Eq.1-44}$$

with $k_0 > 0$. If $r \to 0$ as $t \to \infty$, then $e \to 0$ as $t \to \infty$.

Because the proof of the result is simple, we have omitted it here. The important implication of this observation is that the rotor-tracking problem can be addressed by making *r* converge. As the first step of control design, we define the rotor speed tracking error as

$$e = \omega - \omega^*, \tag{Eq.1-45}$$

where ω^* is the desired speed. Taking the derivative of e with respect to time and using Equation 1-7, we obtain the following equation:

$$\dot{e} = f(.) + g(.)C(\beta,\gamma) - \dot{\omega}^* . \quad \text{(Eq.1-46)}$$

The control objective is to design V_f so that $e \to 0$ as $t \to \infty$. Note that the pitch angel β is controlled by V_f through three different models as discussed previously. Consequently, three different control algorithms are needed. We will address this issue in the following subsection.

Control Algorithm for Case I. In this case, Equations 1-37 and 1-38 determine the system dynamics. We need to design V_f to control β, so that $e \to 0$ as $t \to \infty$. To this end, we rewrite Equation 1-46 as:

$$\begin{aligned} \dot{e} &= f + gC(\beta,\gamma) - \dot{\omega}^* \\ &= -k_0 e + r , \end{aligned} \quad \text{(Eq.1-47)}$$

where $k_0 > 0$ is a design constant and

$$r = k_0 e + f + gC(\beta,\gamma) - \dot{\omega}^* . \quad \text{(Eq.1-48)}$$

Taking the derivative of r with respect to time gives

$$\dot{r} = k_0 \dot{e} + f_\omega \dot{\omega} + g_\omega \dot{\omega} C + g C_\beta \dot{\beta} + g C_\gamma \dot{\gamma} - \ddot{\omega}^* , \quad \text{(Eq.1-49)}$$

where

$$f_\omega = \frac{\partial f}{\partial \omega}, \quad g_\omega = \frac{\partial g}{\partial \omega}, \quad C_\beta = \frac{\partial C}{\partial \beta} \text{ and } C_\gamma = \frac{\partial C}{\partial \gamma} .$$

Meanwhile, according to Equation 1-38, we have

$$\dot{\beta} = d\dot{V}_f . \quad \text{(Eq.1-50)}$$

Also from the definition of γ, we have

$$\dot{\gamma} = \frac{\dot{\omega} R}{V_W} - \frac{\dot{V}_W \omega R}{V_W^2} . \quad \text{(Eq.1-51)}$$

Substituting Equations 1-41, 1-50 and 1-51 into Equation 1-49 gives

$$\dot{r} = A + B\dot{V}_f , \quad \text{(Eq.1-52)}$$

where

$$A = (k_0 + f_\omega + g_\omega C + gC_\gamma \frac{R}{V_W})(f + gC) - k_0\dot{\omega}^* - \ddot{\omega}^* - gC_\gamma \frac{\dot{V}_W \omega R}{V_W^2} \quad \text{(Eq.1-53)}$$

and

$$B = gdC_\beta . \quad \text{(Eq.1-54)}$$

If we design V_f so that

$$V_f = \int_0^t \{(-k_1 r - A)/B\} dt , \quad \text{(Eq.1-55)}$$

where $k_1 > 0$ is a designed constant, we obtain

$$\dot{r} = -k_1 r , \quad \text{(Eq.1-56)}$$

which implies that $r \to 0$ as $t \to \infty$. Then by the observation as made in Equation 1-44, we conclude from Equation 1-56 that $e \to 0$ as $t \to \infty$. This can be summarized as in Theorem 4.

Theorem 4

Consider the dynamic model of wind turbines given by Equations 1-37 and 1-38. If V_f is adjusted according to Equation 1-55, then the rotor speeds ω tracks the desired speed ω^* asymptotically.

Control Algorithm for Case II. In this case, the rotor dynamics are governed by Equations 1-37 and 1-39, First we rewrite Equation 1-41 as

$$\begin{aligned} \dot{e} &= -k_0 e + (k_0 e + f + gC(\beta, \gamma) - \dot{\omega}^*) \\ &= -k_0 e + r, \end{aligned} \quad \text{(Eq.1-57)}$$

where

$$r = k_0 e + f + gC(\beta, \gamma) - \dot{\omega}^* . \quad \text{(Eq.1-58)}$$

According to the observation, we need only focus on making *r* tend to zero as *t* tends to infinite. To this end, we differentiate Equation 1-58 to obtain:

$$\dot{r} = k_0 (f + gC - \dot{\omega}^*) - \ddot{\omega}^* - gC_\gamma \frac{\dot{V}_W \omega R}{V_W^2} + (f_\omega + g_\omega C + gC_\gamma \frac{R}{V_W})\dot{\omega} + gC_\beta \dot{\beta}. \quad \text{(Eq.1-59)}$$

Substituting Equations 1-37 and 1-41 into Equation 1-58 gives

$$\dot{r} = mV_f + n , \quad \text{(Eq.1-60)}$$

where

$$m = gC_\beta d \tag{Eq.1-61}$$

and

$$n = k_0(f + gC - \dot{\omega}^*) - \ddot{\omega}^* + (f_\omega + g_\omega C + gC_\gamma \frac{R}{V_W})(f + gC) - gC_\beta a\beta - gC_\gamma \frac{\dot{V}_W \omega R}{V_W^2}. \tag{Eq.1-62}$$

To make $r \to 0$ as $t \to \infty$, V_f is designed so that

$$V_f = (-k_1 r - n) / m, \tag{Eq.1-63}$$

where $k_1 > 0$ is a design constant. It is apparent that such a controller leads to

$$\dot{r} = -k_1 r. \tag{Eq.1-64}$$

According to the observation we conclude that $e \to 0$ and $\dot{e} \to 0$ as $t \to \infty$.

Theorem 5

Consider the rotor dynamics given by Equations 1-37 and 1-39. If V_f is designed as Equation 1-63, the rotor speed ω tracks the desired speed ω^* asymptotically.

Control Algorithm for Case III. In this case, the system dynamics are given by Equations 1-37 and 1-40. The situation in this case is complicated. To simplify the discussion, we assume that the torque coefficient is only a nonlinear function of pitch angle β. Again, we write Equation 1-40 as:

$$\begin{aligned} \dot{e} &= -k_0 e + (k_0 e + f + gC - \dot{\omega}^*) \\ &= -k_0 e + r, \end{aligned} \tag{Eq.1-65}$$

where $r = k_0 e + f + gC - \dot{\omega}^*$. The derivative of r is

$$\dot{r} = k_0(f + gC - \dot{\omega}^*) - \ddot{\omega}^* + (f_\omega + g_\omega C)(f + gC) + gC_\beta(dV_f - a\beta). \tag{Eq.1-66}$$

Using the same derivation method, we can obtain $\ddot{r}$ as

$$\ddot{r} = r_1 + r_2 + r_3 + gC_\beta \ddot{\beta}, \tag{Eq.1-67}$$

with

$$r_1 = k_0(f_\omega + g_\omega C)(f + gC) + k_0 gC_\beta \dot{\beta} - k_0 \ddot{\omega}^* - \dddot{\omega}^*, \tag{Eq.1-68}$$

$$r_2 = (f_{\omega\omega} + g_{\omega\omega}C)(f + gC)^2 + (f_\omega + g_\omega C)^2 (f + gC), \quad \text{(Eq.1-69)}$$

$$r_3 = (f_\omega + g_\omega C)gC_\beta \dot{\beta} + 2(f + gC)g_\omega C_\beta \dot{\beta} + gC_{\beta\beta}\dot{\beta}^2, \quad \text{(Eq.1-70)}$$

and

$$f_{\omega\omega} = \frac{\partial f_\omega}{\partial \omega}, \; g_{\omega\omega} = \frac{\partial g_\omega}{\partial \omega}, \quad C_{\beta\beta} = \frac{\partial C_\beta}{\partial \beta}. \quad \text{(Eq.1-71)}$$

Upon substituting Equation 1-37 into Equation 1-67, we obtain

$$\ddot{r} = r_1 + r_2 + r_3 + gC_\beta(-a\dot{\beta} - b\beta) + gC_\beta dV_f. \quad \text{(Eq.1-72)}$$

Because we need to have r tend to zero, we choose V_f as

$$V_f = (-r_1 - r_2 - r_3 - (k_1 + k_2)\dot{r} - k_1 k_2 r)\frac{1}{dgC_\beta} + \frac{a\dot{\beta} + b\beta}{d}, \quad \text{(Eq.1-73)}$$

which leads to the augmented system

$$\ddot{r} = -(k_1 + k_2)\dot{r} - k_1 k_2 r. \quad \text{(Eq.1-74)}$$

Now we have the augmented system

$$\frac{d}{dt}\begin{bmatrix} e \\ r \\ \dot{r} \end{bmatrix} = \begin{bmatrix} -k_0 & 1 & 0 \\ 0 & 0 & 1 \\ 0 & -k_1 k_2 & -(k_1 + k_2) \end{bmatrix}\begin{bmatrix} e \\ r \\ \dot{r} \end{bmatrix}.$$

It is easily verified that this augmented system has the following characteristic equation

$$C(\lambda) = (\lambda + k_0)(\lambda + k_1)(\lambda + k_2),$$

which bears the eigenvalues of $-k_0$, $-k_1$, and $-k_2$. Therefore, we have $e \to 0$, $r \to 0$, $\dot{r} \to 0$ as $t \to \infty$.

We can also use Lyapunov stability theory to verify the tracking stability by considering the following Lyapunov function candidate:

$$V = \begin{bmatrix} e \\ r \\ \dot{r} \end{bmatrix}^T \begin{bmatrix} p_{11} & p_{12} & p_{13} \\ p_{12} & p_{22} & p_{23} \\ p_{13} & p_{23} & p_{33} \end{bmatrix}\begin{bmatrix} e \\ r \\ \dot{r} \end{bmatrix},$$

with

$$p_{11} = \frac{q_1}{2k_0},$$

$$p_{13} = \frac{p_{11}}{a + k_0(k_0 + b)},$$

$$p_{12} = p_{13}(k_0 + b),$$

$$p_{33} = \frac{p_{23} + 0.5q_3}{b},$$

and

$$p_{22} = ap_{33} + bp_{23} - p_{13},$$

where $q_1 > 0,\ \ q_2 > 0$ and $q_3 > 0$ are constant real. It can be verified that

$$\dot{V} = -q_1 e^2 - q_2 r^2 - q_3 \dot{r}^2 < 0.$$

Theorem 6

Consider the wind power generation systems represented by Equations 1-37 and 1-40. If the voltage V_f is adjusted according to Equation 1-73, then rotor speed of the wind turbines follows the desired speed asymptotically.

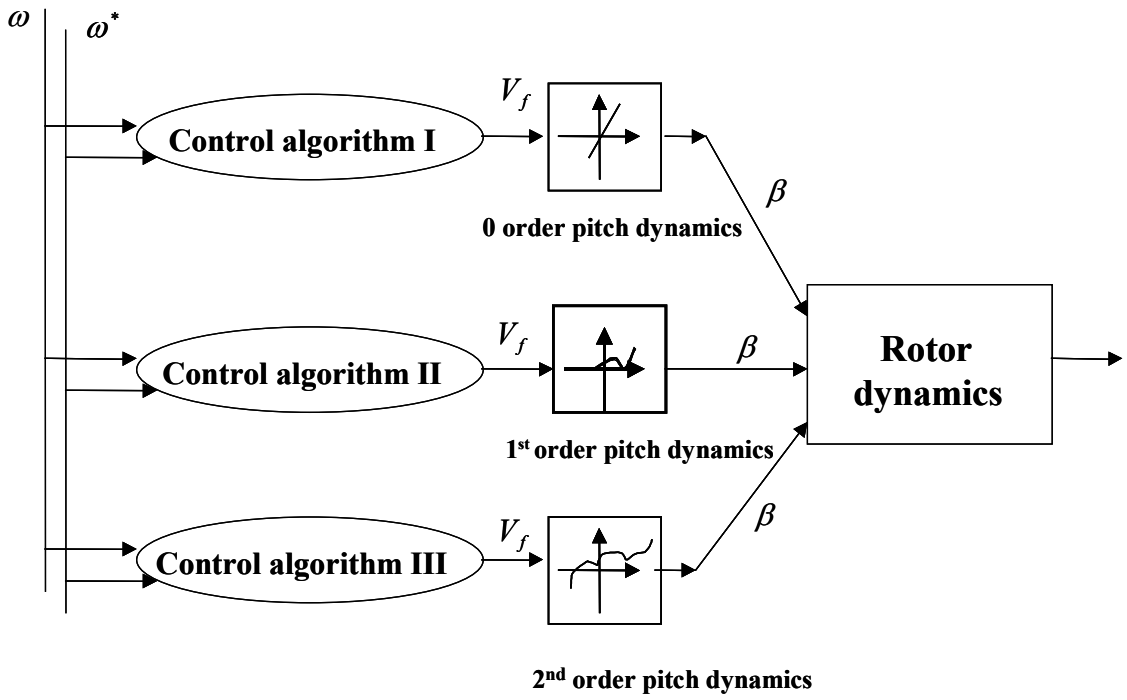

Figure 1-20. Schematic diagram of nonlinear pitch control

Figure 1-20 is the schematic diagram of the nonlinear pitch control scheme presented in this part of report. If pitch angle is adjusted according to the proposed strategies, stable rotor-speed tracking is ensured. The main contribution of this work is the design of controllers using nonlinear analysis. The system model is based on the hybrid dynamic model which contains both rotor dynamics and actuator dynamics. The controllers are derived by the backstepping method.

Simulation Results

The simulation studies were performed to verify the effectiveness of the proposed control strategy. We applied the controller designed in three situations. The following system parameters, which were based on a two-bladed horizontal axis wind turbine similar to DOE MOD-0, were considered.

$$J = 16Kg - m^2,$$

and

$$R_f = 0.02\Omega.$$

The torque coefficient of the following form that is similar the one used in [38] was considered.

$$C(\beta,\gamma) = 0.5 * (\gamma - 0.022 * \beta^2 - 5.6) * e^{-0.17*\gamma}$$

The control parameters chosen were $k_0 = 10$, $k_p = 1$, and $k_m = 7.9$.

Simulation on a Sine Wave Trajectory. Simulation was conducted for the desired sine wave trajectory given as

$$\omega^* = 2 + \sin(t) \text{ (rad/s).} \qquad \text{(Eq.1-75)}$$

Three cases of actuator dynamics were considered separately. Simulation was conducted for the desired trajectory given in Equation 1-75 using the actuator dynamic Equations 1-38, 1-39 and 1-40. Figure 1-21 illustrates the tracking process and the pitch angle for the three cases.

Simulation under a Practical Situation. The second simulation was based on a more practical situation, where the desired rotor speed trajectory is given as in Equation 1-35. The pitch control algorithms based on the three types of actuator dynamics were tested and the results are shown in Figure 1-22. As can be seen, the proposed pitch control algorithms are able to achieve smooth and effective speed tracking in this case as well.

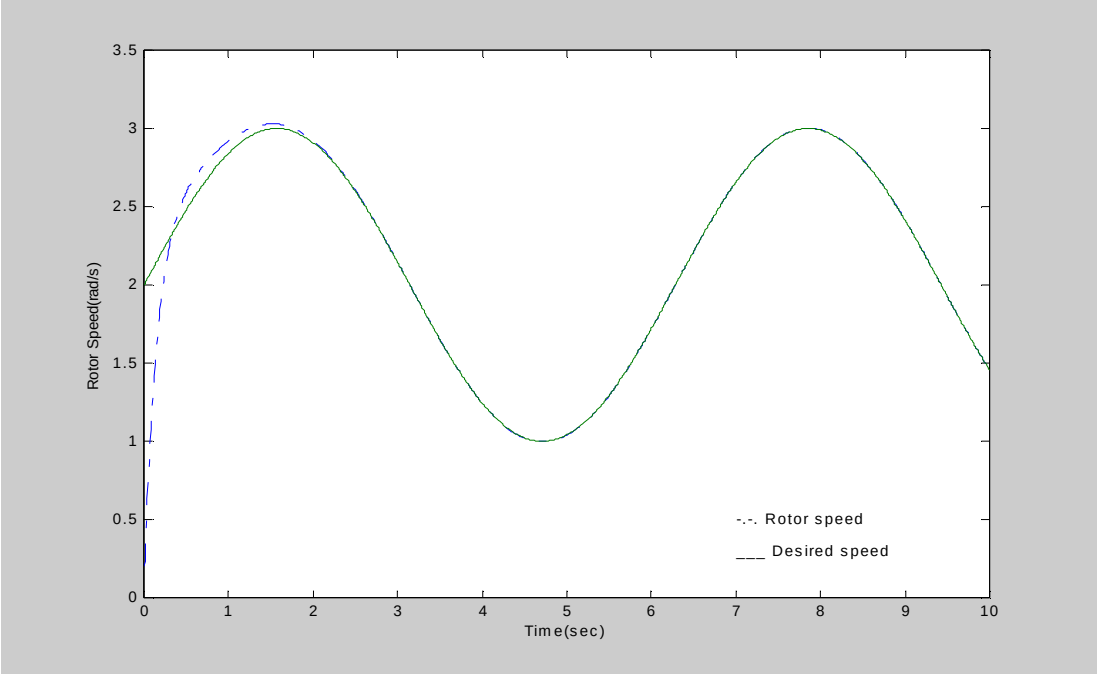

Figure 1-21. Simulation of Algorithm I for since wave- rotor speed tracking

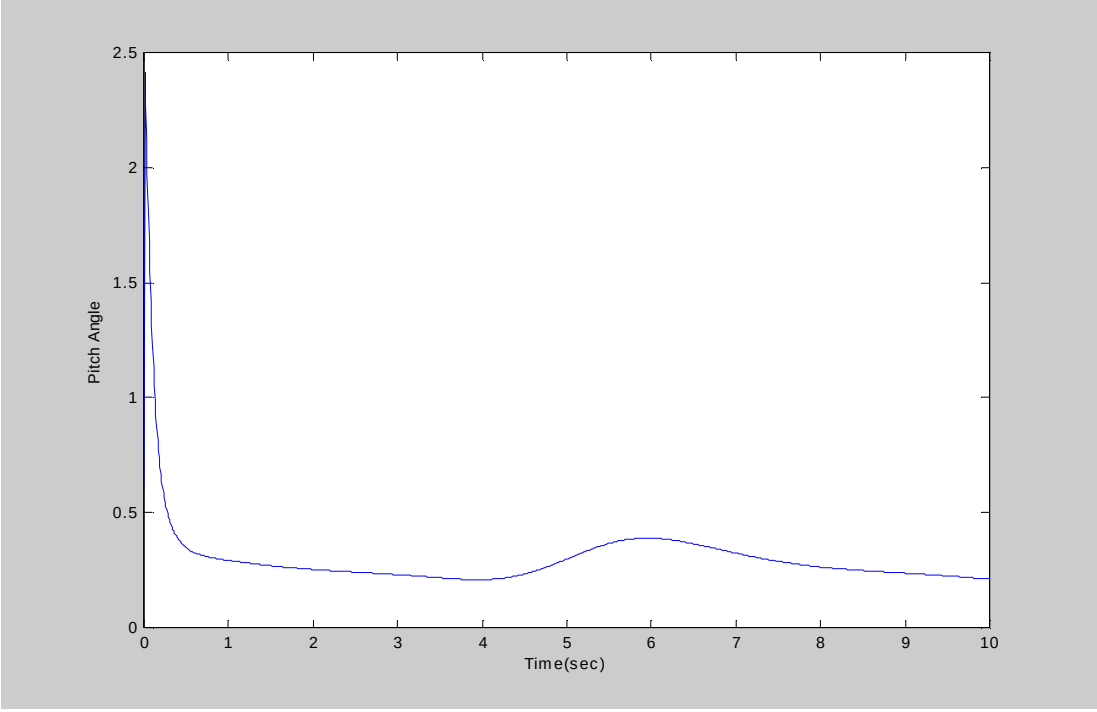

Figure 1-22. Simulation of Algorithm I for since wave – pitch angle

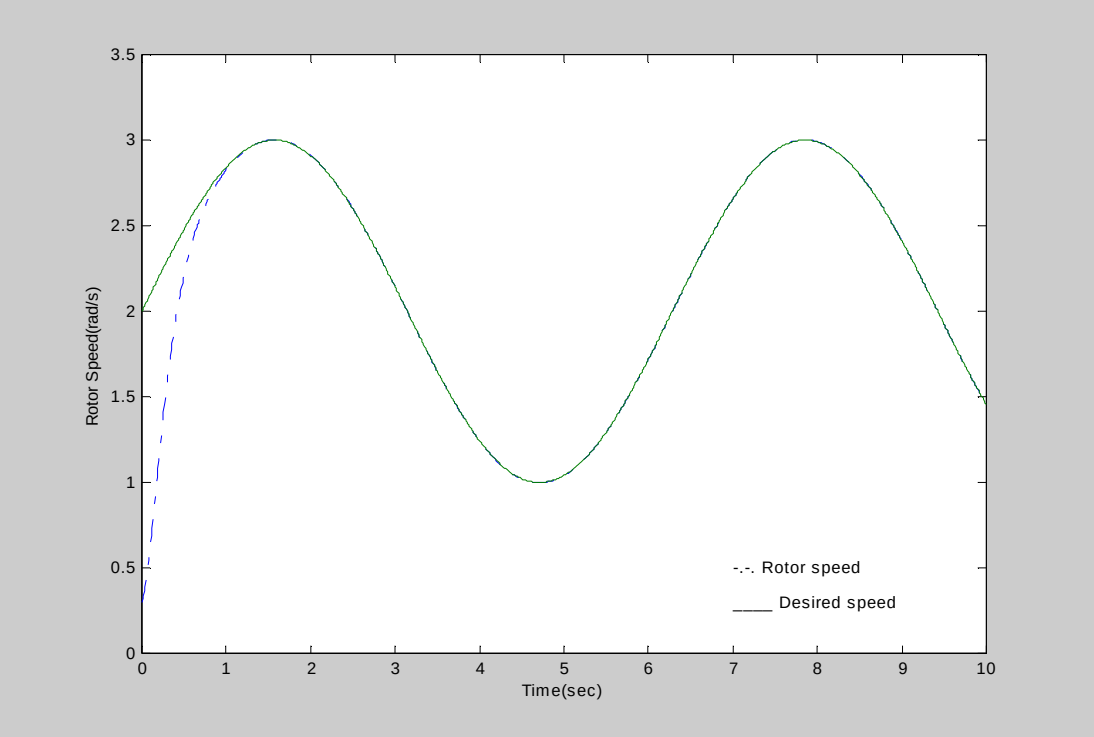

Figure 1-23. Simulation of Algorithm II for since wave- rotor speed tracking

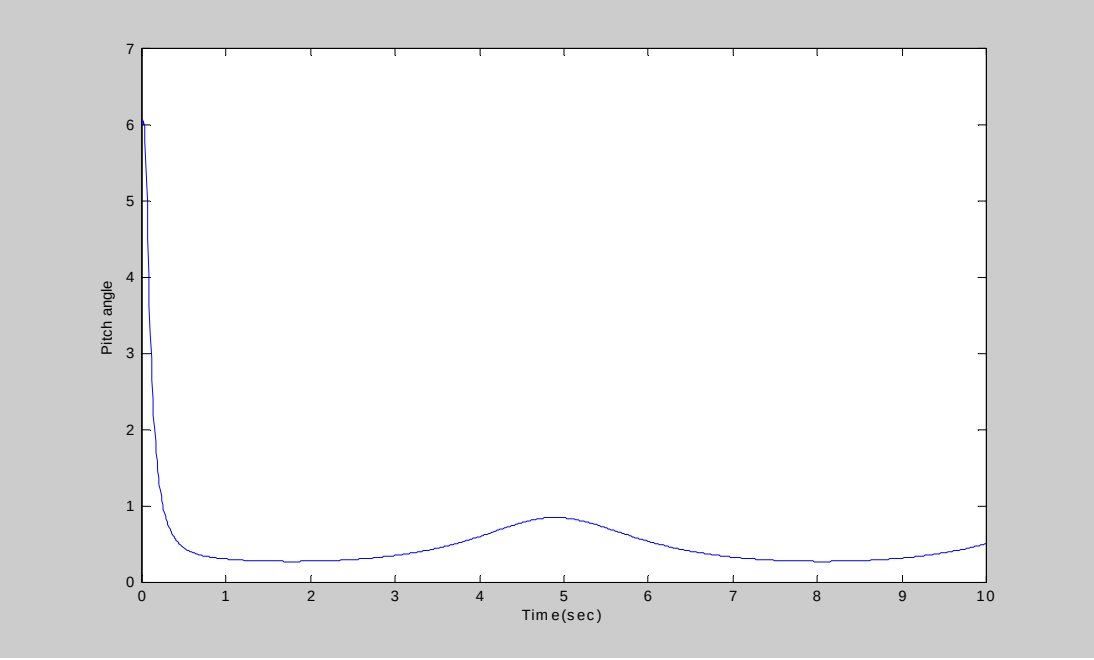

Figure 1-24. Simulation of Algorithm II for since wave – pitch angle

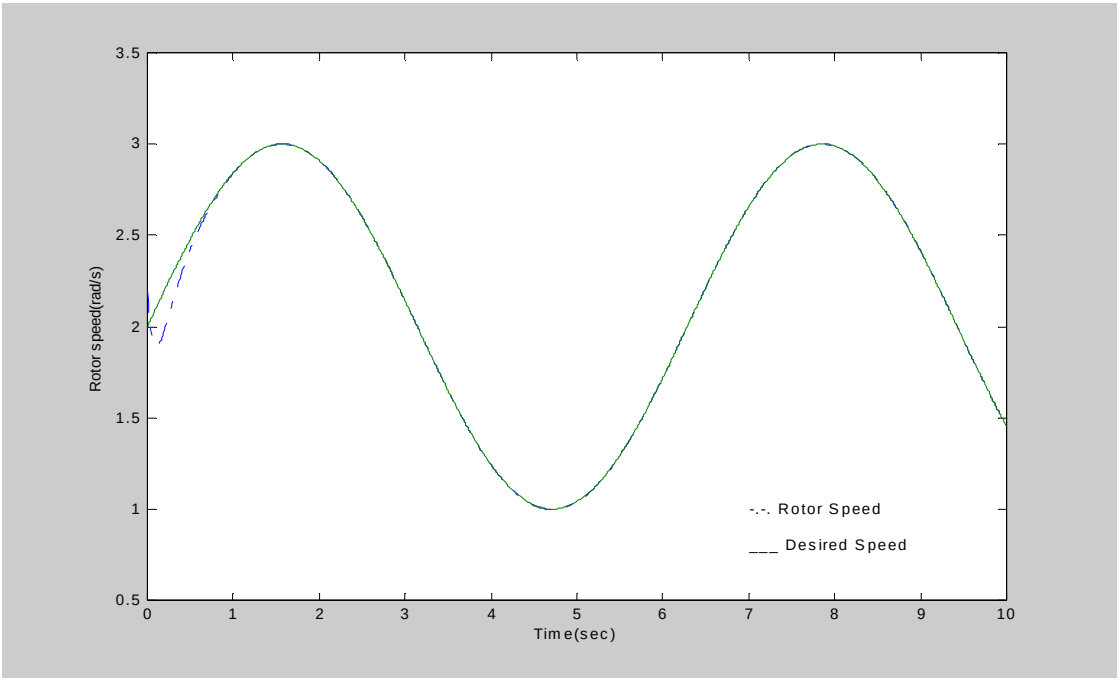

Figure 1-25. Simulation of Algorithm III for since wave- rotor speed tracking

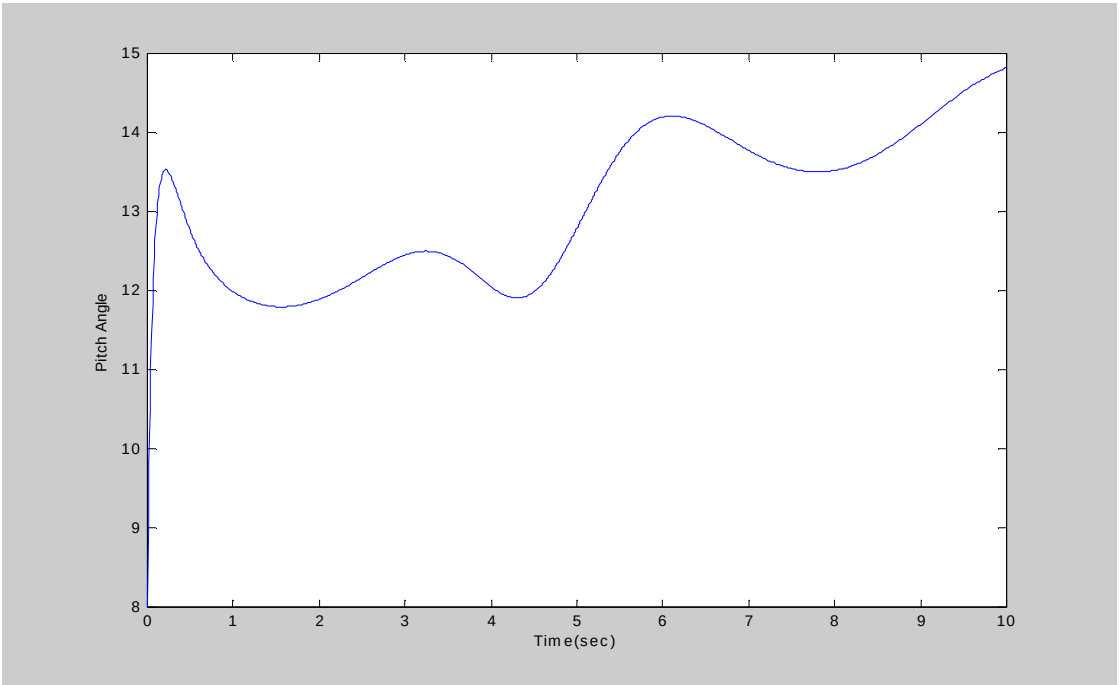

Figure 1-26. Simulation of Algorithm III for since wave – pitch angle

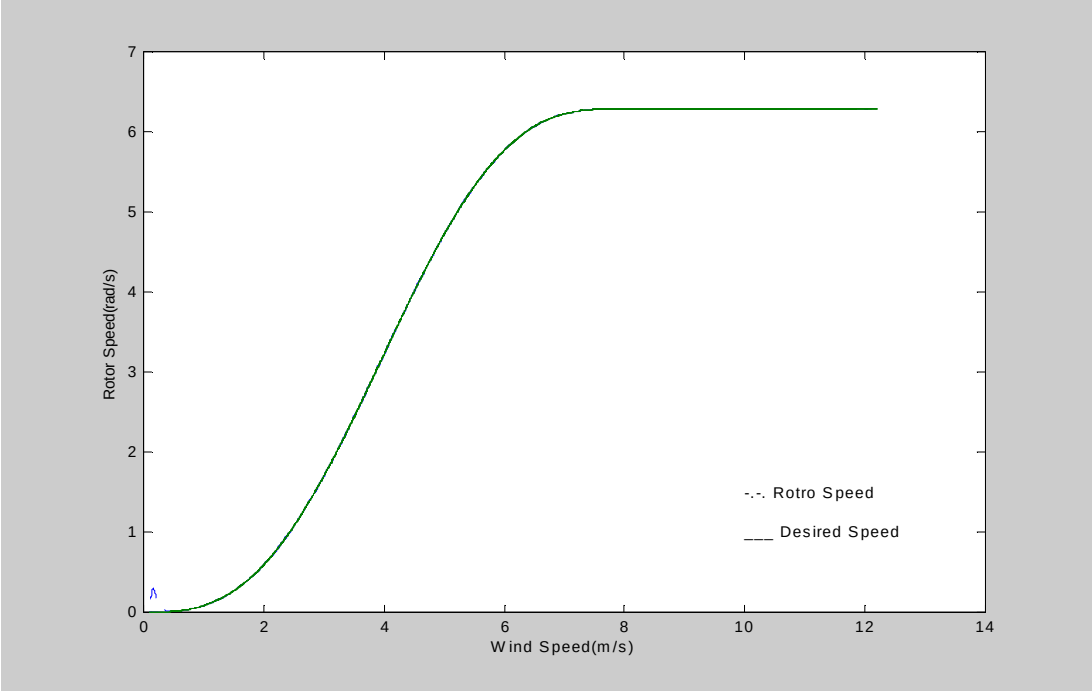

Figure 1-27. Simulation of Algorithm I for a practice situation- rotor speed tracking

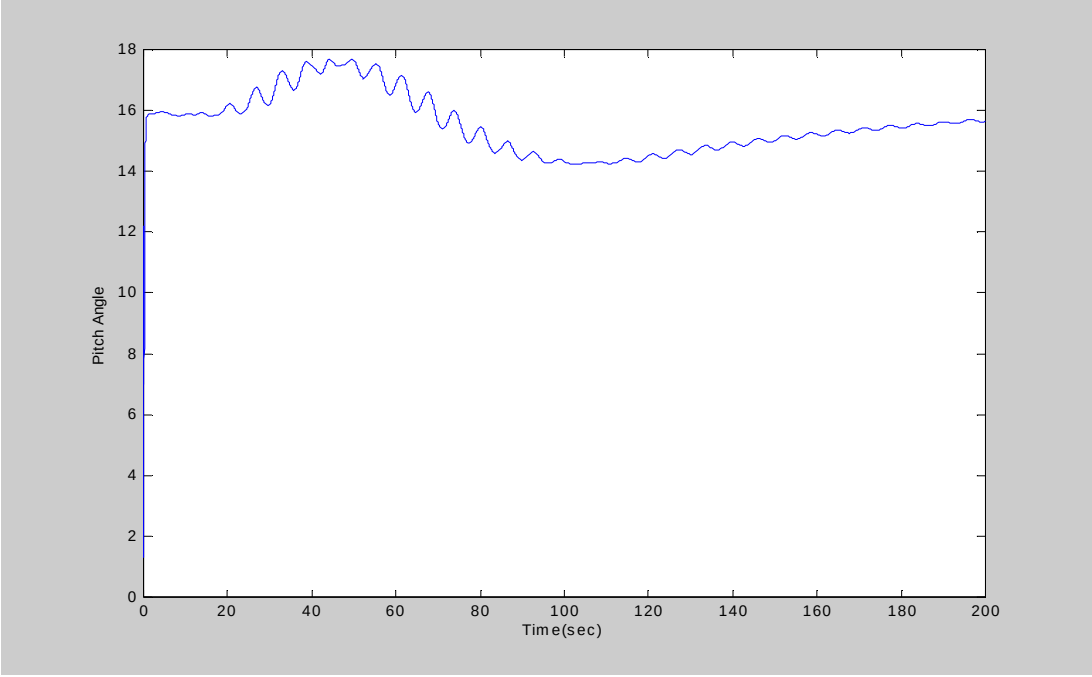

Figure 1-28. Simulation of Algorithm I for a practice situation- pitch angle

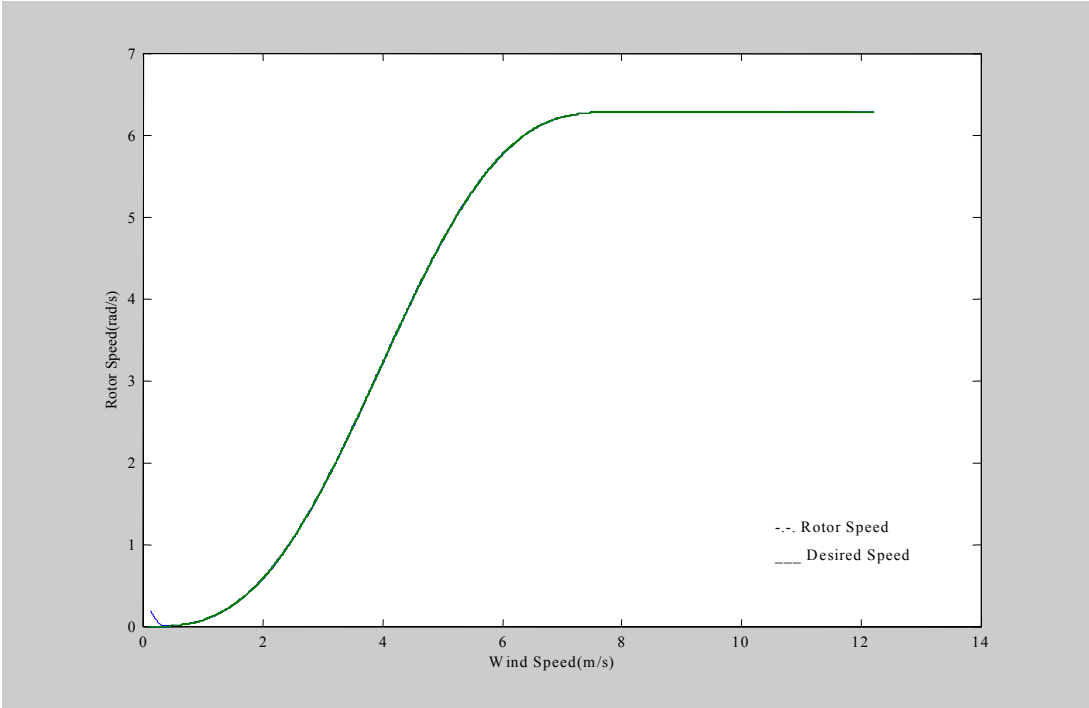

Figure 1-29. Simulation of Algorithm II for a practice situation- rotor speed tracking

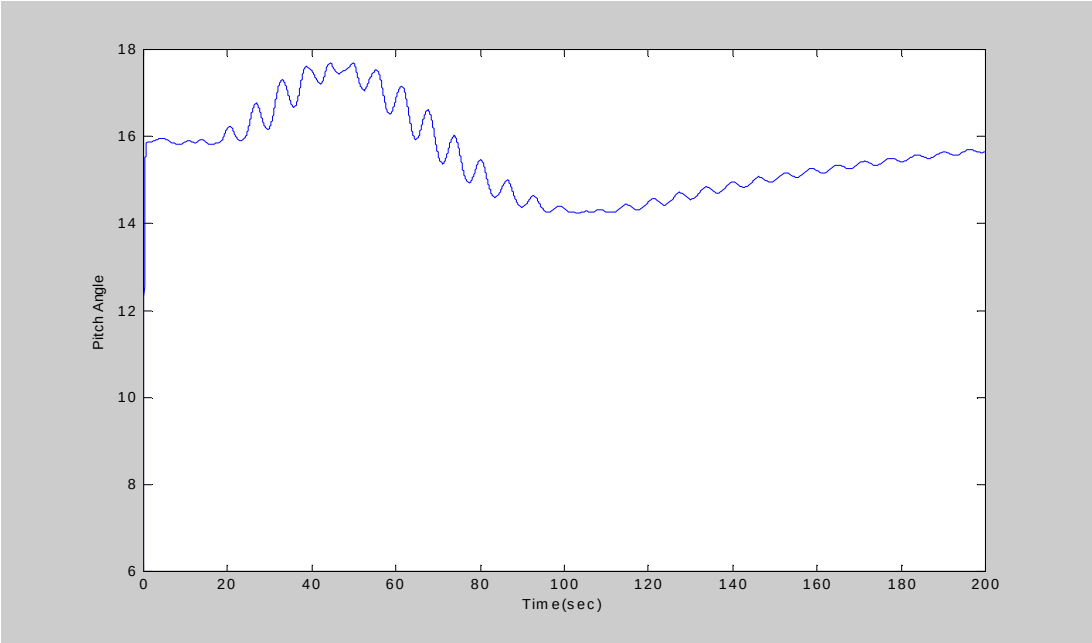

Figure 1-30. Simulation of Algorithm II for a practice situation- pitch angle

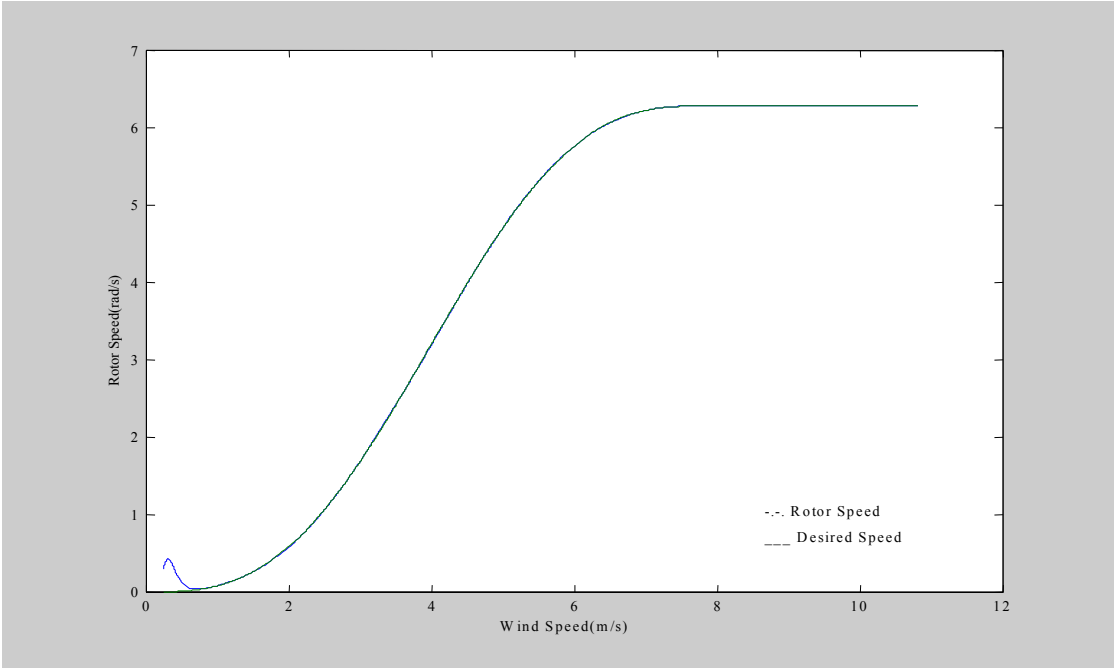

Figure 1-31. Simulation of Algorithm III for a practice situation- rotor speed tracking

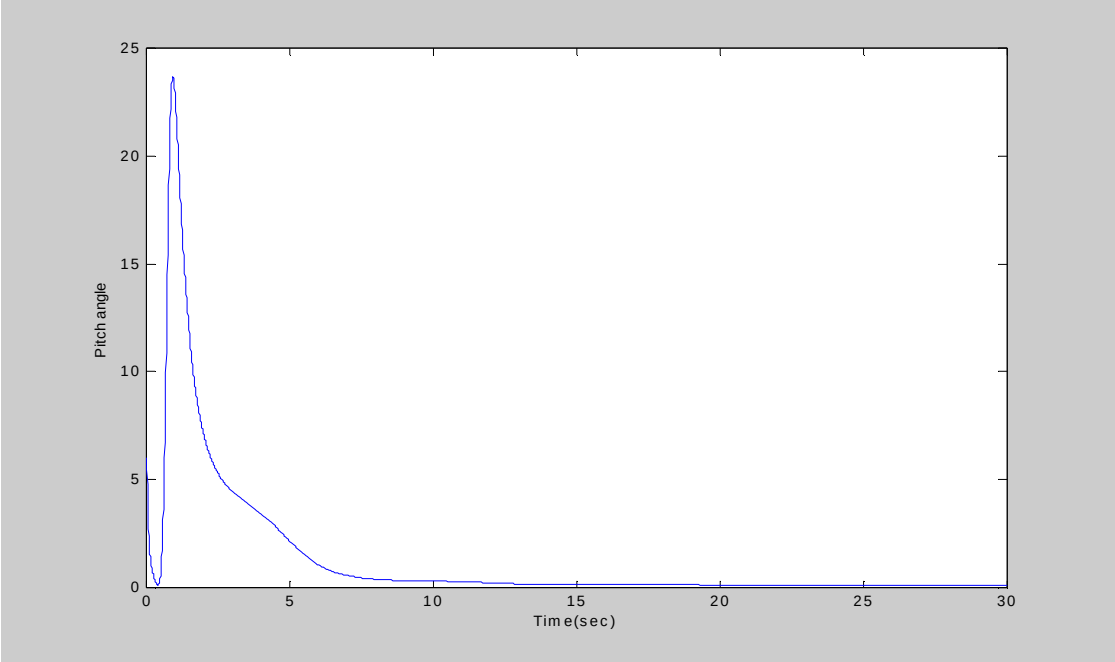

Figure 1-32. Simulation of Algorithm III for a practice situation- pitch angle

Conclusions

With the myriad environmental impacts that result from burning fossil fuels, renewable sources of electrical power generation continue to hold great promise and potential. Significant advancements have been made in several technologies, with wind power generation emerging as the most likely candidate for extensive near-term deployment. Yet even with this maturing technology, many basic issues have yet to be resolved [30–38].

The objective of this subtask was to develop new control algorithms for wind turbines. Three methods for variable speed control of wind turbines were investigated. The first method makes use of a memory-based concept to build pitch control algorithm. This method is based on observing and generalizing past system responses and control experience. It does not demand detailed information about the system dynamics. The method is verified via a numerical example. It is worth mentioning that although memory-based approaches for solving engineering problems have a long history, applying this method to wind turbine control is new. Our initial investigation indicated that this method is able to achieve rotor-speed tracking with a reasonably good accuracy without wind speed measurement. The second method is based on the regulation of excitation winding voltage of the generator. Based on both mechanical and electrical dynamics, nonlinear control algorithms are derived. Analysis and simulation showed that the proposed method is able to achieve smooth and satisfactory rotor-speed tracking. The third method uses nonlinear pitch control. In this method the rotor speed is regulated via a pitch servo-mechanism. Because pitch angle cannot be adjusted directly and instantly, actuator dynamics need to be explicitly considered. In this project we examined three types of pitch actuator dynamics and integrated them into the pitch control scheme. We demonstrated that with the derived control algorithms, smooth and asymptotic rotor speed tracking is ensured.

References of Part 1

1. Atkeson, C. G., and Reinkensmeyer, D. J., "Using Associate Content-Addressable Memories to Control Robots," *Neural Networks for Control*, edited by W. T. Miller, R. S. Sutton, and P. J. Werbos, 1992, pp. 255-285.
2. Cybenko, G., "Approximation by Superposition of a Sigmoidal Function," *Mathematics of Control, Signals, and Systems*, No. 2, 1989, pp. 303-314.
3. Fix, E., and Hodges, J. L. Jr., "Discriminatory Analysis, Non-Parameteric Regression: Consistency Properties, " Technical Report No. 4, USAF School of Aviation Medicine, Randolph Field, TX AF- 41-(128)-31, 1951.
4. Lorenz, E. N., "Atmospheric Predictability as Revealed by Naturally Occurring Analogues," *Journal of Atmospheric Science*, Vol. 26, 1969, pp. 636-646.
5. Moore, A. W., "Efficient Memory-Based Learning for Robot Control," Ph. D. Thesis, Tech. Rep. 229, Computer Laboratory, University of Cambridge, 1990.
6. Schaal, S., and Atkeson, C. G., "Robot Juggling: Implementation of Memory-Based Learning," *IEEE Control Systems*, Vol. 14, No. 1, 1994, pp. 57-71.
7. Stanfill, C., and Waltz, D., "Toward Memory-Based Reasoning," Communications of the ACM, Vol. 29, No. 12, 1986, pp. 1213-1228.

8. Steinbuch, K., and Piske, U. A., "Learning Matrices and their Applications," *IEEE Trans. on Electronic Computers*, Vol. 12, 1963, pp. 846-862.

9. Waltz, D. L., "Applications of the Connection Machine," *Computer*, Vol. 20, No. 1, 1987, pp. 85-90.

10. Albus, J. S., "A New Approach to Manipulator Control: the Cerebellar Model Articulation Controller (CMAC)," *ASME Trans. on J. of Dynamic Systems, Measurement and Control,* Vol. 97, 1975, pp. 220-227.

11. Albus, J. S., "Data Storage in the Cerebellar Model Articulation Controller (CMAC)," *ASME Trans. on J. of Dynamic Systems, Measurement and Control*, Vol. 97, 1975, pp. 228-233.

12. Johnson, G. L., *Wind Energy Systems*, Prentice-Hall Inc., Englewood Cliffs, NJ, 1985.

13. Novak, P., Ekelund, T., Jovik, I., and Schmidtbauer, B., "Modeling and Control of Variable-Speed Wind Turbine Drive-System Dynamics," *IEEE Control Systems Magazine*, August 1995, pp. 28-38.

14. Steinbuch, M., and Bosqra, O. H., "Optimal Output Feedback of a Wind Energy Conversion System," IFAC Power Systems Modeling and Control Applications, Brussels, Belgium, 1988.

15. Liebst, B. S., "Pitch Control System for large-scale Wind Turbines," *Journal of Energy*, Vol. 7, No. 2, 1982.

16. Kreyszig*, K., Advanced Engineering Mathematics*, Second Edition, John Wiley & Sons Inc., New York, 1968.

17. Taylor, C. W., Nassief, F. R., and Cresap, R. L., "Northwest Power Pool Transient Stability and Load Shedding Controls for Generation-Load Imbalances," *IEEE Transactions on Power and Application Systems*, Vol. PAS-100, No. 7, pp. 2486-2495, July 1981.

18. Salle, S. A., Reardon, D., Leithead, W. E., and Grimble, M. J., "Review of Wind Turbine Control," International Journal of Control, Vol. 52, No. 6, 1990.

19. Muljadi, E., Butterfield, C. P., and Migliore, P., "Variable Speed Operation of Generators with Rotor-Speed Feedback in Wind Power Applications," *Fifteenth ASME Wind Energy Symposium*, Houston, TX, 1996.

20. Thirnger, T., and Linders, J., "Control of Variable Speed of a Fixed-Pitch Wind Turbine Operating in a Wide Speed Range," IEEE Trans. on Energy Conversion, Vol. 8, No. 3, 1993, pp. 520-526.

21. Hilloow, R. M., and Sharaf, A. M., "A Rule-Based Fuzzy Logic Controller for a PMW Inverter in a Stand Alone Wind Energy Conversion Scheme," IEEE Trans. on Industry Applications, Vol. 32, No. 1, 1996, pp. 57-65.

22. Novak, P., Ekelund, T., Jovik, I., and Schidtbauer, B., "Modeling and Control of Variable-Speed Wind-Turbine Drive-System Dynamics," IEEE Control System Magazine, Vol. 15, No. 4, 1995, pp. 28-38.

23. Leithead, W. E., and Connor, B., "Control of a Variable Speed Wind Turbine with Induction Generator," *Control '94, Conference Publication,* No. 389, March 1994.

24. Song, Y. D., "Control of Wind Turbines Using Memory-Based Method," *American Control Conference,* June 1998.

25. Leithead, W. E., "Dependence of Performance of Variable Speed Wind Turbine on the Turbulence, Dynamics and Control," *IEEE Proceedings*, Vol. 137, No. 6, November 1990.

26. Steinbuch, M., and Bosqra, O. H., "Optimal Output Feedback of a Wind Energy Conversion System," Power Systems Modeling and Control Applications, edited by Calvaer, A. J., *International Federal Automatic Control Proceeding Series*, No. 9, 1989.

27. Thiringer, T., and Linders, J., "Control by Variable Speed of a Fixed-Pitch Wind Turbine Operating in a Wide Speed Range," *IEEE Transactions on Energy Conversion*, Vol. 8, No. 3, September 1993.

28. Leith, D. J., and Leithead, W. E., "Implementation of Wind Turbine Controller," *International Journal of Control*, Vol. 66, No. 3, 1997.

29. Song, Y. D., Dhrikaran, B., and Bao, X., "Variable Speed Control of Wind Turbines Using Nonlinear and Adaptive Algorithms," ***Journal of Wind Energy and Industrial Aerodynamics***, Vol. 86, No. 1, 2000.

30. Song, Y. D., and Robinson, M., "Wind Turbine Dynamics, Control and Monitoring-Editorial," *Journal of Wind Energy and Industrial Aerodynamics*, Vol. 86, No. 1, 2000.

31. Song, Y. D., Macro, T., and Huang, D., "Power System Synchronization via Nonlinear Field Excitation Approach," *The 31st Southeastern Symposium on System Theory*, Tallahassee, FL, March 2000.

32. Song, Y. D., Dhrikaran, B., and Bao, X., "Viable Speed Operation of Wind Turbines via Nonlinear and Adaptive Control Method," *American Control Conference*, Chicago, IL, June 2000.

33. Song, Y. D., and Dhrikaran, B., "Nonlinear Variable Speed Control of Wind Turbines," *Institute of Electrical and Electronics Engineers International Conference on Control Applications,* December 1999.

34. Song, Y. D., "A New Approach to Wind Speed Estimation with Application to Wind Turbine," *American Power Conference*, April 1998.

35. Song, Y. D., and Huang, D. L., "Nonlinear Pitch Control of Wind Turbines," *International Conference on Measurement and Control*, May 2001, Pittsburgh, Pennsylvania.

36. McIver, A., Holmes, D. G., and Freere, P., "Optimal Control of a Variable Speed Wind Turbine under Dynamic Wind Conditions," *IEEE Thirty-First Annual Meeting on Industry Applications Conference,* 1996.

37. Zinger, D. S., Muljadi, E., and Miller, A., "A Simple Control Scheme for Variable Speed Wind Turbines," *IAS'96 Conference Record of the IEEE Industry Applications Conference 31st IAS Annual Meeting,* 1996.

38. Baars, G. E., and Bongers, M. M., "Wind Turbine Control Design and Implementation Based on Experimental Models," *Proceedings of the 31st Conference on Decision and Control*, Tucson, AZ, December 1992.

Related Publications of Part 1

The following publications are supported in part by the NREL project.

Song, Y. D., "Pitch Control of Wind Turbine Using Memory-based Approach," ***Journal of Wind Energy and Industrial Aerodynamics,*** Vol. 86, No. 1, 2000.

Song, Y. D., "A New Approach to Wind Speed Prediction," ***Wind Engineering***, Vol. 24, No.1, 2000.

Song, Y. D., Dhrikaran, B., and Bao, X., "Variable Speed Control of Wind Turbines Using Nonlinear and Adaptive Algorithms," ***Journal of Wind Energy and Industrial Aerodynamics***, Vol. 86, No. 1, 2000.

Song, Y. D., and Robinson, M., "Wind Turbine Dynamics, Control and Monitoring-Editorial," ***Journal of Wind Energy and Industrial Aerodynamics***, Vol. 86, No. 1, 2000.

Song, Y. D., and Kelly, J. C., "Design and Test of Battery Chargers - A Senior Student Design Project," *American Society for Engineering Education Conference*, June 2000.

Song, Y. D., Homaifar, A., Singh, H., and Salami, Z., "Power Factor Correction under Varying Load Conditions: Part II – Automatic Correction and Simulation," *American Power Conference*, Chicago, April 2000.

Song, Y. D., Macro, T., and Huang, D., "Power System Synchronization via Nonlinear Field Excitation Approach," *The 31st Southeastern Symposium on System Theory*, Tallahassee, FL, March 2000.

Deng, X., and Song, Y. D., "Synchronization of Power Systems via Series Compensation Method," *The 31st Southeastern Symposium on System Theory*, Tallahassee, FL, March 2000.

Wang, L., Song, Y. D., and Uva, L., "Memory-based Control of Hybrid Step Motors," *The 31st Southeastern Symposium on System Theory*, Tallahassee, FL, March 2000.

Song, Y. D., and Hou, J., "Autopilot Design Considering Actuator Dynamics in Missile Systems," *SPIE 2000 14th International Conference on Aerospace/Defense Sensing, Simulation, and Controls,* Orlando, FL, April 2000.

Cao, J., Wang, L., and Song, Y. D., "Neural Network Classifiers with Minimum Misclassification – Criteria and Structures" *IASTED Int. Conference on Modeling, Identification and Control*, Innsbruck, Austria, February 2000.

Song, Y. D., Dhrikaran, B., and Bao, X., "Viable Speed Operation of Wind Turbines via Nonlinear and Adaptive Control Method," *American Control Conference*, Chicago, IL, June 2000.

Wang, L., Cao, J., and Song, Y. D., "Neural Network Classifiers with Minimum Misclassification – Algorithm Design and Analysis" *IASTED Int. Conference on Modeling, Identification and Control*, Innsbruck, Austria, February 2000.

Song, Y. D., and Hou, J., "AGGIE ROVER Robot - Design, Analysis and Test" *Institute of Electrical and Electronics Engineers Southeastern Conference,* Nashville, TN, April 2000.

Cao, J., Wang, L., and Song, Y. D., "Neural Network Classifiers with Minimum Misclassification – Application" *IASTED Int. Conference on Modeling, Identification and Control*, Innsbruck, Austria, February 2000.

Song, Y. D., and Dhrikaran, B., "Nonlinear Variable Speed Control of Wind Turbines," *Institute of Electrical and Electronics Engineers International Conference on Control Applications,* December 1999.

Hou, J., and Song, Y. D., “Voltage Collapse Prevention in Power Systems via Series Compensation,” *Southeastern Symposium on Systems Theory*, Birmingham AL, March 21-23, 1999.

Song, Y. D., “A New Approach to Wind Speed Estimation with Application to Wind Turbine,” *American Power Conference*, April 1998.

Song, Y. D., “Control of Wind Turbine Systems Using Memory-based Approach,” *17th American Control Conference*, June 1998, pp. 1715-1720.

Salami, Z., Singh, H., and Song, Y. D., "Power Factor Correction Under Dynamic Load Condition: Part I - Auto PF Detection," *World Energy Engineering Congress (WEEC)*, Atlanta, GA, November 1998.

Song, Y. D., and Huang, D. L., “Nonlinear Pitch Control of Wind Turbines,” *International Conference on Measurement and Control*, May 2001, Pittsburgh, Pennsylvania.

Part 2

Autofurling of Large Wind Turbines Using Fuzzy Logic

Dr. M. Bikdash

Contents

List of Figures

List of Tables

Executive Summary

Wind Energy has been recognized as a very viable source of sustainable energy [1]. Most small wind turbines use an upwind rotor configuration with a hinged tail vane for passive yaw control mechanism, which is known as furling or autofurling [2]. At higher wind speeds, the generated power of the wind turbines can go above the design limits of the generator or turbine. Furling uses a combination of aerodynamic and gravity forces to turn the rotor out of the wind resulting in the shedding of aerodynamic power. This reduces rotor rpm, which in turn provides overspeed protection.

Unfortunately, this totally passive mechanism to protect wind turbines from overspeeding and failure is not well understood and can perhaps be improved through careful analysis and redesign. For instance, energy loss results from the furling hysteresis in which the wind speed must drop considerably below the rated wind speed before the rotor unfurls and resumes efficient operation.

Our study is modeled after the Bergey Excel 10-kW turbine, which operates in the boundary layer of the earth and is therefore subject to considerable turbulence. A rapid response to wind gusts is important to avoid overspeeding the rotor. This mechanism is entirely passive, fail safe, robust, simple to construct and to maintain, and is therefore in complete agreement with the design philosophy for small wind turbines. In operation, the turbine begins to furl out of the wind at a wind speed of about 33 mph. Because of turbulence – even in the smoothest of winds – it furls in and out over a range of speeds between about 30 mph and 40 mph. This "hunting" behavior, although consistent with the protection function, is not desirable. Above 40 mph, the turbine remains furled with a 70°-angle between the rotor and the tail and a considerable reduction in rpm.

In this task, we seek to model using mathematics and software the autofurling mechanism, to analyze and understand it, and to design an active yaw mechanism that supplements it. Improvement can result from modifying the geometrical characteristics of the turbine based on careful analysis of the mechanism. Alternatively, including an active yaw actuator such as a linear motor to supplement the passive autofurling mechanism by supplying a yaw moment can improve the turbine performance in high winds and strengthen the protection function.

In this report we summarize our work during the three years of the project. This work falls into three general areas: Modeling, analysis, and control.

The first major contribution of the modeling effort was in learning neuro-fuzzy models of the aerodynamics from extensive aerodynamic simulation data provided by a wind engineering code Yawdyn [3]. In principle, experimental data can be used for learning if available. These fuzzy implementations are used to alleviate the complexity of real-time simulation.

Our second major contribution in modeling was to derive an analytical model for the furling mechanism [4]. We have developed a methodology for a more systematic multidisciplinary modeling based on Lagrangian differential algebraic equations [5] that will enable us to build a complete model of the turbine from the aerodynamics to the electrical load.

In the area of analysis, a procedure to characterize the onset of furling was derived, and a linearized model for the furling mechanism was obtained. A procedure to obtain a linearized version of the aerodynamic model was developed and outlined but has not been fully applied yet to the turbine aerodynamics.

In the area of control, a feedforward gain scheduling control was derived based on the model. It will extend the operability of the wind turbine past the onset of furling. This control can be applied using a yaw motor, a motor at the tail, or a linear motor connecting the tail to the body of the turbine. The feedforward control design procedure was shown to be applicable for each of these actuator models. We have also developed a procedure to design bounded control laws that are applicable because of the limited actuation authority of the proposed actuators.

Summary of Achievements

Modeling of the Aerodynamics

We have contacted Bergey Power, Inc., and conducted a site visit to the company's site. As a result, we obtained realistic descriptions of their 10-kW wind turbine as well as preliminary data on the 40-kW turbine.

We have installed Yawdyn [3] and used it to compute the power, thrust, yaw moment, and lateral forces as function of wind speed, wind direction relative to the rotor axis, and rotor angular speed. We contacted Dr. C. Hansen, a consultant for Bergey Power Inc., who provided us with a realistic profile of the blades.

Our simulations showed that the moment produced by the lateral hub forces (in the plane of the blades) is not negligible and must be accurately accounted for in the furling analysis [4].

Fuzzy modeling techniques were then used to learn, in a least-squares sense, a fuzzy Sugeno model [6] of the aerodynamic forces and moments as a function of the wind data and rpm [7,8]. Overall, the approximation was quite good. The approximation can be improved by increasing the complexity of the fuzzy model, but we deemed this to be unnecessary. The fuzzy model code can be substituted for Yawdyn in real-time simulations of the behavior of the turbine, resulting in an increase of efficiency by about two orders of magnitude.

Many alternative fuzzy models of the aerodynamics of a Bergey-type wind turbine were developed [7,8]. Some are constellations of fuzzy inference engines. In particular, we developed a master fuzzy engine that fuses together three fuzzy engines; one is for low tip-speed ratios and does not depend on wind direction; the others are for medium and high tip-speed ratios and depend on the wind direction.

We developed the theory of fuzzy modeling to incorporate and compute derivative information [7,9] more clearly. Because the required fuzzy inference engine has high dimensions there is the issue of whether the consequents are interpretable in terms of aerodynamic coefficients. Another advantage of the developed fuzzy model derives from our recent work to give the fuzzy

coefficients a high level of interpretability. In particular we have developed a highly interpretable form of the Sugeno approximator that incorporates cubic splines [10]. As a result the aerodynamic data generated by Yawdyn can be used to estimate aerodynamic sensitivity derivatives as a function of wind speed and rpm. These derivatives are generally useful for analysis and design [9]. In addition, we developed a "calculus" of interpretable fuzzy approximators. This will allow us to combine systematically many fuzzy engines representing different parts of the turbine dynamics and aerodynamics [9].

We developed local learning algorithms for interpretable Sugeno approximators [8,9]. This will allow a more effective learning of fuzzy aerodynamical models from experimental and/or a computational fluid dynamics simulation data.

We are currently investigating the use and modification of an unsteady aerodynamic code based on the vortex-lattice concept [11]. In this approach, the body (e.g., the tower and hub, etc.) and lifting surfaces are represented by lattices of discrete-vortex line segments. The circulations around these segments are determined by no penetration conditions, by vorticity shedding from the lifting surface into the wake, and by moving the wake so that it remains force-free (i.e., has continuous pressure). Bernoulli's equation is used to determine the pressure distribution over the body, which can then be used by any suitable structural analysis code to study fluid-structure interaction for the purposes of control.

Modeling of Wind Turbine

The equations of motion describing the yaw dynamics of a 40-kW Bergey-type wind turbine have been developed [4,12,13].

We developed and continue to test a simulation software of the autofurling action of the wind turbine based on the derived equations of motion. In particular, we have noticed that the Runge-Kutta simulation code of MATLAB is having some numerical problems in simulating the whole dynamics of the autofurling Bergey-type wind turbine. One problem is that the equations are stiff in the sense that the dynamics of the electrical side after the generator occur on a much faster time scale than the dynamics of the mechanical/aerodynamic side [4,12].

Because of the complexity of the dynamics and aerodynamics involved, and the difficulty of conducting a bifurcation analysis to explain the hunting behavior, we are considering a more systematic modeling approach based on Lagrangian Differential Algebraic Equations (LDAE) [5,14,15]. This will also form the basis of future control designs that incorporate Lyapunov-based passivity.

We developed an LDAE descriptor-based linearization procedure. This will prove helpful in developing linear models of the furling mechanism about an operating point [16].

Control and Actuation

We revised and assessed the control objectives of the autofurling action. One emphasis is to avoid using, measuring, or predicting wind speed in control design and to rely heavily on measurements of the rotor rpm [17].

We conducted a parametric study of the equilibrium conditions at and after the onset of furling. In particular, we developed "furling curves" that show at what wind speed, rotor rpm, and yaw angle the furling occurs given a generator characteristic torque-rpm curve or given a specified power generation level. This latter case can be assumed if power electronics are used to maintain a constant power generation level [17].

We studied the sensitivity of the above curves with respect to the parameters of the wind turbine. These parameters, which include the yaw axis offset and the length of the tail, can be modified in the design process [17].

A model of a Bergey-type furling wind turbine is used to determine a yaw control schedule designed as a feedforward control that maintains high power generation in moderately high winds. We also considered the possibility of using the furling mechanism as a method to achieve maximum power generation efficiency under high winds [17,18].

We have acquired experience in designing nonlinear speed control algorithms that combine the sliding-mode control methodology, nonlinear Smith prediction, mechanical disturbance rejection, and the so-called "sensorless" observers (those that avoid mechanical sensors [19].) The application was motor speed control of a DC motor with nonlinearity resulting from a nonlinear fan load (i.e., a reverse turbine) and from magnetization saturation.

Because the yaw control authority may be limited, we have further developed our earlier work on bounded control. In this approach, the physical limitations on the size of the actuator can be taken explicitly into account when designing the control. Also the work yields a qualitative understanding of the trade-off between fast response and the amount of control authority [20].

We developed energy-based Lyapunov functions to be used in developing stable and robust control algorithms [20]. These functions are developed in the context of LDAEs because this framework is more systematic and capable of dealing with the complexity of the dynamics and aerodynamics involved.

Modeling an Autofurling Wind Turbine

The overall model is shown in Figure 2-1. The aerodynamic, mechanical, electromagnetic, and electrical components are reasonably tightly coupled. For example, changing the electrical load will change the torque needed by the generator, which in turn will change the rpm of the turbine, thus changing the power generated as well as the aerodynamic forces relevant to the yaw motion. This is actually the concept of soft-stall introduced by Muljadi [2].

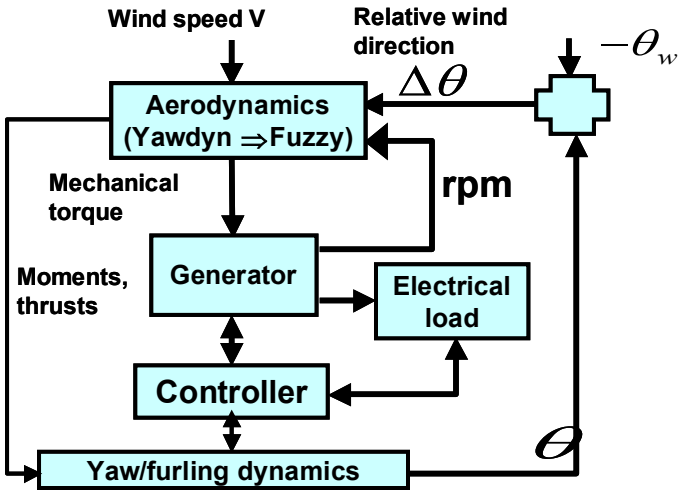

Figure 2-1. Overall model of a furling wind turbine

Our approach to modeling can be summarized as follows:

- Approximate the rotor aerodynamics using codes such as Yawdyn. A fuzzy-logic interpolation scheme is then used to approximate the yaw moments in terms of the three inputs (the wind speed and direction and the rotor rpm) is then used to achieve faster simulations. This will replace part of the aerodynamics block in Figure 2-1. See the section entitled "Modeling the aerodynamics".
- Model the dynamics of the furling dynamics as follows
  - Assume the system is conservative and find expressions for the kinetic co-energy and the potential energy in terms of the generalized coordinates. Then use the Lagrangian method to derive the basic equations of motion [4].
  - Use simple expressions of the tail aerodynamic forces appearing as generalized forces.
  - Effects of friction, control yaw, and mechanical stops are then added.

We have also included equations describing the generator and the electrical load.

Modeling the Aerodynamics

The Use of Yawdyn Code

Models for the power production of a wind turbine have been previously developed [1,21,24,]. The basic model assumes that the amount of power produced by a wind turbine can be expressed as:

$$P = \frac{1}{2}\rho C_p A_B V^3, \qquad \text{(Eq. 2-1)}$$

where P is the power generated by the turbine, C_p is the power coefficient, ρ is the specific density of the air, A_B is the swept area of the blades, V is the effective wind speed based on the component of wind velocity in the direction of the rotor, and ω is the angular velocity of the rotor. Note that C_p is mainly a function of the tip speed ratio (TSR)

$$\lambda = \frac{\omega R_B}{V}, \qquad \text{(Eq. 2-2)}$$

where R_B is the radius of the turbine. Conceivably, however, C_p can also depend on the angle between the wind direction and the rotor axis $\Delta\theta$. For an autofurling wind turbine, the wind thrust on the turbine provides the furling action when the wind speed is high. The thrust can be approximated by $F_{th} = \frac{1}{2}\rho C_{th} A_B V^2$, where C_{th} is the wind thrust coefficient. This coefficient is also dependent on the rpm and hence on the electric load. It may also depend significantly on V and $\Delta\theta$.

A typical relationship between C_p and TSR is shown in Figure 2-2. There is a value of TSR for which C_p is maximized, and which maximizes the power generated by the wind turbine for a given wind speed. Obviously, at any wind speed, the generated aerodynamic power is dependent on the rpm of the turbine because C_p depends on TSR.

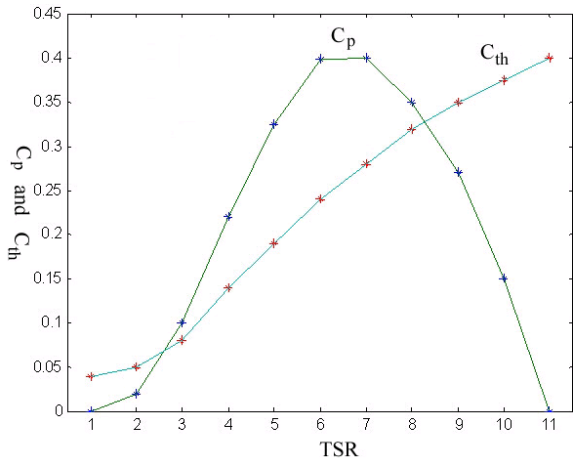

Figure 2-2. Power and thrust coefficients as functions of TSR (after [2])

Note that changing the electric load will change the rpm of the turbine and hence the amount of power generated. The thrust coefficient continuously increases as the TSR increases and that the power coefficient reaches maximum value (C_{pm} =0.4) at a TSR of 6.5 while the coefficient of thrust continues to increase. It is preferable [2] that the wind turbine be operated about a TSR between 4.0 and 6.5. If $\Delta\theta$ denotes the angle between the wind velocity vector and the rotor axis, the effective wind speed in Eq. 2-1 can be thought of as given by: $V = V_{wind} \cos\Delta\theta$. Clearly, this is only a first-order approximation, and $\Delta\theta$ may have additional influences as reflected in the coefficient of thrust, power, and other factors.

In our work, the aerodynamic forces and moments are computed using the software package Yawdyn, which was developed by C. Hansen and his colleagues at the University of Utah (see [3,25-27]).

We show in Figures 2-3 and 2-4 the variations of the generated power and aerodynamic forces and moment relevant to the furling motions as obtained using Yawdyn for a 40-kW Bergey-type wind turbine. Figure 2-5 shows the variations of the generated power and aerodynamic forces and moment relevant to the furling motions. We use this software to generate aerodynamic moments and forces as functions of wind parameters and rotor rpm.

These data include:

- The torque at the hub (and hence the generated power)
- The yaw moment on the body of the nacelle
- The thrust force in the direction of the rotor
- The lateral hub force (in the plane of blade rotation).

For the calculations presented here, we used the fuzzy-logic approximator introduced in [7] to approximate the yaw moments in terms of the three inputs to the aerodynamics block in Figure 2-1; namely, the wind speed V, the wind direction θ_w, and the rpm ω. The remaining blocks are implemented in MATLAB and Simulink.

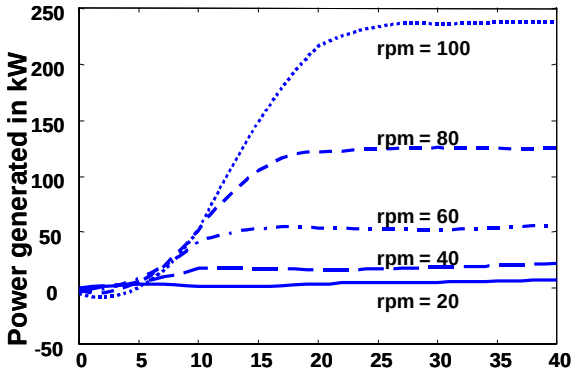

Figure 2-3. Power curves for a 40-kW wind turbine obtained with Yawdyn when the angle between the wind and the rotor is 10 degrees

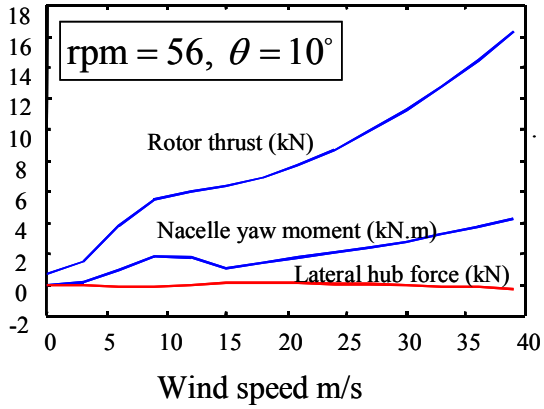

Figure 2-4. Aerodynamic data for a 40-kW wind turbine obtained through Yawdyn

Approximating Yawdyn through Learning

Yawdyn is a software package, programmed using FORTRAN, which runs a simulation of horizontal axis wind turbines. It is computationally expensive for real-time simulations, and hence can be replaced by a Sugeno Fuzzy Inference System (FIS) [28] that approximates it through learning [29]. The different parameters of the turbine are written in a text file–Yawdyn.ipt–according to a specific format. The wind input to the turbine is also defined in another text file–Yawdyn.wnd. The output of the simulation is generated in the file named Yawdyn.plt. Yawdyn is designed for single runs and it comes with YawdynVB, which is a Windows graphical user interface programmed using Visual Basic. YawdynVB interfaces with the Yawdyn.ipt file, keeping the direct user interactions with the text files to a minimum–the user still has to manually edit the Yawdyn.wnd file.

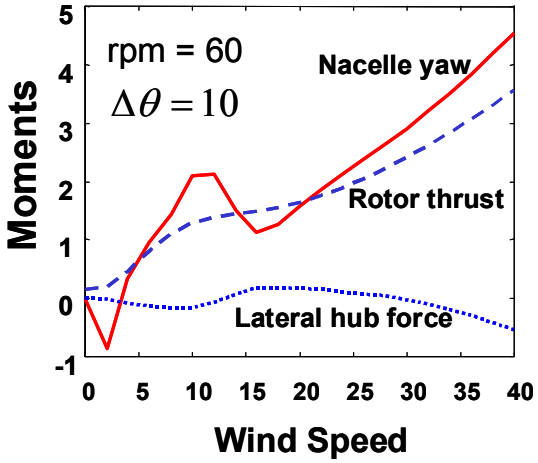

Figure 2-5. Aerodynamic moments for a 40-kW wind turbine obtained through Yawdyn. Note that the moment due to flow over the nacelle is the most significant at high wind speed

MATLAB functions to interface with the Yawdyn program were written to allow the gathering of data points without human interference. Different architectures of fuzzy approximators were proposed and compared. Figure 2-6 represents the different modules of the software and connections between them.

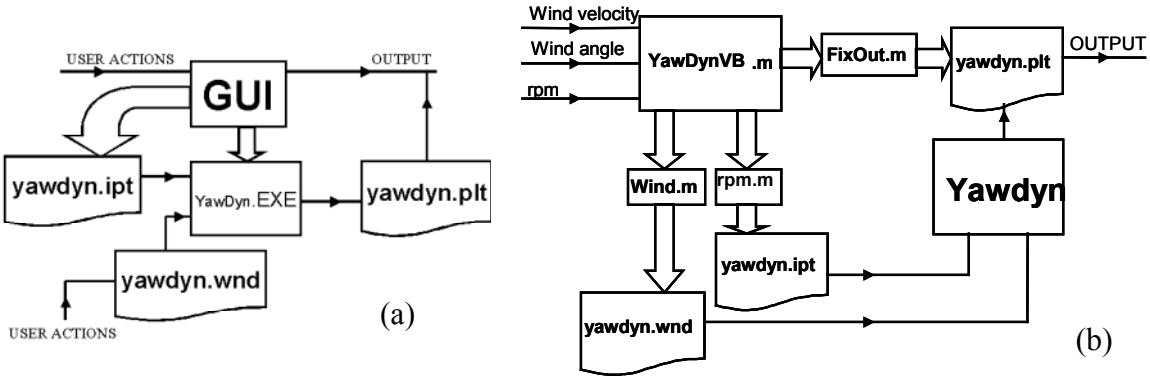

Figure 2-6. Software interfaces

The interface is available from the authors through email (bikdash@ncat.edu) and it includes:

- Wind.m: Updates Yawdyn.wnd with wind speed, and relative wind angle.
- RPM.m: Updates Yawdyn.ipt with a new rpm value.

- FixOut.m: A MATLAB script that modifies the format of Yawdyn.plt so it can be loaded into MATLAB.
- YawdynVB.m: Calls the above functions and runs Yawdyn.exe.

In its basic form, a linear Sugeno approximator is an FIS that maps a crisp vector $x = [x_1, x_2, \cdots, x_n]^T \in \Re^n$ into $y \in \Re$. The output assigned to y by the k^{th} rule, $L_k(x)$ is an affine function of the input vector:

$$\begin{aligned} R^k : \text{IF} \quad & x_1 \text{ is } A_1^k \text{ AND } x_2 \text{ is } A_2^k \text{ ... AND ... } x_n \text{ is } A_n^k, \\ \text{THEN} \quad & \hat{y} = y^k = c_0^k + c_1^k x_1 + \cdots + c_n^k x_n, \end{aligned} \qquad \text{(Eq. 2-3)}$$

where c_0^k, c_1^k, …, c_n^k are the consequent coefficients of the k^{th} fuzzy rule. In Equation 2-3, A_i^k specifies which linguistic value or term of the linguistic variable x_i is being tested by rule k. The output $\hat{y}$ is obtained by a weighted average of all the y^k contributed by all the rules as shown in Equation 2-3. Each y^k represents the crisp output value recommended by the corresponding rule. Hence

$$\hat{y} = \sum_k \beta_k(x) y^k, \qquad \text{where} \qquad \beta_k(x) = \frac{\rho_k(x)}{\sum_k \rho_k(x)}. \qquad \text{(Eq. 2-4)}$$

In the above, $\rho_k(x)$ is the truth value of the antecedent of the k^{th} rule evaluated with input x or $\rho_k(x) = A_1^k(x_1).A_2^k(x_2)\cdots A_n^k(x_n)$ where $A_i^k(x_i)$ is the membership function of x_i in its attribute tested by the k^{th} rule. $\beta_k(x)$ is the normalized truth value of the k^{th} rule. The normalized truth values always possess the addition-to-unity property. A learning procedure based on the least squares solution is used here to learn the coefficients of the Sugeno FIS [6]. A sufficient number of training sample points must be obtained. For more details, see for instance [28].

Increasing the number of membership functions (MF) assigned to every input will improve the performance but the learning time will increase exponentially. In general we chose 6 MF. For three inputs, this implies that 216 rules would cover all combinations of input attributes. With 4 coefficients per rule, this requires 864 coefficients for the approximators. The data used for the learning consisted of 9388 Yawdyn simulations, which is reasonably larger than the number of coefficients to be learned.

Approximation Alternatives

Another consideration is whether pre-processing or post-processing can improve the overall approximation. This will make different configurations of the Sugeno approximators possible. We constructed three such FIS as shown in Table 2-1.

Table 2-1: Definitions of the Different FIS Implementations

FIS Name	Inputs	Outputs	MF	Coefficients	Training Data
GeneralYaw	$V, \omega, \Delta\theta$	$P, M_{thrust}, \cdots$	6	864	9388
CpvsTSR	$\lambda, \Delta\theta$	$P, M_{thrust}, \cdots$	6	108	9388
CthvsTST	$\lambda, \Delta\theta$	C_Y	6	108	9388

One can approximate any output (say power) directly, as is shown in Figure 2-7. Using a randomly generated test data set, the performance is compared to that of Yawdyn. To test the run-time (RT), the built-in MATLAB function clock was used. The FIS is faster by two orders of magnitude. Table 2-2 lists the output and the run time values. The quality of the approximation for each output is shown in Figure 2-8. It is noted that the error does not exceed 2 %, which is a reasonable value.

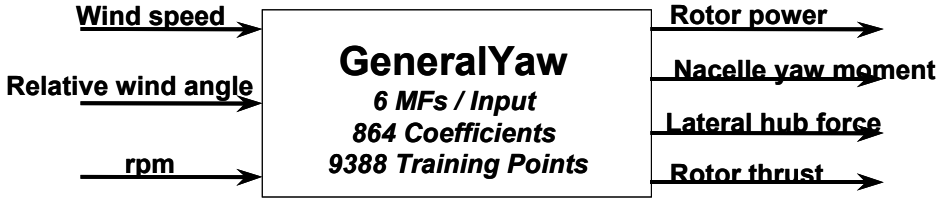

Figure 2-7. A fuzzy inference engine approximating the output of Yawdyn and computing the aerodynamic forces and moments in terms of wind data and rpm

Table 2-2: YawDyn versus the Sugeno FIS 'GeneralYaw' for Random Input Samples

V_{wind}	$\Delta\theta$	Rpm	P_{rotor}	$\hat{P}_{rotor}$	Yawdyn Run Time (sec)	FIS Run Time (sec)
35	31	35	17.95	18.06	4.306	0.110
29	50	21	6.744	6.732	3.185	0.130
17	11	34	9.825	9.848	4.427	0.100
29	18	61	57.33	57.30	7.361	0.110
12	41	48	21.80	22.04	7.691	0.110
23	53	82	83.08	83.37	11.28	0.130
18	17	45	22.88	23.11	6.209	0.130

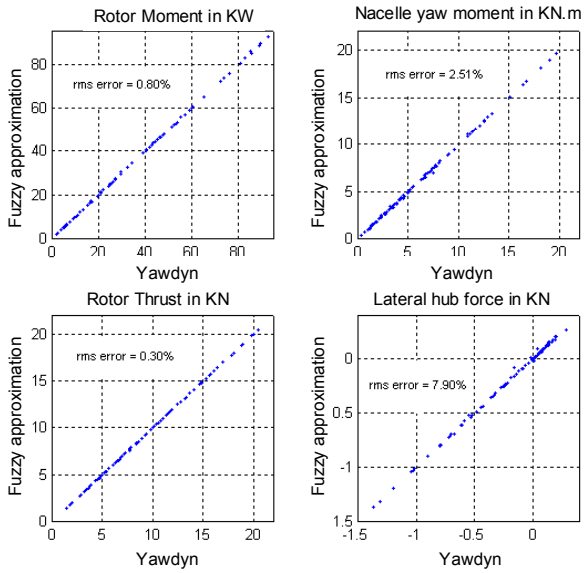

Figure 2-8. The quality of the approximations of the Yawdyn output data versus the output of the Sugeno FIS named GeneralYaw

One can also base the approximations on the coefficient of power C_P. The power coefficient curves are approximately the same for different values of the rpm when TSR is less than 8. So this region can be approximated by a two-input FIS. For ranges of TSR greater than 8, we have to include the rpm as another input. In both cases, the model will be simpler than the more general three-input FIS discussed earlier. This will make the learning process much easier because the system has only two inputs–the tip speed ratio and the relative wind angle. The number of membership functions assigned to those inputs can be further increased without

worrying about the RT.

Clearly it is advantageous to consider a simpler FIS such as the one in Figure 2-9. Its performance is summarized in Table 2-3. There is a significant increase in speed at the expense of a small degradation in performance.

Figure 2-9: A smaller FIS assuming simplified relations in terms of the TSR

Table 2-3: Yawdyn versus the Sugeno FIS 'CpvsTSR' for Random Input Samples

$\Delta\theta$	TSR	P_C	$\widehat{P}_C$	Yawdyn Run Time (sec)	FIS Run Time (sec)
13	1.2732	0.0123	0.0129	7.400	0.0710
1	2.7322	0.1196	0.1209	16.35	0.0100
56	3.2620	0.0924	0.0929	11.71	0.0200
48	0.7716	0.0051	0.0053	3.485	0.0100
16	0.9502	0.0062	0.0059	3.905	0.0200
44	4.8564	0.2233	0.2155	7.351	0.0100
27	1.0104	0.0076	0.0076	5.398	0.0100

A Hierarchical Fuzzy Model

It is possible to further reduce the complexity of the FIS learning by using fewer inputs, which consequently reduces the run-time. But then, the reduced FIS can only operate in specific regions. An example is an FIS that approximates the coefficient of power as a function of the TSR as shown in Figure 2-9.

Simulations show that a one-input FIS based on TSR would perform best for TSR values less than 4, and a two-input performs best for TSR values less than 8. We therefore designed a hierarchical model that consists of a master FIS that decides which of the FIS will be invoked based on the value of the TSR. Such a system is represented in Figure 2-10. If the TSR was 2 for example, it would be intuitive to involve FIS1. If the TSR was 4.3 then the output should be based on participation from both FIS1 and FIS2.

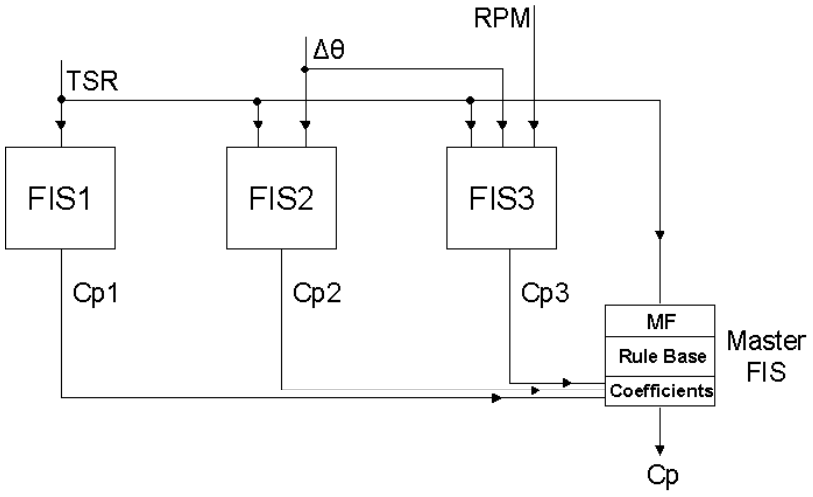

Figure 2-10. The hierarchical architecture of the fuzzy inference system modeling the aerodynamics of the wind turbine.

The rulebase of the master FIS shown below will organizes the handoff among the lower-level FIS:

- IF TSR is "less than 4" THEN C_P is given by FIS1
- IF TSR is "between 4 and 8" THEN C_P is given by FIS2
- IF TSR is "greater than 8" THEN C_P is given by FIS3

where "less than 4", "between 4 and 8", and "greater than 8" are linguistic attributes interpreted using the membership functions of Figure 2-11.

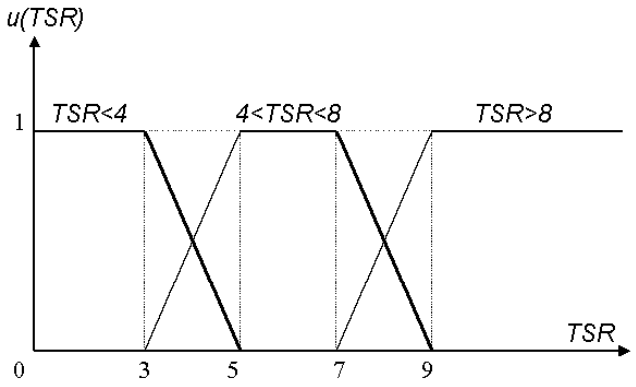

Figure 2-11. Membership functions representing the TSR regions of operation

The performance of the master FIS (called MasterFIS) was measured by taking random input samples and comparing the corresponding outputs to those obtained from other As expected, the MasterFIS yielded better results in the fuzzy area (TSR close to 8 and 4) than did the other two FIS. These results are shown in Table 2-4.

Table 2-4. Comparisons among the Different FIS and Yawdyn

TSR	P_C	MasterFIS (percent error)	FIS2 (percent error)	FIS1 (percent error)
6.511	0.414	+1.615	+1.640	+1.449
6.597	0.347	-0.302	-0.565	+1.199
6.190	0.378	-0.719	-0.806	+1.010
6.108	0.505	-2.450	-2.475	-1.554
6.744	0.439	-5.325	-5.058	-6.493
9.396	0.422	-2.742	-5.464	-2.258
6.760	0.532	-5.113	-5.843	-2.006
7.086	0.417	+0.184	-0.276	+1.419
7.819	0.476	-0.163	-0.216	+0.099

Sensitivity and other derivatives of the aerodynamics can be helpful in understanding the behavior of the rotor or designing improvements. More importantly, they can be used to determine the linear stability of the autofurling mechanism.

The Interpretable Sugeno Approximator (ISA) has been recently introduced [9] to bestow a high level of interpretability on FIS. It requires the two concepts of differentiable Orderly Local Membership Function Basis (OLMF basis) and rule-centered consequent polynomials. The value at some input vector of a mapping approximated in this form can then be interpreted as a convex combination of the truncated Taylor series expansions of the map about the centers of the rules immediately adjacent to the input vector. This form is highly interpretable even when the input and output spaces are of high dimensions. This interpretability comes from that of derivatives, which often have a strong physical interpretation and are easier to characterize.

Other advantages include:

1. Simplification of training and testing. For example, if values of the map and its partial derivatives are available at the centers of the rules, no training would be necessary.
2. Training and testing can be conducted locally, meaning with fewer rules at a time.
3. Meaningful initialization of the consequence coefficients when learning the coefficients.

We illustrate for a scalar input $x \in D \subset \Re$ having M attributes $a^1, a^2, \cdots, a^M$. The MF of the m^{th} attribute is denoted $\mu^m(x) = \mu(x \text{ is } a^m)$. A well-known example [28] of a "local" membership function is the triangular function $\mu_{triang}(x; L, g, U)$ centered at g and of support $[L,U]$. We generalized in [9] these concepts to OLMF which are (1) everywhere smooth; (2) local in the sense that each is zero outside some interval; and (3) properly overlapping meaning that at most two MF are nonzero at a time.
A typical construction can be borrowed from the study of cubic splines [10]. Cubic splines are easy to evaluate and have many desirable properties. First, we consider the "mother" cubic-spline function defined over the interval [-1,1]: $q(x;-1,0,1) = Q_3(x)$ where $Q_3(x) = 1 - 3x^2 + 2x^3$ for $0 \le x \le 1$ and $Q_3(x) = 1 - 3x^2 - 2x^3$ for $-1 \le x \le 0$, and zero otherwise. From this function we can generate the basis. Note that Q_3 and Q_3' vanish at -1, 0, and 1, but that the second derivative Q_3'' is discontinuous at the boundaries. For example, $Q_3''(-1^-) = 0$ but $Q_3''(-1^+) = 6$. An OLMF basis for multiple inputs can be formed using outer products.

The proposed approximator has two main characteristics:

1. On the antecedent side, the membership functions form a differentiable OLMF;
2. On the consequent side, rule-centered consequent affine polynomials are used. This is the form of the Sugeno Approximator that we call the ISA.

One of the main advantages of the ISA is its high interpretability, which follows from that of the coefficients of the consequent polynomials. The consequent have the rule-centered form shown below

R^k : If x_1 is A_1^k and x_2 is A_2^k and… x_n is A_n^k , (Eq. 2-5)

$$\text{THEN} \quad y^k = Y_k(x) = b_0^k + b_1^k(x_1 - r_1^k) + b_2^k(x_2 - r_2^k) + ... + b_n^k(x_n - r_n^k), \tag{Eq. 2-6}$$

where r^k is the rule center. When $x = r^l$, the center of the l^{th} rule, the output of the ISA is simply the constant coefficient of $Y_l(x)$, the consequent polynomial of the l^{th} rule. In other words, $b_0^l = y(r^l)$. Note that if the membership functions were not differentiable at their boundaries (as when triangular or trapezoidal functions are used), the term $\frac{\partial \beta_k}{\partial x_p}$ will not vanish when needed. Moreover, the derivative $\frac{\partial \hat{y}}{\partial x_p}$ does not exist there. This is why the differentiability condition on the OLMF basis is needed.

Theorem 1. *Suppose that $\hat{y}(x)$ is a Sugeno approximator such that (a) the antecedent-side of the Sugeno-type FIS uses a set of differentiable OLMF basis, and (b) the consequent-side affine polynomials are written in the rule-centered form shown in Equation 2-6, then $Y_k(x)$ can be interpreted as a linear Taylor series expansion of $\hat{y}(x)$ about the point $x = r^k$, the "center" of the k^{th} rule.*

For example, the function $y(x) = x_1^2 + 3x_2^2 + \cos\frac{\pi x_1 x_2}{2}$ has the following general form of the consequent polynomial

$$\begin{aligned} Y(x;\eta) = y(\eta) &+ \left(2\eta_1 - \frac{\pi\eta_2}{2}\sin\frac{\pi\eta_1\eta_2}{2}\right)(x_1 - \eta_1) \\ &+ \left(6\eta_2 - \frac{\pi\eta_1}{2}\sin\frac{\pi\eta_1\eta_2}{2}\right)(x_2 - \eta_2) \end{aligned} \tag{Eq. 2-7}$$

for every rule centered at η in the grid.

When using the ISA to learn the aerodynamics, the coefficients of the rule consequents can then be interpreted as the derivative of an output (say the coefficient of power) with respect to the TSR. This is illustrated in Figure 2-12.

Learning through Resampling

The ISA also allows for one additional benefit: The ability to resample the grid on which the approximation is defined using simple-to-implement analytical expressions [8]. Learning mechanisms can benefit appreciably. A typical learning mechanism requires performing a number of learning epochs in order to improve the approximation quality. This could be

computationally expensive if the initial grid is fine. The alternative is to start with a coarse grid then switch to the finer grid at the later learning epochs.

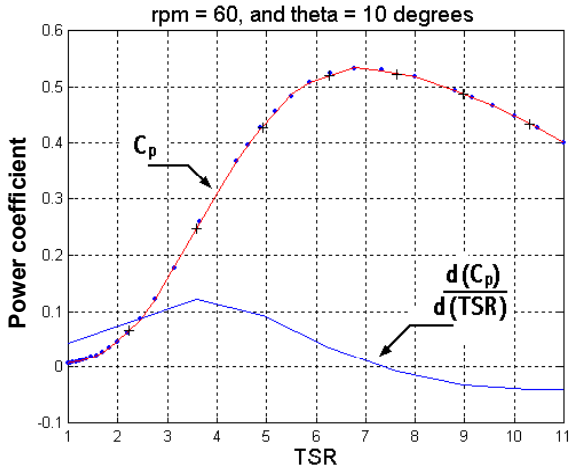

Figure 2-12. Coefficients of the ISA can be interpreted as derivatives of the output (here the coefficients of power) with respect to different inputs evaluated at the rule centers. In this case, these can now be used to compute the aerodynamic sensitivity derivatives.

The idea presented here was tested on a simple function and the results are illustrated [8] in Figure 2-13. In this example, we learn a single input function on a grid consisting of 35 MF. The grid is kept fixed while passing through 10 epochs of learning. After each epoch there is a slight improvement in the quality of the approximation (the indicator was the root-mean-square (RMS) error) till the final epochs where the improvement slows down and the error starts converging to a specific value.

In the second experiment, the same function is learned using a coarse grid consisting of 5 MF. As theoretically predicted, the RMS error was much higher than that of the fine grid. Resampling to 15 MF was applied which increased the RMS error even more. Another epoch of learning was applied in which there was a dramatic improvement of the RMS error. We kept switching between learning and resampling till we reached the fine grid of 35 membership functions. The results reveal that after each resampling there is a slight increase in the RMS error but the learning that follows is characterized by a dramatic decrease of the error. At the fourth learning epoch the RMS error reached a value the other fine grid could not come close to even after its 10 epochs of learning.

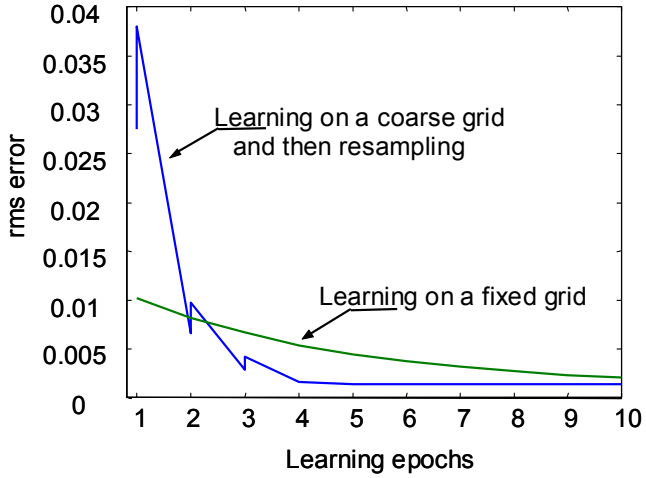

Figure 2-13. Plot of the RMS approximation error versus the learning epoch. The ISA leads to a better and faster recursive learning by starting the learning on a coarse grid then resampling analytically than learning on a coarser grid.

Advanced Aerodynamic Modeling

A major difficulty in the modeling and analysis of a furling wind turbine arises from the uncertainty associated with the aerodynamics. In the preceding sections, we have illustrated how Yawdyn can be used to obtain an aerodynamic model of the flow under many simplifying assumptions; for instance assuming steady flow and small yaw angle. Yawdyn will not give correct aero forces for a rotor operating skewed to the wind. The errors increase with increasing skew angles. The uncertainty precludes effective prediction of the furling behavior. For instance, it seems that even for small yaw angles and yaw rates, the center of pressure in the plane of blade rotation at which the thrust is applied is uncertain and may not be centered at the rotor. This has been an assumption used throughout the research reported here as well as in the literature.

Unfortunately, the uncertainties inherent in furling wind turbines will reappear in all advanced wind turbine research whether or not furling is used. For instance, the aerodynamic uncertainty of using flexible blades will be similar to the uncertainty discussed above.

Relatively recent developments in modeling subsonic flow fields around arbitrary lifting and non-lifting three-dimensional bodies make it possible to add more realism to the aerodynamic analysis of wind-structure-control interactions. One of the most successful general unsteady aerodynamic models is based on the vortex-lattice concept [11]. In this approach, the body (e.g., the tower, hub, etc.) and lifting surfaces are represented by lattices of discrete-vortex line segments. The circulations around these segments are determined by

1. Requiring the normal component of the velocity of the wind relative to the structure to be zero at a finite number of points on the surface;
2. Requiring the pressures in the streams coming off the upper and lower sides of the lifting surface to be equal along the trailing edges and tips, a step that requires vorticity to be shed from the lifting surface into the wake; and
3. Moving the wake so that it remains force-free (i.e., has continuous pressure) at all times. Bernoulli's equation is used to determine the pressure distribution over the body, and then, through numerical integration, the aerodynamic forces and moments acting on the body are determined.

Aerodynamic interference among the various components of the configuration (hub/blade, blade/blade, and blade/tower) and the influence of the wake (history of the motion) are routinely taken into account with this approach. This approach may offer an improved method of estimating the aero effects, but has not been incorporated in this work. The capability of unsteady aerodynamics code is illustrated in Figures 2-14 and 2-15.

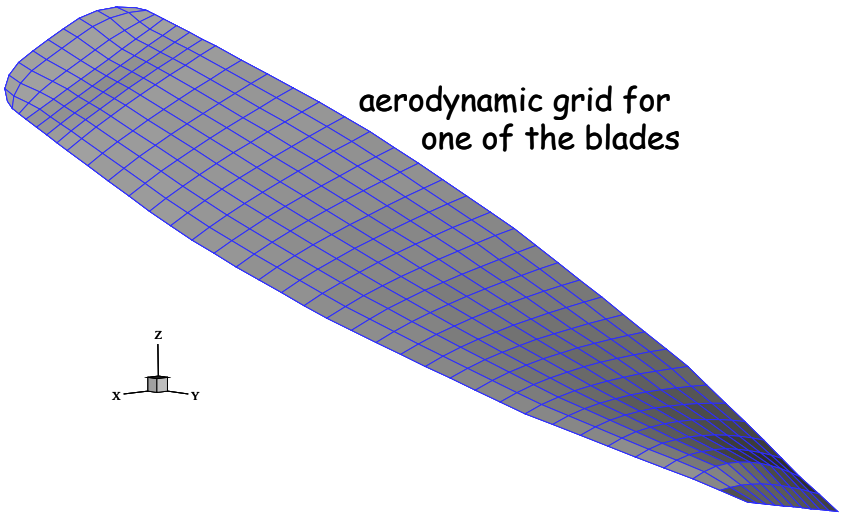

Figure 2-14. Grid used for the unsteady aerodynamic code

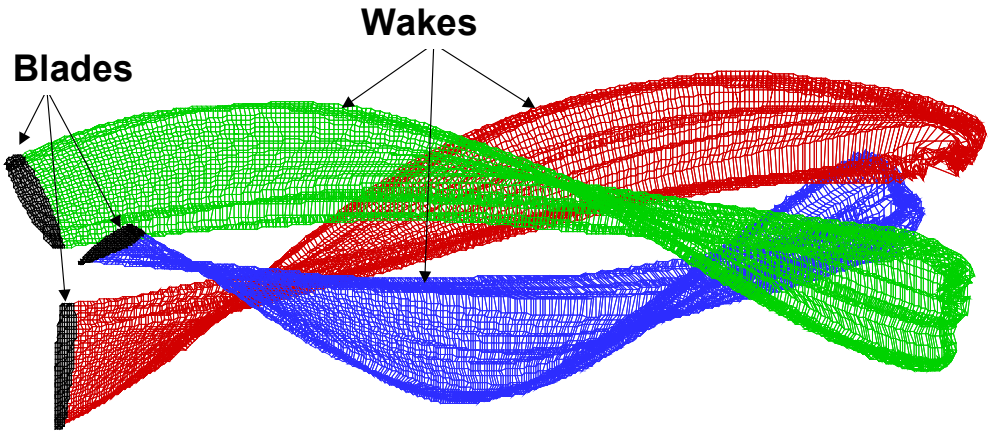

Figure 2-15. Wakes obtained through the unsteady aerodynamic code developed in [11]

Modeling the Furling Mechanism

Notation

- **Inertia Terms**. J_{GY} is the moment of inertia of generator about the yaw axis after tilting. J_{OT} is the moment of inertia of tail about an axis passing by its center of gravity. M_G: Mass of the generator M_T: Mass of the tail.
- **Geometry** (Distances). L_1: Distance between the yaw axis and the rotor axis. L_2: Distance along the rotor between the yaw axis and the tail hinge. L_3: Distance between the hinge and the center of gravity of the tail. L_4: Distance between yaw axis and the plane of the rotation of the blades. L_{AC}: Distance between the yaw axis and the aerodynamic center of the tail.

- **Geometry (Angles)**. β: Tilt angle between the rotor axis and the horizontal. α: Angle between two vertical planes, one containing the tail and the other containing the rotor axis. γ: Angle of rotation around the rotor of the tail hinge axis measured from a vertical plane.
- **Degrees of Freedom.** θ: Yaw angle from the A frame to a vertical plane containing the rotor axis (positive counterclockwise). θ_w: Angle from the A frame to the wind direction (positive counterclockwise). $\Delta\theta = \theta - \theta_w$: Angle from wind to rotor (positive counterclockwise). ψ: Furling angle of the tail about the tail hinge axis. ψ=0 means that the tail is perfectly aligned with the rotor (positive clockwise). $\Delta\theta - \psi$: Angle from the tail to the wind (positive clockwise).
- **Kinematics:** $\vec{\omega}_D^T$: Angular velocity of the tail in the F_D frame. $\vec{\omega}_A^T$: Angular velocity of the tail in the inertial frame $\vec{\omega}_A^T$.

Description and Coordinates

The rotor axis of the wind turbine is tilted by an angle β with respect to the horizontal. Assuming β=0 (no tilting), we show a top view of the turbine in the furled position in Figure 2-16. The tail points more or less always in the direction of the wind. We define the inertial frame $F_A = (\vec{a}_1, \vec{a}_2, \vec{a}_3)$, where $\vec{a}_3$ is vertical (upward), and $\vec{a}_2$ is understood to point in the average direction of the wind.

The body of the turbine, including the generator and rotor, is free to rotate (yaw) around a vertical axis denoted by point O. Note that this vertical axis is offset from the vertical plane containing the rotor axis by a distance L_1. The wind exerts on the plane of the blades a thrust force, which is assumed to be centered along the rotor. This thrust force has a moment that tends to yaw the rotor by an angle θ. After yawing with an angle θ, the frame $F_B = (\vec{b}_1, \vec{b}_2, \vec{b}_3)$ results, where $\vec{b}_3$ is vertical (upward), and $\vec{b}_2$ is horizontal and points in the direction of the rotor. This rotation is prevented by the aerodynamic force on the tail, until the wind thrust becomes large enough (at high winds) to overcome the action of the tail.

Figure 2-17 shows the side view of the turbine after tilting the rotor upward by an angle β with respect to the horizontal. This tilting is introduced to ensure that the blades do not hit the tower in high winds as a result of the flexibility of the blades. Note that when the tail furls, it rises vertically because the tail hinge is NOT vertical. This is illustrated in Figures 2-17 and 18.

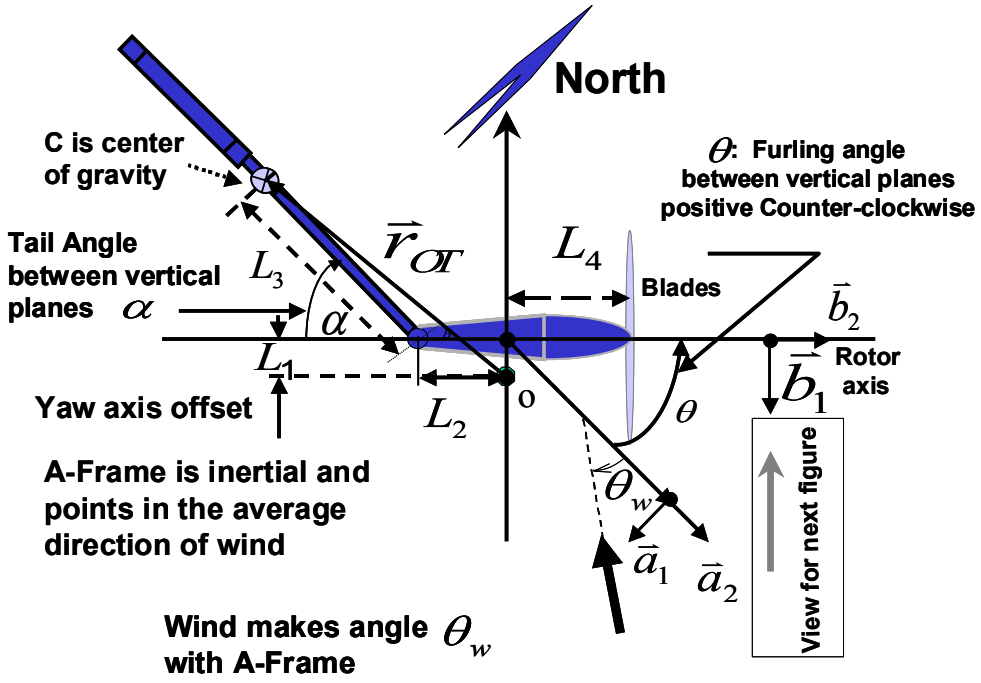

Figure 2-16. Top view before tilting

The generator's frame $F_C = (\vec{c}_1, \vec{c}_2, \vec{c}_3)$ is chosen with $\vec{c}_1$ in the direction of $\vec{b}_2$, and $\vec{c}_2$ being the generator's axis, and $\vec{c}_3$ being perpendicular to $\vec{c}_1$ and $\vec{c}_2$.

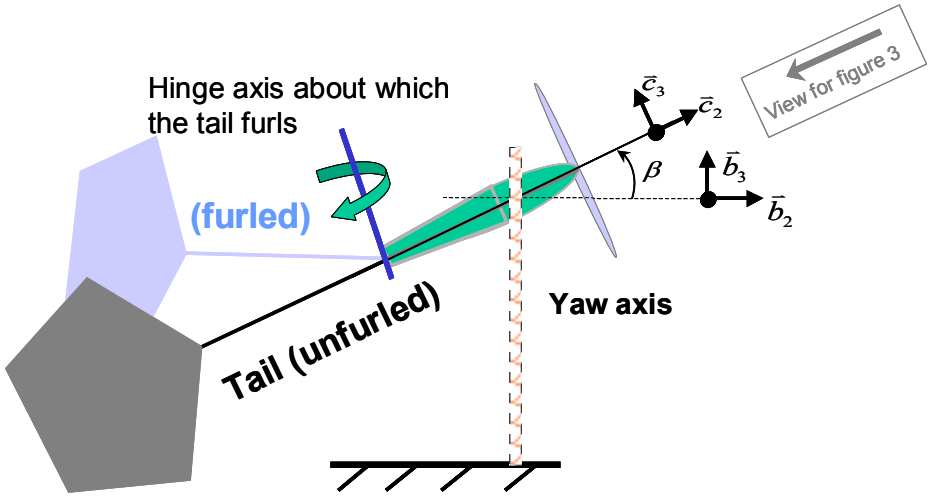

Figure 2-17. Side view

The frame $F_D = (\vec{d}_1, \vec{d}_2, \vec{d}_3)$ is also attached to the generator but is aligned with the tail hinge, which means that it can be easily used to describe the motion of the tail as shown in Figure 2-19. This figure shows a top view along $\vec{d}_1$, which is parallel to the hinge axis. The tail is not free to furl completely because of the two padded stops that prevent the tail from swinging more than a total of 70 degrees. Note that $\vec{d}_1$ makes an angle γ with $\vec{d}_3$.

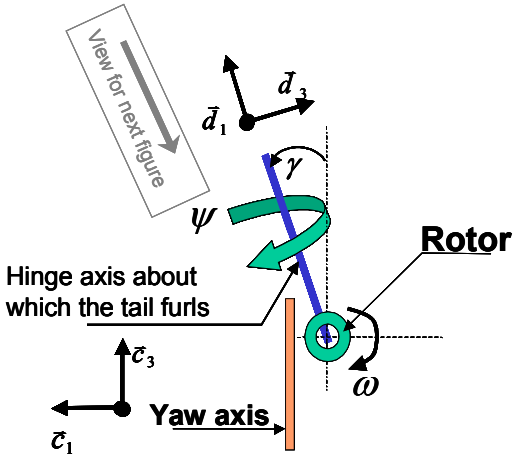

Figure 2-18: Front view along rotor

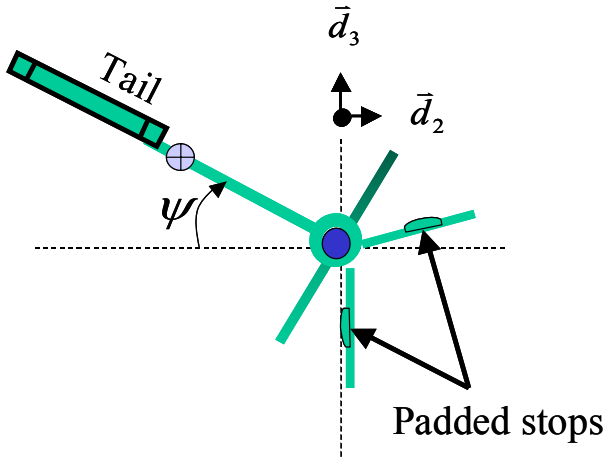

Figure 2-19. Top view along hinge axis

Drag and Lift Forces on the Tail

The magnitudes of the aerodynamic forces acting on the tail are modeled simply as

$$F_{drag} = \frac{1}{2}\rho V_{wind}^2 A_{tail} C_D, \tag{Eq. 2-8}$$

and

$$F_{lift} = \frac{1}{2}\rho V_{wind}^2 A_{tail} C_L, \tag{Eq. 2-9}$$

where C_L and C_D are the coefficients of lift and drag. Here, they are assumed to be those of the flow over a flat plate under a very small angle of attack. The angle of attack here is essentially the angle between the tail and the wind, and hence is known to be small from observation and design. The direction of the drag is along the wind direction, and the lift direction is perpendicular to the drag direction. Both C_L and C_D are functions of $\Delta\theta - \psi$. In the F_A frame, the aerodynamic force on the tail is

$$\vec{F}_{tail} = (F_{drag}\sin\theta_w - F_{lift}\cos\theta_w)\vec{a}_1 - (F_{drag}\cos\theta_w + F_{lift}\sin\theta_w)\vec{a}_2. \tag{Eq. 2-10}$$

Expressions in the $\{\vec{d}\}$ frame can be readily obtained through simple transformations based on the geometry. See [12] for more details.

Lagrange's Equations of Motion for the Yaw Dynamics

Lagrange's equations of motion are

$$\frac{d}{dt}\left(\frac{\partial T^*}{\partial \dot{\theta}}\right) - \frac{\partial T^*}{\partial \theta} + \frac{\partial V}{\partial \theta} + \frac{\partial D}{\partial \dot{\theta}} = Q_\theta, \tag{Eq. 2-11}$$

and

$$\frac{d}{dt}\left(\frac{\partial T^*}{\partial \dot{\psi}}\right) - \frac{\partial T^*}{\partial \psi} + \frac{\partial V}{\partial \psi} + \frac{\partial D}{\partial \dot{\psi}} = Q_\psi, \tag{Eq. 2-12}$$

where Q_θ and Q_ψ represent generalized forces (torques) arising from aerodynamic forces, and friction, and other forces not already accounted for explicitly in the co-kinetic and potential energies, and in the dissipation functions. To find the generalized forces, we must express the virtual work δW arising from those forces aerodynamics as $\delta W = Q_\theta \delta\theta + Q_\psi \delta\psi$.

Energy Expressions

The position vector from the yaw axis to the center of gravity of the tail is

$$\vec{r}_{OT} = -L_1\vec{b}_1 - L_2\vec{c}_2 - L_3\cos\psi\vec{d}_2 + L_3\sin\psi\vec{d}_3. \qquad \text{(Eq. 2-13)}$$

The kinetic co-energy of the system excluding the rotor kinetic co-energy is approximately

$$T^* = \frac{1}{2}M_T\vec{v}_T.\vec{v}_T + \frac{1}{2}J_{OT}\vec{\omega}_A^T.\vec{\omega}_A^T + \frac{1}{2}J_{GY}\dot{\theta}^2 \qquad \text{(Eq. 2-14)}$$

$$= \frac{1}{2}J_1(\psi)\dot{\theta}^2 + \frac{1}{2}J_2\dot{\psi}^2 + J_{12}(\psi)\dot{\psi}\dot{\theta}, \qquad \text{(Eq. 2-15)}$$

where $\vec{v}_T = \frac{d\vec{r}_{OT}}{dt}$, and the angular velocity with respect to the A frame [23] is $\vec{\omega}_A^T = -\dot{\psi}\vec{d}_1 + \dot{\theta}\vec{b}_3$, and

$$\begin{aligned} J_1(\psi) = M_T[&(L_2\cos\beta + L_3\cos\psi\cos\beta + L_3\sin\psi\sin\gamma\sin\beta)^2 \\ &-(L_1 + L_3\sin\psi\cos\gamma)^2] + J_{OT} + J_{JG} \end{aligned}$$

$$\begin{aligned} J_{12}(\psi) = M_T L_3[&(L_1 + L_3\sin\psi\cos\gamma)(-\sin\psi\cos\beta + \cos\psi\sin\beta\sin\gamma) \\ &-\cos\psi\cos\gamma(L_2\cos\beta + L_3\cos\psi\cos\beta + L_3\sin\psi\sin\beta\sin\gamma)] \\ &-J_{OT}\cos\beta\cos\gamma \end{aligned}$$

$$J_2 = M_T L_3^2 + J_{OT}.$$

The system potential energy is

$$V = M_T g\,\vec{r}_{OT}.\vec{b}_3 = -M_T g(L_2\sin\beta + L_3\cos\psi\sin\beta - L_3\sin\psi\sin\gamma\cos\beta).$$

Generalized Forces

The generalized force Q_ψ is obtained by expressing the virtual work done by the $\vec{F}_{tail}$ assuming $\delta\theta = 0$. This leads to

$$Q_\psi = M_{stop} + M_{Tail}^{\psi} + M_{Control}^{\psi},$$

where $M^{\psi}_{control}$ is the control, and M_{stop} is the force exerted by the stop pads on the tail. This can be expressed as

$$M_{stop} = \begin{cases} K_s\psi & if \quad \psi < 0°, \\ 0 & if \quad 0 \le \psi \le 70°, \\ -K_s(\psi - 70°) & if \quad \psi > 70°, \end{cases}$$

where K_s is constant. Moreover M^{ψ}_{tail} is the aerodynamic furl moment due to tail, or

$$M^{\psi}_{tail} = (\vec{r}_{hac} \times \vec{F}_{Tail}).\vec{d}_1,$$

where $\vec{r}_{hac}$ is the distance between the hinge of the tail and the aerodynamic center of the tail; that is, $\vec{r}_{hac} = -L_{ac}\cos\psi\vec{d}_2 + L_{ac}\sin\psi\vec{d}_1$. It can be shown that

$$M^{\psi}_{tail} = F_{drag}L^{\psi}_{drag} + F_{lift}L^{\psi}_{lift},$$

where

$$L^{\psi}_{drag} = L_{ac}[\cos\Delta\theta(\cos\psi\sin\beta\sin\gamma - \sin\psi\cos\beta) + \sin\Delta\theta\cos\psi\cos\gamma], \qquad \text{(Eq. 2-17)}$$

and

$$L^{\psi}_{lift} = L_{ac}[\sin\Delta\theta(\sin\psi\cos\beta - \cos\psi\sin\beta\sin\gamma) + \cos\Delta\theta\cos\psi\cos\gamma]. \qquad \text{(Eq. 2-18)}$$

Now, under the assumption that $\sin\gamma\sin\beta \approx 0$ and $\cos\gamma \approx \cos\beta$, then M^{ψ}_{tail} can be approximated as

$$M^{\psi}_{tail} = \frac{1}{2}\rho V^2_{wind}A_{tail}L_{ac}\cos\beta[C_L\cos(\Delta\theta - \psi) + C_D\sin(\Delta\theta - \psi)].$$

The other generalized force Q_θ is obtained for a constant ψ. It can be expressed as

$$Q_\theta = M_{Yawdyn}(V_{wind}, \Delta\theta, \omega) + M^{\theta}_{tail} + M^{\theta}_{Control},$$

where $M^{\theta}_{Control}$ is a control moment applied at the yaw axis, M^{θ}_{tail} is the aerodynamic moment resulting from forces on the tail, and $M_{Yawdyn}(V_{wind}, \Delta\theta, \omega)$ is the total aerodynamic moment on the nacelle body and the rotating blades (including thrust and lateral force). Hence

$$M_{Yawdyn}\left(V_{wind}, \Delta\theta, \omega\right) = M_{thrust} + M_{nacelle} + M_{LHF}$$

where $M_{nacelle}$ is the yaw moment exerted by the fluid flow on the body of the nacelle, M_{LHF} is the moment exerted by the lateral hub force exerted by the flow at the hub of the blades perpendicular to the rotor, and M_{thrust} is the moment exerted by the thrust of the rotor multiplied by the off-center length

$$M_{thrust} = \text{Rotor thrust} \times \mathrm{L}_1,$$

where L_1 is the yaw axis offset (see Figure 2-16.) Unfortunately, there is an ambiguity as to the location of the center of wind pressure. L_1 is the moment arm of the thrust, assuming that the center of pressure is on the rotor axis exactly. Examples of Yawdyn moments were shown in Figure 2-5. See the discussion in the section entitled "Advanced Aerodynamics Modeling".

The term M^{θ}_{tail} is the moment that results from the aerodynamic forces on the tail. It can be computed as follows. The vector from some point O on the yaw axis to the aerodynamic center of the tail is given by

$$\vec{r}_{Oac} = -L_1\vec{b}_1 - L_2\vec{c}_2 - L_{ac}\cos\psi\vec{d}_2 + L_{ac}\sin\psi\vec{d}_3.$$

The virtual work due to the vertical component of the moment of the tail aerodynamic forces about O for a virtual displacement $\delta\theta$ arises from the moment

$$M^{\theta}_{tail} = (\vec{r}_{Oac} \times \vec{F}_{tail}).\vec{b}_3 = F_{drag}L^{\theta}_{drag} - F_{lift}L^{\theta}_{lift},$$

where the moment arms are functions of the geometry and are given by

$$\begin{aligned} L^{\theta}_{drag} &= L_1\cos\Delta\theta - L_2\cos\beta\sin\Delta\theta - L_{ac}\cos\beta\sin\Delta\theta\cos\psi \\ &\quad + L_{ac}\sin\psi[\cos\gamma\cos\Delta\theta - \sin\gamma\sin\beta\sin\Delta\theta], \end{aligned} \qquad \text{(Eq. 2-20)}$$

and

$$\begin{aligned} L^{\theta}_{lift} &= L_1\sin\Delta\theta + L_2\cos\beta\cos\Delta\theta + L_{ac}\cos\beta\cos\Delta\theta\cos\psi \\ &\quad + L_{ac}\sin\psi[\sin\gamma\sin\beta\cos\Delta\theta + \cos\gamma\sin\Delta\theta]. \end{aligned} \qquad \text{(Eq. 2-21)}$$

Now if we assume that $\sin\gamma\sin\beta \approx 0$, and $\cos\gamma = \cos\beta \approx 1$, then M^{θ}_{tail} becomes a function of $\Delta\theta - \psi$, which is the angle of attack on the tail:

$$L^{\theta}_{drag} = L_1 \cos\Delta\theta - L_2 \sin\Delta\theta - L_{ac} \sin(\Delta\theta - \psi), \qquad \text{(Eq. 2-22)}$$

and

$$L^{\theta}_{lift} = L_1 \sin\Delta\theta + L_2 \cos\Delta\theta + L_{ac} \cos(\Delta\theta - \psi). \qquad \text{(Eq. 2-21)}$$

Yaw Mechanism Dynamics

The equations of motion of the furling mechanism are

$$J_1(\psi)\ddot{\theta} + J_1'(\psi)\dot{\theta}\dot{\psi} + J'_{12}(\psi)\dot{\psi}^2 + J_{12}(\psi)\ddot{\psi} + b_1\dot{\theta} = Q_\theta, \qquad \text{(Eq. 2-24)}$$

and

$$J_2\ddot{\psi} + J'_{12}(\psi)\dot{\theta}\dot{\psi} + J_{12}(\psi)\ddot{\theta} + \frac{\partial V}{\partial \psi} + b_2\dot{\theta} = Q_\psi, \qquad \text{(Eq. 2-25)}$$

where the $'$ denotes differentiation with respect to the argument (here ψ), b_1 and b_2 are friction coefficients, and J_1 and J_2 .are moments of inertia which depend on the furling angle ψ, Q_θ and Q_ψ represent generalized forces (torques) arising from aerodynamic forces, and

$$\frac{\partial V}{\partial \psi} = M_T g L_3 \left(\sin\psi \sin\beta + \cos\psi \sin\gamma \cos\beta\right) \qquad \text{(Eq. 2-26)}$$

is the derivative of the potential energy due to the tail weight.

Generator Model

The mechanical torque supplied to the generator can then be expressed as

$$T_m = T_m\left(V, \omega, \cdots\right) = \frac{P}{\omega}, \qquad \text{(Eq. 2-27)}$$

where P is the mechanical power generated by the rotor and is computed by Yawdyn. The actual mechanical torque supplied to the generator is

$$T_a = T_m - T_f = \tau\left[\delta(t), \omega(t)\right], \qquad \text{(Eq. 2-28)}$$

where T_f is the torque resulting from friction and losses, and δ and ω are the angle and angular speed of the rotor, respectively. The model for an M-phase permanent-magnet synchronous generator is described by the following model in the continuous time domain [31]:

$$\frac{d\delta}{dt} = \omega(t)\,, \tag{Eq. 2-29}$$

$$J_R \frac{d\omega}{dt} = -i(t)'\,K[\delta(t)] + \tau\big[\delta(t), \omega(t)\big], \tag{Eq. 2-30}$$

and

$$L\frac{di}{dt} = -R_s i(t) + \omega(t)K[\delta(t)] - v(t)\,, \tag{Eq. 2-31}$$

where J_R is the moment of inertia of the rotor/generator assembly around the rotor axis, L is the inductance of a single phase, i is the M -vector of stator currents, v is the M -vector of stator voltages, and $'$ denotes matrix transposition.

Several nonlinearities are present, namely the back-electromagnetic force voltage vector $\omega(t)K[\delta(t)]$, the electrical torque $i(t)'K[\delta(t)]$, and the turbine supplied torque $\tau(\delta,\omega)$. The periodical airgap field function $K(\delta)$ satisfies

$$K[\delta] = K\left(\delta + \frac{2\pi}{N_p}\right), \tag{Eq. 2-32}$$

where N_p is the number of pole pairs. Although $K(\delta)$ can be nonsinusoidal, we are using sinusoidal field distribution for simplicity.

Note that the electrical load characteristics relate to the stator voltage and current vectors. For a battery-type load, the stator voltage can be modeled as "constant". Note however that if a power-electronics converter separates the generator from the actual electrical load, and if the converter is controllable, then $v(t)$ can be thought of as a control input. This control input affects not only the rpm of the rotor but also the furling dynamics.

More detailed Simulink models are also available [32] and can be incorporated.

Operating Conditions

The equations describing the furling mechanism can be readily linearized about an operating point to lead to a fourth-order linear system. The operating condition must satisfy the two relations

$$0 = M_{Yawdyn}(V_{wind}, \Delta\theta, \omega) + M^{\theta}_{tail}(V_{wind}, \Delta\theta, \psi) + M^{\theta}_{control}\,, \tag{Eq. 2-33}$$

and

$$\frac{\partial V}{\partial \psi}(\psi) = M^{\psi}_{tail}(V_{wind}, \Delta\theta - \psi) + M_{stop} + M^{\psi}_{control}, \qquad \text{(Eq. 2-34)}$$

in addition to the generator torque-speed characteristics. These are relations between the "unknowns" $\Delta\theta$, ψ, ω, and M_{stop}, $M^{\theta}_{control}$, and $M^{\psi}_{control}$. Clearly there are more equations than unknowns. Some of these are readily obtained under different scenarios; for example, before furling $\psi = 0$, and after furling $M_{stop} = 0$.

First we discuss the general procedure to determine the steady-state operating condition at *any furling angle* $0 < \psi < 70^{\circ}$ with $M_{stop} = 0$. To simplify the discussion, we consider the case where no active control is applied: $M^{\psi}_{control} = M^{\theta}_{control} = 0$. Then Equation 2-34 can be solved for the furling wind speed as a function of $\Delta\theta$ and ψ to obtain $V_{wind}(\Delta\theta, \psi_0)$. Substituting this relation into Equation 2-33, we obtain one equation relating $\Delta\theta$ to ω and ψ_0. Solving this equation will express ω as a function of $\Delta\theta$ to obtain $\omega(\Delta\theta, \psi_0)$. At some specified $\Delta\theta$, V_{wind} and ω, the Yawdyn code can be used to determine the rotor shaft torque and power. Hence the torque-speed characteristics of the turbine can then be obtained and intersected with the generator torque speed characteristics to yield the operating rpm ω at the specified furling angle ψ_0. Then the relation $\omega(\Delta\theta, \psi_0)$ can be solved for $\Delta\theta$, and $V_{wind}(\Delta\theta, \psi_0)$ is obtained.

When the procedure is repeated for every ψ_0 of interest, the operating condition at every tail or furling angle ψ_0 can be obtained. The whole procedure can then be repeated for different values of control moments $M^{\psi}_{control}$ and $M^{\theta}_{control}$ and the different relationships noted. More efficient and pointed solution procedures seeking to establish specific conclusions will be outlined in the following sections, but essentially they are very similar to the general procedure shown here.

Onset of Furling

As a first example, we sought to determine the operating conditions at the onset of furling. This is defined by $\psi = 0$ and $M_{stop} = 0$. In the absence of any active control, $M^{\psi}_{control} = M^{\theta}_{control} = 0$, Equation 2-34 can be solved for the furling wind speed as a function of $\Delta\theta$ and ψ. The solution is approximately

$$V_{furl}(\Delta\theta) = \sqrt{\frac{M_T g L_3 \sin\gamma \cos\beta}{\frac{1}{2}\rho A_{tail} L_{ac} \cos\beta (C_L \cos\Delta\theta + C_D \sin\Delta\theta)}},$$

as shown in Figure 2-20a.

Substituting this relation into Equation 2-33, we obtain one equation relating $\Delta\theta$ to ω. Solving this equation will express ω as a function of $\Delta\theta$. The solution $\omega(\Delta\theta)$ is shown in Figure 2-20b. With $V_{furl}(\Delta\theta)$ and $\omega(\Delta\theta)$ found, Yawdyn then finds $P(\Delta\theta) = P(V_{furl}(\Delta\theta), \omega(\Delta\theta), \Delta\theta)$ as well as the corresponding torque $T(\Delta\theta) = P(\Delta\theta)/\omega(\Delta\theta)$. These are shown in Figures 2-20c and 2-20d respectively. Eliminating the intermediate variable $\Delta\theta$, we can plot the torque-speed and the power-speed characteristics of the about-to-furl wind turbine as shown in Figures 2-20e and 20f respectively.

On Figure 2-20e we have also shown a typical torque-speed characteristic of the generator. The intersection of the two characteristics yields the desired operating point at the onset of furling. This point is marked by an arrow in each part of Figure 2-20.

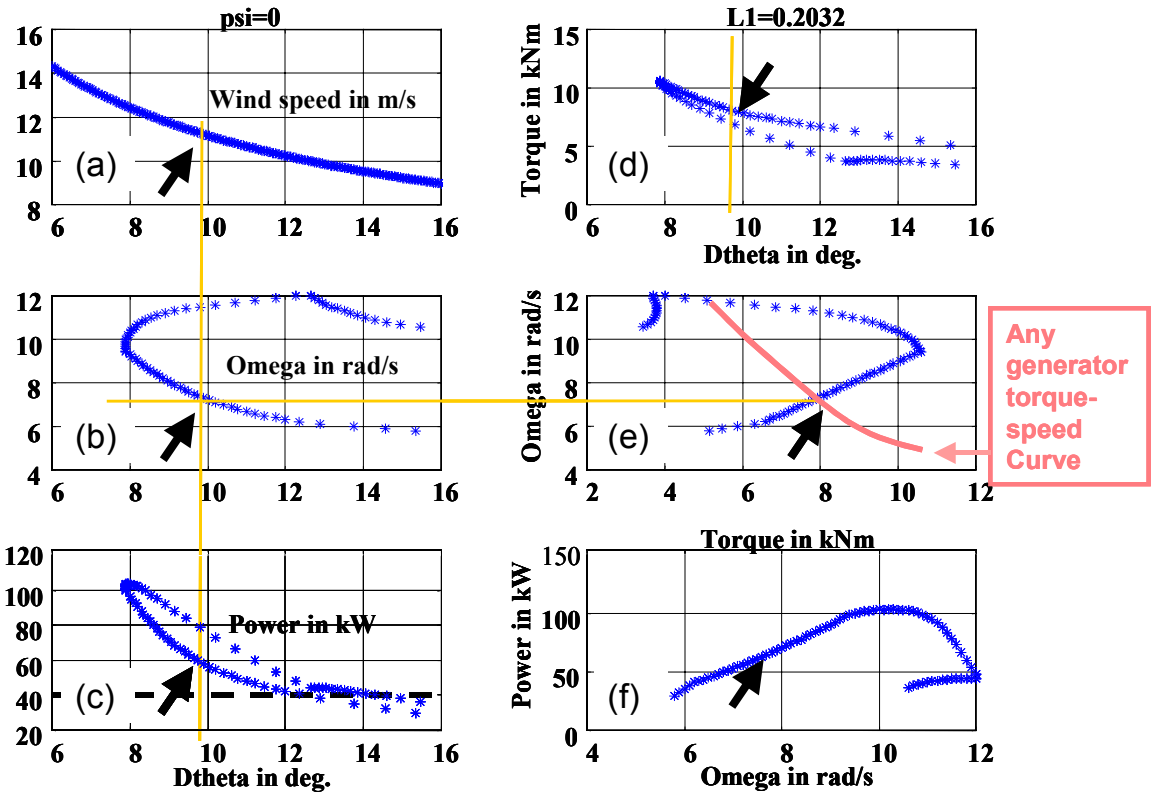

Figure 2-20. Onset of furling in the absence of active control

The torque-speed characteristics of the generator depends on its electrical loading. A very interesting case is when the generator is connected to the utility grid and is assumed to deliver constant rated power to the grid at the generator rated speed. Then the above procedure can be modified slightly to yield the furling condition as illustrated in Figure 2-21. Essentially, the turbine torque-speed characteristics and the dependence of delivered power on $\Delta\theta$ do not change. From Figure 2-21c, one can find $\Delta\theta$ that corresponds to the rated power. The corresponding furling wind speed can be found from Figure 2-21a to be about 12.7 m/s.

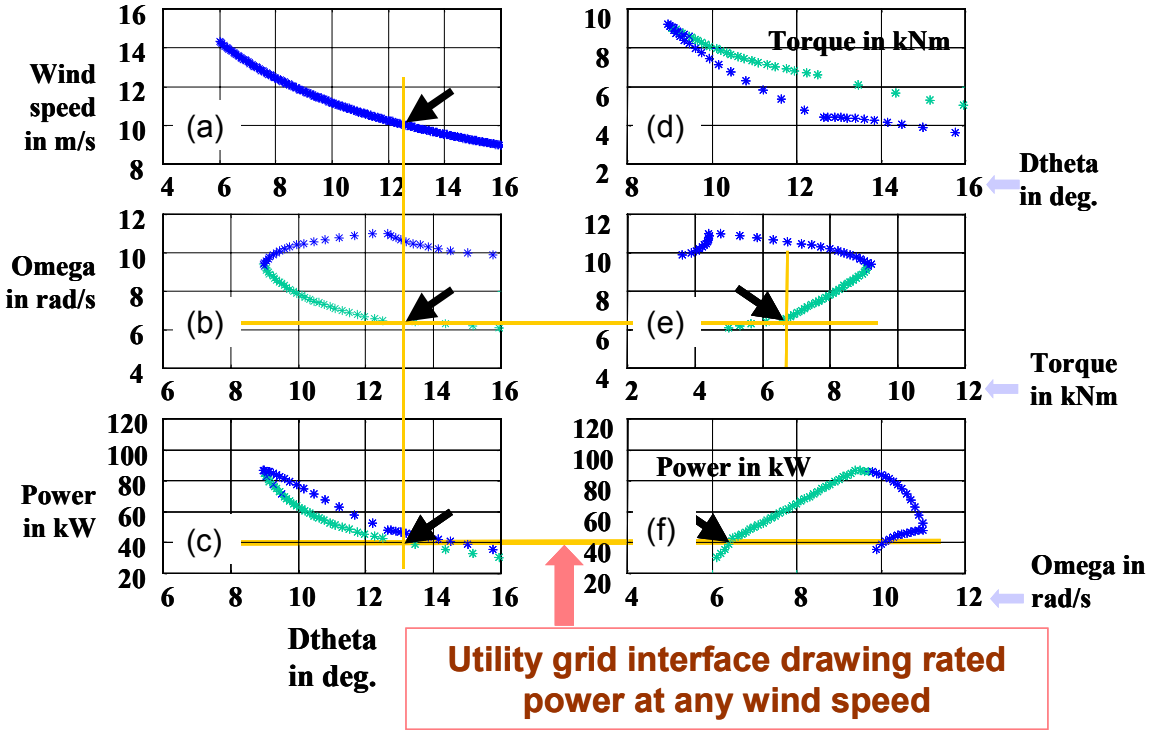

Figure 2-21. Finding the yaw control moment that allows rated power generation at partial furling at a sensed (given) wind speed

Feedforward Control

One limitation of the furling mechanism is that energy is lost because of the furling hysteresis, in which the wind speed must drop considerably below the rated wind speed before the rotor unfurls and resumes efficient operation. Although this hysteresis is an indication of conservative design, it is generally undesirable because it leads to power loss and to unnecessarily high structural stresses in the blade during the furling action. This is illustrated in Figure 2-22.

Maintaining Rated Power Generation

Next we assume a feedforward yaw control $M^{\theta}_{control}$ that will modify the yaw angle $\Delta\theta$ as to maintain the rated generated power after the onset of furling. Here the power delivered to the generator is 40kW (rated power) at the rated rpm. Using Yawdyn output, the relationship

$$P_{Yawdyn}(V_{wind}, \Delta\theta, \omega) = 40kW$$

becomes a relationship between $\Delta\theta$ and V_{wind}. Then Equation 2-34 yields a relationship between $\Delta\theta$ and ψ; for example, $\Delta\theta(\psi)$. If this relationship is substituted into Equation 2-33, a relationship between ψ and $M^{\theta}_{control}$ is obtained. Ultimately, all quantities can be indexed on V_{wind}. Hence for a given wind speed, the yaw control moment needed to maintain rated generated is determined. All corresponding quantities (angles) are also obtained as was illustrated in Figure 2-21.

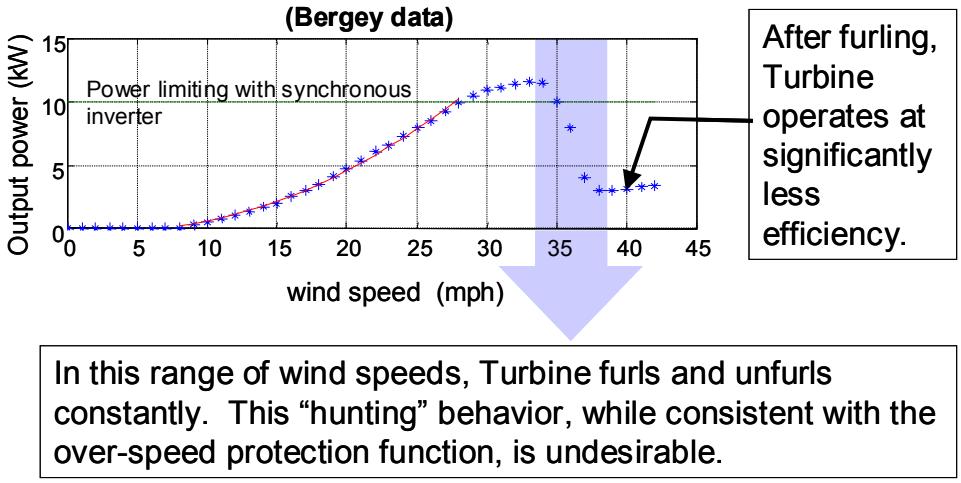

Figure 2-22: Typical behavior of Bergey-Type wind turbine

Collecting these results at all wind speeds of interest leads to the scheduled furling curves shown in Figure 2-23. Note that to maintain 40-kW generation as the wind speed increases, both the yaw and furling angles increase, but their difference, which is the angle between the tail and the wind, decreases. This is not unexpected. Curiously, however, the moments delivered by the tail aerodynamics decrease only slightly and are essentially constant. The slack is picked up by the control moment $M^{\theta}_{control}$, which increases rather linearly. This shows that keeping a tail is beneficial in reducing the required control authority as well as providing a fail-safe mechanism for dealing with actuator failure.

Allowing Some Overspeed

The control yaw moments can be reduced if some overspeed can be tolerated. The above procedure is repeated with

$$P_{Yawdyn}(V_{wind}, \Delta\theta, \omega) = \text{any desired } P_{Yawdyn}(V_{wind}),$$
$$\text{where} \qquad \omega = \text{any desired } \omega(V_{wind}).$$

The resulting scheduling control is shown in Figure 2-24 when a 10% overspeed is allowed at 19 m/s wind speed while maintaining constant rated generated power. This results in a 27%

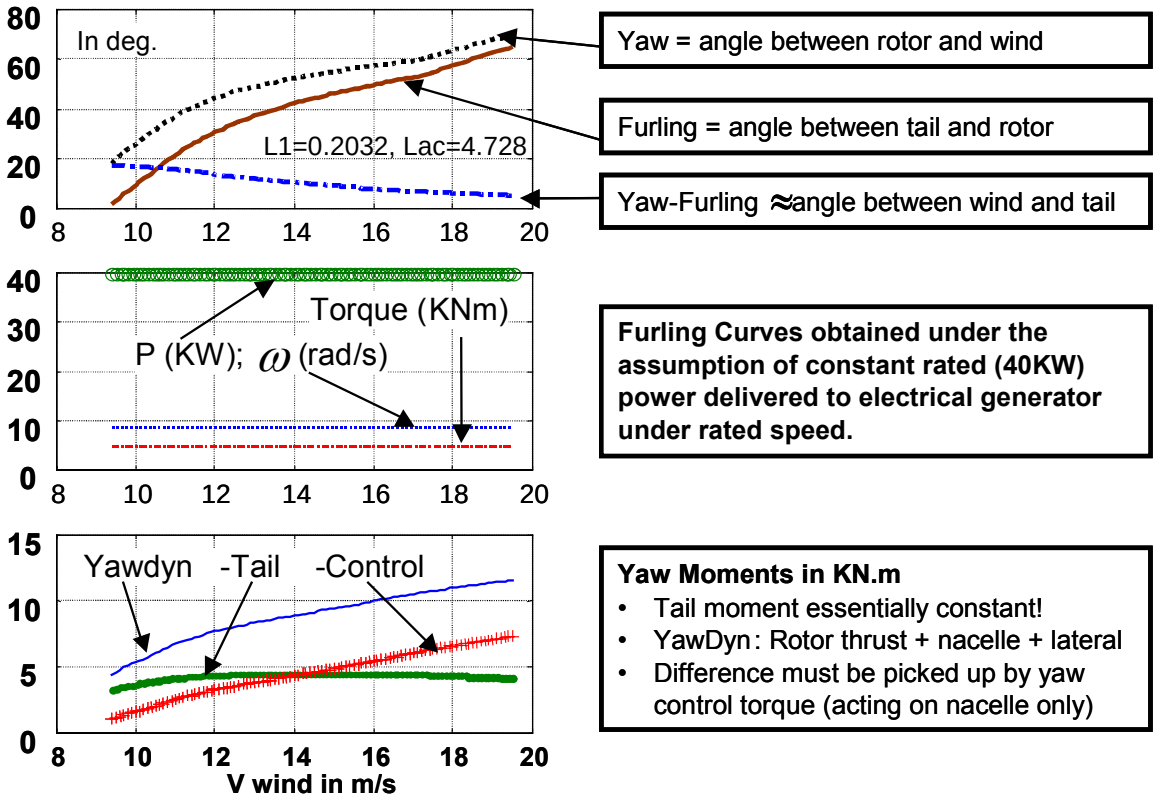

reduction of the required control authority.

Figure 2-23. Yaw feed-forward control that maintains rated power generation beyond furling

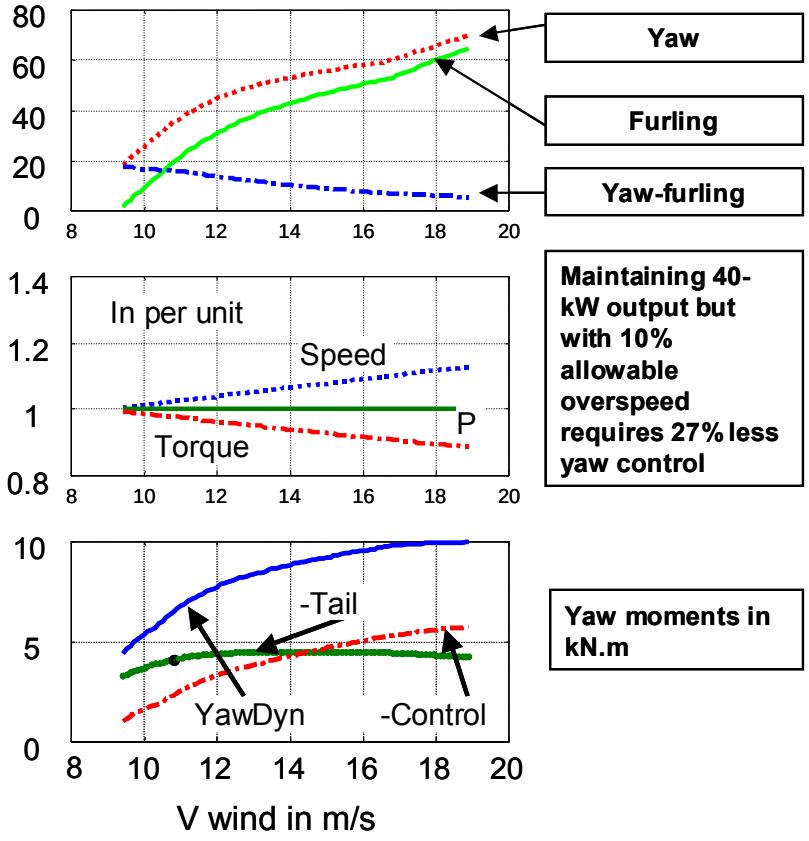

Figure 2-24. **Scheduling the yaw torque as to achieved a desired power generation profile. The curve denoted "-Tail" represents the negative of the torque provided by the tail. Similary for the cuve denoted "-Control".**

Scheduling for a Linear Motor Actuator

An actuator implementation of interest consists of a linear motor attached as shown in Figure 2-25. Note that $\overrightarrow{BD}\times\overrightarrow{DC}=(\overrightarrow{BP}+\overrightarrow{PD})\times\overrightarrow{DC}=\overrightarrow{BP}\times\overrightarrow{DC}$ and $\overrightarrow{AD}\times\overrightarrow{DC}=(\overrightarrow{AQ}+\overrightarrow{QD})\times\overrightarrow{DC}$ $=\overrightarrow{AQ}\times\overrightarrow{DC}$. Hence, the moment of a linear motor force F about point A is

$$\left|M^{\theta}_{control}\right| = F\left|\overrightarrow{AQ}\right| = F\frac{\left|\overrightarrow{AD}\times\overrightarrow{DC}\right|}{\left|\overrightarrow{DC}\right|}.$$

Hence the moment of the force F about point B is

$$\left|M^{\psi}_{control}\right| = F\left|\overrightarrow{BP}\right| = F\frac{\left|\overrightarrow{BD}\times\overrightarrow{DC}\right|}{\left|\overrightarrow{DC}\right|},$$

and hence

$$\frac{\left|M^{\theta}_{control}\right|}{\left|M^{\psi}_{control}\right|} = \frac{\left|\overrightarrow{AD}\times\overrightarrow{DC}\right|}{\left|\overrightarrow{BD}\times\overrightarrow{DC}\right|}$$

is a function of ψ only.

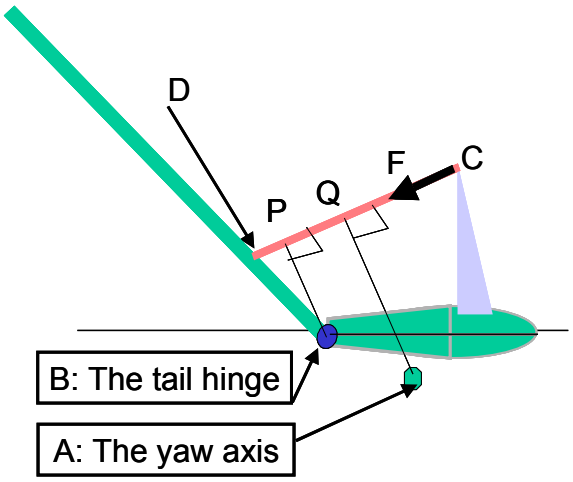

Figure 2-25: Linear Motor Proposed Configuration

Therefore this is a special case of a class of actuators where $M^{\psi}_{control} = \rho(\psi)M^{\theta}_{control}$. Then the equilibrium conditions in Equations 2-33 and 2-34 can be rewritten as

$$0 = M_{Yawdyn}(V_{wind}, \Delta\theta, \omega) + M^{\theta}_{tail}(V_{wind}, \Delta\theta, \psi) + M^{\theta}_{control},$$

and

$$\frac{\partial V}{\partial \psi}(\psi) = M^{\psi}_{tail}(V_{wind}, \Delta\theta - \psi) + M_{stop} + \rho(\psi)M^{\theta}_{control}.$$

The solution procedures follow as shown above.

Feedforward/Feedback Control

To stabilize and improve the performance of the above nonlinear feedforward control, we can append a simple linear feedback controller based on the desired operating condition. To do so, the system model must be first linearized. The main equations are

$$J_1(\psi^e)\delta\ddot{\theta} + J_{12}(\psi^e)\delta\ddot{\psi} + b_1\delta\dot{\theta} = \left.\frac{\partial Q_\theta}{\partial\theta}\right|_e \delta\theta + \left.\frac{\partial Q_\theta}{\partial\psi}\right|_e \delta\psi\,, \qquad \text{(Eq. 2-35)}$$

and

$$J_2\delta\ddot{\psi} + J_{12}(\psi)\delta\ddot{\theta} + \frac{\partial}{\partial\psi}\left(\frac{\partial V}{\partial\psi}\right) + b_2\delta\dot{\psi} = \left.\frac{\partial Q_\psi}{\partial\theta}\right|_e \delta\theta + \left.\frac{\partial Q_\psi}{\partial\psi}\right|_e \delta\psi\,, \qquad \text{(Eq. 2-36)}$$

where

$$\frac{\partial}{\partial\psi}\left(\frac{\partial V}{\partial\psi}\right) = M_T g L_3\left(\cos\psi\sin\beta - \sin\psi\sin\gamma\cos\beta\right). \qquad \text{(Eq. 2-37)}$$

There is of course the issue of computing the derivatives of the aerodynamic forces such as $\left.\frac{\partial Q_\theta}{\partial\theta}\right|_e$ and $\left.\frac{\partial Q_\theta}{\partial\psi}\right|_e$ evaluated at the desired equilibrium points. Generally, these aerodynamic forces are in general numerically computed, using Yawdyn for instance. The ISA introduced in [9] and discussed earlier has the advantage that the coefficients of the fuzzy approximators obtained through training are nothing but Taylor series coefficients of the approximated functions about every rule center. In [7], the ISA was applied to the desired aerodynamical quantities such as Q_θ, and the desired corresponding derivatives, such as $\left.\frac{\partial Q_\theta}{\partial\theta}\right|_e$, were shown to be easily obtainable from the coefficients of the resulting ISA.

Conclusions

Although the autofurling technology is old, it is generally not well understood, because of the many difficulties in modeling the aerodynamics, the furling mechanism itself, and the interactions in the overall systems. It is perhaps one of the least understood wind technologies. Despite the fact that furling turbines are a small part of the overall wind turbine market, resolving these difficulties in modeling and design is important because the tools developed to resolve these difficulties will be greatly helpful in all advanced turbine technology.

In this work, we developed a model of a small wind turbine including the equations of motions describing the furling mechanism, the permanent-magnet generator, and the aerodynamics. We then used the model developed to design feedforward control laws and developed a simulation package. The possibility of using the active yaw control to achieve partial furling, overspeed protection, and maximum power generation was illustrated. A fuzzy inference system was used

to approximate the Yawdyn program. A feedforward yaw control law was proposed to achieve a desired power generation and furling profile. A feedback control law can then be added to stabilize the scheduled behavior determined by the feedforward control.

Future Work

The following topics are suggested for future research.

- A more complete validation of the simulation software
- The use of advanced unsteady-aerodynamics CFD codes to reduce the uncertainty in the aerodynamics of furling, especially in the presence of complications such as blade flexibility blade pitch control
- A more complete model of the power electronics and electrical loads applied
- A stability analysis of the linearized models obtained at different wind speeds to identify possible bifurcations such as the Hopf bifurcation [33]. This bifurcation is known to be a good predictor of hunting behavior observed in furling.
- Advanced actuator design such as blade pitch and blade tip spoilers
- Bounded control designs given the limitations of actuation and measurement.

References of Part 2

1. Gipe, P., *Wind Energy Comes of Age,* New York, John Wiley & Sons, 1995.
2. Muljadi, E., "Soft–Stall Control Versus Furling Control for Small Wind Turbine Power Regulation," *Windpower'98,* Bakersfield, CA, April 27-May 1, 1998.
3. Yawdyn Software by C. Hansen and his Colleagues: http://www.nrel.gov/wind /software/Yawdyndesc.html.
4. Bikdash, M., Chen, Da., and Harb, M., "Modeling and Control of the Autofurling mechanism of Wind Turbines," *Journal of Vibrations and Control,* Vol. 7, 2001, pp.127–148.
5. Layton, R., *Principles of Analytical System Dynamics,* Berlin, Springer-Verlag, 1998.
6. Takagi, T., and Sugeno, M., "Fuzzy Identification of Systems and its Applications to Modeling and Control." *IEEE Transactions on Systems, Man, Cybernetics,* Vol. 25, No. 5, May 1995, pp. 841–851.
7. Harb, M. and Bikdash, M., "A Fuzzy Model of Wind Turbine Aerodynamics Learned From Yawdyn Data", *Artificial Neural Networks in Engineering (ANNIE) Conference,* Rolla, MO, November 7–10, 1999, pp. 1195–1200.

8. Harb, M., *Interpretable Fuzzy Inference Systems with Applications in Wind Turbines,* M. S. Thesis, North Carolina A &T State University, 1999.

9. Bikdash, M., "A Highly Interpretable Form of the Sugeno Approximation System," *IEEE Transactions on Fuzzy Systems,* Vol. 7, No. 6, December 1999, pp. 686–696.

10. Wang, C.-H., Wang, T. T., Lee, T., and Tseng, P.-S., "Fuzzy B-spline Membership Function (BMF) and its Applications in Fuzzy Neural Control," *IEEE Transactions on Systems, Man, and Cybernetics,* Vol. 25, No. 5, May 1995, pp. 841–851.

11. Mook, D. and Preidikman, S., "Numerical Simulations of the Wind–Generator Aerodynamics," *Private Communication* September 2000.

12. Bikdash, A., Chen, D., and Harb, M., "Dynamics of a Furling Wind Turbine," *The 1999 American Society of Mechanical Engineers (ASME) Mechanics and Materials Conference* Blacksburg, Virginia, June 27–30, 1999. Invited.

13. Chen, D., Bikdash, M., and Harb, M., "Modeling of the Autofurling Mechanism of Small Wind Turbines," paper 99–0051, *The 18th American Society of Mechanical Engineers (ASME) Wind Energy Symposium/37th AIAA Aerospace Sciences Meeting and Exhibit,* Reno, NV, January 11-14, 1999.

14. Layton, R., and Bikdash, M., "A Modal Analysis Comparison of Lagrangian Descriptor Models," *2000 American Control Conference,* Chicago, IL, June 28–30, 2000, pp. 2415–2419.

15. Bikdash, M., and Layton, R., "An Energy-Based Lyapunov Function for Physical Systems," *International Federation of Automatic Control (IFAC) Workshop on Lagrangian and Hamiltonian Methods for Nonlinear Control*, March 16–18, 2000, Princeton University, NJ, Editors: N.E. Leonard and R. Ortega, pp. 86-91.

16. Bikdash, M. and Layton, R., "Towards an Energy–Based Linear Analysis of Nonholonomic Systems", The *1999 International Mechanical Engineering Congress and Exhibition (IMECE),* Nashville, TN, November 14–19, 1999.

17. Bikdash, M., "Feedforward Control for Furling Wind Turbines Using Rotary and Linear Motors," *submitted for publication to Journal of Vibrations and Control.*

18. Bikdash, M., "Feedforward Control of Furling in a Small Wind Turbine" submitted to *the American Control Conference, ACC 2001.*

19. Bikdash, M., Kunchithapadam, V., Ragunathan, K., and Homaifar, A., "Comparison of Quasi Bang–Bang and Sliding Mode Controls for a DC Shunt Motor with Time Delay," *Nonlinear Dynamics,* Vol. 23, 2000, pp. 87–102.

20. Bikdash, M., "Boundedness Properties of the Soft-Constrained Time-Optimal Control," the *International Journal of Control* Vol. 72, No. 9, 1999, pp. 755–763.

21. Bernard, E., and Lloyd, D. R., *Dynamics of Flight Stability and Control,* 3rd Edition, New York, John Wiley & Sons.

22. Eggleston, D. M., and Stoddard, F. S., *Wind Turbine Engineering Design,* New York, Van Nostrand Reinhold Co., 1987.

23. Etkin, B. and Reid, L. D., *Dynamics of Flight Stability and Control*, 3rd Edition, New York, John Wiley & Sons, 1982.

24. Johnson, G. L., *Wind Energy Systems,* Englewood Cliffs, N.J.: Prentice Hall, 1985.

25. Hansen, A. C., *Yaw Dynamics of Horizontal Axis Wind Turbines,* Final Subcontract Report., *NICH Report No. TP-442-4822,* Golden, CO, National Renewable Energy Laboratory, 1992. 186 pp.

26. Hansen, A. C., and Laino, D. J., 1997, "Validation Study for Aerodyn and Yawdyn Using Phase III Combined Experiment Data," *Technical Paper AIAA–97–0943*.

27. Hansen, A. C., and Laino D. J., 1998, *Yawdyn and Aerodyn for ADAMS,* User's Guide to the Wind Turbine Dynamics Computer Programs.

28. Jang, J. Y. R., Sun, C.-T., and Mizutani, E., *Neuro-Fuzzy and Soft Computing,* Englewood Cliffs, NJ, Prentice Hall, 1997.

29. Wang. L.X., and Mendel. J. M., "Generating Fuzzy Rules by Learning from Examples," *IEEE Transactions on Systems, Man, and Cybernetics,* Vol. 22, No., 6, pp. 1414–1427, 1992.

30. Shimojima, K., Fukuda, T., and Arai, F., "Self-Tuning Fuzzy Inference Based on Spline Functions," *Proceedings of the Institute of Electrical and Electronics Engineering (IEEE) International Conference on Fuzzy Systems,* June 1994, pp. 690–695.

31. Shouse, K. R. and Taylor, D. G., "Sensorless Velocity Control of Permanent–Magnet Synchronous Motors," *IEEE Transactions on Control Systems Technology,* Vol. 6, No. 3, May 1998, pp. 313–324.

32. Ong, C.-M., *Dynamic Simulation of Electric Machinery Using Matlab/Simulink,* Upper Saddle River, NJ, Prentice Hall, 1998.

33. Nayfeh, A. H., and Mook, D., *Nonlinear Oscillations,* New York, NY, John Wiley and Sons, 1979.

Publications Supported Totally or In Part by NREL

Bikdash, M., Chen, Da., and Harb, M., "Modeling and Control of the Autofurling mechanism of Wind Turbines," *Journal of Vibrations and Control,* Vol. 7, 2001, pp.127–148.

Harb, M. and Bikdash, M., "A Fuzzy Model of Wind Turbine Aerodynamics Learned From Yawdyn Data", *Artificial Neural Networks in Engineering (ANNIE) Conference,* Rolla, MO, November 7–10, 1999, pp. 1195–1200.

Harb, M., *Interpretable Fuzzy Inference Systems with Applications in Wind Turbines,* M. S. Thesis, North Carolina A &T State University, 1999.

Bikdash, M., "A Highly Interpretable Form of the Sugeno Approximation System," *IEEE Transactions on Fuzzy Systems,* Vol. 7, No. 6, December 1999, pp. 686–696.

Bikdash, A., Chen, D., and Harb, M., "Dynamics of a Furling Wind Turbine," *The 1999 American Society of Mechanical Engineers (ASME) Mechanics and Materials Conference* Blacksburg, Virginia, June 27–30, 1999. Invited.

Chen, D., Bikdash, M., and Harb, M., "Modeling of the Autofurling Mechanism of Small Wind Turbines," paper 99–0051, *The 18th American Society of Mechanical Engineers (ASME) Wind Energy Symposium/37th AIAA Aerospace Sciences Meeting and Exhibit,* Reno, NV, January 11-14, 1999.

Layton, R., and Bikdash, M., "A Modal Analysis Comparison of Lagrangian Descriptor Models," *2000 American Control Conference,* Chicago, IL, June 28–30, 2000, pp. 2415–2419.

Bikdash, M., and Layton, R., "An Energy-Based Lyapunov Function for Physical Systems," *International Federation of Automatic Control (IFAC) Workshop on Lagrangian and Hamiltonian Methods for Nonlinear Control*, March 16–18, 2000, Princeton University, NJ, Editors: N.E. Leonard and R. Ortega, pp. 86-91.

Bikdash, M. and Layton, R., "Towards an Energy–Based Linear Analysis of Nonholonomic Systems", The *1999 International Mechanical Engineering Congress and Exhibition (IMECE),* Nashville, TN, November 14–19, 1999.

Bikdash, M., "Feedforward Control for Furling Wind Turbines Using Rotary and Linear Motors," *submitted for publication to Journal of Vibrations and Control.*

Bikdash, M., "Feedforward Control of Furling in a Small Wind Turbine" submitted to *the American Control Conference, ACC 2001.*

Bikdash, M., Kunchithapadam, V., Ragunathan, K., and Homaifar, A., "Comparison of Quasi Bang–Bang and Sliding Mode Controls for a DC Shunt Motor with Time Delay," *Nonlinear Dynamics,* Vol. 23, 2000, pp. 87–102.

Bikdash, M., "Boundedness Properties of the Soft-Constrained Time-Optimal Control," the *International Journal of Control* Vol. 72, No. 9, 1999, pp. 755–763.

Harb, M., Bikdash, M., and Homaifar, A., "Guaranteeing data contiguity for inverse–learning control in higher dimensions", *Artificial Neural Networks in Engineering (ANNIE) Conference,* Rolla, MO, November 7–10, 1999, pp. 19-24.

Part 3

Modeling and Health Monitoring of Horizontal Axis Wind Turbine Blades

Dr. Mark Schulz

Contents

List of Figures

List of Tables

Executive Summary

Advanced large wind turbines are being developed to meet U.S. Department of Energy (DOE) future goals for wind power production, and to reduce the cost of wind energy. These large turbines represent a significant capital investment and the turbine must operate for 10 to 30 years to be profitable. Failure of one rotor blade can cause catastrophic damage to a wind turbine and jeopardize the user's investment and confidence in wind energy. Health monitoring of the rotor blades is a solution that can warn of damage to the blade and protect the entire horizontal axis wind turbine from failure. In addition, a condition-based maintenance program can be adopted using the health monitoring information. This may minimize labor costs for inspection of turbines, prevent unnecessary replacement of components, uncover design weaknesses before failure, improve the availability of power, allow repair rather than replacement of blades by detecting damage early, and protect the investment in wind power by the utility company and the government. A health monitoring system may also permit the use of lighter blades that will allow the large turbines to react to wind changes more quickly, and thus capture more wind energy.

In this project, we developed and tested new analytical techniques for detecting initial damage to prevent failures of wind turbine rotor blades. The techniques consider the particular requirements for wind turbines related to cost, materials, size, and life expectancy to develop a practical system. Different sensor types were also modeled and tested, including accelerometers, piezoceramic patches, and a scanning laser doppler vibrometer. Modeling and simulation of wave propagation in a fiberglass plate was performed and different configurations of passive piezoceramic sensor systems were evaluated and shown to be capable of measuring propagating strain waves and identifying damage. We conducted a preliminary experiment to determine the damage detection capability of piezoceramic sensors and actuators during a static test of a wind turbine blade at the National Wind Technology Center (NWTC), a laboratory of the National Renewable Energy Laboratory (NREL) in Golden, Colorado. The stress wave propagation characteristics of the blade were monitored as the load level on the blade was increased until blade failure occurred. The results indicated that the technique can detect evolving damage in composite wind turbine blades. The effects of the blade stress and curvature on wave propagation need further modeling and testing, and ways to predict buckling failure of the blade need further study.

The analyses, simulation and testing performed in this project led to the concept of an "intelligent blade" that will continuously monitor its condition, warn of initiating damage, and provide instant information that can be used to regulate loading in the blade to prevent fatigue damage. This can decrease maintenance costs, improve reliability, and make wind energy more affordable. There are existing techniques that can detect damage on small thin plates. These approaches may not be practical for health monitoring of wind turbine blades that can be 30 m long with thick sections, spars, and where damage can occur on two surfaces. Moreover, there are two or three blades per turbine, and the blades operate in a rotating system. This places severe restrictions on the number of channels of data that can be practically recorded and transferred to the fixed tower. Therefore, we are modeling the human nervous system as a highly efficient sensor system for monitoring wind turbines. We are replicating the human neural system using continuous sensors made from piezoceramic ribbons, integrated circuits, and digital data transmission (patent pending). This structural neural system can be integrated throughout the blade to passively detect acoustic emissions and high dynamic strains as "pain" caused by high loading or damage. Initial modeling and simulations are described in this report and verify the sensitivity of the neural system. Development of the neural system and the intelligent blade is proposed for future work. TPI and Zond Corporations, along with the Wind Energy Technology Group at Sandia Laboratories are interested in the development of the intelligent blade. North Carolina A&T will design and build the sensor system, TPI could integrate the neural sensor into a blade, the NREL could test the blade, and Sandia could work with NCA&T to use the sensor data to predict the remaining fatigue life of the blade.

Introduction

Wind turbine blades are designed to have a lifetime ranging from 10 to 30 years. These blades accumulate on the order of 10^9 load cycles [1,2], and the fatigue life of the blade is an important design consideration. Wind turbine blades can become damaged by moisture absorption, fatigue, wind gusts, or lightning strikes. In wind farms, aerodynamic interaction between different turbines can cause unpredictable and excessive loads on the blades. These loads accelerate fatigue damage to the blade. In addition, normal aerodynamic loads and loads that result from changing gravity moments cause fatigue damage to the blades. The blades are made from fiberglass, which is a cost-effective material for this application. However, because of the low specific modulus of fiberglass, the blade natural frequencies are low and the deflections of the cantilevered blade can be large. If a fatigue-damaged rotor blade fails, it can cause catastrophic damage to the wind turbine and possibly damage nearby structures or injure people. Predicting the exact fatigue life of a blade is difficult, and it is difficult to tell the extent of fatigue damage that might have occurred to a blade. Thus, we are seeking a method to continuously monitor the condition of the blade and warn of damage or impending failure.

Wind turbine blades sometimes fail near the root section or the third of the blade near the root. Buckling of the blade's surface at the maximum chord section is one type of failure. The blades may operate for a large number of cycles with little reduction in strength and elastic properties, then the damage may propagate quickly to failure. Health monitoring of the rotor blades and timely identification of potential failure areas can help prevent damage or failure of the horizontal axis wind turbine. A health monitoring system that is reliable, low cost, and integrated within the blade may reduce wind turbine life-cycle costs and make wind energy more affordable. The health monitoring techniques investigated will monitor the condition of the blades during operation. Other methods used with the laser vibrometer can be employed when the turbine is stopped. The structural health monitoring (SHM) information gathered could be used in a condition-based maintenance program that could minimize the time needed for inspection of components, prevent unnecessary replacement of components, prevent failures, and allow utility companies to be confident of power availability. In addition, SHM may allow the use of lighter blades that would provide higher performance with less conservative margins of safety. A wind turbine with lighter blades can respond to wind changes quicker and capture more energy.

SHM techniques have been able to detect minor damage sites in structures [3-67]. It is anticipated that these methods can detect damage in operational wind turbine blades before the damage sites can combine and propagate to cause blade failure. The wave propagation methods may be the most sensitive in situ method. They make use of a set of piezoceramic patches to generate and propagate stress waves through critical regions of the structure. After propagation through the critical zones, the stress waves and their reflections are intercepted and measured using other piezoceramic patches. This approach propagates ultrasound in the plane of the material rather than through the thickness of the material. Damage detection using ultrasound through the thickness is a well-developed technique and requires mapping a sensor over the entire surface. However, this is very time consuming and not possible during operation of the turbine. The techniques in the literature using wave propagation in the plane consider uniform panels or shells with closely spaced sensor/actuator elements. However, a SHM system to monitor wind turbine blades must be designed considering thick structural sections, a complex built-up structure with curvatures, and the use of a minimum number of sensor/actuator elements.

Various existing techniques [68] including visual inspection, C-scan, acoustic emissions, and shearography can detect damage in composite blades. These techniques are labor intensive, inaccurate, difficult to use during operation, or accessibility of the blade is required for an extended time. In this work, we developed and tested vibration-based and wave propagation techniques to detect damage in

fiberglass wind turbine blades. Piezoceramic patches are used to excite the blade because they are in situ and convenient to use, the excitation is more repeatable than when conventional excitation methods are used, and very high-frequency excitation can be used. High-frequency excitation is more sensitive to damage than lower frequency excitation such as from wind loading. The piezoceramic lead zirconate titnate (PZT) patches can be used to detect damage during operation of the turbine. The scanning laser doppler vibrometer (SLDV) can be used to perform a detailed investigation of damage indicated by the PZT patches. The SLDV can measure the vibration of many spatial points over a wide frequency range quickly without contacting the blade. Light and electrical conductivity techniques were also tested on a bench-top experiment as simple approaches to detect damage. Finally, new highly distributed sensor concepts are being investigated to improve the level of sensitivity of damage detection and to develop an intelligent blade for in-operation damage detection. One of NREL's concerns in the development of an intelligent blade is the cost of the materials. Because the PZT material is used for sensing or actuating high-frequency low-amplitude signals, the amount of material used is small. The cost of the material and signal processing hardware would be justified by the increased reliability of the turbine. The intelligent blade could also provide blade response information to control the turbine performance and to increase the efficiency of the turbine.

The blade health monitoring system could monitor each blade on all turbines in a wind farm during operation, as shown in Figure 3-1. If damage is indicated, the particular turbine and blade could be identified and this information communicated to an operator through an advanced diagnostic monitoring system. A damaged blade could be pitched to reduce loads, or the turbine could be stopped for blade inspection and repair.

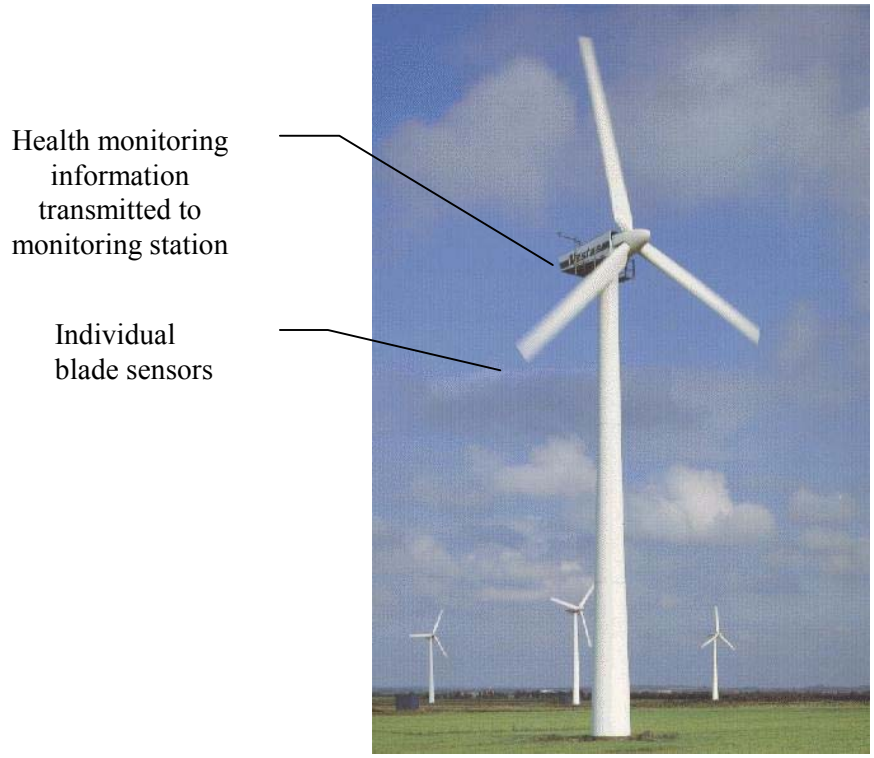

Figure 3-1. SHM of wind turbines on a wind farm

Damage Detection Theories

Different techniques were developed at North Carolina A&T State University (NCA&T) to detect damage in wind turbine blades and other flexible structures. These methods can be classified into two general categories: vibration methods, and wave propagation methods. The vibration-based methods attempt to detect, locate, and quantify damage based on theories that describe the vibration response of structures. The vibration response can be thought of as the response when all parts of the structure are moving simultaneously. Steady-state vibration is also considered as a standing-wave motion. The wave propagation methods attempt to detect damage by measuring the propagation and reflection of waves. The wave response can be thought of as the localized response of a structure when particle motion occurs only when the wave reaches that section of the structure. The algorithms we developed do not use structural models, such as a finite element model, because models are not accurate enough to detect small damage. Damage detection methods can be further categorized by the type of interrogation that is used: either active or passive interrogation. The active damage detection methods are based on exciting the structure with PZT patch actuators and measuring the vibration response using PZT patch sensors or a scanning laser doppler vibrometer (SLDV). A passive method measures acoustic emissions (AE) or high strains that occur during the normal operation of the wind turbine.

The various methods are briefly discussed below. For the vibration-based methods, the damage detection analyses that were performed can be found in the references. An algorithm to cancel environmental effects on measured data, such as from temperature changes, along with a clipping algorithm to remove low-coherence data were developed to improve the repeatability of vibration measurements; these are also described in the references. We discuss the modeling and simulation of wave propagation in plates in a little more detail here because the wave propagation methods are considered the most feasible for detecting small damage. The vibration-based methods are considered suitable for detecting larger damages in a structure.

The Transmittance Function (TF) Method

The first method considered is transmittance function monitoring [6,17,19,22]. Here the technique is specialized for use with a laser vibrometer that measures structural velocities. The equations of motion for a linear structure with periodic excitation are

$$M\ddot{x} + C\dot{x} + Kx = \mathrm{Re}(fe^{j\omega_{dr}t}) \qquad \text{(Eq. 3-1)}$$

where M, C, and K are the structural mass, damping, and stiffness matrices, and f is the excitation force. To solve Equation 3-1, let

$$x(t) = \mathrm{Re}[X(j\omega_{dr})e^{j\omega_{dr}t}] \qquad \text{(Eq. 3-2)}$$

and substitute Equation 3-2 into Equation 3-1. This gives

$$\mathrm{Re}[AX(j\omega_{dr})e^{j\omega_{dr}t}] = \mathrm{Re}[fe^{j\omega_{dr}t}], \qquad \text{(Eq. 3-2)}$$

where $A = (K - \omega_{dr}^2 M + j\omega_{dr} C)$ is the system matrix, and Re(a+b)=Re(a)+Re(b) has been used, where a and b are some complex constants. Thus, from Equation 3-3

$$X(j\omega_{dr}) = Hf \qquad \text{(Eq. 3-4)}$$

where $H = A^{-1}$ is the receptance frequency response function (FRF) matrix of the system. The quantity $X(j\omega_{dr})$ in Equation 3-4 is the frequency domain representation of the system displacement response. The system velocity is

$$v(t) = \mathrm{Re}[V(j\omega_{dr})e^{j\omega_{dr}t}], \qquad \text{(Eq. 3-5)}$$

where the frequency domain velocity response of the system is $V(j\omega_{dr}) = j\omega_{dr}X(j\omega_{dr})$. Thus

Equation 3-4 can be written for velocities as

$$V(j\omega_{dr}) = j\omega_{dr} Hf \,. \qquad \text{(Eq. 3-6)}$$

The velocity function given by Equation 3-6 is used in this testing because the laser vibrometer measures velocity directly, and the velocity FRF is flatter than the displacement or acceleration FRFs. From Equation 3-6, the velocity frequency response at degree of freedom (DOF) or measurement point *r* is

$$v_r = j\omega_{dr} \sum_{k=1}^{N} H_{rk} f_k \,, \qquad \text{(Eq. 3-7)}$$

where f_k is the *kth* element of *f* and H_{rk} is the *rkth* element of *H.* The transmittance functions (TF) are formed as the ratios of the velocity responses at different points on the structure, as

$$T_{rs} = \frac{v_r / f_0}{v_s / f_0} = \frac{\sum_k H_{rk}}{\sum_k H_{sk}}, \qquad \text{(Eq. 3-8)}$$

where $k = (l_1, l_2, l_3, ...)$ define the dofs where the forces are applied. The quantities $h_{r0} = v_r / f_0$ and $h_{s0} = v_s / f_0$ are the mobility FRFs computed by the SLDV for forces of magnitude f_0 acting simultaneously at dofs defined by the *k* vector. Thus, the TF is computed using the laser data as

$$T_{rs} = \frac{h_{r0}}{h_{s0}} \,. \qquad \text{(Eq. 3-9)}$$

A variance damage indicator between dofs *r* and *s* is

$$d_{rs} = 1 - \frac{\upsilon_{rs}^h}{\upsilon_{rs}^d}, \qquad \text{(Eq. 3-10a)}$$

where

$$\upsilon_{rs}^h = \frac{1}{(f_2 - f_1)} \int_{f1}^{f2} (T_{rs}^h - \mu_{rs}^h)^2 \, df \,, \qquad \text{(Eq. 3-10b)}$$

and

$$\mu_{rs}^h = \frac{1}{(f_2 - f_1)} \int_{f1}^{f2} T_{rs}^h \, df \qquad \text{(Eq. 3-10c)}$$

for the healthy structure. The subscript *h* is replaced with *d* for the damaged structure. Only υ_{rs}^h is stored as historical data. The DOF corresponding to the peak damage indicator locates the damage, and the indicator is more accurate with symmetric or closely spaced points. An advantage of using TF is that the excitation force is cancelled and does not need to be measured if it is equal in amplitude at all points where applied. In addition, the ratio of responses partially cancels changes in the TF that result from environmental effects such as temperature changes. Because TFs are ratios of two continuous functions with peaks and valleys, they are quite sensitive to shifts in frequencies or damping caused by damage.

The Operational Deflection Shape (ODS) Method

Operational deflection shapes are computed by the SLDV system [55,62,64] for the healthy and damaged structures. Changes in the shapes are used to indicate and locate damage. The following describes how the SLDV uses a complex representation of harmonic vibration to determine the ODS. Putting Equation 3-4 into Equation 3-2 gives

$$x(t) = \mathrm{Re}[Hfe^{j\omega_{dr}t}] \,. \qquad \text{(Eq. 3-11)}$$

The ODS is defined by evaluating Equation 3-11 at different angles or times during a steady-state sinusoidal response. The angles are

$$\theta_m = \omega_{dr} t_m , \qquad \text{(Eq. 3-12)}$$

where ω_{dr} is one specific driving or excitation frequency. The ODS can be evaluated at specified angles, such as $\theta_m = \frac{2\pi m}{p}$, where p is the number of points in one cycle of vibration, and m=0,1,2,…*p-1*. Therefore the times to evaluate the ODS are given by

$$t_m(\omega_{dr}) = \frac{\theta_m}{\omega_{dr}} = \frac{m2\pi}{p\omega_{dr}} . \qquad \text{(Eq. 3-13)}$$

The ODS are then given by:

$$x\left(\frac{\theta_m}{\omega_{dr}}\right) = \mathrm{Re}[X(j\omega_{dr})e^{j\theta_m}] \qquad \text{(Eq. 3-14)}$$

or for velocities,

$$v\left(\frac{\theta_m}{\omega_{dr}}\right) = \mathrm{Re}[j\omega_{dr} X(j\omega_{dr})e^{j\theta_m}] . \qquad \text{(Eq. 3-15)}$$

The SLDV uses a periodic chirp excitation and the vibration response is measured for an integral number of periods of the excitation. A Fourier transform is performed and the complex vibration response at the particular measurement point is stored. Multiple samples can be averaged. This is repeated for all scan points and the real amplitudes are plotted at selected phase angles. This is called the ODS and it approximately coincides with the more familiar mode shape if the mode shapes of the structure are well spaced, damping is small, and the excitation is at a natural frequency of vibration of the structure. The ODS may be more accurate at detecting damage because the exact response of the structure is used, subject only to errors in performing the Fourier transform. Mode shapes, however, involve additional assumptions and procedures to compute. This may remove some of the effects of damage to a structure.

The Resonant Comparison Method

The resonant comparison technique [3,10] can be used with a small number of PZT patches as sensors to detect damage in critical areas of the structure. Localized symmetry properties of the structure are exploited in this approach to minimize the need for pre-damage data and to compensate for changes in the structure not related to damage. Damage is determined using the differences in the response at the resonances of the healthy/damaged structure defined as

$$d_{ij} = \Delta_{ij}^d - \Delta_{ij}^h , \qquad \text{(Eq. 3-16)}$$

where $\Delta_{ij}^d = \max\left|(\varepsilon_i^d - \varepsilon_j^d)/f\right|$, $\Delta_{ij}^h = \max\left|(\varepsilon_i^h - \varepsilon_j^h)/f\right|$ ε is the strain measured at point i or j, the superscripts on Δ_{ij} denote damaged (d) or healthy (h), and f is excitation force amplitude. For symmetric structures, $\Delta_{ij}^h \approx 0$.

The Impulse Response Method

The impulse response technique [3] can be used with a small number of PZT patches, which function as sensors to detect damage in critical areas of the structure. Damage is determined using the differences in the time impulse response of the healthy minus the damaged structure defined as

$$d_{ij} = \frac{1}{Tf}\int_0^T \left|\varepsilon_{ij}^d - \varepsilon_{ij}^h\right| dt , \qquad \text{(Eq. 3-17)}$$

where ε is the strain measured at point i or resulting from an impulse at point j, the superscripts denote damaged (d) or healthy (h), T is the time of integration, and f is the excitation force amplitude.

The Frequency Response Reference Function (FRRF) Method

A damage vector algorithm that does not require measurement of the excitation force has been simulated [5]. The algorithm uses FRRF and sparse measurements to locate damage with a spatial resolution equal to the distance between the closest sensors. Damage-force spectral densities and mean-square damage forces are computed to give an estimate of the damage magnitude. The equations for the method are given as

$$r = (d + f^d) = A^h x^d \qquad \text{(Eq. 3-18)}$$

and

$$R_{ij} = \sum_{p=1}^{n} \sum_{q=1}^{n} A_{ip}^h G_{pq}^d A_{qj}^{h*} \qquad \text{(Eq. 3-19)}$$

and

$$D = \frac{1}{\Delta f} \int_{f_1}^{f_2} R \circ R^* df, (i = j) \qquad \text{(Eq. 3-20)}$$

In Equations 3-18 through 3-20, r is the combined force vector, f is the external force vector, d is the damage vector, A is the system matrix, G is the cross-spectral density matrix, and D is the damage indicator. A simulation was performed that detected damage in cantilever beams, but translational and rotational measurements are required at each sensor location. Approaches to measure rotations are being studied.

The Damage Vector Method

The damage vector method [20] is similar to the FRRF method, except the excitation force must be measured. The equations describing the method are

$$\begin{bmatrix} x_1 \\ x_2 \end{bmatrix} = \begin{bmatrix} H_{11} & H_{12} \\ H_{21} & H_{22} \end{bmatrix} \begin{bmatrix} f_1 \\ f_2 \end{bmatrix} \qquad \text{(Eq. 3-21)}$$

and

$$x_1 = H_{11} f_1, \; d_1 = A^h x_{11}^d - f_{11}^d \qquad \text{(Eq. 3-22, a and b)}$$

and

$$D = \frac{Lim}{T_o \to \infty} \frac{2}{T_o} \mathrm{E}(d_1 d_1^*) \qquad \text{(Eq. 3-23)}$$

and

$$d_{rms} = \left(\int_0^{\infty} diag(D) df \right)^{0.5}. \qquad \text{(Eq. 3-24)}$$

In Equations 3-21 through 3-24, x is the displacement vector, H is the FRF matrix corresponding to the number of sensors on the structure, and d is the damage vector. The damage vector can be used with sparse measurements and minimizes the problem of spatial aliasing present in most damage detection methods. The damage vector method has worked well in simulation and is being tested in the laboratory. A damage vector algorithm based on axial vibration has also been simulated. The algorithm uses axial displacements and sparse measurements to locate damage with a spatial resolution equal to the distance between the sensors. A damage force vector and frequency response functions from the healthy structure were used in the damage algorithm. Damage force spectral densities and root-mean-square (RMS) damage forces are computed to give an estimate of the damage magnitude. An algorithm has been developed to correct FRFs for changes in the environment. A damage detection simulation was

performed using a bar model, the results are not published yet. The RMS damage forces are plotted using only three sensors on the bar. The damage is always located between the two closest sensors. A comparison shows that the approximate and exact RMS damage forces are very close.

The Wave Propagation Method

The wave propagation method [52,53,69-79] is discussed considering the use of active fiber composite (AFC) materials for sensing and/or actuation. AFC materials have recently become commercially available [69,70] and consist of PZT fibers embedded in a polymeric matrix with symmetric interdigitated electrodes on the top and bottom surfaces of the matrix. A capton sheet over the electrodes protects and electrically insulates the material. This material has several advantages for use in sensing and actuation. The AFC material has a high strain capability and high energy density, it is more rugged than monolithic piezoceramics, it is conformable, and it can be bonded to the surface or embedded within complex composite structures [80-84]. If a fiber breaks, the matrix tends to arrest the crack and the electroding allows the rest of the fiber to actuate. Drawbacks of the material are the high cost of manufacturing and the high voltage needed for actuation.

In the literature, the current applications being investigated for use of AFC materials include control of blade vibration of rotorcraft, suppression of vibration and noise on torpedos, and improving the dynamics of tennis rackets [69]. Relatively less work has been done on the use of AFCs for sensing purposes. In the NREL project, we developed initial designs of continuous AFC sensors for the applications of operational structural integrity monitoring, readiness assessment, and survivability. A continuous sensor is defined here as one with multiple segments that are spatially distributed and electrically interconnected, with one electrical output signal measurable by one channel of data acquisition. The advantage of a continuous sensor is that damage events such as impacts, cracks, and delaminations, which produce dynamic strains and AE, can be detected at different spatial locations on the structure using only one channel of data acquisition. This simplifies the connections and hardware required and reduces the cost and size of the sensor system. On the downside, interpreting the output from the continuous sensor to locate the source of an AE is more difficult than when multiple individual sensors are used. We will discuss modeling of AFC sensors on a plate, simulation of strain wave propagation and vibration, and predicting the response of the AFC sensor to acoustic waves. Approaches for locating a damage event are being developed. One method uses the measured response of a continuous sensor and the patterns of the time waveforms at the different sensor nodes to approximately locate the source of the damage signal. Another method uses the spacing and geometry of the sensor nodes to determine the direction of travel and source location of the damage. We performed testing that simulated damage using a pencil lead break or PZT patches to generate a pulse to determine the advantages and limitations of continuous sensors.

Modeling and Simulation

This section discusses the modeling of AFC sensors and the simulation of the sensor response caused by acoustic waves propagating in a plate. We are using the simulation model to optimize the design of the sensor system including the size, number, connectivity, and locations of the sensor nodes.

Sensor Modeling

An AFC patch is shown in Figure 3-2. The modeling performed to study this material couples the elastic equations of a plate structure to the piezoelectric constitutive equations.

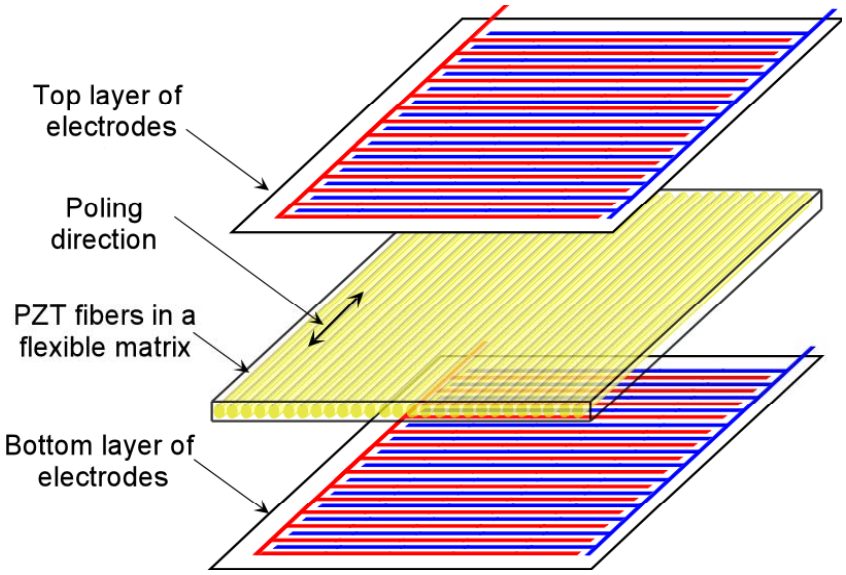

Figure 3-2. Construction of an AFC patch

The piezoelectric matrix equations to model an AFC sensor/actuator are:

$$\begin{bmatrix} D \\ T \end{bmatrix} = \begin{bmatrix} \varepsilon^S & e \\ -(e)^t & c^E \end{bmatrix} \begin{bmatrix} E \\ S \end{bmatrix}, \qquad \text{(Eq. 3-25)}$$

where D is the electric displacement (charge/unit area) in coulombs/m^2, T is the stress in N/m^2, $E = V / h$ is the electric field in volts/m where V is the voltage at the AFC, h is the electrode spacing of the AFC, S is the strain, $\varepsilon^S = \varepsilon_r^T \varepsilon_0 - dc^E d$ is the clamped dielectric in Farads/m, ε_r^T is the AFC dielectric constant relative to air, ε_0 is the dielectric constant of air (N/V^2), d is the AFC-induced strain constant (m/V), e is the induced stress constant in Coluomb/m^2 or equivalently N/(m*volt), $(\,)^t$ is transpose, and c^E is the constant field stiffness in N/m^2. Considering a unidirectional PZT fiber material and using a one-dimensional approximation, the first Equation in 3-25 becomes

$$D_j = \varepsilon^S E_j(t) + e \frac{\partial w(x_j, t)}{\partial x} \text{sgn}(j), \qquad \text{(Eq. 3-26)}$$

where j represents the *jth* segment or electroded section of the sensor, t is time, $w(x_j, t)$ is the displacement at segment j, $S_j = \dfrac{\partial w(x_j, t)}{\partial x}$ is the strain, and the *sgn* function is to allow connection of the segments of the sensor in positive or negative polarities. The current generated by the *jth* segment of the AFC is

$$i_j = \dot{D}_j A_e = C_p \dot{V} + e \frac{\partial^2 w(x_j, t)}{\partial x \partial t} A_e \text{ sgn}(j) \qquad \text{(Eq. 3-27)}$$

where $\varepsilon^S = C_p h_e / A_e$ has been used, A_e is the area of the electrodes (m^2) on the AFC, and C_p is the capacitance of one segment (which is assumed to be the same for all segments). An electric circuit representation of an AFC sensor [52,53] that corresponds to Equation 3-25 is shown in Figure 3-3. The stress in the AFC from Equation 3-25 is

$$T = -eE + c^E S. \qquad \text{(Eq. 3-28)}$$

The stress T comprises the stress resulting from the voltage acting on each segment of the sensor, and a uniform stress caused by the elasticity and strain of the AFC. Here, the stress multiplied by the cross-sectional area of the AFC patch is the force that is applied to the structure. If the patch is on the surface of the panel, a moment is applied to the structure, as well as an in-plane force at the edges of the patch. This approximate model is named the pin-force model and is used to allow a simple closed-form solution of the plate equation.

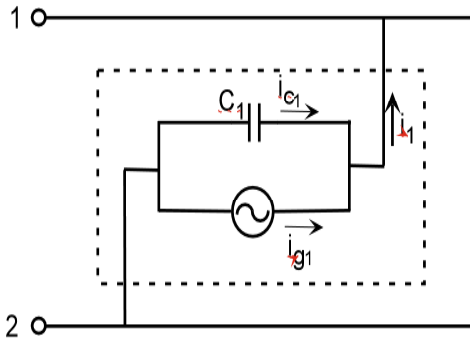

Figure 3-3. Electric circuit model of the AFC patch

In designing the AFC for use in a sensor system, three important parameters must be considered: the poling direction of the nodes (same or alternating); the connectivity of the nodes (series, parallel, or a combination); and minimizing the resistance of the circuit. An optimal combination is discussed in [85]. An elastic model of a plate is used to simulate the response of the plate and AFC sensor to an impulse load. The segments $s1, s1, \ldots sn$ model the interdigitated electrodes over certain lengths of the AFC. The finger electrodes allow poling of the AFC in the plane of the fiber to give a larger voltage/strain coefficient. Because the AFC is poled using the interdigital electrodes, each segment acts as a separate sensor, with all sensors connected together. The segments can be spaced appropriately and connected with alternating polarities to filter a desired frequency of structural vibration. The length of the segments can be matched to the half wavelength of the modes to be measured. This approach, for example, can use the continuous nature of the sensor as a spatial filter to cut off the low frequency response that masks the AE response from cracks in metals or fiber breakage in composite materials. If small segments are used, the continuous sensor is actually designed as an acoustic filter to measure Lamb waves or other waves produced by crack propagation.

The simply supported plate is modeled to study the benefits of an AFC sensor for measuring strain and acoustic emissions. The equation of motion for the plate under an impulse load is

$$D\nabla^4 w(x,y,t) = -\rho h \ddot{w} + \frac{F(x,y,t)}{ab}, \qquad \text{(Eq. 3-29)}$$

where the impulse $\mathrm{F} = \pm f_o \delta(t)\delta(x - x_c)\delta(y - y_c)$ locates the crack or excitation, w = deflection, ρ = mass density, $\nabla^4 = (\frac{\partial^2}{\partial x^2} + \frac{\partial^2}{\partial y^2})^2$, and the plate flexural rigidity is *D*. The impulse excitation produces wave patterns that are easy to understand. Other excitations such as moment step functions can also be used to model cracks. The boundary conditions are

$$w = 0, \frac{\partial^2 w}{\partial x^2} = 0, x = 0, x = a \quad \text{and} \quad w = 0, \frac{\partial^2 w}{\partial y^2} = 0, y = 0, x = b. \qquad \text{(Eq. 3-30, a and b)}$$

The total solution for the plate displacement is

$$w(x,y,t)=\sum_n\sum_m \frac{\overline{F}_{mn}}{\omega_{d_{mn}}} e^{-\zeta_{mn}\omega_{mn}t}\sin(\omega_{d_{mn}}t)\sin(\frac{m\pi x}{a})\sin(\frac{n\pi y}{b}). \quad \text{(Eq. 3-31)}$$

The corresponding strains are

$$s_x(x,y,t)=-z\frac{\partial^2 w}{\partial x^2}=z\sum_n\sum_m a_{mn}(t)\sin\frac{m\pi x}{a}\sin\frac{n\pi y}{b}(\frac{m\pi}{a})^2 \quad \text{(Eq. 3-32)}$$

and

$$s_y(x,y,t)=z\sum_n\sum_m a_{mn}(t)\sin\frac{m\pi x}{a}\sin\frac{n\pi y}{b}(\frac{n\pi}{b})^2 \quad \text{(Eq. 3-33)}$$

and

$$\gamma_{xy}(x,y,t)=-2z\frac{\partial^2 w}{\partial x\partial y}=-2z\sum_n\sum_m a_{mn}(t)\sin\frac{m\pi x}{a}\sin\frac{n\pi y}{b}(\frac{m\pi}{a})(\frac{n\pi}{b}). \quad \text{(Eq. 3-34)}$$

The average strains over the area of the sensor are used to compute the voltage output from the sensor. The voltage output is computed from Equation 3-25 and the thickness and the capacitance of the sensor. For a simple approximation to model a unidirectional AFC on a plate, the open circuit voltage V_0 can be approximated assuming the current flow is zero and using the average strain over the sensor nodes as

$$V_0=-\left(eh_e/\varepsilon^s\right)\overline{s}+V_{IC}=-\left(eA_e/C_p\right)\overline{s}+V_{IC}, \quad \text{(Eq. 3-35)}$$

where V_{IC} is the initial voltage across the sensor. The open circuit voltage calculation Equation 3-35 neglects the internal resistance of the piezoceramic material, which will discharge the capacitor slowly and prevent measurement of signals that are at very low frequency (less than about 0.5 Hz). The average strain in the *x* direction is computed for the nodes as

$$\overline{s}_x(t)=\frac{h}{2}\frac{1}{\Delta x\Delta y}\int_{y_1}^{y_2}\int_{x_1}^{x_2}\sum_n\sum_m(\frac{m\pi}{a})^2 a_{mn}(t)\sin\frac{m\pi x}{a}\sin\frac{n\pi y}{b}dxdy, \quad \text{(Eq. 3-36)}$$

where $\Delta x=x_2-x_1$ and $\Delta y=y_2-y_1$. The strain in the y-direction is computed similarly. In the simulation, the elastic solution is computed at small time steps, and equation 3-35 is used to compute the voltage. The solution approach presented requires that the rate of change of the excitation is less than the speed of propagation of waves in the material [73,75,84]. Using this solution, continuous sensors can be practically designed to sense AE signatures and wave propagation.

Wave Propagation Simulation

The simulation is performed for a quasi-isotropic composite fiberglass plate with an integrated AFC tape sensor Figure 3-4. The AFC sensor strip is called a dendrite in analogy with the human nervous system. An impulse load is applied at the center, at one corner, and at the side of the plate, and different configurations of the AFC sensor can be examined to measure strains and AE. The composite plate is 1 m * 1 m * 8 mm in size. The elastic modulus E for the plate is 22.063GPa, the weight density of the fiberglass plate ρ_w is 16015 N/m^3, and the damping ratio ζ for all vibration modes is 0.05.

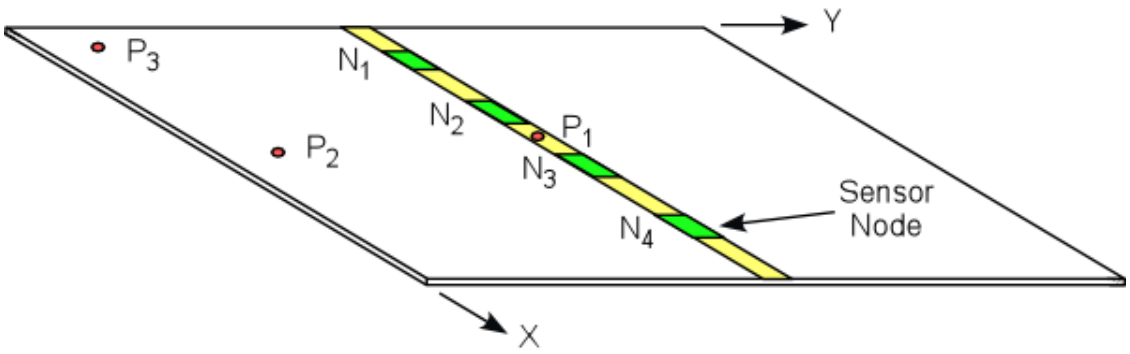

Figure 3-4. Schematic of the continuous sensor with four sensor nodes on a fiberglass panel

The AFC covers only a small surface area of the plate, and is electroded only at specific locations. The AFC sensor tape has one strip as shown in Figure 3-4. There are four electroded segments (called nodes) in the AFC sensor tape. The AFC nodes are 0.0127 m (0.5in.) * 0.0508 m (2in.) in size and are unidirectional. The segments are evenly spaced across the tape. The AFC is 0.0127 m (0.5 in.) wide and $165 \mu m$ (0.0065 in.) thick. The AFC was modeled based on the available properties of the AFC materials [69]. In this simulation, unidirectional AFC sensor nodes are modeled and strain is sensed only in the direction perpendicular to the sensor tape. The sensor could also use a monolithic PZT sensor material to allow bidirectional strain to be measured. In addition, there is great freedom to optimize the geometry of the sensor for particular materials and applications. For example, the node shape and size can be adjusted; the line node connectivity pattern can be replaced by a rectangular, radial, or a cross pattern; and sensors can overlap or be nested to improve location of the damage source. In general, multiple dendrites will be used on a structure, a redundancy that will allow detection and location of the damage event.

An impulse in the form of a Dirac delta function of magnitude 0.001 N-s is assumed to be generated from a crack located at the different points on the panel. The simulation is performed by computing the plate solution in closed form at each time step, and the sensor response is computed at each time step. The time step used in computing the solution is one microsecond. The first 50 modes are used in the calculation of the plate response to the impulse. The results of the simulations are shown as sensor time responses and wave patterns in Figures 3-5 through 3-10. All figures show the response at times $t=1 \ \mu - s$ to $350 \ \mu - s$.

Figure 3-5 gives the voltage output from the continuous sensor (all 4 nodes) versus time because of an impulse located at the center of the panel (location P1 of Figure 3-4). Figure 3-6 shows the displacement wave propagation resulting from an impulse at the center of the panel. The peaks in Figure 3-5 correspond to the times when the circular wavefronts pass over the sensor nodes. The largest peak of about 1 V occurs at about 0.1 ms when all four sensor nodes are riding the Lamb waves simultaneously. Figure 3-6 shows how the wavefront propagates and reflects from the edge of the plate. Because the sensor nodes are unidirectional and their sensing direction is poled in the Y-axis, the radial wave propagation does not produce as high of voltage as another shape of sensor, such as that from a circular sensor tape. The uniformity in peaks is lost after 0.04 ms in Figure 3-5. This is due to lower frequency and reflected waves passing over the sensor.

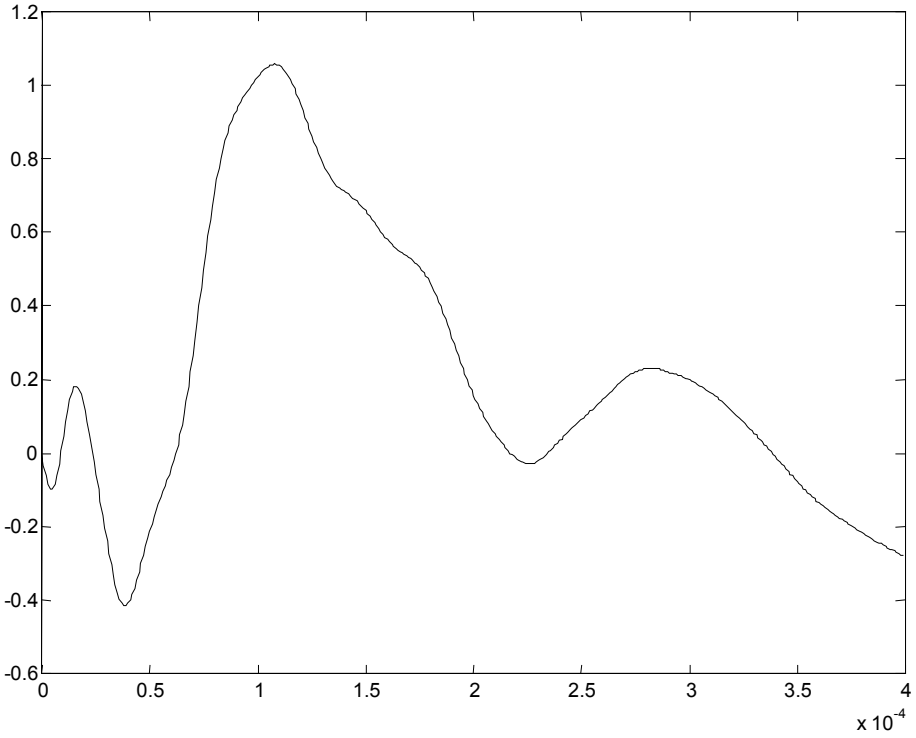

Figure 3-5. Voltage of the continuous sensor versus time for an impulse at the center of the panel

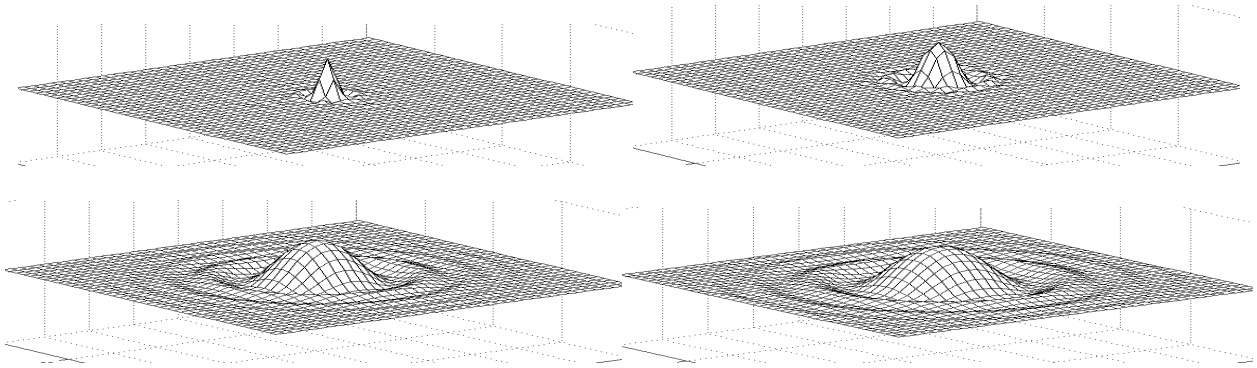

Figure 3-6. Displacement waves resulting from an impulse at the center of the panel ($t = 1,50,200,350\mu s$)

Figure 3-7 gives the voltage from the continuous sensor versus time for an impulse located near one of the edges of the plate (location P2 of Figure 3-4). Figure 3-8 shows the displacement wave propagation that results from an impulse near one of the edges of the panel. The amplitude of the peak voltage is about 0.7 V in Figure 3-7 within the simulation time period shown.

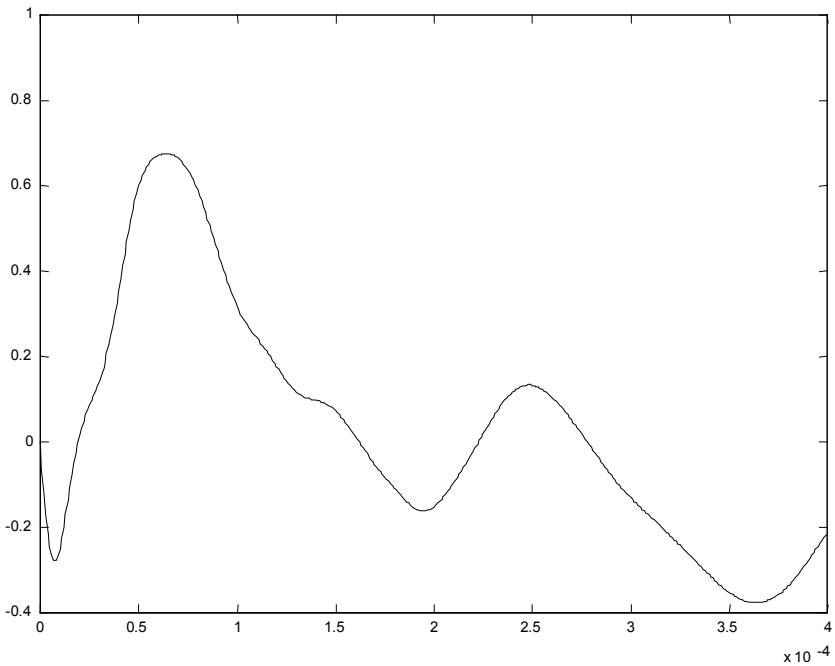

Figure 3-7. Voltage of the continuous sensor versus time for an impulse at the side of the panel

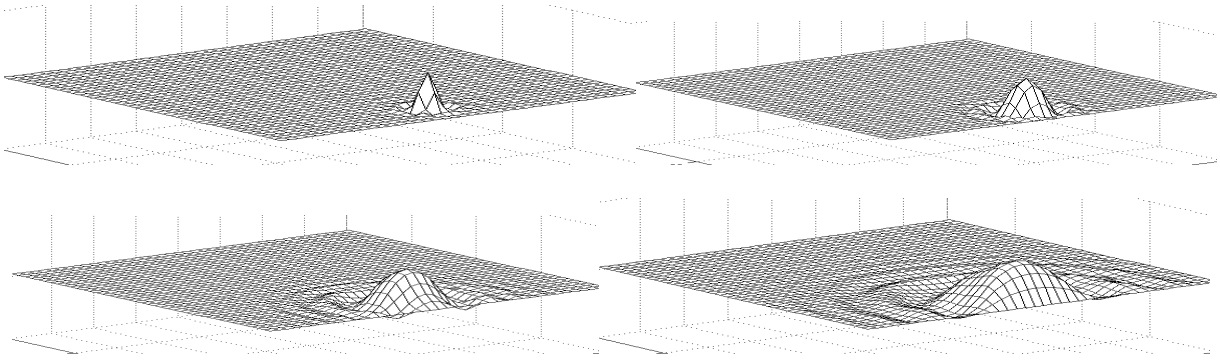

Figure 3-8. Displacement waves resulting from an impulse at the side of the panel ($t = 1,50,200,350\mu s$)

Bending wave propagation in panels is dispersive, and the wave propagation velocity depends on the wavelength of the vibration mode. The first peak of significant amplitude in Figure 3-7 occurs at around 0.07 ms, when the simulated Lamb wave front reaches an edge of a sensor node. Then the voltage increases as the wavefront passes over the four nodes. Damping added to each mode causes the wave to decay in time if a long simulation is run. The maximum voltage occurs in the initial part of the response when the wave passes over the sensor. After reflecting and returning, the wave is decaying and the sensor voltage is smaller.

Figure 3-9 shows the output voltage from the continuous sensor versus time for an impulse near a corner of the panel (location P3 of Figure 3-4). In Figure 3-9, the peak voltage is about 0.08 V for the time period of the simulation, whereas in Figure 3-5 and Figure 3-7 the peak voltage is approximately 1.0 V

and 0.7 V, respectively. Figure 3-10 shows the displacement wave propagation resulting from an impulse near a corner. The peak amplitudes and the change in uniformity of the peaks in the voltage response plots might be used to indicate the position of the crack. A crack near the corner may produce uniform peaks in the voltage curve but the amplitude may be 10 times smaller than the other cases. The nearer the crack is to the middle of the plate, or the nearer it is located to the sensors, the higher the peak voltage output is. We plan to apply neural network analysis to these signals to characterize the damage.

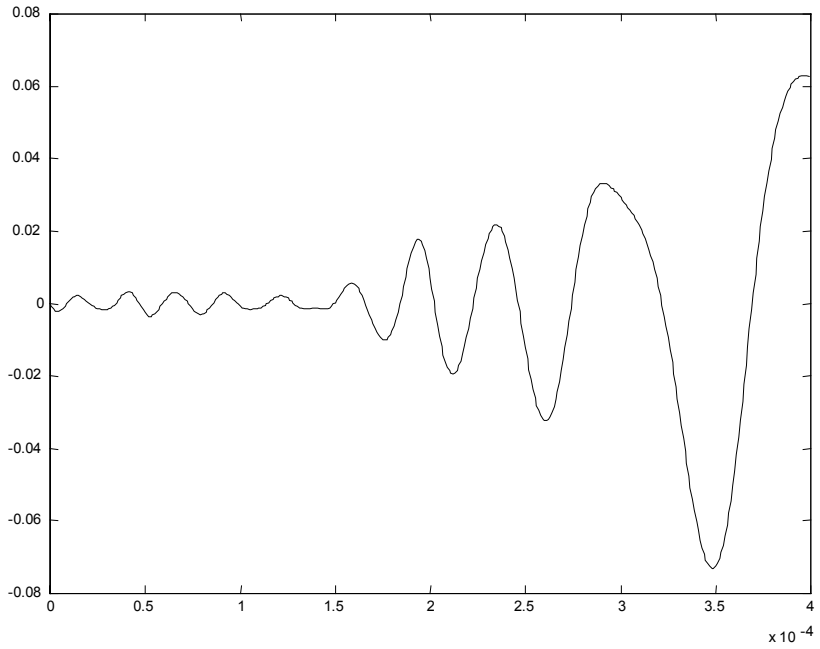

Figure 3-9. Voltage of the continuous sensor versus time for an impulse at the corner of the panel

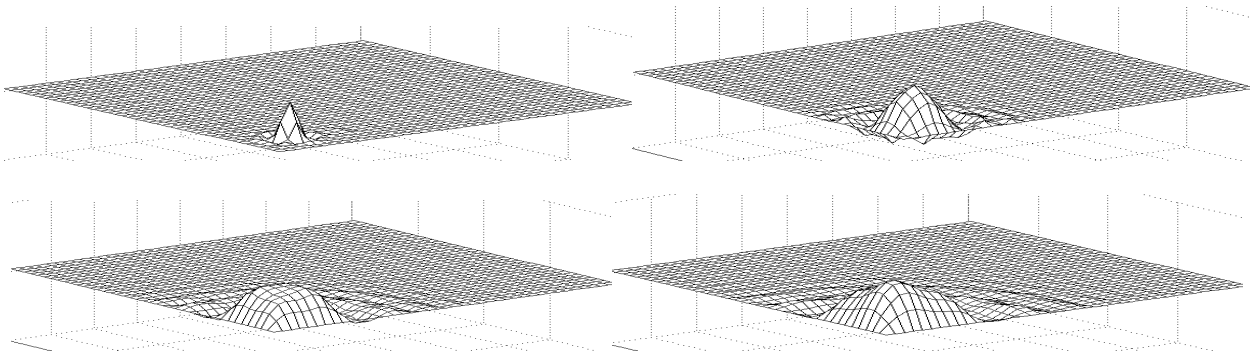

Figure 3-10. Displacement waves due to an impulse at the corner of the panel $(t = 1,50,200,350\mu s)$

The continuous sensors tested showed an improved capability for detecting simulated cracks, although the damage location cannot be exactly determined. This sensor design can lead to improvements in safety and simplification of maintenance procedures for large structures. The AFC continuous sensor can be self-powered and passive, simultaneous sensing can detect AE, large area coverage on structures is

possible, and the signal processing instrumentation is simple and relatively inexpensive (commercial AE hardware can be used directly). Active sensing (excitation and sensing) can be used to interrogate structures not in operation.

Damage Detection Experimentation

We used fiberglass bars and panels and an 8-ft long section of a fiberglass wind turbine blade to test the damage detection techniques. Cantilever bars and edge supported plates were also tested. The section of the fiberglass wind turbine blade tested at NCA&T was donated by Tom Baca of Sandia National Laboratories, Albuquerque, New Mexico. The wind turbine blade section was supported by ropes to prevent rigid body motion and give nearly free-free boundary conditions. The SLDV system (Figure 3-11) was used to compute operational deflection shapes (ODS) and FRFs; these are written to a universal file by the SLDV system. The universal file is converted to MATLAB input files that can be read by different algorithms in a damage detection toolbox we are developing. The TF and ODS methods use the data generated from the SLDV. The resonant comparison and wave propagation methods use a signal generator and oscilloscope or LABVIEW to excite the structure and capture the structural response. The SLDV is positioned about 15 ft from the blade. Because the laser reflectivity from the bare fiberglass blade was very poor, the blade was painted with reflective safety paint to improve the signal level. The intensity of the reflected laser then became very good. Still, curvature of the blade reduces reflectivity at some points, and small motions of the blade caused by ambient vibration in the laboratory cause speckle pattern motion, which can cause noise in the measurements. Six piezoceramic patches were bonded on the blade. Two 2-in.*1.5-in.*0.02-in. actuator patches are located at the center length one on each side of the blade, and four 2-in.*1-in.*0.01-in. sensor patches are located between the center patch and ends, two on each side. The sensor patches are for use during operational monitoring, and are used with the resonant comparison and wave propagation methods. The specific testing performed is discussed next.

Figure 3-11. The SLDV system

Transmittance Function Testing

Damage detection testing using curvature TF and PZT patches has been successful in computer simulations and testing on fiberglass beams and panels [3,6,19,22]. We also tested this approach on the section of a wind turbine blade. The method was found to be sensitive to damage, but requires a lot of data storage and computation for detecting small damage on a large structure. This experiment has shown that the TF method is sensitive to damage as well as noise in the measurements. Because the blade has two surfaces separated by spars, it may be necessary to scan both surfaces to find small damages. Also, small damage inside the blade, such as in the spar, may be difficult to detect.

Operational Deflection Shape Testing

The ODS testing is discussed in [3,11,14,55,64]. For this test we painted the blade with retroreflective paint as shown in Figure 3-12. ODS for the healthy (at 337 Hz) and damaged (at 336 Hz) blades are shown in Figures 3-13 and 3-14, respectively. The difference in the ODS contours of the two cases indicates damage. It should be noted that the healthy case indicates normally symmetric contours while the damaged case is nonsymmetric. The black lines in the figures correspond to near zero deflections. In the ODS of the healthy blade shown in Figure 3-12, the horizontal black lines correspond to the locations of three spars in the blade, which are very stiff. Once damage occurs, the symmetric ODS pattern is destroyed. A simple method of detecting damage is to plot the healthy symmetric ODS and monitor this pattern for change. Differences in ODS are also observed at other frequencies.

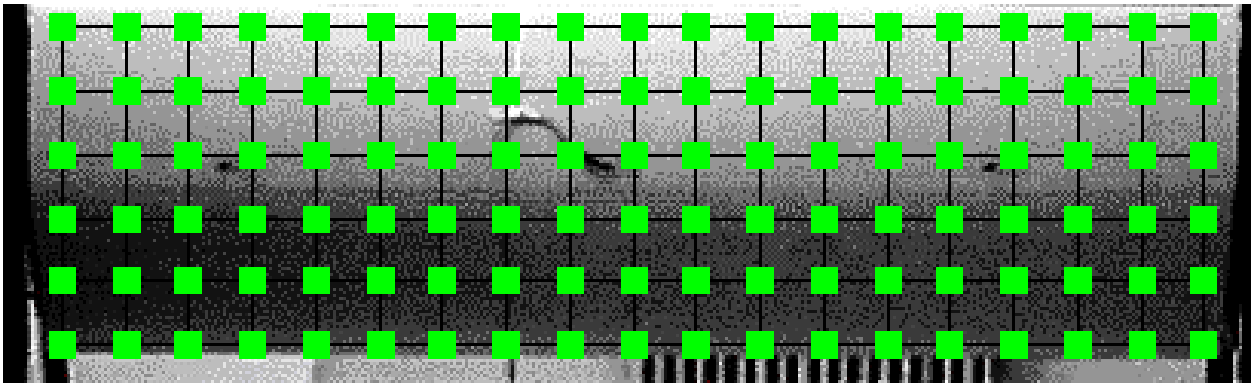

Figure 3-12. Wind turbine blade with PZT patches and 114 scan points for the laser

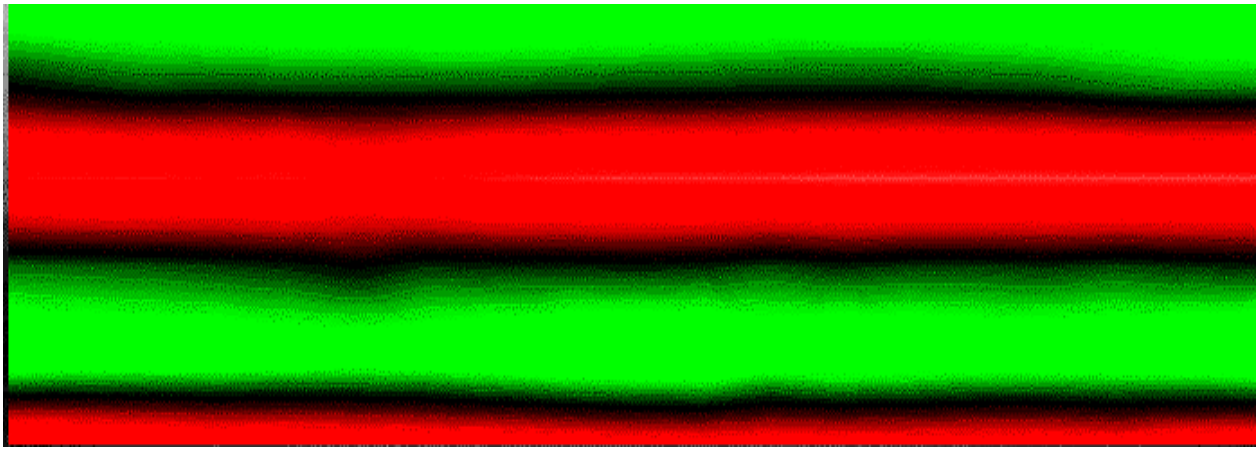

Figure 3-13. ODS for the healthy blade at 337 Hz

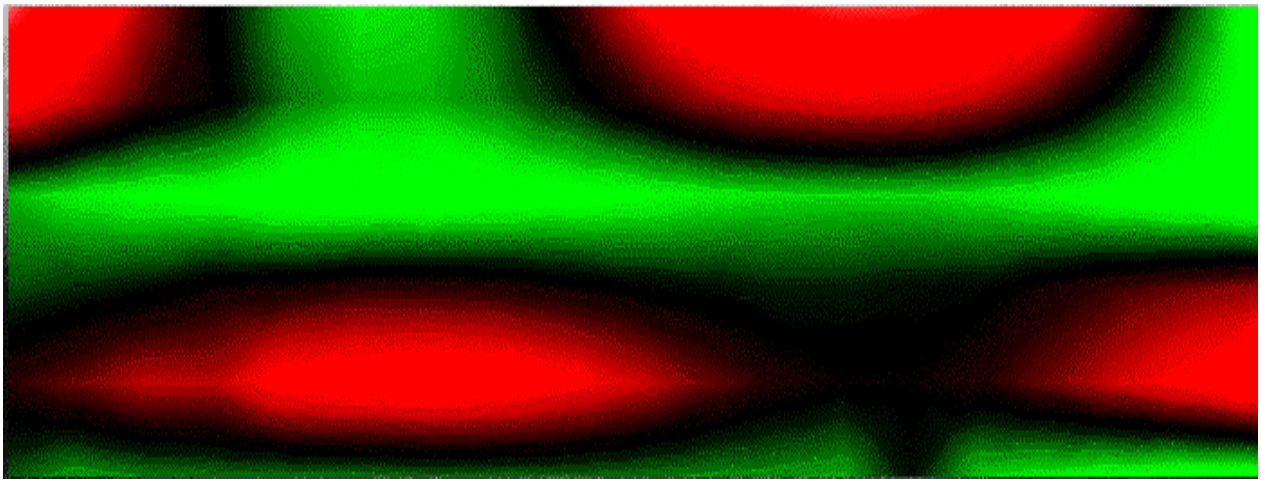

Figure 3-14. ODS for the damaged blade at 336 Hz

Frequency response functions for the blade are shown in Figure 3-15 for all points averaged, and in Figure 3-16 for the point at x1y4. These plots show that the effect of the simulated damage is to lower the natural frequencies and split some frequency peaks into two nearby peaks. The ODS method using the SLDV is a practical and easy-to-use technique for detecting damage with pattern recognition.

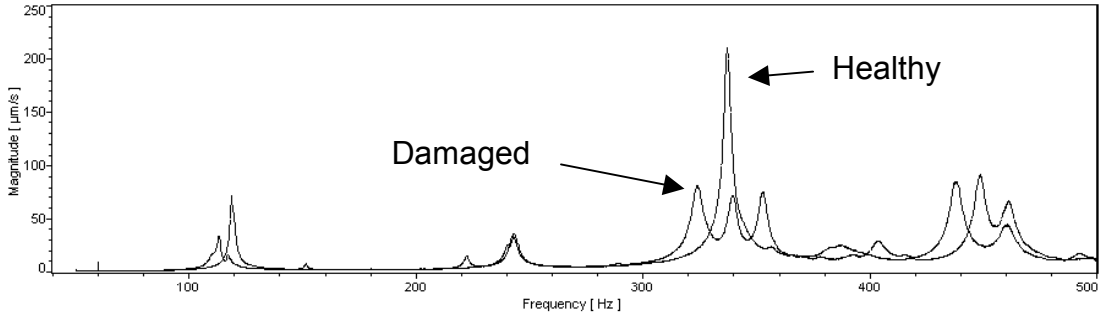

Figure 3-15. Averaged spectra for damage (mass) on front surface

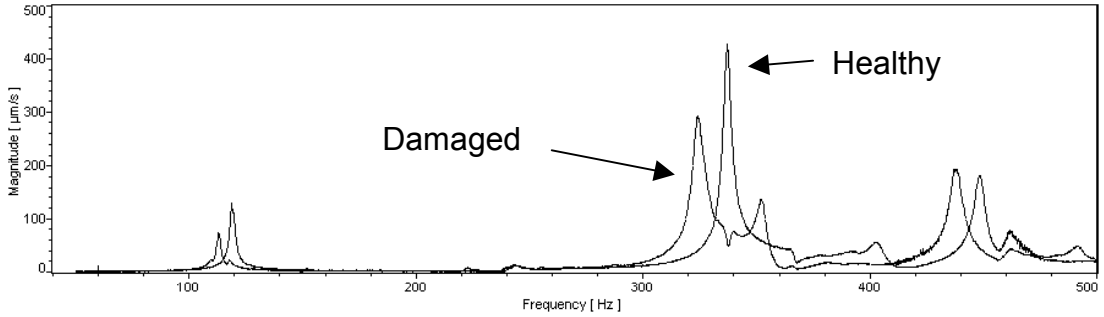

Figure 3-16. Spectra at x1y4 location of coarse mesh for damage (mass) on front surface

Resonant Comparison Testing

The resonant comparison method [3,10,11] compares the responses of pairs of sensors symmetrically placed on structures. Damage is detected by the difference in responses of the sensors at the resonances of the beam/damage. No historical data are needed in this approach, except one value per pair of sensors that indicates the nonsymmetry of the structure/sensors. We tested fiberglass beams using the resonant comparison method, as shown in Figure 3-17. In this testing, the beams are stationary. The beam with a delamination was tested with longitudional and transverse vibration. The delamination detection experiment uses two separate fiberglass cantilever beams 48 in. long, 3 in. wide, and 0.75 inches thick, one healthy and the other damaged (delaminated). Delamination on the damaged beam is located 6 in. from the clamped end of beam. Two PZT patches (nominally 2 in. * 1 in. * 0.010 in. collocated exactly halfway along the length) are bonded onto each beam. The two patches are the sensors. One piezoelectric inertial actuator is bonded at the free end of each beam for longitudinal vibration, whereas it is bonded at 36 in. or 44 in., respectively, from the clamped end of the beam for transverse vibration. The configuration for longitudinal testing is shown in Figure 3-18. A sinusoidal wave from the signal generator is input to the amplifier with a gain set at 20. The output of the amplifier (100 V) is then passed to the piezoelectric inertial actuator to excite the structure. Signal processing is done using a TDS 420A four-channel digitizing oscilloscope. The experiment is first performed for the healthy beam and then for the damaged beam with the same set of parameters. The experiment was performed in the frequency range of 0–1400 Hz. The experiment is performed for both longitudinal and transverse vibration, but only the longitudinal results are shown here. Figure 3-19 shows the effect of delamination damage for longitudinal vibration.

These test results are summarized next. For the beam with delamination, at resonance, the longitudinal vibration of the top- and bottom- collocated PZT patches showed different vibration or voltage levels, successfully indicating damage. For transverse vibration, the top and bottom patches showed a phase shift that indicated damage. This experiment showed that delamination changed the magnitude of longitudinal vibration and the phase of transverse vibration. We tested the second beam (with a bonded steel plate to simulate damage) with longitudinal and transverse vibration. At resonance, the longitudional vibration of the top- and bottom- collocated PZT patches showed different levels successfully indicating damage. For transverse vibration, the vibration levels of the top and bottom patches did not always significantly change. Thus damage on the top of the beams caused a magnitude change in longitudinal vibration and a possible change in transverse vibration, depending on the actuator location. Thus, in the frequency range 1 - 1,400 Hz, longitudinal vibration at resonance is very sensitive to damage and is potentially an accurate damage indicator for health monitoring. In the testing done, the PZT patch on the damaged side of the beam had an increased vibration level at resonance, compared to the PZT on the undamaged side of the beam. The resonant comparison method is a simple approach for health monitoring using PZT patches and structural symmetry to detect damage without storing historical data. The method senses either bending strain or axial stress waves. Away from resonance, the damage is not obvious.

For the testing using longitudinal vibration, a standing plane wave was excited in the frequency range where the waves were not dispersive. Thus damage changed the amplitude but not the phases of the response of the two patches. For the testing using transverse vibration, a standing bending or asymmetric Lamb wave was excited in the frequency range where the waves were dispersive. Thus, the damage changed the magnitude and phase of the response of the two patches. It is usually desired to excite nondispersive Lamb waves for damage detection. However, for realistic structures with complex geometry it is often difficult to generate nondispersive waves.

Figure 3-17. Composite beams used for damage detection testing

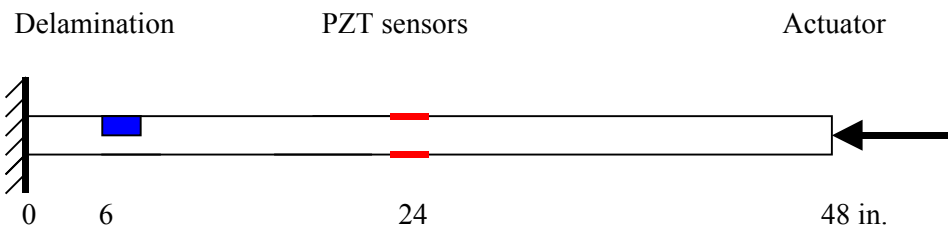

Figure 3-18. Longitudinal vibration of a bar with delamination on the top

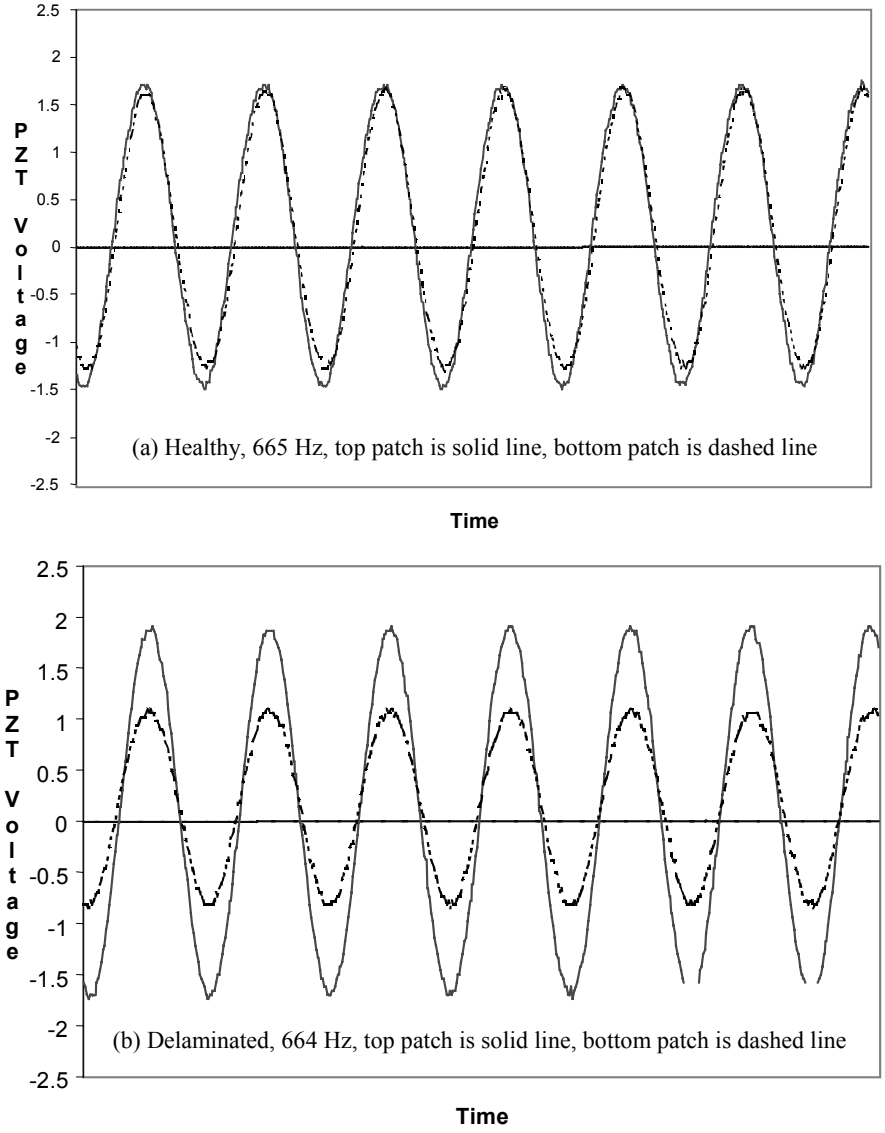

Figure 3-19. Healthy and delaminated beams, PZT voltage versus time for longitudinal vibration

Resonant comparison testing was also performed on the wind turbine blade section (Figure 3-12). A signal generator is used to produce a sine wave input to an amplifier, which drives the PZT patches in the center of the blade. The outer pairs of PZT patches are used as sensors and the two sensors on each side of the blade are compared to detect damage. The data acquisition is done using a digital oscilloscope. The data are captured and transferred to a word processing program to perform the computations and plotting. The test is performed by exciting the blade with a 693-Hz sine input, which corresponds to a resonant frequency of the blade. The response of the four sensor patches is recorded on the oscilloscope and transferred to a spreadsheet for processing and plotting. Figure 3-20 shows the response of the four patches for the healthy case. The damage indicator is run using the healthy data to establish a baseline noise or nonsymmetry level of the response that results from variations in construction of the blade or application of the patches. The damage indicator plots for the healthy case

are shown in Figure 3-20. The same experiment was repeated with a steel plate representing damage attached at the lower left part of the blade. The responses at 692 Hz of the four patches are shown in Figure 3-21, which also includes plots of the damage indicators. This testing shows that the damage indicator for the no-damage or healthy case is 0.3 between sensors 1 and 3, and 0.2 between sensors 2 and 4. With an added mass damage, the values are 0.9 between sensors 1 and 3, and 0.6 between sensors 2 and 4 at the 692 Hz frequency, Thus, the damage is identified by the technique. The resonant comparison method is a practical technique for damage detection because minimal historical data are needed, the algorithm is very simple, and the method can be used on operating wind turbines.

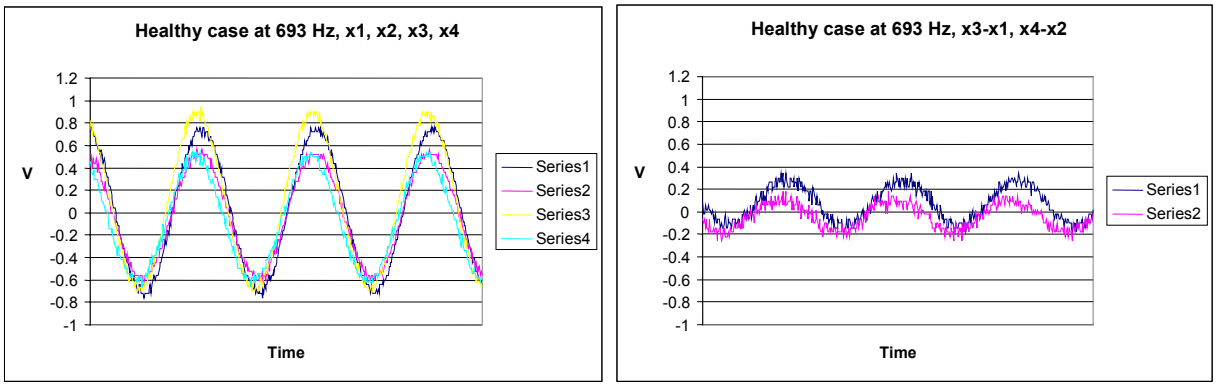

Figure 3-20. Sensor voltage versus time responses for healthy case at ~693 Hz (left), and nonsymmetry values |x3-x1|=0.3, |x4-x2|=0.2 (right)

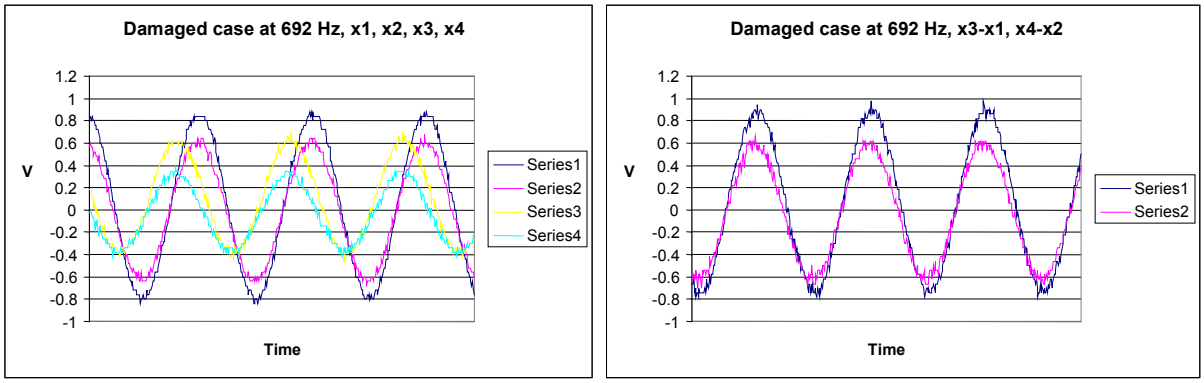

Figure 3-21. Sensor voltage versus time responses for damaged case at ~692 H (left) and damage values |x3-x1|=0.9, |x4-x2|=0.6 (right)

Impulse Response Testing

In this technique [3] the same instrumentation is used as in the resonant comparison method except an impulse excitation is used rather than a sine dwell. An experiment is performed by sending an impulse to the two actuator patches at the center of the blade (Figure 3-12), one side at a time. The sensor responses are measured for the healthy and damage cases. The damage indicator integrates the absolute difference of the two responses. The input impulse is 45 V peak with an approximate half sine duration of one thousandth of one second. The damage is a 2.938 in. * 2.938 in. * 0.275 in. steel plate bonded on the

back lower left end of the blade. Because this damage is not located between the actuator and the sensor, the change in wave propagation is small. The trailing part of the impulse response is changed the most as a result of the damage. Although the damage was indicated in this experiment, the impulse response method appears to have a low sensitivity to damage that is not in the path or between the actuator and sensor and when the actuator and sensor are far apart, as in this case. To overcome this limitation, we are developing a technique for readiness assessment of structures using a PZT actuator and the SLDV. The technique transmits and receives stress waves by step scanning the laser over hundreds of locations on the structure to detect flaws. The scanning overcomes the need to have a large number of receiver sensors as with other methods. This may also be the first technique that can fully map in time and space the acoustic wave propagation in a structure. The experimental results will be compared to the simulation model of wave propagation in a plate.

Conductivity Techniques for Damage Detection

Light conductivity in an optical fiber and electrical conductivity in carbon fibers are examined in this section as simple approaches for damage detection. A cantilever beam experiment was set-up to demonstrate the approaches, as shown in Figure 3-22. The fibers were put on the surface of the beam and conductivity was measured to determine the practicality of the technique. The fibers would need to be put into an actual laminate to verify the method. The light transmission experiment is described first, then the electrical conductivity experiment in a carbon fiber circuit.

The objective of the light transmission experiment is to detect damage or a break in the optical fiber by monitoring light transmission through the optical fiber. As shown in Figure 3-22, the optical fiber is connected to the end of the beam and split. One part vibrates with the beam and the other end is mounted in the wood base. The beam is given a small vibration and the light transmission is monitored by a flashing light-emitting diode (LED). An infrared laser is powered by AA batteries and when the optical circuit opens, the LED stops flashing. We tested different sizes of optical fibers. This experiment showed that the optical fibers are difficult to cause to break as a result of damage, connect, and handle. A large misalignment of fiber ends (laterally, axially, or angle) at the break is needed to indicate damage (stop the light transmission). Because of the insensitivity for small misaligments, damage detection using light transmission seems most suitable for large brittle structures such as concrete. The experiment could be improved by using a photodetector in place of the LED to measure the level of light transmitted. Although we did not attempt strain measurement using gratings in the optical fiber, it has been done successfully for bridges and other structures. The optical fiber with Bragg gratings is a local strain measurement and would require an optical analyzer, many fibers, and multiplexing to detect damage on a large turbine blade. Also, damage can occur anywhere on a large blade. Optical fibers may not have sufficient spatial coverage for use in damage detection as they only measure strain at discrete points along the length of a fiber.

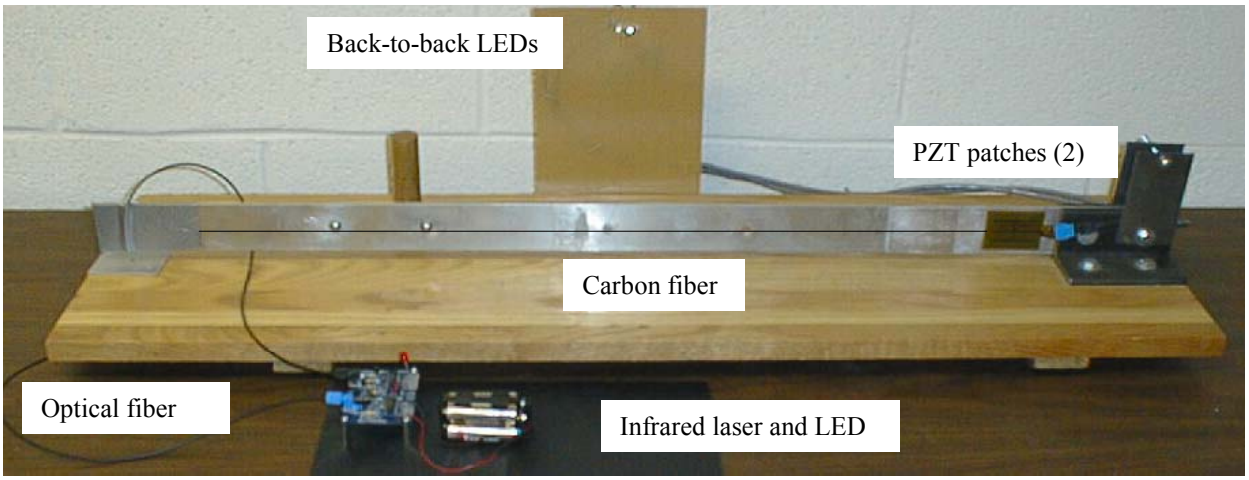

Figure 3-22. Experiment showing conductivity circuits for crack detection

The objective of the carbon fiber conductivity experiment is to implant carbon fibers into the fiberglass blade. The failure strain of carbon fiber is ~1.5%, and the failure strain of the fiberglass blade material is ~2.5%. The concept is that electrical conductivity/breakage of carbon fibers in the blade can indicate damage before failure of the fiberglass blade. In the experiment, ends of a carbon fiber tow were overlayed to test conductivity. The carbon fiber is illustrated by the black line in Figure 3-22. It was taped onto the beam to electrically insulate it from the aluminum. Vibration of the cantilever beam produces strain and a voltage in the PZTs and this is conducted through the carbon fiber to the two back-to-back LEDs mounted on the vertical panel. The flashing LEDs indicate that the structure is healthy. The experiment showed that the PZT, carbon fiber, and LED circuit works well. When the structure is vibrating and the carbon fiber is opened, the LEDs stop flashing. The simplicity of this technique is attractive, but the method has limitations: the breaking of fibers may not be complete and at the same location for all fibers; and there is a large statistical variation in fiber strength. This method appears suitable only as a rough indicator of damage, but testing a fiberglass laminate with carbon fibers would be needed to determine the exact sensitivity of the method. The light and electrical conductivity methods are attractive because of their low cost and simplicity and because they can be self-powered by the PZT and vibration of the blade. On the downside, they are a go or no-go indicator and may not detect small damages unless many fibers and sensors were used. The conclusion of the conductivity experiments that large spatial coverage is needed to detect damage suggests that the architecture of the biological nervous system might be appropriate for structural health monitoring.

Acoustic Emission Testing

Experiments are being performed [9,11,12,13,30,56,57,61] to verify the characteristics and potential of AFC continuous sensors for use in damage detection. However, because AFC sensors are currently expensive, standard discrete 1.27 cm * 0.95 cm * 0.25 mm PZT sensors are used in this experiment to present the concept of continuous sensors. The small size of the PZTs will allow higher frequency components of acoustic waves to be measured. The PZT patches sense strain in any direction in the plane of the plate. The experiment is performed using a 0.91 m * 1.2 m * 6.3 mm fiberglass panel (Figure 3-23) with a continuous sensor. The voltage response caused by a lead break on the panel is shown in Figure 3-23. The top and bottom traces correspond to the single sensor and the continuous sensor, respectively. The high frequency part of the AE is nearly missing in the response of the single sensor, while the continuous sensor is able to capture the leading edge of the signal. Capturing the leading edge is crucial to identifying the source mechanism because the later part of the signal is dominated by the structural

characteristics and may resemble ambient vibration and noise that likely is present in the structure. In this case, the continuous sensor is superior to the single sensor for AE detection. Thus, continuous sensors are particularly advantageous for monitoring attenuative materials such as carbon or glass epoxy composites.

The acoustic emission amplitude and energy as measured by the AE monitor are shown in Figure 3-24. Amplitude comparisons between the continuous sensor (DS) and the single PZT sensor (SS) for three different locations of lead breaks are shown. The continuous sensor registered a larger amplitude signal and a larger AE energy, as measured by the commercial AE monitoring system. The continuous sensor can detect and locate damage within the coverage area of the sensor, but cannot exactly locate the AE source because of the continuous nature of the sensor. Unidirectional AFC sensor nodes and characterization of waveform types are being investigated to locate the damage source more precisely. The maximum number of nodes possible to use in a continuous sensor depends on the resistance and shielding.

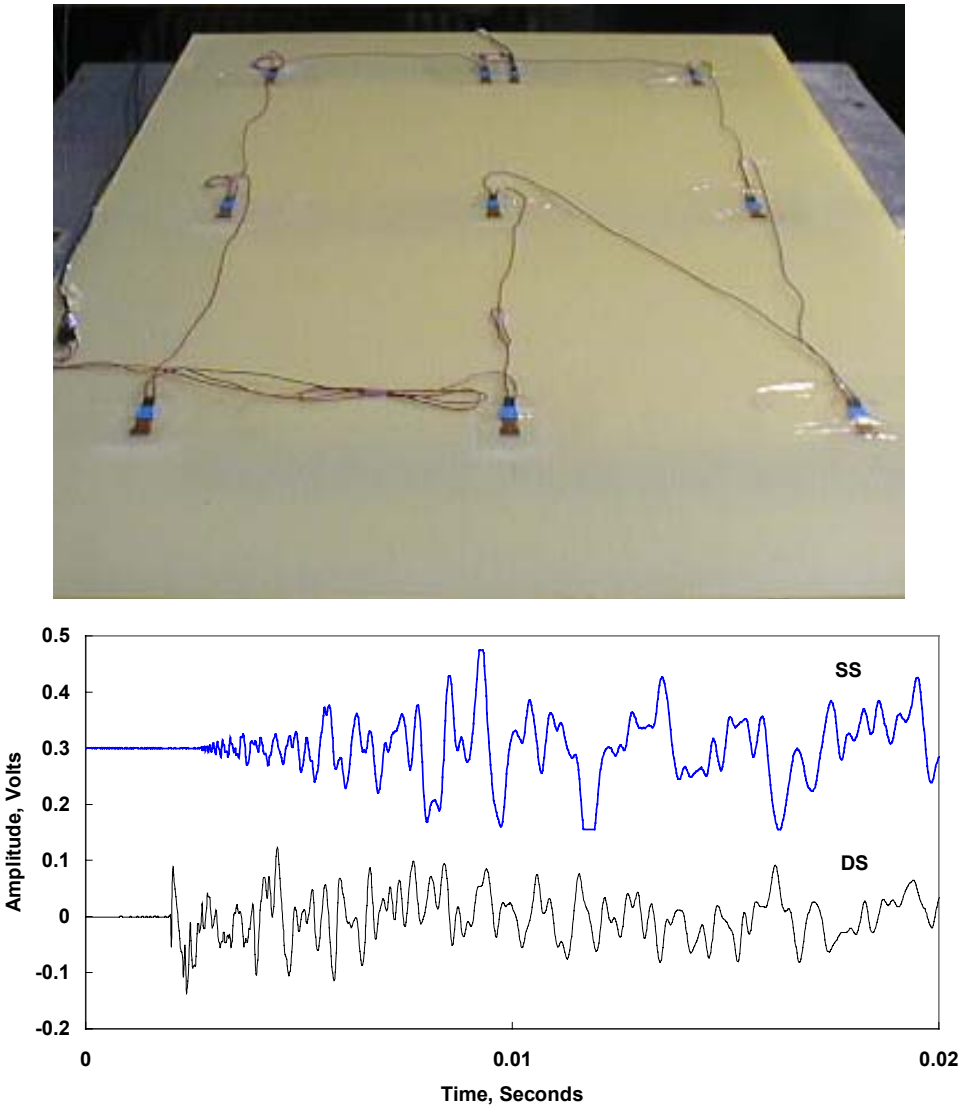

Figure 3-23. Voltage response resulting from a lead break on a fiberglass panel. The top curve is for the single PZT sensor; the bottom curve is for the continuous sensor with nine PZT nodes

The experiment with the composite panel showed that the energy levels from AE captured by the continuous sensor are considerably higher than for the single sensor. This occurs because damping causes high attenuation in composites and high frequency data are lost when the AE source is away from the sensor. Testing of complex structures will be performed to optimize the continuous sensor for detecting damage on large structures. Algorithms to add intelligence to the sensor based upon wave propagation patterns, multiple continuous sensor data fusion, and sensor directionality are being developed.

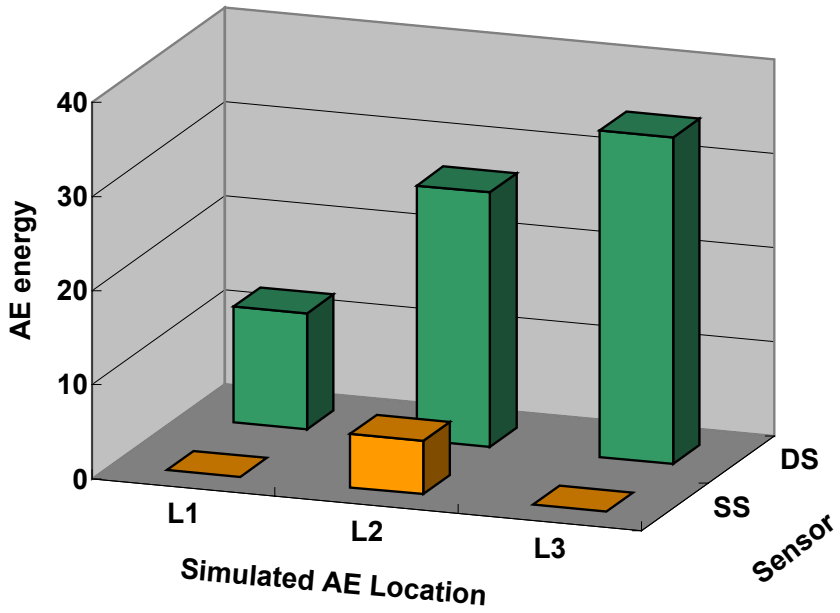

Figure 3-24. Comparison of the energy of the continuous sensor (DS) and a single PZT sensor (SS) from a lead break on the fiberglass panel acquired using an AE monitoring system

Different piezoceramic materials (Table 3-1) are being tested for use as sensors. In Figure 3-25, three patches are bonded to an aluminum panel of dimensions 1.22 m * 1.22 m * 3.2 mm. A monolithic PZT patch 2.5 cm * 2.5 cm * 0.25 cm is shown at the top, an AFC patch 13.3 cm * 6.35 cm * 0.13 mm is shown in the center, and a PZT patch 5.0 cm * 2.5 cm * 0.13 mm with interdigital electrodes (PZT-IDE) is shown at the bottom. The monolithic PZT patch is poled through the thickness and is bi-directional and measures strain in both in-plane directions. The AFC and PZT-IDE patches are poled along their length, are unidirectional, and measure strain in the horizontal direction (Figure 3-25). The coefficient (d_{33}) for the monolithic patch poled in the direction in the plane of the patch is about 50% greater than the transverse coefficient (d_{31}) for the patch poled through the thickness.

TABLE 3-1. Piezoceramic Properties

Property	Monolithic PZT	Monolithic IDE-PZT	AFC
Nominal size	50.8 * 38.1 * 0.38 mm	52.1 * 30.2 * 0.38 mm	133 * 63.5 * 0.2 mm
Capacitance	100 nF	1.02 nF	4.4 nF
Piezoelectric coefficient	$d_{31} = -179x10^{-12}$ m/V	$d_{33} = 350x10^{-12}$ m/V	$d_{33} = 115x10^{-12}$ m/V
Relative permittivity	1800	-	495
Voltage range	+200/-200	+1200/-1200	+2800/-1500

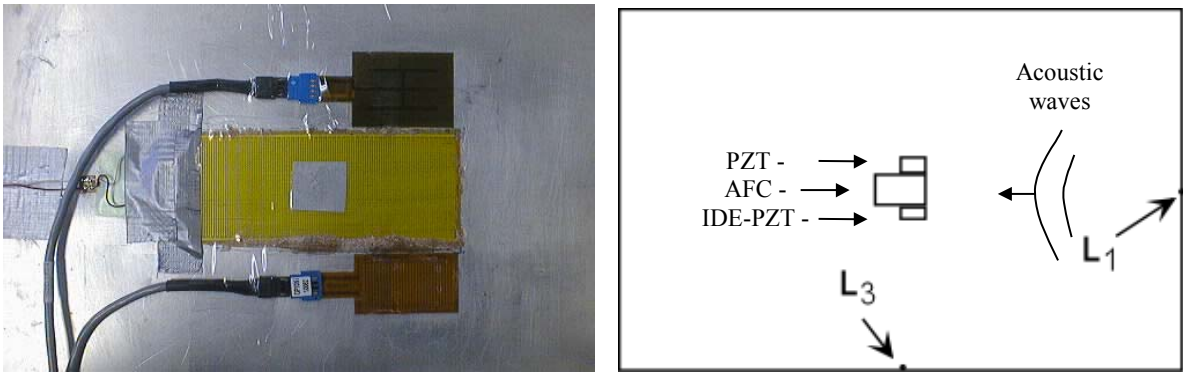

Figure 3-25. Sensor patches: (top) monolithic PZT; (center) AFC; and (bottom) PZT-IDE

A pencil lead break is made at the two edges of the aluminum panel in the plane of the plate (Figure 3-25). The lead break simulates an AE from a crack in the panel. The voltage response of the three patches is shown in Figure 3-26 for the lead break at location L1. The signal from the monolithic PZT patch (top signal in Figure 3-26) has a peak voltage level of about 0.3 V, and the high frequency content of the signal is close to the noise level of the signal. The signal from the AFC patch (center signal) has a peak voltage level of about 0.5 V and the high frequency content of the signal is clear. The signal from the PZT-IDE patch (bottom signal) has a peak voltage level of about 0.4 V and the high-frequency content of the signal is clear. The high frequency part of the signal is from longitudinal vibration, and the lower frequency part is from bending vibration of the plate. The higher voltage and better sensitivity to high frequency vibration of the AFC and PZT-IDE patches may be due to their unidirectional sensing capability and higher *d* coefficients. Smaller size patches than those tested would normally be used when measuring acoustic waves. The voltage response of the three patches was also recorded for the lead break at location L3. The signal from the monolithic PZT patch is larger at the beginning of the wave and then smaller when the bending waves arrive, as compared to the other sensors. The testing in two axes indicates that the unidirectional AFC and IDE sensors are more sensitive to longitudinal and bending acoustic waves in their fiber axis direction than monolithic sensors. The unidirectional sensors also were able to measure vibration transverse to their fiber axis because of the Poisson ratio effect in the aluminum panel.

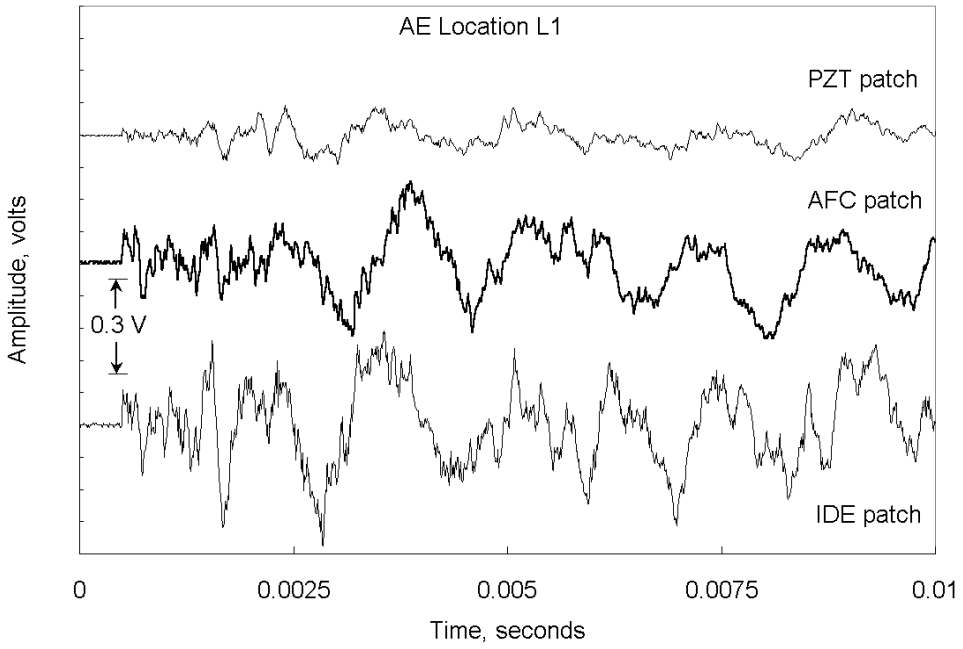

Figure 3-26. Waveforms from patches, lead break in-plane at location L1 of panel

Proof Testing of a Wind Turbine Blade

The testing reported here was an exploratory study in which the evolving damage to a blade was monitored using piezoceramic patch actuators and sensors during a structural proof test. The full test is described in [59]. The wind turbine blade is a composite construction and a static proof test was being performed to verify the design of the blade. Stress wave propagation data related to damage progression as the blade was loaded was collected without interfering with the static test. The objective was to determine if damage occurring to the wind turbine blade during the test loading cycle could be detected by propagating stress waves through critical sections of the blade. Stress wave parameters were compared to identify damage as the loading was increased. This may be the first structural health monitoring testing performed on a full wind turbine blade during loading using the stress wave propagation technique. Details of the testing are described next.

The approximate shape of the blade and the locations of the six PZT patches bonded to the blade are shown in Figure 3-27. The blade is 9 m (29.5 ft.) long with a maximum chord width of 1035 mm (40.7 in.). The detailed locations of the PZT patches are shown in Figures 3-27(b) and 3-27(c). The patches were bonded using a standard strain gauge bonding procedure using the strain gage adhesive. The cross-sectional geometry of the blade is shown in Figure 3-28. The blade consists of a shear web, unidirectional spar caps, a high-pressure skin section, a low-pressure skin section, and balsa wood coring, as shown in Figure 3-28. The high- and low-pressure skin segments refer to the pressure used in the molding process for the respective skin segments. The skin is fabricated in segments and assembled by adhesive bonding to form the blade. The spar cap regions around the axial locations of 37.5% and 72% of blade length were expected to be the critical regions based on testing of earlier blades, so these regions were monitored using stress wave propagation. The PZT patches were bonded approximately above the top spar caps on the blade skin.

The blade was loaded using a four-point whiffle tree arrangement, by which a single point load applied through a calibrated load cell was divided into four individual loads applied at axial locations corresponding to 50%, 65%, 80%, and 90% of length measured from the root end. Four whiffle tree load saddles were mounted on the blade at the corresponding load locations. PZT patches [71] were used for transmitting as well as receiving the stress waves. The patches were 0.8 * 0.4 * 0.025 cm. They were installed only on the top surface of the blade (subjected to compression during the static loading cycle) with their 0.8-cm length oriented in the chordwise direction of the blade. Because the PZT patches were not expected to survive the high tensile strains seen on the lower side of the blade, no patches were used on that surface. The PZT patches were used in the test because they are low cost. A different piezoceramic sensor that is conformable and withstands higher strain, such as an AFC patch, will be used in the actual field turbines on both surfaces of the blade. The PZT patches were located approximately above the shear web and the unidirectional spar cap on the top surface (compression high-pressure side) of the blade. Therefore, it is likely that the stress wave responses will be most sensitive to the damage initiating in the spar cap and the skin above the spar cap. The balsa wood bonded to the low-pressure section of the skin attenuates the stress waves significantly. The stress waves were generated and monitored using a portable instrumentation system built of commercial components (Figure 3-29). Signals were generated using an arbitrary function generator. These signals were amplified using two single channel power amplifiers and then used to excite the transmitting patches T1 and T2 (Figure 3-27).

Two receiving patches were located on either side of these transmitters. The distance between the transmitters and receivers was based on the space limitations between the whiffle tree load saddles and the expected failure locations. Because of the constraints imposed by the loading arrangement, the distance between the transmitters and receivers at the two locations was different. The signals received from the patches R1 to R4 were digitized using a digital oscilloscope, and downloaded to the hard drive on a laptop computer. The oscilloscope was set to start the waveform acquisition based on reaching the trigger level of the response in channel 1 for receiver R1. For this static proof test, 30 strain gages and 20 acoustic emission sensors were mounted on the blade. Some strain gage data were used in interpreting the stress wave results.

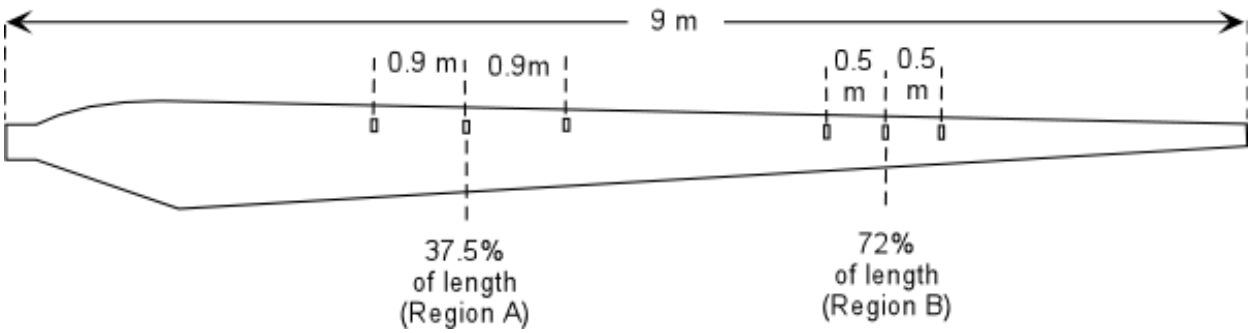

(a) Plan view of the blade showing PZT locations

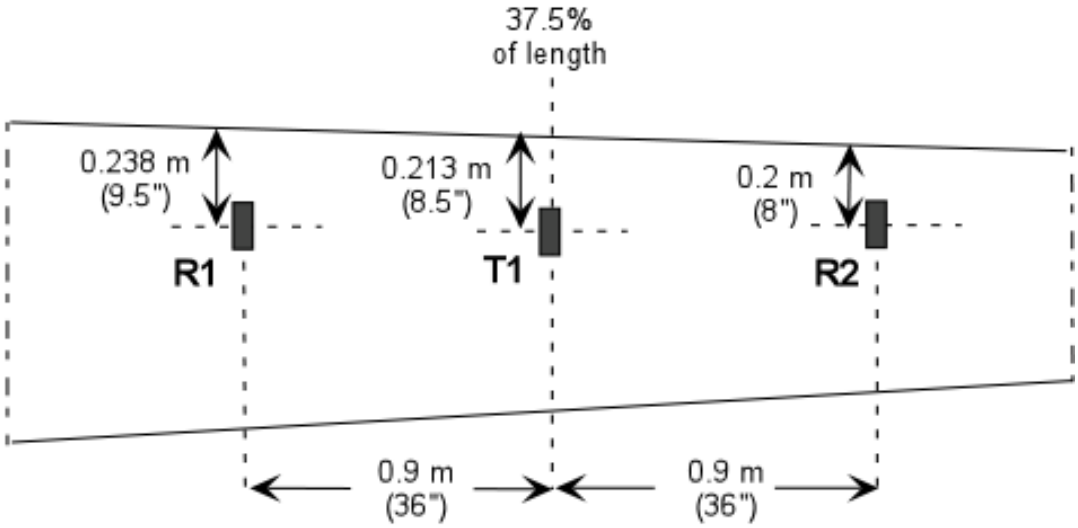

(b) transmitters and receivers in region A

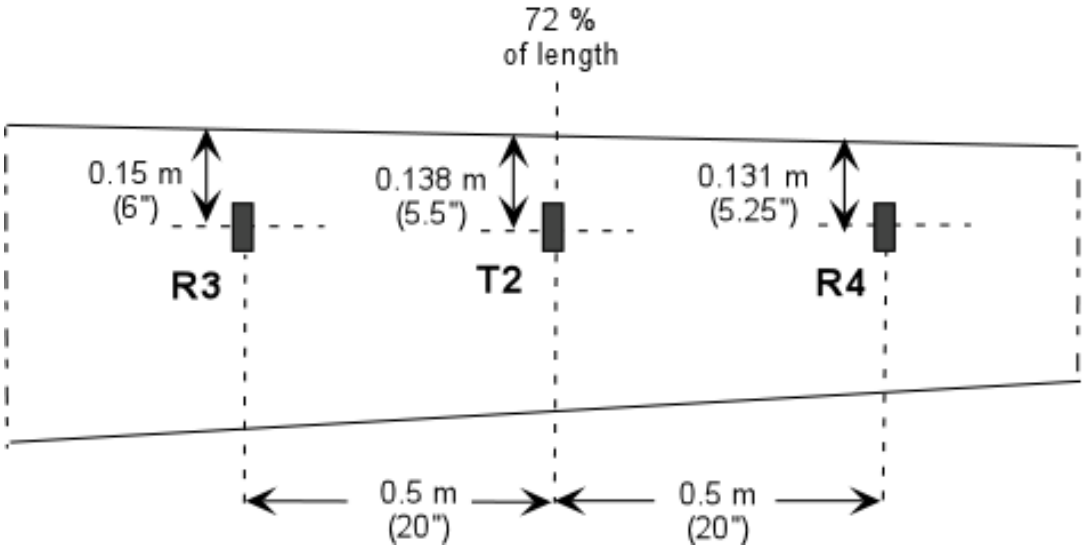

(c) transmitters and receivers in region B

Figure 3-27. Wind turbine blade plan view geometry and PZT patch locations

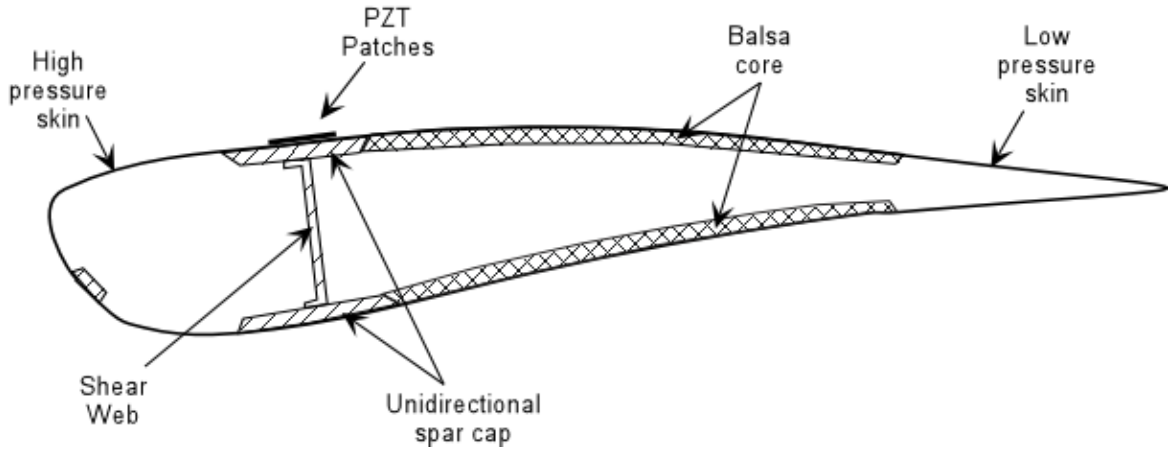

Figure 3-28. Wind turbine blade cross-sectional geometry and PZT patch locations

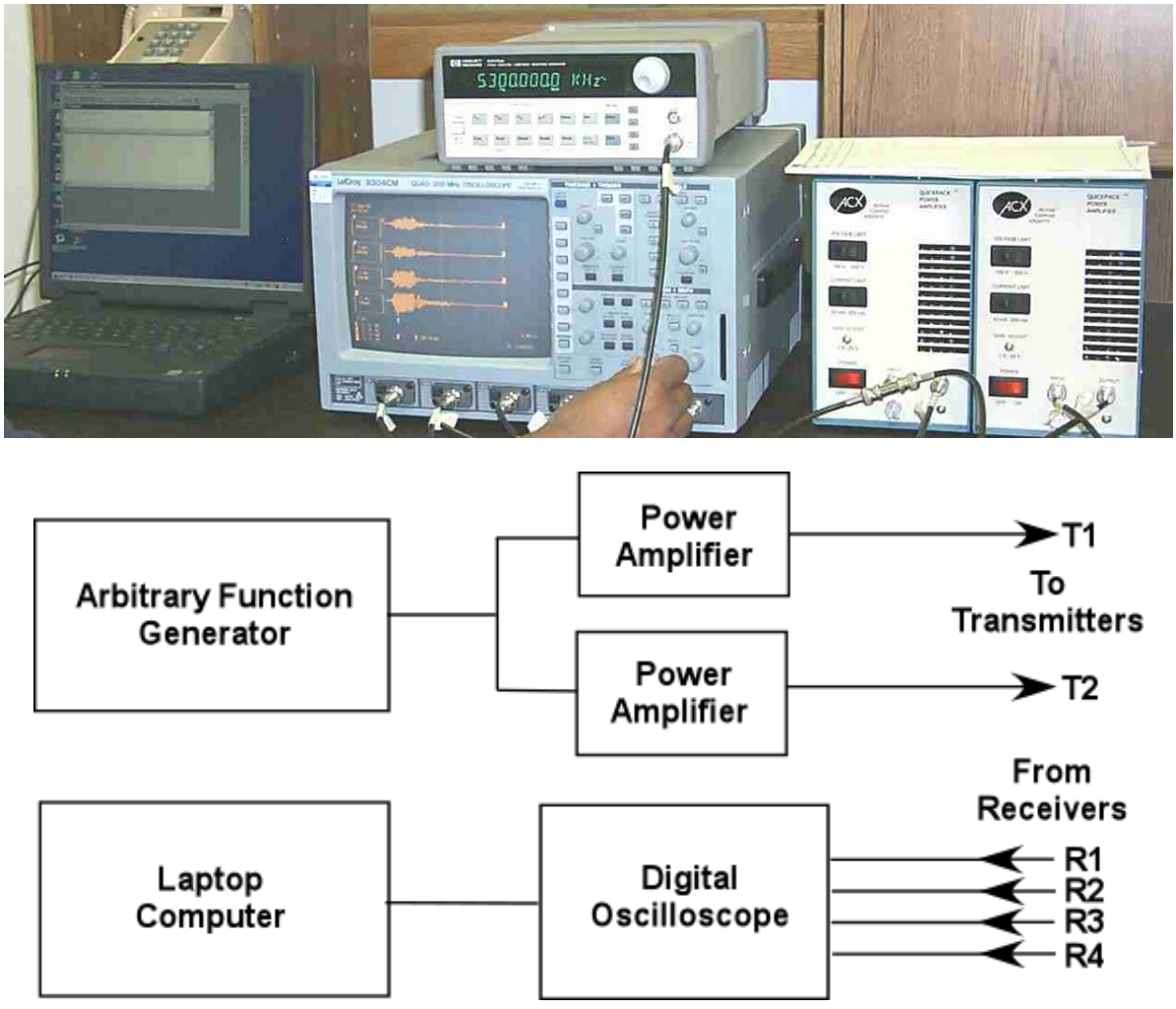

Figure 3-29. Field portable Structural Health Monitoring Instrumentation

Test Results

Different types of stress wave signals were evaluated before the actual test by transmitting these signals across the test section using the bonded PZT patches. Different frequencies and burst lengths were used. Frequencies ranging from 1 KHz to 20 KHz were examined. Based on these initial experiments, and to keep the comparison of signals at different frequencies simple, we decided to use tone bursts lasting 7 to 10 complete sine wave cycles. We then plotted the signals received corresponding to the undamaged blade at various frequencies using tone bursts with 10 cycles. The transmission distance at region A is nearly double the transmission distance in region B, and the cross-section of the blade at region A is much larger than at region B. This causes the signal amplitude at region A to be smaller than the signal amplitude at region B. When the signal frequency is increased from 3 KHz to 10 KHz, there is a decrease in the signal amplitude. This occurs because for a given power input, the vibration displacement amplitude of a structure decreases with frequency, except at resonant frequencies. Further, the received tone bursts have distorted waveforms, and the level of distortion varies as a function of the frequency. This happens because more than one mode can be excited and there is dispersion in propagating waves where the higher frequency waves can travel faster than the low-frequency waves. In this experiment, a rectangular window and a sine wave were used for excitation, and we chose the excitation frequency to give sufficient amplitude of response at the receivers. During the load cycle, only a few seconds would be available to stop the load and obtain the stress wave readings. For this reason, we decided to use a tone burst containing 7 cycles at 5 KHz.

Tone bursts containing 7 cycles at 5 KHz were obtained during the test at load levels ranging from zero load to 4,500 lb. The waveforms corresponding to the four sensors were plotted at different load levels. The deformed shape of the blade during loading is shown in Figure 3-30. The blade failure occurred at an axial location of about 37.5% from the root end, near the transmitting patch T1. The maximum load reached was about 5,500 lb. Figure 3-31 shows the location of the failure in the blade. The buckling occurred near T1 between T1 and R1 in Figure 3-27(b). No apparent damage was seen at any other location on the blade length. Because the objective of the blade health monitoring using stress waves was to track the evolving damage, an independent measure of damage as well as the damage location would be very useful. With no other means of quantifying the evolving damage in the blade available, the strain gage data in the neighborhood of the transmitters T1 and T2 were examined. These data showed some nonlinearity in the load strain plot from about 2,500 lb. load. However, significant deviation from linear response in the strain data occurred at 4,000 lb. These strain data might also be used as an indicator of damage because the strain gage in this case is at the damage site. Because strain is a very localized measurement, in general a large number of strain gages would be required to monitor a structure for damage. This is in contrast to the stress wave technique that uses wave propagation through the structure to detect damage using a small number of channels of data acquisition.

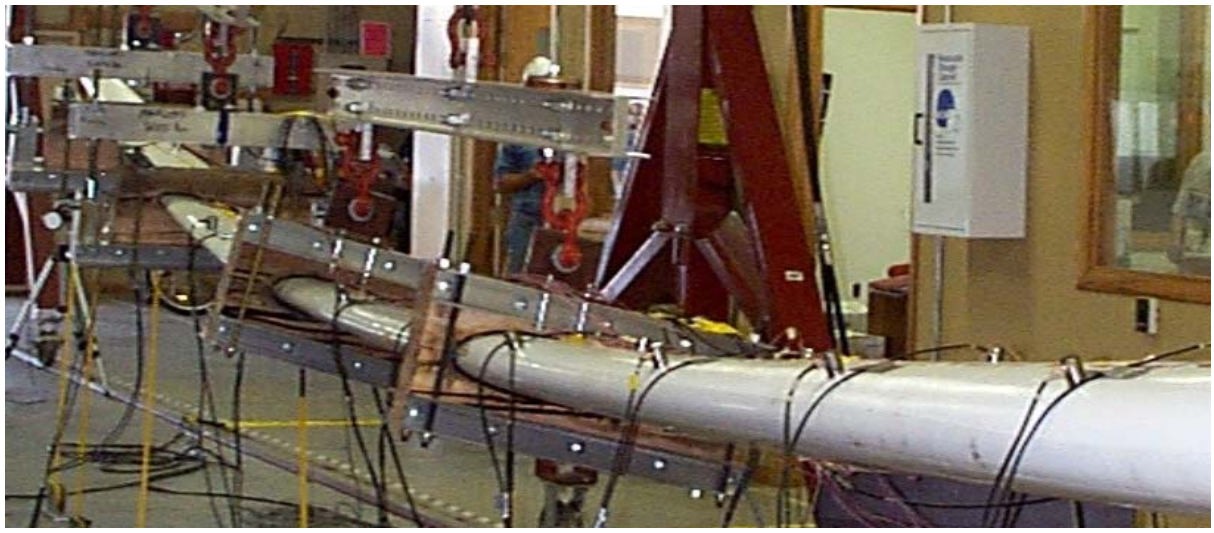

Figure 3-30. Deformed blade during loading

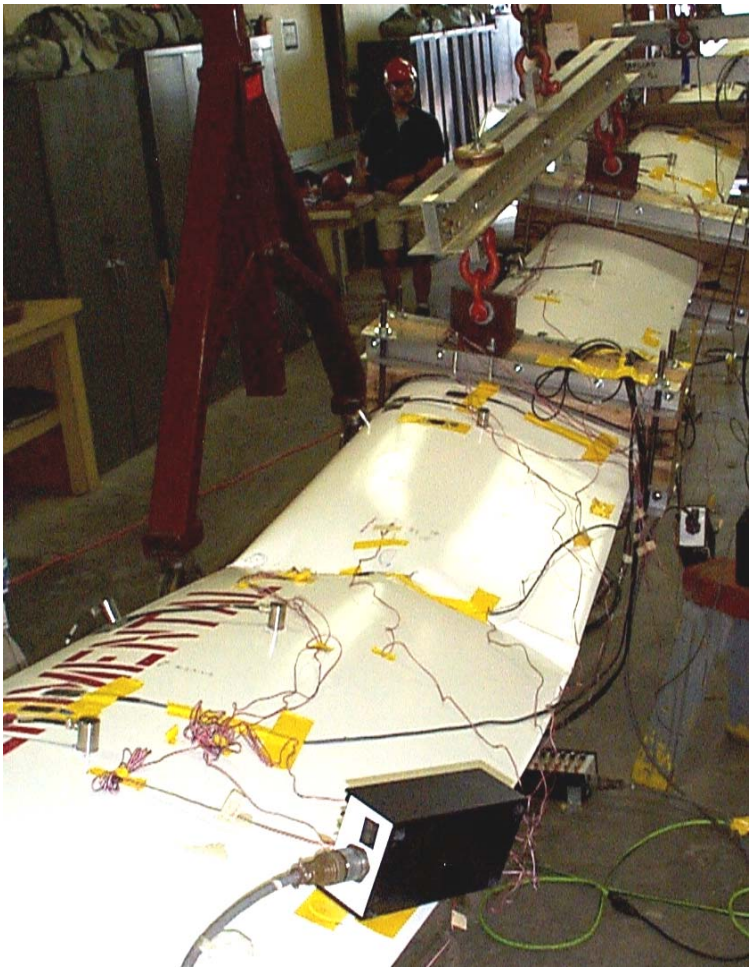

Figure 3-31. Failed blade viewed from the root end

We will now discuss the test results and relate them to damage evolution. The stress wave amplitudes from sensors R1 to R4 were examined at the no load condition (Figure 3-32) and at different load levels (Figure 3-33). Because the oscilloscope sweep of all four signals (R1 to R4) is triggered at the same instant, we were able to compare the relative time of arrival of the four signals. The amplitude and the waveform of the stress wave signals changed as the load level was increased, with the maximum changes occurring near the failure of the blade. Significant changes in the amplitude were seen in receivers R1 and R4 at the 4,000 lb load. For receivers R2 and R3, the amplitude remained the same or slightly increased with the load level. For receiver R1, as seen in Figure 3-33(a), when the load level was increased to 4,000 lb, the time of arrival of the second peak after the trigger point is delayed. However, subsequent peaks did not show additional delays. Similar shifts are also seen in signals from the other three sensors, but the maximum shift occurred for sensor R2. Hence, this exploratory test indicated that stress wave parameters are sensitive to the evolving structural change or damage occurring in the blade.

Because the geometry of the blade and the stress state in the blade were also changing (as a result of bending) during the test, this will have some effect on the stress wave propagation. The waveforms show a phase delay in all receivers. However, the delay goes to zero after about 1 ms for receiver R1. This may be due to a reflection of the wave from transmitter T1 at the root end of the blade and the combination of the transmitted and reflected signals at receiver R1. The other three receivers have load saddles outboard of them. The load saddles have foam against the blade that attenuates the stress waves and they do not reflect. Thus their phase delay remains for the entire signal period shown. The stress in the actuators and sensors was also changing with loading and will have some effect on the wave sensing. As the blade curvature increases, the preload strain in the PZT patches will increase. This may require that a larger signal level of the excitation signal reach the receiver patches to trigger the data acquisition, which may cause a phase change in recording the waveforms. The effects mentioned above must be verified by further modeling and testing. As a cantilever bar becomes curved, it will become stiffer. The lower natural frequencies of the bar will increase with curvature [72], and the wavelength of the modes will decrease. The velocity of propagation of flexural waves in a bar increases with decreasing wavelength up to a point at which it becomes constant [73]. This indicates that the wave speed would increase or stay the same as the blade increases in curvature. However, this effect must also be verified. To partly compensate for the curvature effect, the experimentation is done at high frequencies. Also, an exciter patch is used with two outboard receiver patches equally spaced from the generator patch. Comparison of the responses of the two receiver patches will indicate any nonsymmetric damage about the generator patch. This approach can propagate waves long distances and damage can be detected using a small number of patches and channels of data acquisition. Also, experimentation by loading and reloading the blade can quantify the effect of blade curvature, and wave propagation signals can be saved for different load levels. The geometry and stress effects may then be removed from the waveforms, leaving the damage effects.

There are multiple paths along the blade (which is a closed tube) for the propagation of the stress waves. The shortest distance for wave travel between the transmitters and the respective receivers is on the surface of the blade. Hence, changes occurring in the material properties between the transmitter and receiver are likely to have the greatest effect on the received signals. The balsa wood bonded to the low-pressure skin of the blade is highly attenuative and stress waves are not expected to travel very far through the low-pressure skin. The high-pressure skin, spar cap, and shear web are in the vicinity of this propagation path, and changes occurring to these components are likely to affect the received signal characteristics. In this exploratory study, changes in signal amplitude and relative phase were seen in the received signal, particularly near the final failure of the blade. However, these empirical observations need to be substantiated with additional detailed experiments and analysis. One likely precursor to the final failure mode is local buckling of the shear web. If this is the failure mode, it may be advantageous

to monitor the shear web directly by bonding patches on it. A damage detection analysis is performed in the next section to provide a metric for evaluating damage in the blade.

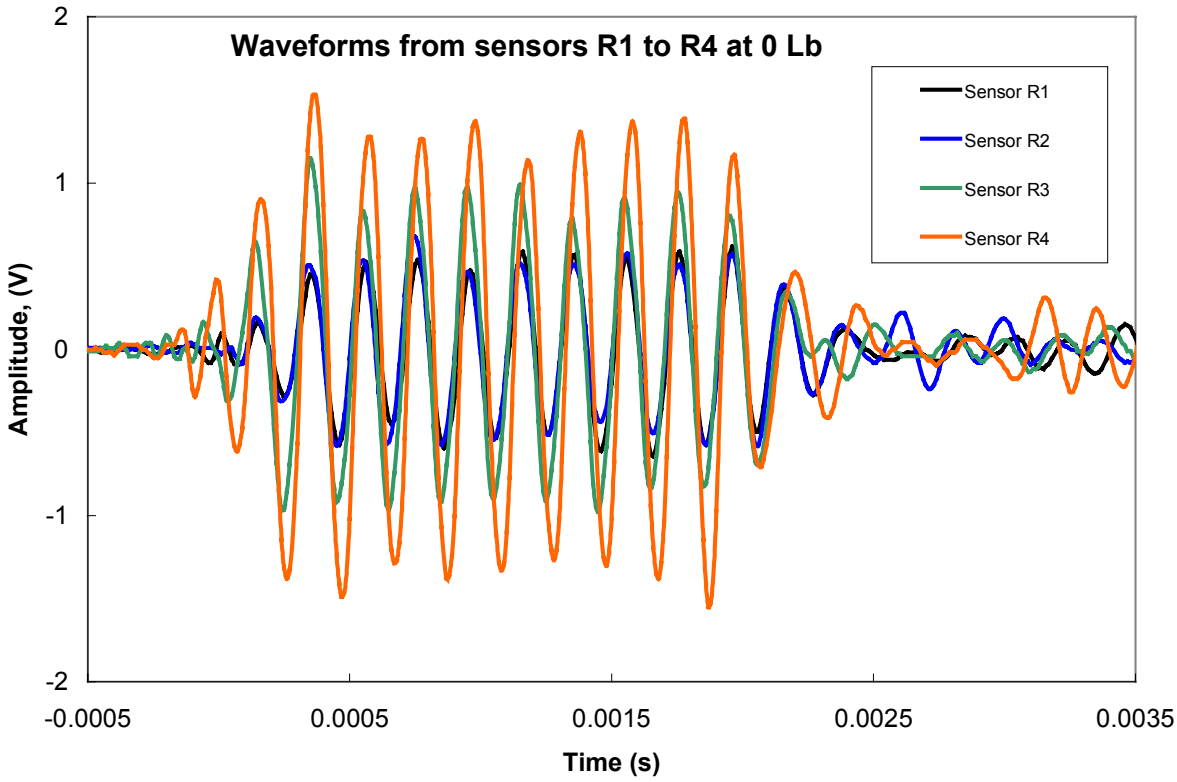

Figure 3-32. Waveforms for the no load condition

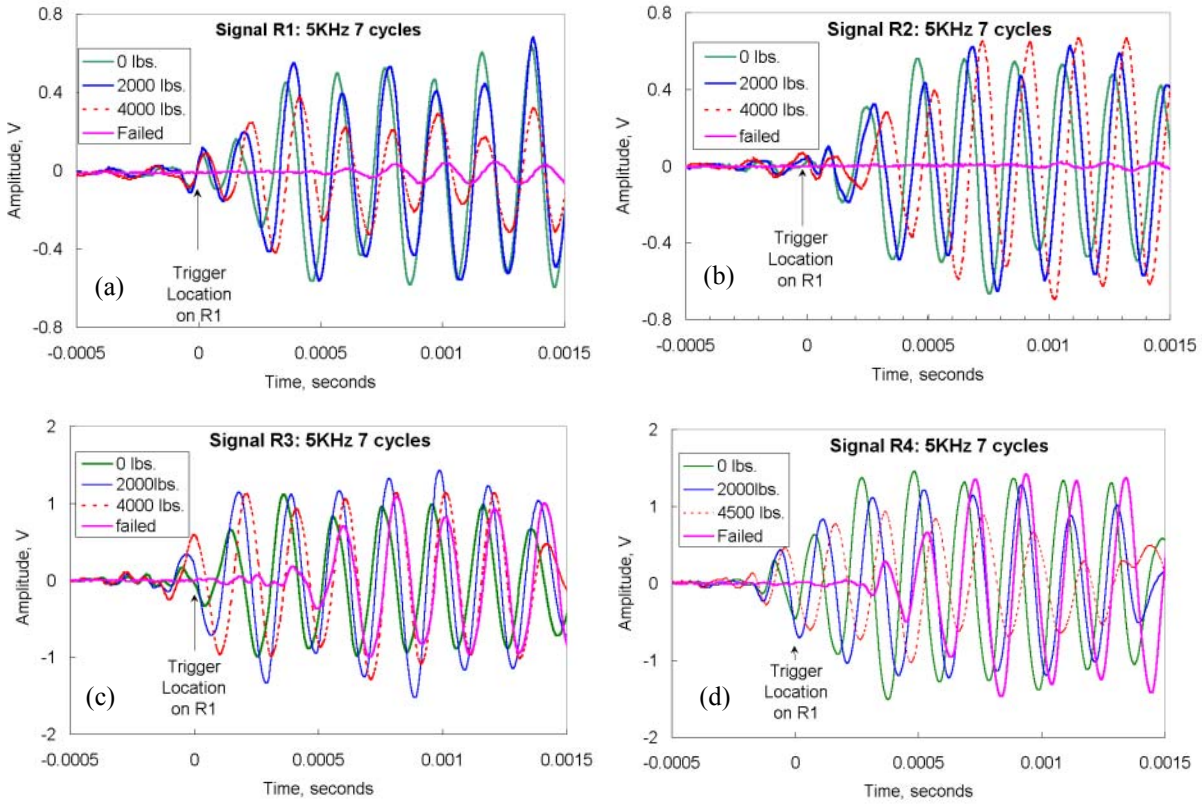

Figure 3-33. Sensor waveforms during different load levels; (a) sensor R1, (b) sensor R2, (c) sensor R3, and (d) sensor R4

Blade Damage Detection Analysis

Damage detection algorithms are used to measure the evolution of the damage. Before computing the damage detection indicators, damage can be observed by comparing the four receiver waveforms at different loads. The significant changes in phase and amplitude indicate that the structure has changed. Different methods including the resonant comparison, variance, and wavelet methods were investigated for damage detection. The model-independent resonant comparison method is shown here to predict if damage had occurred to the blade. In this approach, the exciting actuator is located at the center of a symmetric region, and the sensors are symmetrically located on either side of the actuator to measure the response. Any unsymmetrical damage growing in this region could be identified from a comparison of the signals from the two sensors. The method compares responses of symmetrically placed sensors at resonance to detect damage using minimal historical data from the healthy structure. The method is used here with a tone burst input.

The damage indicator values computed (Table 3-2) are $d_{12} = 0.96$ and $d_{34} = 0.06$. These values indicate a significant change in the structure resulting from damage and the change in geometry (bending). This damage indicator is based on the change in the peak amplitude of the difference in the response of pairs of receiver patches. A large change (damage) occurs for receivers R1 and R2, and a small change (damage) occurs for receivers R3 and R4. In future blade testing, more time must be

allocated for performing a detailed pre-test survey of the wave propagation characteristics of the blade with the load saddles attached to help interpret the SHM results.

Table 3-2. Resonant Comparison Results for the Sensors in Regions A and B

Resonant comparison of symmetrically located sensors-damage based on peak amplitudes					
Sensors R1-R2			Sensors R3-R4		
No load	4000 lb load	Damage indicator	No load	4000 lb R3, 4500 lb R4 Load	Damage indicator
0.46	0.90	0.96	1.67	1.57	0.06

The purpose of the blade proof test was to determine the static strength of the blade. Thus, unloading and reloading the blade to correlate damage levels with stress wave characteristics was not possible. Considering an initially straight beam in bending, as the curvature increases the beam becomes stiffer and the natural frequency increases, the wavelength of the modes remains the same or decreases with increasing frequency, and the velocity of propagation of flexural waves in a beam increases with increasing frequency. The natural frequency equations depend on stiffness and not stress for an elastic material. The results obtained show that the peak amplitudes of the stress waves change with increasing loading until the blade fails by buckling. The percentage change in the difference in amplitudes of symmetric receiver sensor amplitudes is greater near the damage area than away from the damage area. Thus the damage indicator seems to be sensitive to damage, although the stress waves also change due to the loading and curvature of the blade. Testing and modeling of simple bars will be done to quantify how the curvature and stress in the blade and sensors affects the wave propagation.

Blade Post-Failure Analysis

It is of interest to determine the failure origin in wind turbine blades so that redesign for increased strength can be done confidently. It is not possible to trace fracture origins on failed composite material parts as one would do with many homogeneous materials [2]. Neither is it possible to distinguish fatigue fractures from static overload cases. Only in the case of stress corrosion cracks is fractography analysis useful. Generally, some combination of detailed stress analysis (like finite element analysis) and/or careful observation during the test, before failure, is necessary.

Although typical fractography analysis cannot be applied, some information on the failure mode of the blade was gathered from the cross-section of the blade at the failure location (Figure 3-34). Figure 3-34 shows the cross-section of the blade on the root side of the failure location shown in Figure 31. Figure 35 shows the cross-section of the shear web. Of particular interest is the shear web, because failure of the blade shown in Figure 3-31 was likely preceded by buckling of the shear web. Several features may be noted in Figure 3-35. The channel-shaped web section is damaged. Delaminations between layers are evident in the cross-section of the web, both in the top of the vertical portion and in the top flange. The web portion of the channel section that is expected to be straight and normal to the base has a bent portion at the top. Because the adhesive bond between the web and top skin of the blade is still undamaged, it appears that the bend in the web section was present in the as-fabricated blade. Such deviations in the geometry and alignment are likely to reduce the buckling strength of the blade. The delaminations in different parts of the web can also be seen in the side views of the web, as shown in Figure 3-35 as bright patches. The buckling of the web likely causes these delaminations. Figure 3-35

shows wider damage to the web beyond the delaminations. There is a difference in the translucency in the web as indicated by the difference in the shades between the two regions. The portion of the web having the lighter shade became less translucent probably because of the appearance of microcracks in the web that resulted from the buckling of the shear web. Figure 3-34 also shows the leading edge of the blade. The complete separation of the top and bottom portions of the leading edge of the blade is evident. The lack of penetration of the crack into either of the two parts suggests the bond is the weak link between the two surfaces. Changes in the web and bond design may increase the buckling strength of the blade, but the manufacturing and cost implications of the changes are not considered here.

The different types and locations of damage occurring in a wind turbine blade could be determined by a SHM sensor system integrated inside the blade. This would provide information useful for preventing catastrophic failure of the blade and for redesigning weak areas of the blade. As an example, a sensor integrated in the shear web in Fig. 3-35 could detect the start of delamination.

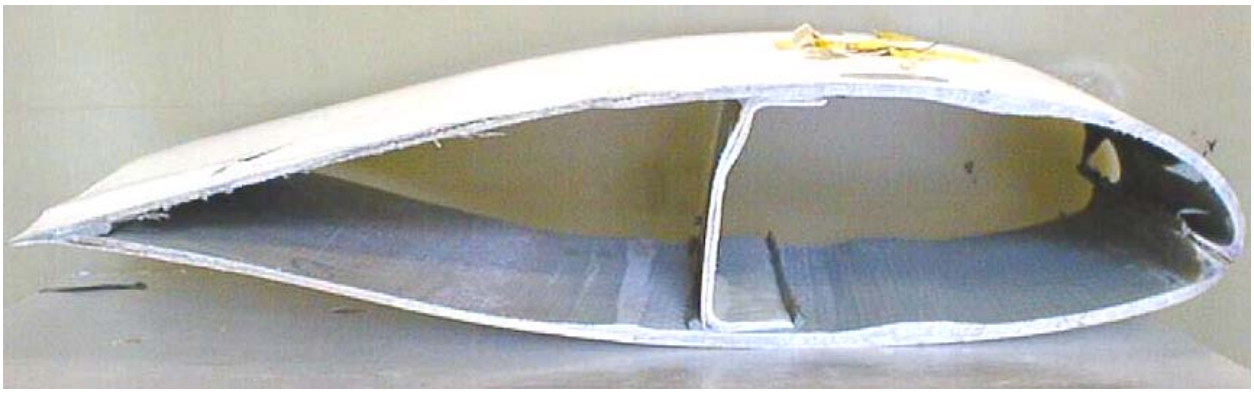

Figure 3-34. A segment of the blade adjacent to the buckling region

Figure 3-35. Enlarged view showing delaminations in the web and flange part of the channel section at the top and bottom, and relatively opaque and translucent regions

Discussion of Blade Testing

In a preliminary investigation, we monitored structural damage occurring to a wind turbine blade during the loading cycle through propagating stress waves. Bonded PZT patches were used for generating and receiving the stress waves. The wind turbine blade failed by local buckling at 37.5% blade length measured from the root end, at a load level of 5,500 lb. Because of the constraints imposed by the required minimum loading rate specified for this test, readings were obtained only up to a load level of 4,000 lb. for two of the sensors and 4,500 lb. for the other two sensors. Of the four sensors, the signals from receivers R1 and R2 showed the largest changes in the stress wave parameters. The R1 and R2 sensors were located across the damage region. These sensors were able to identify the occurrence and bound the location of the structural change or damage. Hence, stress wave propagation appears to have a promising potential for the detection of evolving structural changes or damage in composite structures such as wind turbine blades. A postfailure analysis of the blade indicated that changes in the web and bond design may increase the buckling strength of the blade.

A SHM sensor system integrated inside the blade would result in improved sensitivity and could identify the different types and locations of damage occurring in a wind turbine blade. This would provide information useful to prevent catastrophic failure of the blade in operation. It would also be a valuable tool for understanding the failure process during laboratory tests for advanced wind turbine blade development. Based on what we learned in the testing described in this report, here are some recommendations for further steps in the development of the intelligent blade:

- Laboratory tests on simpler structures such as plates under compressive loading should be performed to verify the sensitivity of the propagating stress waves to structural damage, buckling, and geometry changes caused by buckling. The PZT patches could be optimized to launch stress waves of appropriate frequency. The effect of high stresses on the sensors must also be evaluated, as the PZT patches can fail in high-stress regions.

- A number of changes in the signal shape and the data acquisition procedure could be made to increase the accuracy and depth of information gathered during the experiments. This includes triggering the data acquisition by the transmitted signal, using rising and falling tone burst signals, optimizing the excitation frequency to minimize dispersion of the waves, and optimizing the sensor spacing and size.

- A neural sensor is being developed using AFC material and this should be tested. This sensor is a continuous distributed sensor that can be used for active interrogation or passive listening for damage. The large coverage of this sensor would furnish a closer indication of the damage location.

- The SHM sensor should be embedded within a blade during manufacture, and the blade should be tested to failure. The sensor design should be optimized and another blade with the embedded sensor should be built, put into the field, and monitored in real time. The AFC sensor can be integrated into the blade without affecting the strength or stiffness of the blade.

Development of an Intelligent Blade

The intelligent blade will have the functions of real-time SHM and damage detection, providing information that can be used for load regulation to reduce fatigue damage or to mitigate the effects of damage. The approach we considered uses an attached or embedded neural system to continuously monitor the blade during operation. Blade strains, wave propagation, and/or AE are monitored. This results in real-time information that can be used to automatically regulate blade loading through the generator field, brake, ailerons, or other devices to prevent fatigue of the blade and to increase wind capture. Optimal approaches for SHM have been developed in this project and a patent is pending on a "Sensor Array System." Continuous sensor modeling, simulation, and experimentation has been performed. This section outlines the research to build and field test an intelligent blade.

The neural system will be developed as a continuous sensor system that mimics a biological nervous system. The sensor system will consist of an array of autonomous unit cells, each having several sensing elements and a neural processor capable of detecting and quantifying damage in its neighborhood. In addition, each of these neural processors will be capable of bi-directional communication with a central processor over a digital data bus. Conformable PZT fibers will be used to form the distributed sensor elements. Key to the feasibility of the neural sensor is the recent development at NCA&T State University of a new continuous sensor technology that has been demonstrated to make AE monitoring practical on a large scale. This sensor concept can reduce the number of signal processing channels by an order of magnitude while simultaneously improving the sensitivity and bandwidth. Further, the neural cells lend themselves to embedding in structural composites that are likely to benefit most from health monitoring technologies. This continuous highly distributed sensor system can monitor large components with a single digital data bus, eliminating the bulky cables and greatly reducing the hardware and communication needs for a field-deployable health monitoring system for wind turbines.

Sensory Signal Processing in Biological Neural Systems

The nervous system enables a living organism to sense the environment and respond appropriately. This system is exceedingly complex, with a large number of components and an extremely large number of interactions among these components. We will describe briefly the architecture of the neural system, how the system processes information, and how its principles can be applied to SHM. Because our interest is in sensory information, we will focus on how the neural system processes such information. Later, we would also extend our analysis to study how the system responds to this information.

The structure of neural systems is discussed next. A typical neural system consists of a large number of relatively few types of nerve cells or *neurons* (Figure 3-36a). For example, a mammalian brain has billions of neurons. Simpler neural systems have fewer neurons (Figure 3-36b), as few as tens to hundreds. All these systems exhibit the ability to process complex information. Neurons are cells that have all the structures common to all living cells. They have a nucleus and other cell organelles, and they are delineated from the environment by a cell membrane. Information transfer in the neurons occurs at the level of the membrane by means of electrical signals that propagate along the membrane without attenuation. Although the mechanism of generation and propagation of this signal (called an *action potential*) is known, a detailed description of this process is not germane to this discussion. It suffices to note that the neuron is an electrical device with multiple analog inputs (called *dendrites*) and a digital output (called an *axon*). We can visualize the neural system in terms of *levels of organization*. The system is arranged hierarchically (Figure 3-36c). At the top is animal *behavior*, mediated by *systems and pathways* in the brain; these systems are made up of *centers and local circuits*, which in turn are made up of *neurons*. Neuronal activity (action potential) is initiated by *microcircuits* of *synapses*. Synapses are

actually chemical connections that result in ion channel regulation and local changes in membrane potential.

We can also think of the neural system in terms of levels of information processing. It is obvious that the further we move into the system from the input, the higher the level of information processing. Taking the visual system as an example, the retinal ganglion cells respond to the local intensity of light; this is the information processed at this level. But at the level of the visual cortex (the area of the brain that deals with stimuli from the eye), cells respond, for example, to oriented bars of light. This information has to do with large areas within the field of vision of the animal. In the primate brain, 25 areas have been identified that predominantly or exclusively process visual information. The information from each area of the retina is fed into all these areas. For the purpose of SHM, we can consider the following properties of a neural system:

- Information proceeds through the system through different levels (hierarchies)
- Information is processed at each level; the level of processing is higher the farther away from the input
- Information is synthesized at each level, and a decision is made as to what is sent forward to the next level
- The system has mechanisms for noise suppression.

The above insights into human neurobiology are used to develop sensory intelligence in structures by creating artificial systems of neurons with simulated dendrites, axons, and synapses. The neural composite material mimics the biological nerve cells that are designed for one special function: the rapid processing and transmission of information over long distances. The basic mechanisms and architecture responsible for neuron activity are idealized using engineering materials to produce continuous distributed nerves for composite materials. The generalized neuron (Figure 3-36) is a biological cell whose morphology is designed to receive many inputs, produce a single output, and have that single output rapidly distributed to one or more other neurons. The neuron axon is analogous to an electrical transmission line with a transverse time varying negative resistance element in parallel with a high capacitance. The equations describing the propagation of neuron action potentials derive from the classical equations for wave propagation along electrical transmission lines. The basic mechanisms and architecture responsible for neuron activity can be modeled using neural network analysis and replicated using engineering materials. This is described next.

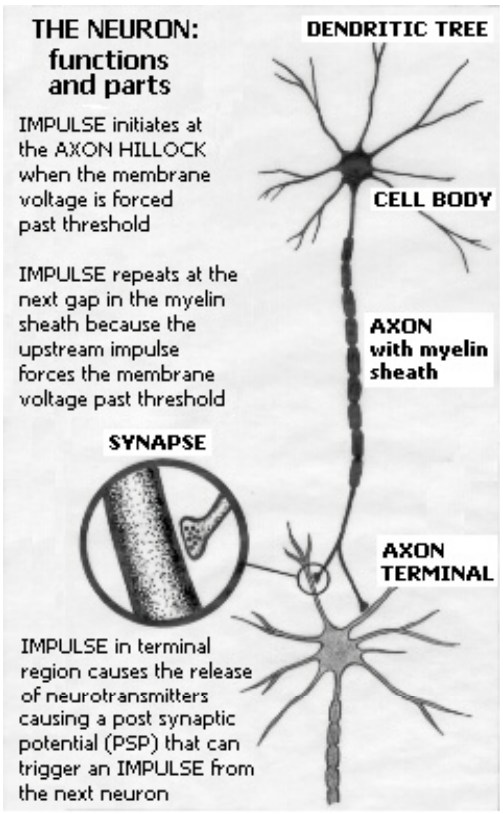

(a) The generalized neuron

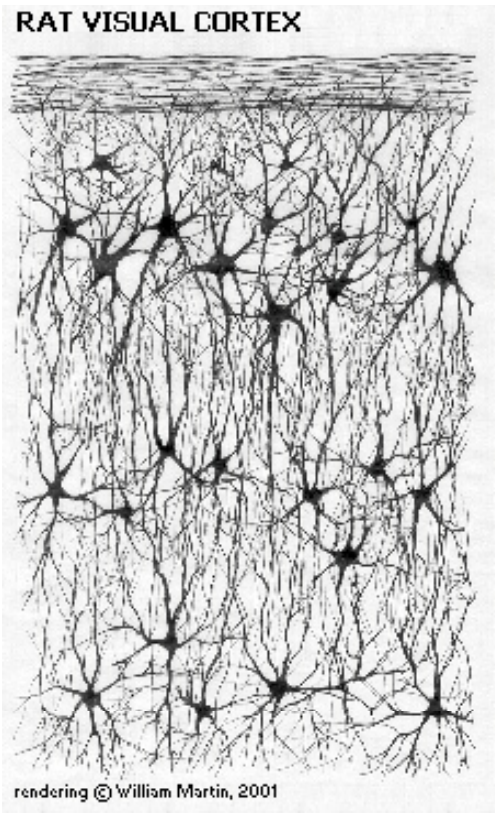

(b) The visual cortex

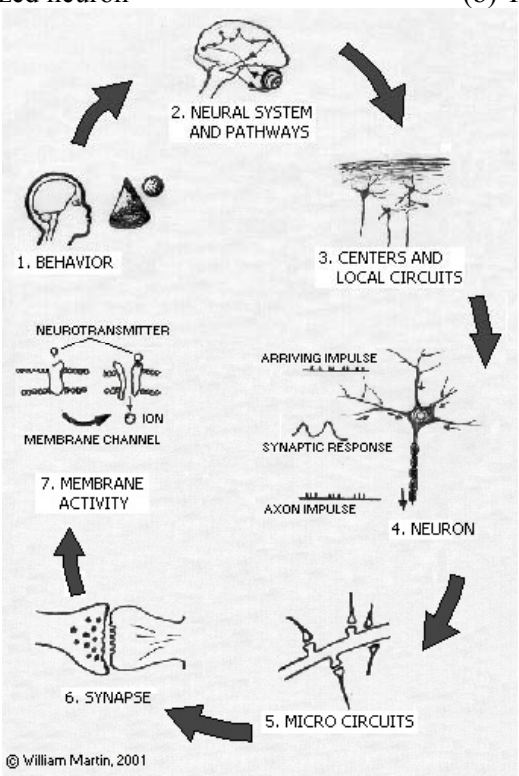

(c) Levels of information processing in man

Figure 3-36. The biological nervous system

Neural Composite Materials

AFC patches (Figure 3-37), PZT ribbons (Figure 3-38), and integrated circuits and components will be used to model the human nervous system. A neural unit cell (Figure 3-39) is the basic unit of the sensor system and local signal processor modules, a digital data bus, a transducer bus controller, and a centralized processing unit (CPU) to form the structural monitoring and control system. To develop the neural system for wind turbine blades, we propose a collaboration among NCA&T State University, a biophysics professor at the University of North Carolina at Greensboro, and a sensor manufacturer.

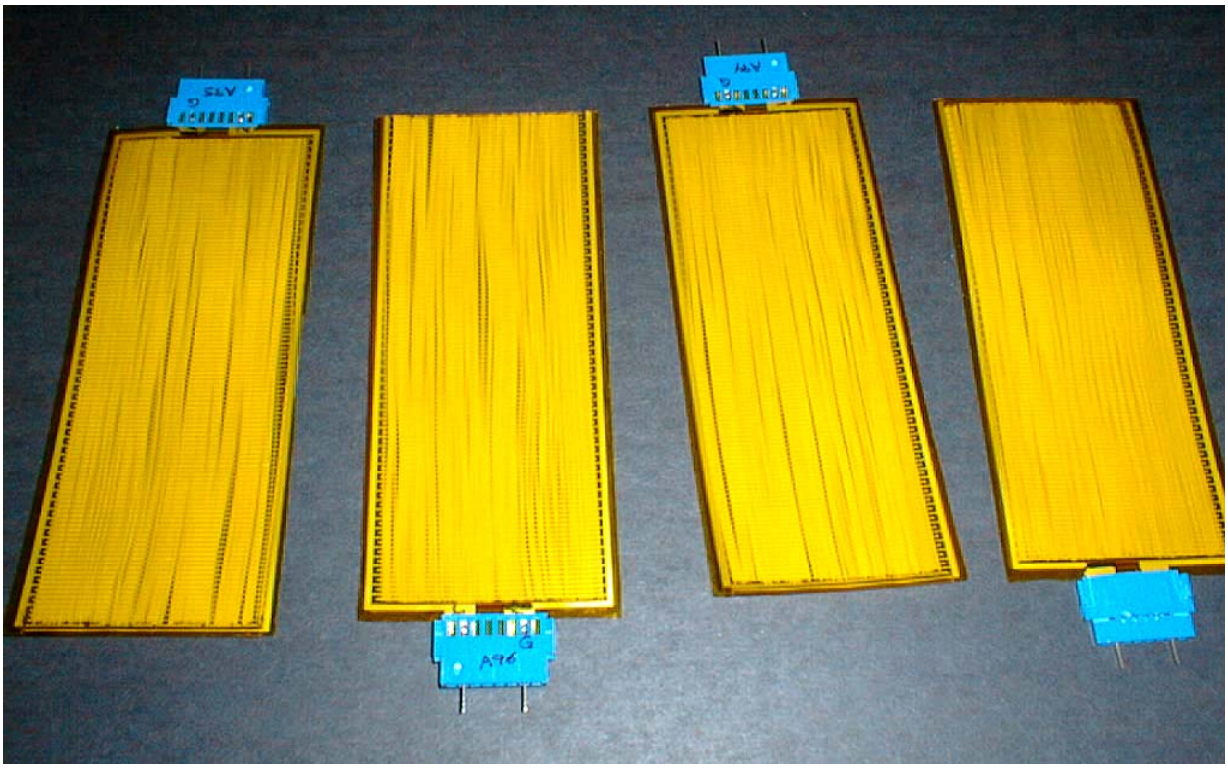

Figure 3-37. AFC actuator/sensors (5.25 * 2.25 * 0.08 in.)

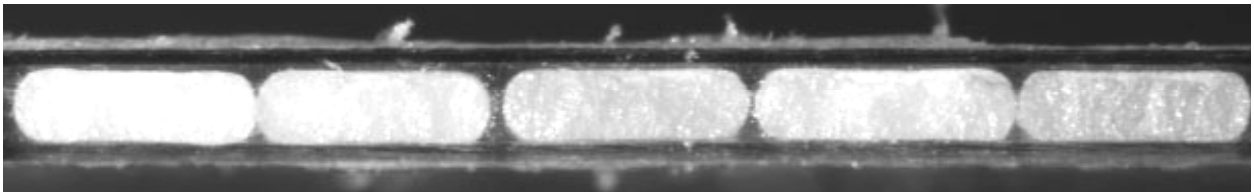

Figure 3-38. Active fiber composite to model nerve dendrites (five PZT ribbons AR = 3:1, w = 450 microns, t = 150 microns, photo courtesy of Continuum Control Corp. and CeraNova Corp.)

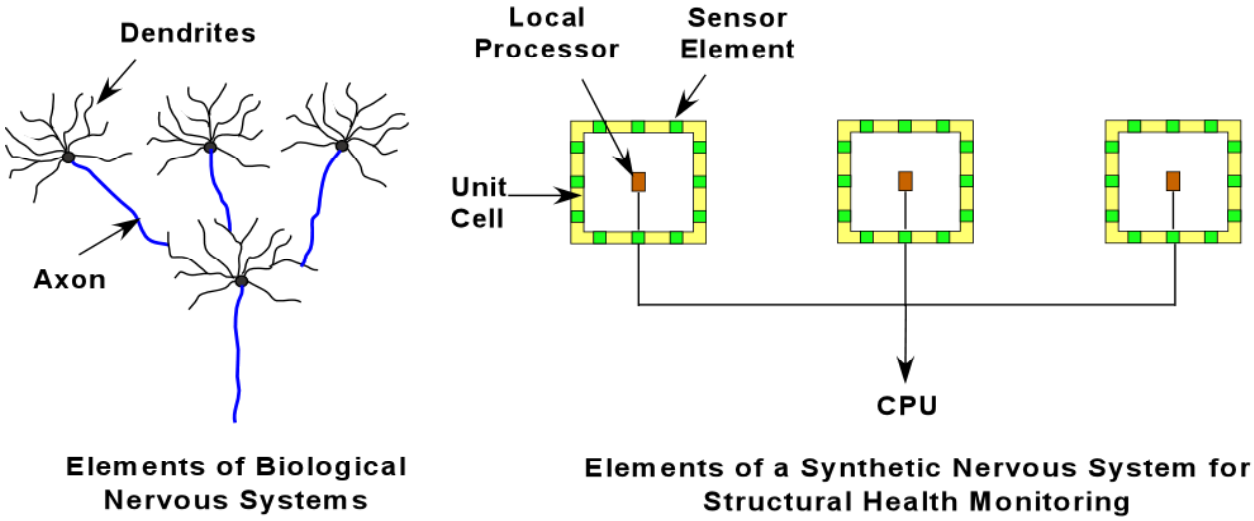

Figure 3-39. Modeling the human nervous system using engineering materials

Figure 3-40 shows a concept blade that can function passively or actively. The electronic components of the sensor system can be developed by a sensor manufacturer using currently available technology (Figure 3-41). The neural system will be able to sample dynamic strains and detect acoustic emissions. The algorithms to do this are being developed and tested using large-scale instrumentation. The algorithms are based on the superposition principle of the Fourier transform, analog filtering, thresholding, triggering, and waveform parameter extraction methods. Most of the signal processing will be done locally within the transducer bus interface module (TBIM), and information on the blade condition will be sent to the CPU at regular intervals. Some functions of the TBIM will also be remotely programmable. The procedure for extracting an AE signal from the continuous sensor follows. Consider the signal output from the continuous sensor f_{cs} as a sum of the signals from all the N sensor nodes

$$f_{cs}(t) = \sum_{i=1}^{N} f_i(t) \,. \qquad \text{(Eq. 3-37)}$$

The Fourier transform of Equation 3-37 is

$$F_{cs}(\omega) = \sum_{i=1}^{N} F_i(\omega) \qquad \text{(Eq. 3-38)}$$

where $F_{cs}(\omega) = \int_{-\infty}^{\infty} f_{cs}(t) e^{-i\omega t} dt$, $F_i(\omega) = \int_{-\infty}^{\infty} f_i(t) e^{-i\omega t} dt$ and ω is frequency. Equation 3-38 shows that the frequency content of the output from the continuous sensor is the sum of the frequency content from all the individual sensor nodes. Thus, all the high frequency AE information will be contained in the response of the continuous sensor. The sensor nodes in the neighborhood of the AE location will receive the AE signal and the remaining sensors will not. Analog filtering will remove the low-frequency content and then triggering and thresholding can be done to extract the pertinent features of the AE signal. The signal without filtering can be monitored to detect high dynamic strains in the blade. This information can possibly be used to predict the remaining fatigue life of the blade using the fatigue data in [1].

The intelligent blade could be coupled to a remote monitoring station that would log health information from the wind turbine. An approach has also been outlined to make the intelligent blade autonomous. The PZT nerves are already self-powered, and the AFC material can also be used for micropower generation to power the TBIM for signal processing. Wireless transmission of the reduced health information could

simplify the health monitoring system. We estimate that a passive health monitoring system will require about 1 W of power per TBIM unit cell to operate. Thus each blade might require a few watts of power generation. This could be achieved by harvesting strain energy in the blades produced by the gravity moments and the wind loading. The cost of development of the neural system would be leveraged by different agencies and applications that can use this technology, including the Army and NASA. The improved reliability, reduced maintenance, and increased wind capture would make the intelligent blade cost effective.

.

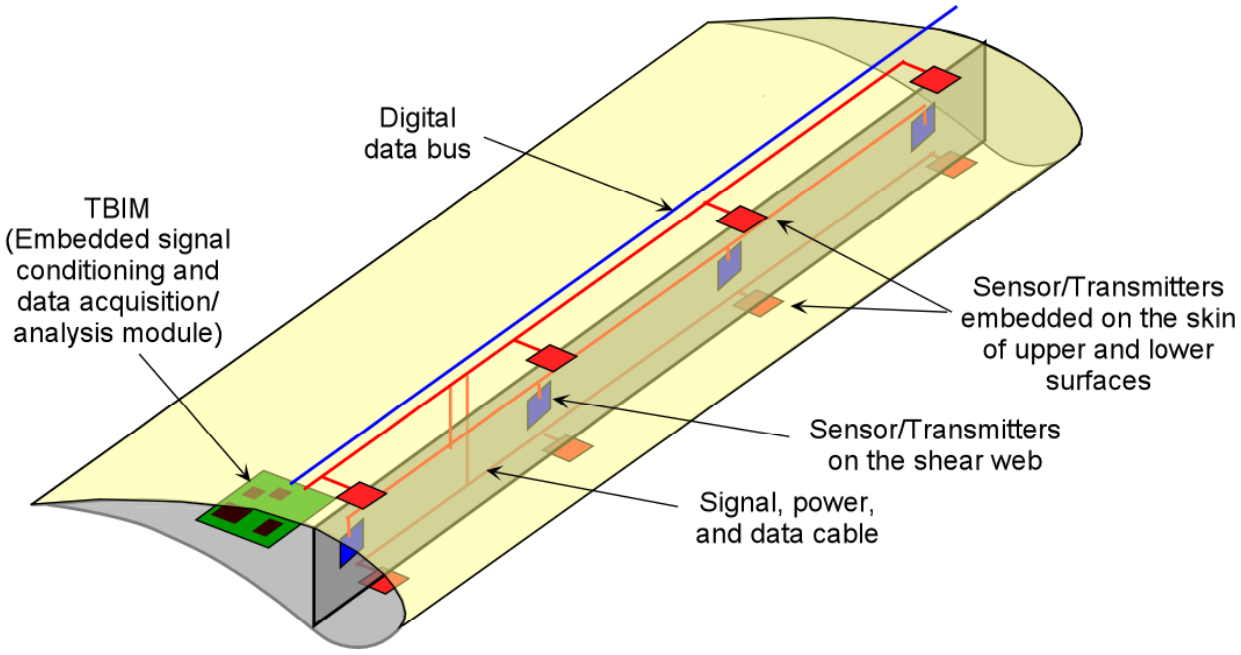

Figure 3-40. Concept for the intelligent blade

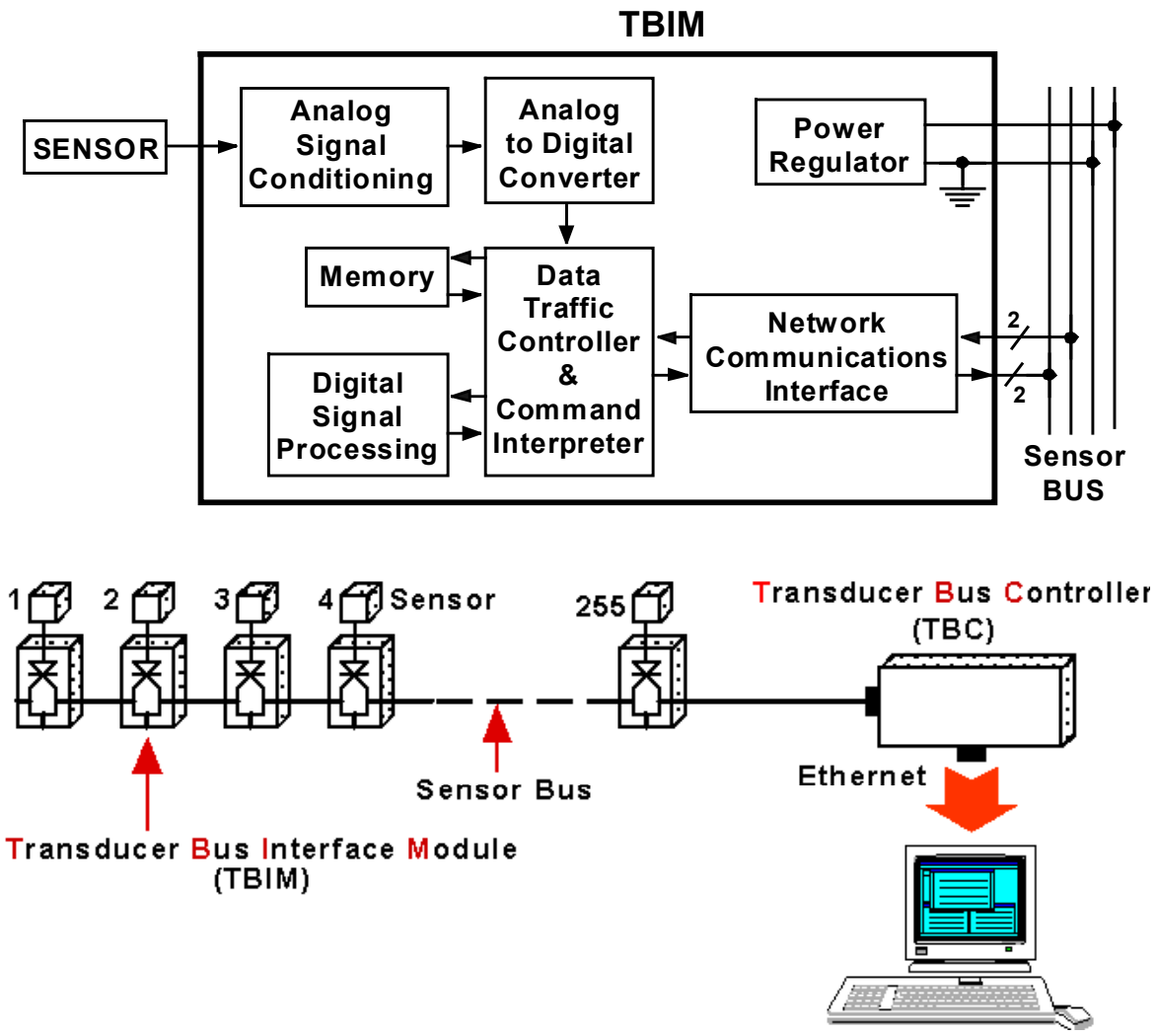

Figure 3-41. TBIM block diagram and transducer bus controller (TBC) and computer interconnection (figure courtesy of Endevco Incorporated)

Conclusions

Modeling, simulation, and experimentation have shown the feasibility of detecting damage in composite structures using different sensor types and algorithms. The algorithms developed in this work are based on detecting damage using a minimum number of channels of data acquisition. In developing the algorithms we considered the cost, the large size of the blades, and the fact that the system must operate from 10 to 30 years. Vibration-based methods were developed first, which give a more global measure of the health of the structure using a small number of sensors. Wave propagation methods were then considered for detecting small damages. Active and passive interrogation methods were considered. The active methods require extra hardware to generate diagnostic signals, and they can be used when the turbine is operating or stopped. Active methods require storage of pre-damage healthy data. Passive methods sense high strains and listen for AE resulting from damage. The passive methods require greater spatial coverage of the structure with sensors.

Health monitoring using distributed AFC sensors is thought to be a very practical technique. Vibration, AE, and strains can be measured using the distributed sensors. We introduced and discussed a concept for an intelligent blade that uses AFC materials and microelectronics to mimic the biological nervous system. Testing of continuous sensors showed that they were capable of detecting AE on large composite structures and simultaneously reducing the number of channels of data acquisition by an order of magnitude. The intelligent blade could be developed in a follow-on phase project. Both a blade manufacturer and Sandia Laboratory are interested in participating in the development of the intelligent blade.

References for Part 3

1. Sutherland, H. J., "A Summary of the Fatigue Properties of Wind Turbine Materials," *Wind Energy*, Vo. 3, No. 1034, 2000.
2. Mandell, John, University of Montana, Personal Correspondence, johnm@coe.montana.edu, August 4, 2000.
3. Ghoshal, A., Sundaresan, M.J. Schulz, M.J., Pai. P.F., "Structural Health Monitoring Techniques for Wind Turbine Blades," *Journal of Wind Engineering and Industrial Aerodynamics*, Vol. 85, pp. 309-324, 2000.
4. Schulz, M.J., Pai, P.F., Inman, D.J., "Health Monitoring and Active Control of Composite Structures Using Piezoceramic Patches," *Composites B Journal*, Vol. 30B, No. 7, pp. 713-725, 1999.
5. Schulz, M.J., Pai, P.F., Naser, A.S., and Chung, J.H., "Locating Structural Damage Using Frequency Response Reference Functions," *Journal of Intelligent Materials Systems and Structures*, Vol. 9, No. 11, pp. 899-905, 1999.
6. Zhang, H., Schulz, M.J., Naser, A.S., Ferguson, F., and Pai, P.F., "Structural Health Monitoring Using Transmittance Functions," *Mechanical Systems and Signal Processing*, Vol. 13, No. 5, pp. 765-787, 1999.
7. Thyagarajan, S.K., Schulz, M.J., Pai, P.F., and Chung, J., "Detecting Structural Damage Using Frequency Response Functions," letter to the editor, *Journal of Sound and Vibration*, Vol. 210, No. 1, pp. 162-170, 1998.
8. Schulz, M.J., Ghoshal, A., Sundaresan, M.J., Ferguson, F., Pai, P.F., and Chung, J. H., "Distributed Sensors for Health Monitoring of Composite Materials," *ACUN-2 International Composites Meeting*, *Composites in the Transportation Industry*, University of New South Wales, Sydney, Australia, February 14-18, 2000.
9. Ghoshal, A., Sundaresan, M.J., Schulz, M.J., and Pai, P.F., "Continuous Sensors for Structural Health Monitoring," *Adaptive Structures and Material Systems Symposium at the International Mechanical Engineering Congress and Exposition Winter Annual Meeting of the American Society of Mechanical Engineers*, November 5-10, 2000, Walt Disney World Dolphin, Orlando, FL.
10. Mickens, T., Schulz, M.J., Sundaresan, M.J., Ghoshal, A., and Ferguson, F., "Structural Health Monitoring Using The Resonant Comparison Method," *NASA URC-SC 2000 Conference*, Nashville, TN, April 7-10, 2000.
11. Ghoshal, A., Harrison, J., Sundaresan, M.J., Schulz, M.J., and Pai, P.F., "Toward Development of an Intelligent Rotor System," *American Helicopter Society Annual Meeting*, Virginia Beach, VA, May 2000,
12. Schulz, M.J., Sundaresan, M.J., and Ghoshal, A., "Active Fiber Composites for Structural Health Monitoring," *Society of Photo-Optical Instrumentation Engineers 7th International Symposium on Smart Materials and Structures*, March 5-9, 1999.
13. Sundaresan, M.J., Ghoshal, A., Schulz, M.J., and Pai, P.F., "Acoustic Emission Sensing Using Piezoceramic and Active Fiber Composite Patches," *American Society of Nondestructive Testing 1999 Fall Conference*, Phoenix, AZ, October 11-15, 1999.

14. Sundaresan, M.J., Schulz, M.J., Hill, J., Wheater, E.A., Ferguson, F., and Pai, P.F., "Damage Detection on a Wind Turbine Blade Section," *International Modal Analysis Conference XVII*, Orlando, FL, February 3-8, 1999.
15. Martin, W.N., Schulz, M.J., Naser, A.S., Pai, P.F., and Wilkerson, C., "Detecting Damage on Symmetric Structures Using Vibration Measurements," *Fifth International Conference on Composites Engineering*, Las Vegas, NV, July 5-11, 1998.
16. Schulz, M.J., Naser, A.S., Wori, L., and Pai, P.F., "Damage Detection in Composite Beams using Longitudional Vibration," *5th International Conference on Composites Engineering*, Las Vegas, NV, July 5-11, 1998.
17. Martin, W.N., Jr., Naser, A.S., Schulz, M.J., Turrentine, D.F., and Eley, S.M., "Health Monitoring of Aerospace Structures Using Symmetric Transmittance Functions*," NASA URC-TC'98 Technical Conference Abstracts*, Huntsville, AL, February 22-25, 1998,.
18. Schulz, M.J., Pai, P.F., Naser, A.S., Thyagarajan, S.K., and Mickens, T.D., "A New Approach to Overcoming Spatial Aliasing in Structural Damage Detection," *NASA URC Technical Conference*, Huntsville, AL, February 22-26, 1998.
19. Zhang, H., Naser, A.S., Schulz, M.J., and Pai, P.F., "Health Monitoring of Composite Beams Using Piezoceramic Patches And Curvature Transmittance Functions," *American Society of Civil Engineering, Engineering Mechanics Division,* San Diego, CA, May 17-20, 1998.
20. Schulz, M.J., Brannon, G.S., Naser, A.S., and Pai, P.F., "Structural Health Monitoring using Frequency Response Functions and Sparse Measurements," *IMAC-XVI Conference*, Santa Barbara, CA, February 2-5, 1998.
21. Schulz, M.J., Naser, A.S., Pai, P.F., and Chung, J., "Locating Structural Damage Using Frequency Response Reference Functions and Curvatures," *International Workshop on Structural Health Monitoring*," Stanford University, Stanford, CA, September 18-20, 1997.
22. Schulz, M.J., Pai, P.F., Abdelnaser, A.S., and Chung, J., "Structural Damage Detection Using Transmittance Functions," *IMAC-XV Conference*, Orlando, FL, February 3-6, 1997.
23. Schulz, M.J., Pai, P.F., and Abdelnaser, A.S., "Frequency Response Function Assignment Technique for Structural Damage Identification," *IMAC-XIV Conference*, Dearborn MI, February 12-15, 1996.
24. Lichtenwalner, P.F., Dunne, J.P., Becker, R.S., and Baumann, E.W., "Active Damage Interrogation System for Structural Health Monitoring," *Proceedings, SPIE Symposium on Smart Structures and Materials*, San Diego, CA, 1997.
25. Chang, F., "Structural Health Monitoring: Demands and Challenges," *SPIE 7th International Symposium on Smart Structures and Materials*, keynote paper 3990-17, Newport Beach, CA, March 5-9, 2000.
26. Sun, F., Rogers, C.A., and Liang, C., "Structural Frequency Response Function Acquisition Via Electric Impedance Measurement of Surface-Bonded Piezoelectric Sensor/Actuator", *American Institute of Aeronautics and Astronautics*, AIAA-95-1127-CP, pp. 3450-3458, New Orleans LA, 1995.
27. Schoess, J., Malver, F., Iyer, B., and Kooyman, J., "Rotor Acoustic Monitoring System (RAMS)-A Fatigue Crack Detection System," *American Helicopter Society (AHS) Forum 53*, Virginia Beach, VA, May 1, 1997,.
28. Prosser, W.H., Jackson, K.E., Kellas, S., Smith, B.T., McKeon, J., and Friedman, A., "Advanced Waveform Based Acoustic Emission Detection of Matrix Cracking in Composites," *Materials Evaluation*, Vol. 53, No. 9, pp. 1052-1058, September 1995.
29. Prosser, W.H., "Acoustic Emission Structural Health Monitoring," *Nondestructive Evaluation Sciences Branch Aviation Safety NRA Meeting*, internal document, NASA Langley Research Center, Hampton VA, December, 17, 1998.
30. Sundaresan, M. J., and Shankar, G., "The Use of AET for Classifying Failure Modes in Composite Materials," *ASME Winter Annual Meeting*, New Orleans, LA, November 23, 1993.
31. Seydel, R.E., and Chang, F., "Implementation of a Real-Time Impact Identification Technique for

Stiffened Composite Panels," *Proceedings of Second International Conference on Structural Health Monitoring,* Stanford University, Sept. 8-10, 1999, p. 225-233.
32. Wang, C.S., Chang, F., "Built-In Diagnostics for Impact Damage Identification of Composite Structures," *Proceeding of the Second International Conference on Structural Health Monitoring*, Stanford University, Stanford CA, pp. 612-621, Sept. 8-10, 1999.
33. James, George H., III, "Development of Structural Health Monitoring Techniques Using Dynamics Testing," *Sandia Report: SAND96-0810*, UC-706, Sandia National Laboratories, Albuquerque, NM, April 1996.
34. Doebling, S.W., Farrar, C.R., Prime, M.B. and Shevitz, D.W., "Damage Identification and Health Monitoring of Structural and Mechanical Systems from Changes in their Vibration Characteristics: A Literature Review," *Los Alamos National Laboratory (LANL) Report* LA-13070-VA5, LANL, Los Alamos, NM, 1996.
35. Friswell, M.J., and Penny, J.E., "The Practical Limits of Damage Detection and Location using Vibration Data," *11th Symposium on Structural Dynamics and Control*, Blacksburg, VA, May 12, 1997.
36. Banks, H.T., Inman, D.J. Leo, D.J. and Wang, Y., "An Experimentally Validated Damage Detection Theory in Smart Structures," *Journal of Sound and Vibration*, Vol. 191, No. 5, pp. 859-880, 1996.
37. Stevens, P.W., Hall, D.L., and Smith, E.C., "Multidisciplinary Approach to Rotorcraft Health and Usage Monitoring,"*AHS 52 Annual Forum*, Washington, DC, June 4-6, 1996.
38. Gerardi, T. G., "Health Monitoring of Aircraft," *Journal of Intelligent Material Systems and Structures*, Vol. 1, July 1990.
39. Cronkhite, J. D., "Practical Application of Health and Usage Monitoring (HUMS) to Helicopter Rotor, Engine, and Drive Systems," *AHS 49 Annual Forum*, St. Louis, MO, May 19-21, 1993.
40. Ganguli, R., Chopra, I., and Haas, D.J., "Helicopter Rotor System Health Monitoring Using Numerical Simulation and Neural Networks," *AHS 53 Annual Forum*, Virginia Beach, VA, April 29-May 1, 1997.
41. Pines, D.J., "Damage Detection using Wave Element by Element Sensitivity Analysis," *38th AIAA/ASME/ASCE/AHS/ASC Structures, Structural Dynamics, and Materials Conference and Exhibit, AIAA/ASME/AHS Adaptive Structures Forum*, April 7-10, Kissimmee, FL, 1998.
42. Zimmerman, D.C., and Kaouk, M., "Structural Damage Detection Using A Subspace Rotation Algorithm," *AIAA Conference*, AIAA-92-2521-CP, pp. 2341-2350, 1992.
43. Zimmerman, D.C., Simmermacher, T., and Kaouk, M., "Model Correlation and System Health Monitoring Using Frequency Domain Measurements," *AIAA Conference*, AIAA-95-1113-CP, New Orleans LA, 1995.
44. Schulz, M.J., Naser, A.S., Pai, P.F., Martin, W.N., Turrentine, D., and Wilkerson, C., "Health Monitoring of Composite Material Structures Using A Vibrometry Technique," *4th International Conference on Composites Engineering*, Hawaii, July 6-11, 1997.
45. Wori, L., Schulz, M.J., Naser, A.S., and Pai, P.F., "Damage Detection in Composite Beams using Longitudinal Vibration," *5th International Conference on Composites Engineering*, Las Vegas, NV, July 5-11, 1998.
46. Pai, P.F., Young, L.G., Schulz, M.J., and Tu, K.C., "A Hybrid Modeling Approach for Structural Health Monitoring," *5th International Conference on Composites Engineering*, Las Vegas, NV, July 5-11, 1998.
47. Mayes, R.L., "An Experimental Algorithm for Detecting Damage Applied to the I-40 Bridge over the Rio Grande," *Proc. 13th International Modal Analysis Conference*, pp. 219-225, 1995.
48. James, G.H., Zimmerman, D.C., Farrar, C.R. and Doebling, S.W., short course, "Current Horizon for Structural Damage Detection," *Course Notes*, *IMAC-XV Conference*, Orlando, Fla., January 30-February 1, 1997.
49. Simmermacher, T., James, G.H., III, Hurtado, J.E., "Structural Health Monitoring of Wind Turbines," *Proceedings of the International Workshop on Structural Health Monitoring*, Stanford,

CA, September 18-20, pp. 788-797, 1997.
50. Chen. S., Venkatappa, S., Petro, S.H., Dajani, J.N., GangaRao, H. V.S., “Damage Detection Using Scanning Laser Vibrometer,” *3rd International Conference on Vibration Measurements by Laser Techniques,*" Ancona, Italy, June 16-19, 1998.
51. Staszewski, W.J., and Tomlinson, G.R., "Application of the Wavelet Transform to Fault Detection in a Spur Gear", *Mechanical Systems and Signal Processing*, Vol. 8, No. 3, pp. 289-307, 1994.
52. Sundaresan, M.J., Ghoshal, A., and Schulz, M.J., "A Distributed Sensor to Measure Acoustic Waves in Plates," submitted to the *Journal of Intelligent Material Systems and Structures*.
53. Sundaresan, M.J., Ghoshal, A., and Schulz, M.J., "An Intelligent Sensor for Damage Detection in Bars," submitted to the *Journal of Smart Materials and Structures*.
54. Mickens, T., Schulz, M. Sundaresan, M., Ghoshal, A., Naser, A.S., and Reichmeider, R., "Structural Health Monitoring of an Aircraft Joint," submitted to the *Journal of Mechanical Systems and Signal Processing*.
55. Waldron, K., Ghoshal, A., Schulz, M. J., Sundaresan, M.J., Ferguson, F., Pai, P.F., and Chung, J.H., "Damage Detection Using Finite Elements and Laser Operational Deflection Shapes," in press, *Journal of Finite Elements in Analysis and Design*.
56. Sundaresan, M.J., Pai, P.F., Ghoshal, A., Schulz, M.J., Ferguson, F., and Chung, J., "Methods of Distributed Sensing for Health Monitoring of Composite Material Structures," submitted to the special issue of the *Composites A Journal*, April, 2000.
57. Sundaresan, M.J., Schulz, M.J., Ghoshal, A., and Pratap, P., "A Neural System for Structural Health Monitoring," *SPIE 8th international Symposium on Smart Materials and Structures*, March 4-8, 2001.
58. Sundaresan, M.J. Schulz, M.J., Ghoshal, A., and Ferguson, F., "Active Fiber Composite Sensors and Actuators," *ACUN-3 International Composites Meeting, Technology Convergence in Composites Applications*, University of New South Wales, Sydney, Australia, February 6-9, 2001.
59. Sundaresan, M. J., Schulz, M.J., Ghoshal, A., Laxson, A., Musial, W., Hughes, S., and Almeida, T., "An Intelligent Blade for Wind Turbines," *39th AIAA/ASME Aerospace Sciences Meeting and Exhibit, Wind Energy Symposium*, Reno, NV, January, 8-11, 2001.
60. Hughes, D.R., Sundaresan, M.J., Ghoshal, A., McMichael, J., and Schulz, M.J., "Fatigue Crack Detection Using Wavelets," *International Conference on Composites Engineering/7*, Denver, CO, July 2000.
61. Sundaresan, M.J., Ghoshal, A., Schulz, M.J., and Wilkerson, C., "Acoustic Emission Monitoring using Distributed Sensors," *ASNT Spring Conference and 9th Annual Research Symposium*, Birmingham, AL, March 27-31, 2000.
62. Waldron, K., Ghoshal, A., Schulz, M.J., Sundaresan, M.J., and Ferguson, F., "Structural Damage Detection Using Operational Deflection Shapes," *NASA URC-SC 2000 Conference*, Nashville, TN April 7-10, 2000.
63. Pai, P.F., Jin, S., and Schulz, M.J., "Structural Damage Detection Using a Scanning Laser Vibrometer," *AHS Annual Meeting*, Virginia Beach, VA, May 2000.
64. Waldron, K., Ghoshal, A., Schulz, M.J., Sundaresan, M.J., Ferguson, F., Pai,. P.F., and Chung, J. H., “The Use of Operational Deflection Shapes for Structural Damage Detection,” *IMAC XVIII*, San Antonio, TX, Feb. 7-10, 2000.
65. Sundaresan, M.J., Ghoshal, A., Schulz, M.J., Ferguson, F., Pai, P.F., and Chung, J.H., “Crack Detection Using a Scanning Laser Vibrometer,” *Second International Conference on Structural Health Monitoring*, Stanford University, Stanford, CA, 1999.
66. Ghoshal, A., Sundaresan, M.J., Schulz, M.J., and Pai, P.F., “Damage Detection in Composite Structures using Vibration Measurements,” *6th International Conference on Composites Engineering*, Orlando FL, June 27-July 3, 1999.

67. Sundaresan, M.J., Ghoshal, A., Schulz, M.J., Ferguson, F., Pai, P.F., and Wilkerson, C., "Damage Detection Using a Laser Vibrometer and Active Fiber Composite Patch," *6th International Conference on Composites Engineering*, Orlando, FL, June 27-July 3, 1999.
68. Ness, S., and Sherlock, C.N., "Nondestructive Testing Handbook, Vol. 10, Nondestructive Testing Overview," *American Society for Nondestructive Testing*, Columbus OH, 1996.
69. Continuum Control Corporation, company literature, 45 Manning Park, Billerica, MA 01821.
70. CeraNova Corporation, company literature, 101 Constitution Boulevard, Suite D, Franklin, MA 02038-2587.
71. Active Control Experts, company literature, 215 First St., Cambridge MA 02142.
72. Soedel, W., Vibration of Plates and Shells, second edition, Marcel Dekker, New York, 1992.
73. Kolsky, H., "Stress Waves in Solids," Dover, London, 1961.
74. Personal conversations with W.J. Staszewski, The University of Sheffield, Department of Mechanical Engineering, United Kingdom, March, 2000.
75. Achenbach, J.D., Wave Propagation in Elastic Solids, North Holland Publishing Company, NY, 1973.
76. Ballentine, D.S., White, R.M., Martin, S.J., Ricco, A.J., Zellers, E.T., Frye, G.C., and Wohltjen, H., Acoustic Wave Sensors, Theory, Design and Physico-Chemical Applications, Academic Press, San Diego CA, 1997.
77. Campbell, C.K., Surface Acoustic Wave Devices for Mobile and Wireless Communications, Academic Press, San Diego CA, 1997.
78. Schmerr, L.W. Jr., Fundamentals of Ultrasonic Nondestructive Evaluation, Plenum Press, NY, 1998.
79. Wasley, R.J., Stress Wave Propagation in Solids, Marcel Dekker, New York, 1973.
80. Bent, A.A., and Hagood, N.W., "Piezoelectric Fiber Composites with Interdigitated Electrodes," *Journal of Intelligent Material Systems and Structures*, 8, 1998.
81. Bent, A. A., Active Fiber Composites for Structural Actuation, Ph.D. thesis, MIT, January 1997.
82. Hagood, N.W., Pizzochero, A., "Residual Stiffness and Actuation Properties of Piezoelectric Composites: Theory and Experiment," *Journal of Intelligent Material Systems and Structures*, Vol. 8, pp.724-737, September 1997.
83. Chee, C.Y.K., Tong, L., and Steven, G.P., "A Review on the Modeling of Piezoelectric Sensors and Actuators Incorporated in Intelligent Structures," *Journal of Intelligent Material Systems and Structures*, Vol. 9, pp. 3-19, January 1998.
84. Dong, J.J. "A Continuum Mixture Theory of Wave Propagation in Axially Polarized Piezoelectric Fibrous Composites," Ph.D. dissertation, University of Cincinnati, 1993.
85. Patent Application: "Sensor Array System," M. J. Sundaresan, A. Ghoshal, and M. J. Schulz, patent pending June 2000.

Publications and Students Supported

The publications below are from work that was supported partly by the NREL project and partly by other projects.

Sundaresan, M.J., Ghoshal, A., and Schulz, M.J., "A Distributed Sensor to Measure Acoustic Waves in Plates," submitted to the *Journal of Intelligent Material Systems and Structures*.

Sundaresan, M.J., Ghoshal, A., and Schulz, M.J., "An Intelligent Sensor for Damage Detection in Bars," submitted to the *Journal of Smart Materials and Structures*.

Waldron, K., Ghoshal, A., Schulz, M.J., Sundaresan, M.J., Ferguson, F., Pai, P.F., and Chung, J.H., "Damage Detection Using Finite Elements and Laser Operational Deflection Shapes," in press, *Journal of Finite Elements in Analysis and Design*.

Sundaresan, M.J., Pai, P.F., Ghoshal, A., Schulz, M.J., Ferguson, F., and Chung, J., "Methods of distributed sensing for health monitoring of composite material structures," submitted to the special issue of the *Composites A Journal*, April 2000.

Ghoshal, A., Sundaresan, M. J. Schulz, M. J., and Pai. P.F., "Structural Health Monitoring Techniques for Wind Turbine Blades," *Journal of Wind Engineering and Industrial Aerodynamics*, Vol. 85, pp. 309-324, 2000.

Schulz, M.J., Pai, P.F., and Inman, D.J., "Health Monitoring and Active Control of Composite Structures Using Piezoceramic Patches," *Composites B Journal*, Vol. 30B, Number 7, pp. 713-725, 1999.

Schulz, M.J., Pai, P.F., Naser, A.S., and Chung, J. H., "Locating Structural Damage Using Frequency Response Reference Functions," *Journal of Intelligent Materials Systems and Structures*, Vol. 9, No. 11, pp. 899-905, 1999.

Zhang, H., Schulz, M.J., Naser, A.S., Ferguson, F., and Pai, P.F., "Structural Health Monitoring using Transmittance Functions," *Mechanical Systems and Signal Processing*, Vol. 13, No. 5, 765-787, 1999.

Sundaresan, M.J., Schulz, M.J., Ghoshal, A., and Pratap, P., "A Neural System for Structural Health Monitoring," *SPIE 8th international Symposium on Smart Materials and Structures*, March 4-8, 2001.

Sundaresan, M. J. Schulz, M.J., Ghoshal, A., Ferguson, F., "Active Fiber Composite Sensors and Actuators," *ACUN-3 International Composites Meeting, Technology Convergence in Composites Applications*, University of New South Wales, Sydney, Australia, February 6-9, 2001.

Sundaresan, M.J., Schulz, M.J., Ghoshal, A., Laxson, A., Musial, W., Hughes, S., and Almeida, T., "An Intelligent Blade for Wind Turbines," *39th AIAA/ASME Aerospace Sciences Meeting and Exhibit*, *Wind Energy Symposium*, Reno, NV, January 8-11, 2001.

Ghoshal, A., Sundaresan, M.J., Schulz, M.J., Pai, P.F., "Continuous Sensors for Structural Health Monitoring," *Adaptive Structures and Material Systems Symposium at the International Mechanical Engineering Congress and Exposition Winter Annual Meeting of the ASME*, Walt Disney World Dolphin, Orlando FL, November 5-10, 2000.

Hughes, D.R., Sundaresan, M.J., Ghoshal, A., McMichael, J., and Schulz, M.J., "Fatigue Crack Detection Using Wavelets," *International Conference on Composites Engineeirng/7*, Denver, CO July 2000.

Sundaresan, M.J., Ghoshal, A., Schulz, M.J., and Wilkerson, C., "Acoustic Emission Monitoring Using Distributed Sensors," *American Society of Nondestructive Testing, Spring Conference and 9th Annual Research Symposium*, Birmingham, AL, March 27-31, 2000.

Schulz, M.J., Ghoshal, A., Sundaresan, M.J., Ferguson, F., Pai, P.F., and Chung, J.H., "Distributed Sensors for Health Monitoring of Composite Materials," *ACUN-2 International Composites Meeting, Composites In The Transportation Industry*, University of New South Wales, Sydney, Australia, February 14-18, 2000.

Schulz, M.J., Sundaresan, M.J., Ghoshal, A., "Active Fiber Composites for Structural Health Monitoring," *SPIE 7th International Symposium on Smart Materials and Structures*, March 5-9, 2000.

Waldron, K., Ghoshal, A., Schulz, M.J., Sundaresan, M.J., Ferguson, F., Pai,. P.F., and Chung, J. H., "The Use of Operational Deflection Shapes for Structural Damage Detection," *IMAC XVIII Conference*, San Antonio, TX, February 7-10, 2000.

Ghoshal, A., Sundaresan, M.J., Schulz, M.J., and Pai, P.F., "Damage Detection in Composite Structures Using Vibration Measurements," *6th International Conference on Composites Engineering,* Orlando FL, June 27-July 3, 1999.

Sundaresan, M.J., Ghoshal, A., Schulz, M.J., and Pai, P.F., "Acoustic Emission Sensing Using Piezoceramic and Active Fiber Composite Patches," *ASNT Fall Conference*, Phoenix, AZ., October 11-15, 1999.

Sundaresan, M.J., Ghoshal, A., Schulz, M.J., Ferguson, F., Pai, P.F., and Wilkerson, C., "Damage Detection using a Laser Vibrometer and Active Fiber Composite Patch," *6th International Conference on Composites Engineering*, Orlando FL, June 27-July 3, 1999.

Sundaresan, M.J., Schulz, M.J., Hill, J., Wheater, E.A., Ferguson, F., Pai, P.F., "Damage Detection on a Wind Turbine Blade Section," *IMAC XVII Conference*, Orlando FL, February 3-8, 1999.

Pai, P.F., Young, L.G., Schulz, M.J., and Tu, K.C., "A Hybrid Modeling Approach for Structural Health Monitoring," *5th International Conference on Composites Engineering*, Las Vegas NV, July 5-11, 1998.

Schulz, M.J., Naser, A.S., Wori, L., and Pai, P.F., "Damage Detection in Composite Beams using Longitudional Vibration," *5th International Conference on Composites Engineering*, Las Vegas NC, July 5-11, 1998.

The work leading to the patent application: "Sensor Array System," M. J. Sundaresan, A. Ghoshal and M. J. Schulz, patent pending from June 2000, was partially sponsored by the NREL project.

Six NCA&T students performed structural health monitoring research that was partially supported by this project. Their names and degrees are listed below.

Jeremy Harrison, BSME 2000, current MS student

Ken Waldron, BSME 1999, current MS student

Travluss Mickens, MSME 2000

Dave Turrentine, BSME 1999, current MS student

Chavis Raynor, BSME 2000

Jamaal Hill, BSME 2000

Acknowledgment

The grant technical monitor for the first year was Dr. Peter Tu, and for the second and third years was Mr. Alan Laxson. Their contributions in directing the research and providing contacts with other researchers at the NREL, Sandia Labs, and industry helped the project tremendously. Their contributions are gratefully acknowledged. The blade proof testing was performed during August 1999 at the National Wind Technology Center, a laboratory of the National Renewable Energy Laboratory (NREL) in Golden CO. The opportunity for using the facilities and to participate in the blade testing and the support of Mr. Walt Musial and Mr. Scott Hughes is gratefully acknowledged. Technical advice on conducting the testing was provided by Mr. Mark Rumsey of Sandia National Laboratory. His help is also gratefully acknowledged.

REPORT DOCUMENTATION PAGE

Form Approved
OMB NO. 0704-0188

1. AGENCY USE ONLY (Leave blank)	2. REPORT DATE	3. REPORT TYPE AND DATES COVERED
	September 2001	Subcontract Report - July 10, 1997 to July 10, 2000

4. TITLE AND SUBTITLE
Control and Health Monitoring of Variable-Speed Wind Power Generation Systems

5. FUNDING NUMBERS
RCX-7-16469

6. AUTHOR(S)
Yong D. Song, Marwan Bikdash, and Mark J. Schulz

7. PERFORMING ORGANIZATION NAME(S) AND ADDRESS(ES)
College of Engineering
North Carolina A&T State University
Greensboro, North Carolina

8. PERFORMING ORGANIZATION REPORT NUMBER

9. SPONSORING/MONITORING AGENCY NAME(S) AND ADDRESS(ES)
National Renewable Energy Laboratory
1617 Cole Blvd.
Golden, CO 80401-3393

10. SPONSORING/MONITORING AGENCY REPORT NUMBER
NREL/SR-500-29708

11. SUPPLEMENTARY NOTES

NREL Technical Monitor: Alan Laxson

12a. DISTRIBUTION/AVAILABILITY STATEMENT
National Technical Information Service
U.S. Department of Commerce
5285 Port Royal Road
Springfield, VA 22161

12b. DISTRIBUTION CODE

13. ABSTRACT *(Maximum 200 words)*

This document reports accomplishments on variable speed control, furling analysis, and health monitoring of wind turbines. There are three parts, prepared by Song, Bikdash, and Schulz, respectively. The first part discusses variable-speed control of wind turbines, exploring a memory-based method for wind speed prediction and wind turbine control. The second part addresses the yaw dynamics of wind turbines, including modeling, analysis, and control. The third part of the report discusses new analytical techniques that were developed and tested to detect initial damage to prevent failures of wind turbine rotor blades.

14. SUBJECT TERMS
Variable speed control; furling analysis; wind speed prediction; wind turbine control; yaw dynamics

15. NUMBER OF PAGES

16. PRICE CODE

17. SECURITY CLASSIFICATION OF REPORT	18. SECURITY CLASSIFICATION OF THIS PAGE	19. SECURITY CLASSIFICATION OF ABSTRACT	20. LIMITATION OF ABSTRACT
Unclassified	Unclassified	Unclassified	UL